CGE

Centre of Geodetic Earth System Research

The Earth's gravity field from GOCE

Weiyong Yi

CGE Report 2
2012

FAKULTÄT FÜR BAUINGENIEUR-
UND VERMESSUNGSWESEN

The Earth's gravity field from GOCE

Dissertation

Weiyong Yi

TUM

TECHNISCHE UNIVERSITÄT MÜNCHEN

Technische Universität München

Institut für Astronomische und Physikalische Geodäsie

The Earth's gravity field from GOCE

Weiyong Yi

Declaration

I herewith declare that I have produced this paper without the prohibited assistance of third parties and without making use of aids other than those specified; notions taken over directly or indirectly from other sources have been identified as such. This paper has not previously been presented in identical or similar form to any other German or foreign examination board.

This work was done under the guidance of Professor Reiner Rummel, at the Institut für Astronomische und Physikalische Geodäsie, Technische Universität München.

Munich, March 29, 2012

Abstract

This study deals with the determination of a global model of the Earth's gravity field from the measurements of the Gravity field and steady-state Ocean Circulation Explorer (GOCE) mission. GOCE is the first satellite mission with a gravitational gradiometer on-board. It measures the elements of the gravitational gradient tensor (GGT). The orbit measurements by GPS are sensitive to the long wavelength part of the gravity field, the gradiometer measurements are used for the determination of the short wavelength part with very high accuracy. Both observation types are studied and analyzed in this work.

The integral equation approach is applied to the kinematic orbits. It is modified in several ways. First, continuous transition of successive short arcs is realized in our computation. Second, empirical accelerations are introduced in order to absorb the non-gravitational accelerations and mis-modeling errors. The result obtained with this approach is compared to a very precise GRACE model, resulting in a standard deviation of 7.3 cm up to degree and order 70, based on only two months of GOCE kinematic orbit data.

The gradients obtained from the GOCE gradiometer are analyzed in various aspects, namely in the time domain, in the frequency domain, and in the geographical space domain. The gradiometer exhibits very good performance. Tectonic features are found in the data directly, before a spherical harmonic analysis (SHA) is applied. With a bandpass filter, the gradiometer data are used for SHA. The results from individual components are obtained.

The combination of GOCE SST and SGG is realized by taking the weighted sum of the corresponding parts of the normal matrices as well as of their right hand sides. The reciprocals of the variances of each individual observation type serve as relative weights for their combination. A gravitational field model is obtained purely based on GOCE data, together with a constraint in the polar areas for stabilization. The model is then compared to other recently developed models. It shows very good consistency with them. Validation experiments of our model show a good consistency to external data, namely "GPS leveling" data in several regions. Contributions of individual components are obtained by means of resolution matrices. Their analysis demonstrates that the V_{zz} component is very strong and contributes up to 32.7% of the

total solution. The constraint in the polar areas as applied in our solution contributes mainly to the zonal and near-zonal coefficients with a percentage of 0.2%.

Apart from the GOCE only solution, also a combined gravitational field model named GOGRA01s is obtained by the combination of GOCE with GRACE. This model is very accurate in the long wavelength part (due to GRACE) and short wavelength part (due to GOCE). The contribution of GRACE in this model is 30.06%, whereas that of GOCE is 69.9%.

The gravity field model derived from GOCE-only measurements is analyzed in terms of degree RMS and degree cumulative error, formal error in terms of geoid height propagated from the variance-covariance matrix, as well as validation with external data. It shows that the GOCE-only model reaches an accuracy of 4 to 6 cm in terms of geoid height. It is quite close to the objective of the mission.

Zusammenfassung

Es soll gezeigt werden, wie ein Schwerefeldmodell aus Messungen der Satellitenmission GOCE hergeleitet wird. GOCE ist die erste Satellitenmission, die mit einem Gravitationsgradiometer ausgestattet ist. Satellitengravitationsgradiometrie (SGG) ist die Messung der zweiten Ableitungen des Gravitationspotential. Es werden die Komponenten des Gravitationstensors (GGT) gemessen. Die Bahnbestimmung dient hauptsächlich dazu, die langen Wellenlängen des Erdschwerefeldes zu detektieren, während die Gradiometermessungen für die Bestimmung der kürzeren Wellenlängen des Schwerefeldes verwendet werden. Beide Arten von Messungen sollen in dieser Arbeit untersucht und analysiert werden.

Die kinematischen Bahnen des GOCE Satelliten sind das Ergebnis des "satellite-to-satellite tracking (SST)". Sie sind die Grundlage des Schwerefeldmodellierung mit der Integralgleichungsmethode. Hierbei wurden einige Neuerungen eingeführt. Erstens ist die Nahtstelle zweier benachbarter Kurzbögen durchgängig, d.h. stetig. Zweitens werden empirische Beschleunigungen eingeführt, um nicht-gravitative Anteile in den Beschleunigungen sowie Fehleranteile zu eliminieren. Das Resultat dieses Ansatzes ist in seiner Qualität vergleichbar mit einem hochpräzisen GRACE Modell. Es wurde eine Standardabweichung von 7.3 cm erreicht unter Verwendung einer Kugelfunktionsentwicklung bis Grad und Ordnung 70 und basierend auf zwei Monaten kinematischer GOCE-Bahn.

Die durch das GOCE Gradiometer ermittelten Gravitationsgradienten werden auf verschiedene Arten analysiert, nämlich im Zeitraum, im Frequenzraum und in ihrer räumlichen Verteilung. Die gemessenen und gefilterten Gradiometerdaten sind von guter Qualität. Tektonische Anteile werden in den Daten direkt sichtbar, noch bevor eine sphärisch-harmonische Analyse (SHA) erfolgt ist. Für die SHA wurden die Gradiometerdaten mit einem Bandpassfilter gefiltert. Jede einzelne Komponente weist eigene Charakteristiken auf.

Die Kombination von SST und SGG erfolgt durch eine gewichtete Summe der korrespondierenden Elemente der Normalmatrix sowie der rechten Seiten des linearen Gleichungssystems. Die Reziproken der Varianzen jedes einzelnen Beobachtungstyps dienen als Relativgewichte für die Kombination. Zu Testzwecken wurde ein Schwerefeldmodell nur aus GOCE-Daten abgeleitet, mit einer Stabilisierung in den beiden Polgegenden in denen keine Daten vorliegen. Anschließend wurde das Modell mit anderen kürzlich erschienenen Modellen verglichen. Das GOCE-Modell zeigt sehr gute Übereinstimmung zu den anderen Modellen. Die Validierung unseres Modell weist eine sehr gute Übereinstimmung auf zu externen Daten, nämlich zu GPS-Nivellementdaten in mehreren Regionen dieser Erde. Der Informationsgehalt der einzelnen Komponenten wurde durch die Berechnung einer Auflösungsmatrix ermittelt. Es zeigt sich, dass die V_{zz}-Komponente einen starken Einfluss von 32,7% auf die Gesamtlösung hat. Die Regularisierung in den polaren Regionen, die wir in unserer Lösung verwenden, hat hauptsächlich einen Einfluss

auf die zonalen und beinahe zonalen Koeffizienten. Dieser Einfluss ist sehr wichtig, beträgt aber nur 0,2% der Gesamtlösung.

Neben einem reinen GOCE Modell wurde ein kombiniertes Schwerefeldmodell aus einer Kombination von GOCE und GRACE berechnet, genannt GOGRA01s. Der Anteil der GRACE-Daten in diesem Modell beträgt 30,06% und der von GOCE 69,9%.

Das Gravitationsfeldmodell nur basierend auf Messugen von GOCE wurde untersucht mit Hilfe von Gradvarianzen, dem kumulativen Fehler pro Grad, dem formalen Fehler der Geoidhöhen auf der Kugel und abgeleitet aus Varianz-Kovarianz-Fehlerfortpflanzung und durch eine Validierung mit unabhängigen Daten. Es zeigt sich, dass der Geoidfehler des GOCE-Modells 4 bis 6 cm beträgt.

Acknowledgements

Contents

List of Figures

List of Tables

1

Introduction

1.1 Motivation

Since the first satellite, Sputnik I, was launched on October 4th, 1957, scientists have benefited tremendously from satellites in their understanding of the evolution and dynamics of the Earth. Since then, many satellite missions have dealt with Earth science. Geodetic satellite belongs, in general, to one of the four following categories (Rummel 1992; Sneeuw 2000):

  i. they serve as a geometric target for point positioning, such as LAGEOS-I and LAGEOS-II,

 ii. as a measurement platform equipped with cameras, SAR or altimetry such as TOPEX/Poseidon, ERS-1 & 2,

iii. as a proof mass in free fall in the Earth's gravitational field for gravity field determination, e.g., CHAMP, GRACE and GOCE, or

 iv. the gyroscopic motion of the orbit plane is used for Earth rotation determination, relative to an inertial reference frame, e.g., again LAGEOS-I and LAGEOS-II.

The knowledge of the Earth's gravitational field (EGF) always needs to be improved in terms of accuracy and resolution. Within reasonable time, substantial improvements can only be achieved by exploiting new approaches based on satellite gravitational observation methods (Freeden et al. 2008). The observations from satellites can be divided essentially into two main categories: geometrical and physical. Since satellites orbit the Earth under the influence of the Earth's gravitational field, almost all the observations can be related to the EGF and are therefore functionals of it. In turn, the EGF can be recovered either from the satellite motion itself, from the relative motion of two or several satellites (satellite-to-satellite tracking (SST)), or from a gravimetric payload, such as a gravitational gradiometer (SGG). In Geodesy attempts are made to extract the maximum information from these data for the purpose of determining the EGF. Nowadays, more and more data are becoming available, resulting in better and better knowledge of the gravity field. The observations collected by satellites are more homogeneous than terrestrial observations, not only in

space, but also in time. This gives us the possibility to explore also the time-varying gravitational field (Wahr et al. 2004).

This dissertation is dedicated to the investigation of the methodologies of SST and SGG as well as to actual gravity modeling from SST and SGG data from the GOCE mission. GOCE is the first satellite mission with a gravitational gradiometer. Despite many investigations (Klees et al., 2003; Rummel, 1996; Rummel and van Gelderen, 1992), there are still many aspects to be learned from the actual GOCE mission, concerning subjects such as the performance of the payload, the characteristics of each individual component, their combination, etc.

The dissertation will address three themes related to gravity field analysis from GOCE. The first of the three topics is SST. Since the GOCE orbit can be computed from GPS data, similar to the case of CHAMP, i.e. by the high-low SST concept, one can recover the EGF based on the kinematic orbits of GOCE. The advantages of GOCE over CHAMP are thereby its lower altitude, which results in a better spatial resolution; second, the higher sampling rate of GOCE, which also increases resolution and precision; and third, the air drag in flight direction of GOCE to be compensated by ion thrusting, which reduces the effect of mis-modeling of air drag. The integral equation approach will be used for gravitational field recovery from GOCE orbits in this study.

The second topic is SGG. The basic observables are accelerations at six locations inside the spacecraft. The gravitational gradients are derived from the differences of the measured accelerations, by removing the contribution of angular motion. From the mathematical point of view, the concept of SGG is the use of the second derivatives of the gravitational potential for the estimation of the spherical harmonic (SH) coefficients. With the test masses very close to each other, the SGG measurements are very sensitive to high-frequency variations, but less sensitive to low-frequency ones. The gradiometer measurements contain colored noise, of which the power-spectrum density (PSD) at lower frequency is larger than at higher frequencies. It is therefore an important aspect to extract the gravitational information in the presence of the colored noise.

The third topic is the optimal combination of SST and SGG. The performance of SST is better than that of SGG for lower degree coefficients; it is the other way round for higher degree coefficients. The gravitational information content of SST and SGG should be combined correctly, otherwise the results will be not optimal or even biased. The variance factor is an important index in such an analysis. It represents the information content of the observation types and can therefore be used for weighting of the various contributions.

Earth science is dedicated to the study of the Earth as a static and/or dynamic system which is composed of the solid Earth, ice, oceans and atmosphere. The gravitational field of the Earth is related to the spatial distribution of matter, and its temporal variation. Determination of the EGF and its fine structure as well as its temporal variations is not only one of the basic objectives of geodesy, but also provides important information for the understanding of the Earth as a system. It is therefore desirable to obtain the Earth's gravitational field with high resolution and high accuracy, both globally and regionally.

In geodesy, EGF with a high precision and global consistency is central for the establishment of a global unified height datum, and a long-distance height control. It will also provide a height constraint between land and sea, ocean and islands. With a high-accuracy and high-resolution geoid, it is possible to replace expensive first- and second-order leveling networks by "GPS-leveling". The geoid is the most appropriate reference surface for a global height datum. Because of the unknown offsets between various datums, there exist deviations among maps from different countries or institutions. Many applications need a very detailed and highly accurate global-scale geoid, see Fig. 1.1.
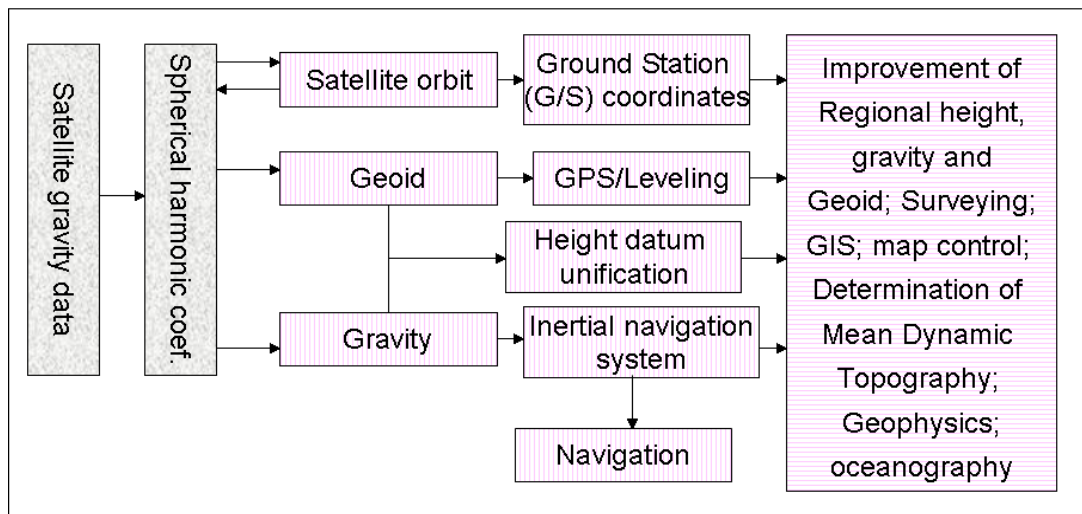
Figure 1.1: applications of Earth's gravitational field

This work is dedicated to the methodology and realization of how to obtain the spherical harmonic coefficients from satellite gravity data. Many applications, as illustrated in Fig. 1.1, will hopefully benefit from the spherical harmonic coefficients obtained with satellite gravity data in this study.

1.2 Overview of Satellite Gravitational Missions

With the development of dedicated satellite gravimetry, in particular with the three missions, CHAllenging Minisatellite Payload (CHAMP), Gravity Recovery and Climate Experiment (GRACE), Gravity field and steady-state Ocean Circulation Explorer (GOCE), our knowledge of the Earth's gravitational field and its temporal component has been and will be improved significantly. These missions are based on different innovative measurement concepts.

CHAMP, in operation from 2000 till 2010, utilized the measurement concept of satellite-to-satellite tracking in high-low mode (SST-hl). The low Earth orbiting (LEO) satellite CHAMP, initially at 450 km altitude, was continuously tracked by the high GPS satellites. The accelerometer on board CHAMP measured three-dimensionally non-gravitational accelerations acting on

1. INTRODUCTION

the spacecraft along the orbit. This principle can be considered as 'in-situ' determination of 3-D positions. It allows accurate determination of the long-wavelength part of the gravitational field. Among others the polar regions were covered, which were difficult to access prior to CHAMP.

Launched on March 17th, 2002, the GRACE mission is based on the concept of satellite-to-satellite tracking in a low-low mode (SST-ll). With two satellites in the same LEO orbit (about 400 km altitude) and approximately 200 km apart, the biased ranges between them are measured with a very accurate K-Band ranging system, with an accuracy of several micrometers. The range rate and range accelerations are derived by numerical differentiation from the biased ranging measurements. The satellite positions are determined by GPS tracking. The ranges are strongly influenced by gravitational field variations. Therefore, the gravitational field can be recovered accurately. Additionally, micro-accelerometers are located very close to the center of mass of each satellite. They measure the non-gravitational accelerations acting on the satellites and caused in particular by air drag and solar radiation pressure. GRACE provides temporal gravity variations, such as monthly changes in the gravitational field, as well as a global medium-resolution gravitational field of the Earth with high accuracy. Many representative models such as AIUB-GRACE01S (Jäggi et al., 2010a) and ITG-2010s (Kurtenbach et al., 2009) derived from GRACE show very good accuracy in the lower degree coefficients. The time series of the EGF solutions shows the temporal changes of the gravity field. Many important findings are obtained from them.

With the SST technique of current accuracy, it is difficult to achieve an even higher spatial resolution. A new technology with high sensitivity in higher frequencies is therefore desirable. At the beginning of the 20th century, the Hungarian physicist Eötvös (1848-1919) developed an instrument for measuring gravity gradients. This instrument is the so-called torsion balance (Koop 1993). Instead of one proof mass as used in a gravimeter, a torsion balance consists of two point masses, (asymmetrically) suspended to the arm of a balance. The gravity gradients produce a torque on the beam of the balance, resulting in a rotation of the beam. The gravity torque is counterbalanced by a restoring torque exerted by the fiber with which the beam is suspended. The restoring torque is a measure of the gravity gradients. Eötvös achieved with his instrument a precision of 1 E (1 E = l Eötvös unit = 10^{-9} s^{-2}). In general, instruments which measure gravity gradients are called gradiometers, and the measurement technique is called gradiometry (measuring the gradients of the components of the gravity vector), analogously to the word gravimetry (measuring gravity). The idea of satellite gradiometry was pursued soon after the successful launch of the first satellite in 1957. In the late 1980s and early 1990s, ESA supported studies of a mission called Aristoteles, which was later succeeded by the concept of the GOCE mission.

Launched on March 17th, 2009, GOCE is the first satellite mission with a gravitational gradiometer. The mission objectives of GOCE, as formulated in 1998 (European Space Agency, 1999; Johannessen et al., 2003), are the determination of the global field of geoid heights with an accuracy of 1 to 2 cm and of gravity anomalies with an accuracy of 1 mGal, and to achieve this with a spatial resolution of a 100 km half-wavelength, which corresponds to the degree and order

of 200 in terms of spherical harmonics (SH) of a gravity field model. With the long-wavelength signal recovered with high-low SST and short-wavelength signal with the on-board gradiometer, see Fig. 1.2, a gravity field model with high resolution and high accuracy is expected to be recovered.
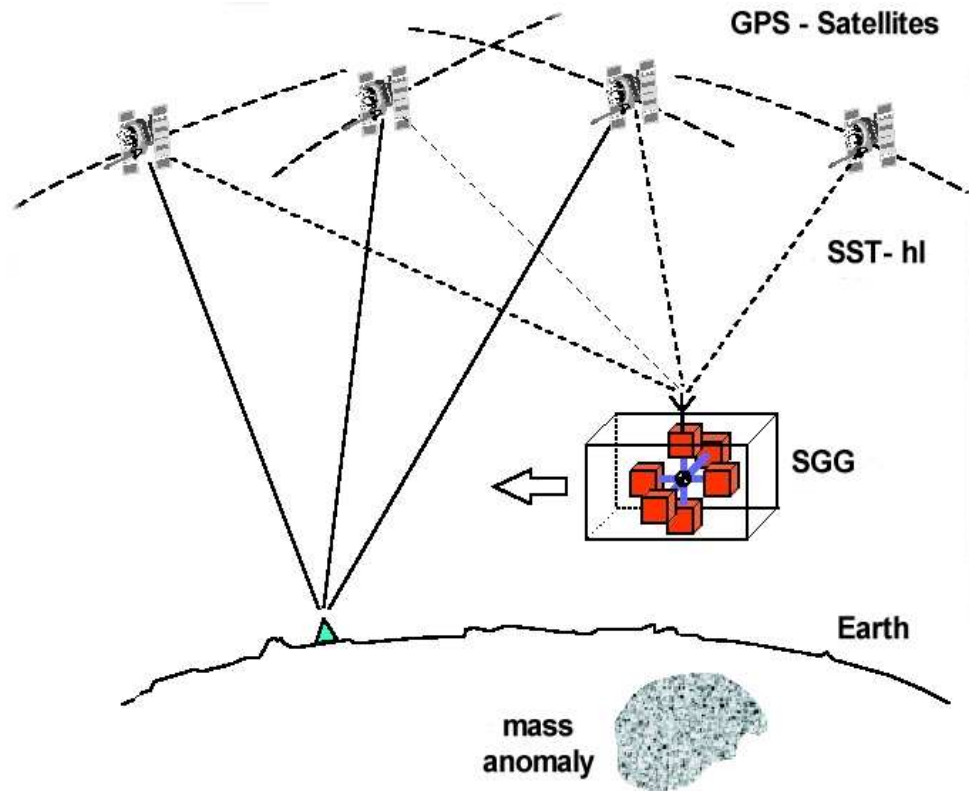
Figure 1.2: Satellite gravity gradiometry (credited by ESA)

GOCE is a scientific drag-free mission, a requirement necessary for drag elimination, but also for the maintenance of the low altitude of the satellite: without drag compensation, the very low altitude of the mission would lead to its loss in the atmosphere within a few weeks. The atmospheric drag compensation in the direction of motion is done by a pair of ion thrusters with proportional thrust control. In order to provide enough power for the thrusters, the orbit is designed to be sun-synchronous to continuously absorb solar radiation with its solar panels for power supply. An inclination of $96.7°$ is chosen for such an orbit. A complete coverage of the Earth with orbit trajectories is obtained in a 61-day repeat cycle.

Figure 1.3 shows the GOCE orbit coverage in an Earth-centered Earth-fixed frame (ECEF) based on the actual orbits in 10 days (left) and 61 days (right), respectively. It can be seen that there are gaps in the polar areas due to the orbit inclination of $96.7°$. For coverage of the polar gaps, other data such as those from GRACE or terrestrial measurements have to be used.

<div align="center">

(a) 10 days   **(b)** 61 days

</div>
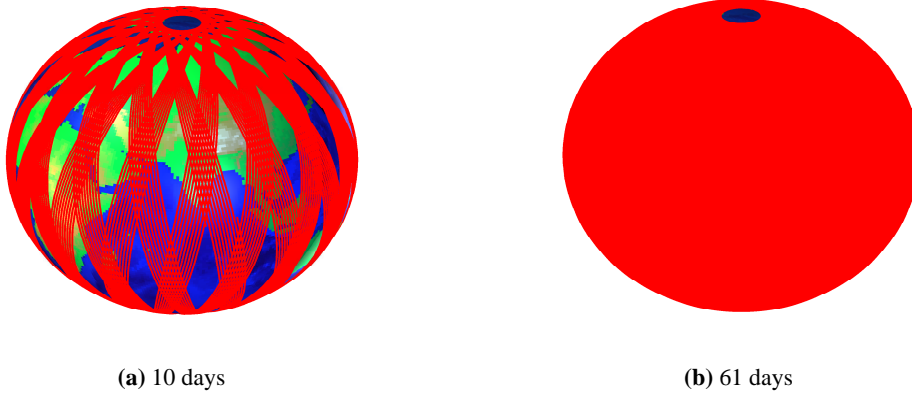
Figure 1.3: GOCE orbit coverage viewed in ECEF frame, over 10 days (left) and 61 days (right)

1.3   Outline of this Work

The primary objective of this work is to study gravity field modeling based on the actual gradio-metric measurements of GOCE as well as their combination with SST.

We start with a representation of the Earth's gravitational potential in Chapter 2. The inter-action between SH coefficients and a satellite orbit is formulated with the relation between the acceleration of the satellite and SH coefficients. The various sources of perturbation of the orbit are discussed. Using orbit integration, a case study is presented for the illustration of the GOCE orbit perturbation. Chapter 2 provides the basic theory and is followed by the actual computation in Chapters 4 and 5.

Chapter 3 presents the ideas of a large least squares problem as applied in our study. Sequential least squares is discussed for the case of GOCE. Due to the existence of the polar gap, the zonal and near-zonal coefficients are correlated in the resulted gravity model if no further constraint was applied. It is worthwhile to apply some regularization to the least squares system for overcoming this problem. An idea of polar constraint is used in this study. The principle of contribution analysis is formulated based on the normal matrices. The relationship between weight matrix and filtering is derived. The designed filter is then used for the actual data analysis.

Chapter 4 presents the SST part. The observation model is constructed based on the integral equation approach. Empirical accelerations are applied along the orbit for absorption of not-well-enough-modeled perturbation forces, as well as non-gravitational accelerations. A GOCE SST-only solution is derived. The effect of polar constraint on the SST only solution is analyzed.

Chapter 5 introduces the concept of GOCE satellite gravity gradiometry (SGG). The gradiome-ter data are analyzed in the frequency, time and space domain. The observation model is derived in the Gradiometer Reference Frame (GRF), to avoid the rotation of gradiometric components. Spherical harmonic analyses are applied to each of the four accurate components. Intermediate results from the SGG data are obtained and studied.

Chapter 6 deals with the combination of SST and SGG. The final combined solution is presented in this chapter. The results are analyzed in terms of error per degree, triangular form of the coefficient set, comparison of various gravity field models, and contribution from various observation types. In addition, a combination of GOCE and GRACE is presented.

Last but not least, Chapter 7 draws conclusions and offers some perspectives.

2

Theory about Orbit Perturbations and Case Study

This chapter presents the fundamental theory, specifically about the representation of the gravitational field and of satellite orbits. The representation of the gravitational field with spherical harmonic series is discussed. The perturbations of satellite orbits due to factors such as the non-spherical part of the gravitational force, air drag and solar radiation pressure, etc. are presented. Although the GOCE satellite is a drag-free mission in flight direction, it is necessary to remove the effect of non-gravitational forces either by using the accelerometer data or by modelling it with some empirical parameters.

   The gravitational field and geoid are discussed in section 2.1; the relationship between the gravity coefficients and the specific patterns of the geoid are outlined in this section. Section 2.2 is dedicated to the force model of satellite orbits. Section 2.3 presents variational equations. Section 2.4 is dedicated to the numerical integration strategies. Simulations for the case of GOCE are presented in section 2.5. Section 2.6 finally gives the summary of this chapter.

2.1   Gravitational Field and Geoid

Based on Newtonian mechanics, the Earth gravitational potential can be represented as the following spherical harmonic series (Hofmann-Wellenhof and Moritz 2006):

$$V(\phi, \lambda, r) = \frac{GM_\oplus}{R_\oplus} \sum_{n=0}^{N_{\max}} \left(\frac{R_\oplus}{r} \right)^{n+1} \sum_{m=0}^{n} \overline{P}_{nm} (\sin\phi) \left(\overline{C}_{nm} \cos(m\lambda) + \overline{S}_{nm} \sin(m\lambda) \right), \qquad (2.1)$$

where $GM_\oplus$ is the product of the gravitational constant and the mass of the Earth; $R_\oplus$ is the reference radius of the gravitational field; (r, ϕ, λ) is the spherical coordinate triplet of a point in the Earth-fixed frame where we want to compute the potential; $\overline{P}_{nm}(\sin\phi)$ are the fully normalized associated Legendre polynomials of nth degree and m[th] order; $\overline{C}_{nm}$ and $\overline{S}_{nm}$ are the fully normal-

ized spherical harmonic (SH) coefficients to be estimated. The maximum resolvable degree, $N_{\max}$, corresponds approximately to the spatial resolution of D = $20000/N_{\max}$ half-wavelength in kilometers. The second summation runs from zero order m up to actual degree n which means that $m \leq n$. The higher the d/o, the more detail of the gravitational field is represented.

Radial-symmetric of the mass distribution is a good approximation resulting in a constant gravity. However, there are small temporal variations, too. The core and mantle convection, plate tectonics, glacial isostatic adjustment, ice melting, sea-level rise, ocean re-distribution, the global water cycle, atmospheric dynamics, all of these are changing the gravitational field. Thus the coefficients of the gravitational field become functions of time. Since GOCE is designed to determine the static gravitational field, we will not investigate the recovery of temporal variations in this study.

Let us assume that the SH coefficients $\overline{C}_{nm}$ and $\overline{S}_{nm}$ are known. Then the gravitational potential V can be computed by Eq. (2.1). This is referred to as spherical harmonic synthesis (SHS). Gravity quantities other than V can be derived by small modifications of this equation, such as taking derivatives. Such derived gravity functions include geoid heights N (in meters above the adopted reference ellipsoid), gravity anomalies Δg (in mGal, where 1 mGal = 10^{-5} m/s^2) as well as the second order derivatives of the gravitational potential with respect to the three spatial directions, also known as gravitational gradients (in Eötvös, where 1 Eötvös Unit= 1 E = 10^{-9} s^{-2}).

The geoid height can be computed with spherical approximation as

$$N(\phi,\lambda,r) = R_{\oplus} \sum_{n=0}^{N_{\max}} \left(\frac{R_{\oplus}}{r}\right)^{n+1} \sum_{m=0}^{n} \overline{P}_{nm}(\sin\phi)\left(\Delta\overline{C}_{nm}\cos(m\lambda) + \Delta\overline{S}_{nm}\sin(m\lambda)\right), \qquad (2.2)$$

where the coefficients $\Delta\overline{C}_{nm}$ and $\Delta\overline{S}_{nm}$ are gravity field coefficients, subtracted the corresponding coefficients of adopted ellipsoidal normal field, cf. (Burša and Picha, 1971).

If $V(\phi,\lambda,r)$ is continuously given on a closed sphere, the SH coefficients can be derived by integral formulae:

$$\left.\begin{array}{c}\overline{C}_{nm}\\\overline{S}_{nm}\end{array}\right\} = \frac{R_{\oplus}}{4\pi GM_{\oplus}} \int\limits_{\phi=-\pi/2}^{\pi/2} \int\limits_{\lambda=0}^{2\pi} V(\phi,\lambda,r)\overline{P}_{nm}(\sin\phi)\left\{\begin{array}{c}\cos m\lambda\\\cos m\lambda\end{array}\right\}\cos\phi \cdot d\lambda d\phi. \qquad (2.3)$$

The signal strength per degree can be represented with degree Root Mean Square (RMS) values evaluated as

$$\sigma_n = \sqrt{\frac{1}{2n+1}\sum_{m=0}^{n}\left(\overline{C}_{nm}^2 + \overline{S}_{nm}^2\right)}. \qquad (2.4)$$

Our subject is spherical harmonic analysis (SHA). In this case, the coefficients up to degree and order N_{max} of the spherical harmonic series are the fundamental gravity unknowns. Now the

left-hand side of Eq. (2.1) or its functionals is assumed to be observed. In satellite geodesy, the determination of the coefficients is based on satellite measurements, e.g., of the orbits of satellites or gravitational gradient along the orbits.

The observations collected from satellite are, in general, discrete and with finite number, it is necessary to make use of least squares approach for the determination of the SH coefficients. The maximum of the degree and order represents the spatial resolution of the gravitational field we can achieve. With the set of coefficients, the geoid of the Earth can be determined with a well-defined resolution.

It is convenient to represent the SH coefficients in the form of a triangle, as shown in Fig. 2.1, where the vertical axis of the triangle represents the degree n of the SH coefficients (or the corresponding spatial resolution D). The horizontal axis refers to the order $m \leq n$ with the cosine coefficients $\overline{C}_{nm}$ on the right and the sine coefficients $\overline{S}_{nm}$ on the left side. Coefficients of order zero are called zonal harmonics, those of the same degree and order $m = n$ sectorial harmonics, and all other coefficients tesseral harmonics.
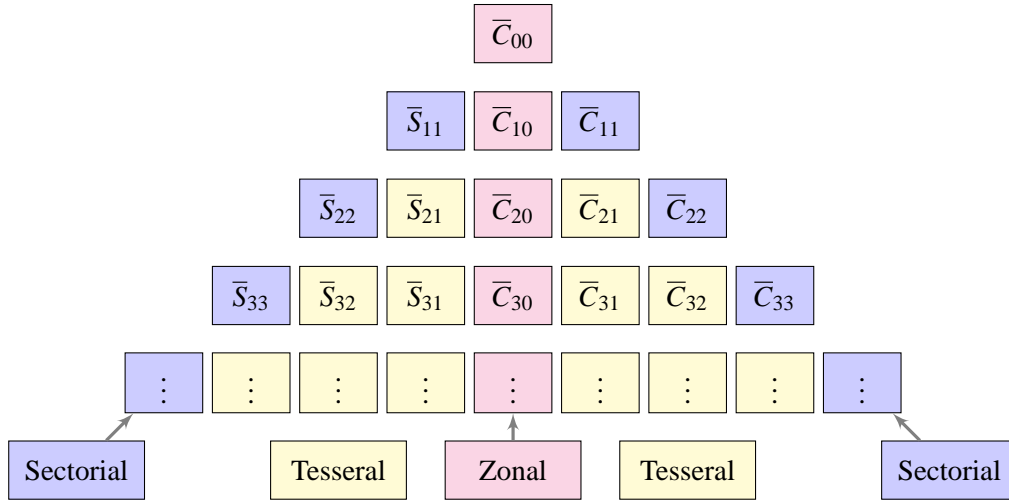
Figure 2.1: Triangular representation of SH coefficients

For programming, the SH coefficients are in general saved in a matrix, as shown in Fig. 2.2. It is more compact to store the coefficients in this way. There are other possibilities, such as in the Bernese software, where the cosine terms and sine terms are saved in two vectors. One can see in Fig. 2.2 that the total number of coefficients is $(N_{\max} + 1)^2$ for a gravitational field model up to degree and order $N_{\max}$. One may decide only estimate the coefficients of degrees from $N_{\min}$ to $N_{\max}$. In case of $N_{\min} = 2$, a common choice is to fix the degree zero to a constant and degree one to zero. The latter choice implies that the geocenter coincides with the pre-defined origin of the coordinate system in which the measurements are derived. Then the total number to be estimated is $(N_{\max} + 1)^2 - (N_{\min})^2$.

With the gravitational field as presented in Eq. (2.1), plus the centrifugal potential due to the rotation of the Earth, the geoid of the Earth is defined as an equipotential surface at mean sea level, i.e. $W = V + Z = W_0 = \text{const}$, where Z is the centrifugal potential due to Earth rotation. Thus, the geoid is an equipotential surface which coincides (approximately) with the mean ocean surface. According to C.F. Gauss, it is the "mathematical figure of the Earth", in fact, of the gravity field. Because the centrifugal potential can be easily obtained from the angular rate of the Earth, the term gravity field model in this dissertation has the same meaning as gravitational field model.

The geoid of the Earth is defined by the set of gravity coefficients and a set of additional auxiliary parameters. We distinguish three types of SH coefficient: zonal, tesseral and sectorial, compare again Fig. 2.1. The type of coefficient describes a particular pattern of the SH functions. Figure 2.3 shows the different patterns of SH functions to the different types of coefficients.
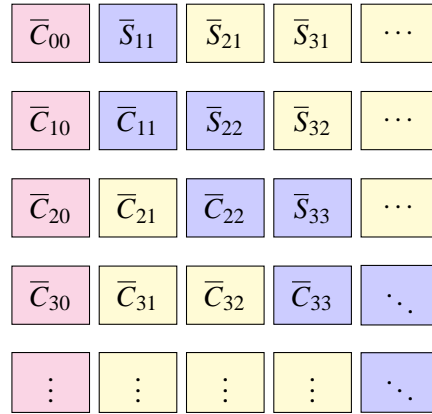
Figure 2.2: Matrix representation of SH coefficients

One can see that zonal coefficients in Fig. 2.3a correspond to a pattern only changing in north-south direction. These harmonics represent bands of latitude, invariant to longitude. The tesseral coefficients correspond to a pattern represented as "tesserae" of the Earth, rather than bands, see Fig. 2.3b. The sectorial coefficients correspond to a geoid representing bands of longitude. These bands of longitude divide the Earth into $2m$ (for a harmonic of degree and order of m) "orange-slice" sectors, as shown in Fig. 2.3c. The sum of the three Figures is displayed in Fig. 2.3d.

2.2 Satellite Orbit and Perturbation

A satellite orbiting the Earth will experience several kinds of perturbation forces. Thus, the six Keplerian elements are functions of time. The types of perturbation forces include the Earth's non-spherical gravitation, third body attraction (in particular the moon and the sun), solid Earth tides, ocean tides, pole tides, atmosphere drag, solar radiation, Earth radiation, as well as other non-gravitational perturbations. The most dominant perturbation force is the Earth's non-spherical gravitational field. Any perturbation will make the actual satellite orbit deviate from a two-body orbit, a Kepler ellipse, so we need to model the perturbation forces as accurately as possible, in

(a) $C_{20,0}$

(b) $C_{20,10}$ and $S_{20,10}$

(c) $C_{20,20}$ and $S_{20,20}$

(d) sum of the previous three
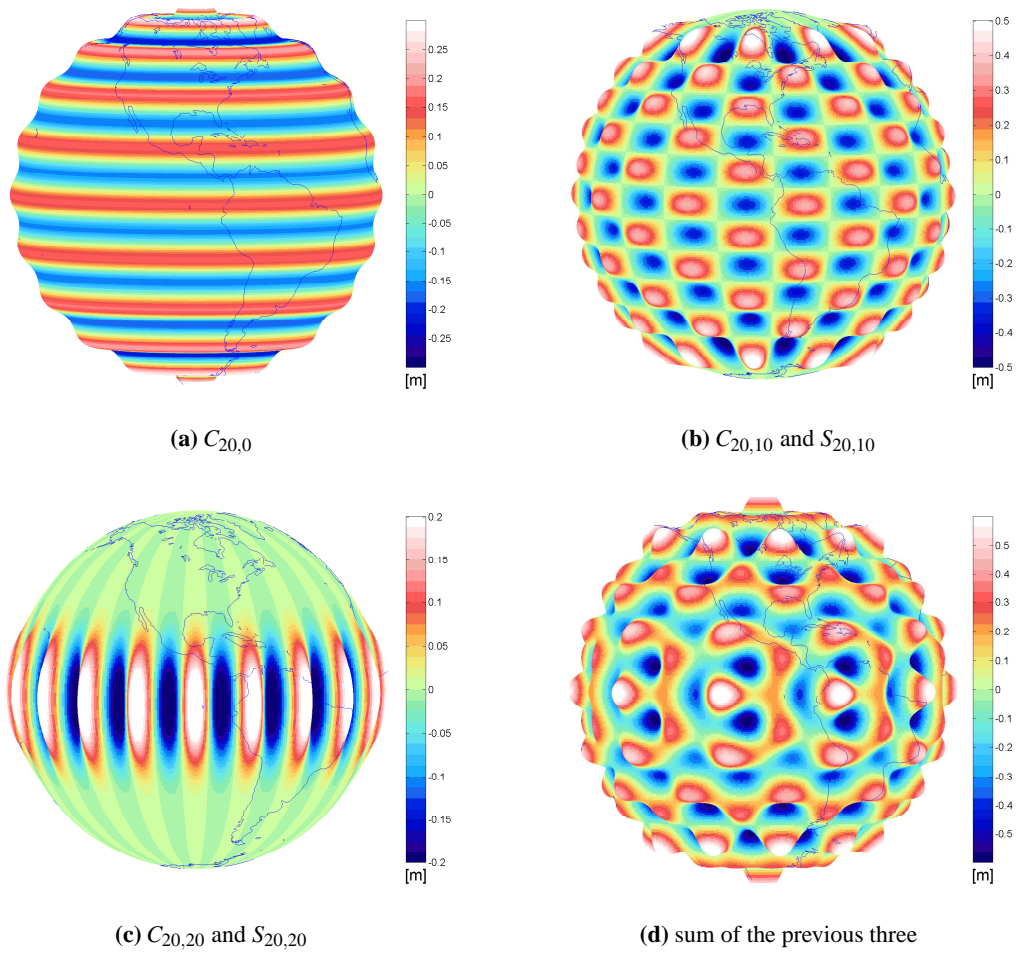
Figure 2.3: Characteristic patterns of spherical harmonic functions: zonal, tesseral, sectorial and their sum

order to arrive at a precise orbit. The acceleration of the satellite can be expressed as

$$\ddot{\mathbf{r}} = \mathbf{a}_{eg} + \mathbf{a}_{et} + \mathbf{a}_{ot} + \mathbf{a}_{nb} + \mathbf{a}_{drag} + \mathbf{a}_{srp} + \mathbf{a}_{erp} + \mathbf{a}_{ge} + \mathbf{a}_{other}$$
$$= \mathbf{f}(t, \mathbf{r}, \dot{\mathbf{r}}, \mathbf{p}) + \mathbf{f}_{stc} ,$$

(2.5)

where $\mathbf{a}_{eg}$ is the force (per unit mass) due to Earth's static gravitational field; the $\mathbf{a}_{et}$ is the force due to the solid Earth tides; the $\mathbf{a}_{ot}$ is the ocean tides; the $\mathbf{a}_{nb}$ is the third body attraction (in particular the moon and the sun); the $\mathbf{a}_{drag}$ is the air drag; the $\mathbf{a}_{srp}$ is the solar radiation pressure; the $\mathbf{a}_{erp}$ is the Earth radiation pressure (albedo); the $\mathbf{a}_{ge}$ is the effect of general relativity; the $\mathbf{a}_{other}$ represents the forces which are not modeled or not known to us. The force can be decomposed into $\mathbf{f}(t, \mathbf{r}, \dot{\mathbf{r}}, \mathbf{p})$ described with an analytical force model which one uses for perturbation computation, and $\mathbf{f}_{stc}$ the so-called stochastic forces, introduced to absorb mis-modeled and un-modeled forces. An overview of the forces from different sources is displayed in Fig. 2.4.
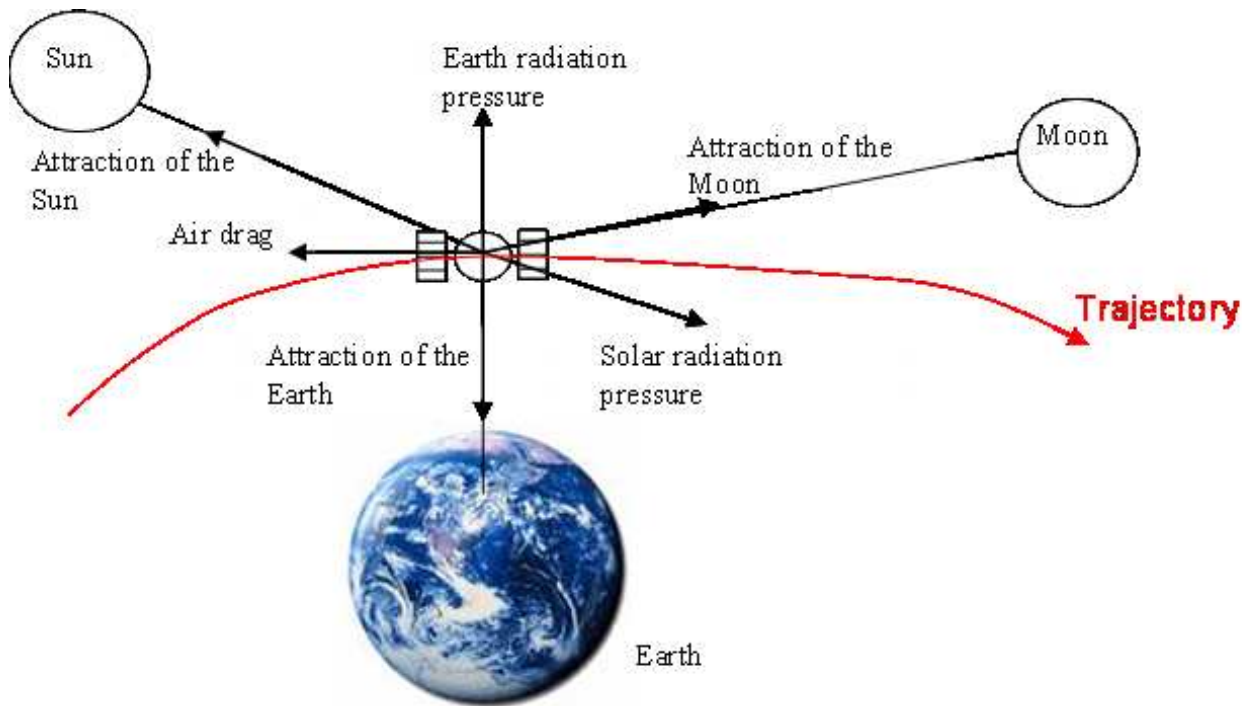
Figure 2.4: Some of the forces experienced by Earth-orbiting satellite

In addition to the disturbing forces mentioned above, short-term mass variations in the atmosphere and in the ocean must be removed, since these mass changes also cause time-variant gravitational field forces acting on the orbiting satellites, see (Flechtner, 2007). This type of perturbation will be discussed in Chapters 4 and Chapter 5.

2.2.1 Earth's Gravitational Acceleration

The largest contribution of all the forces experienced by orbiting satellites is from the Earth itself. The Earth's gravitational field is neither spherical nor ellipsoidal, as the mass distribution of the

2. THEORY ABOUT ORBIT PERTURBATIONS AND CASE STUDY

Earth is inhomogeneous. Thus, there are non-spherical perturbations. The potential presented in Eq. (2.1) can be rewritten as

$$V = \frac{GM_\oplus}{R_\oplus} \sum_{n=0}^{N_{max}} \sum_{m=0}^{n} \left(\overline{C}_{nm} \overline{V}_{nm} + \overline{S}_{nm} \overline{W}_{nm} \right), \tag{2.6}$$

where

$$\overline{V}_{nm} = \left(\frac{R_\oplus}{r} \right)^{n+1} \cdot \overline{P}_{nm}(\sin\phi) \cos m\lambda \quad \text{and} \quad \overline{W}_{nm} = \left(\frac{R_\oplus}{r} \right)^{n+1} \cdot \overline{P}_{nm}(\sin\phi) \sin m\lambda . \tag{2.7}$$

There are several approaches to derive the gravitational acceleration from the potential formula: the traditional formulation in terms of associated Legendre functions in spherical coordinates; a variant of the first method based on the Clenshaw summation formula (Casotto and Fantino, 2007); the non-singular method of Pines; and the algorithm developed by Cunningham and extended by Métris et al. (1999). For this study, the Cunningham approach is chosen for spherical harmonic computations. In some references such as (Montenbruck and Gill, 2000), the formulas are given with unnormalized quantities. This would lead to overflow and underflow for the coefficients of high degree and order in our case. The normalized version of the formulas is derived here and used for our spherical harmonic analysis.

The normalization factor for conversion between normalized and unnormalized quantities is

$$N_{nm} = \sqrt{\frac{(2 - \delta_{0m})(2n+1)(n-m)!}{(n+m)!}}, \tag{2.8}$$

which is used to derive normalized formulas based on unnormalized ones.

With

$$\frac{x}{r} = \cos\phi \cos\lambda$$
$$\frac{y}{r} = \cos\phi \sin\lambda$$
$$\frac{z}{r} = \sin\phi ,$$

the recursive computations for spherical harmonic functions are

$$\overline{V}_{00} = \frac{R_\oplus}{r} \quad \text{and} \quad \overline{W}_{00} = 0 , \tag{2.9}$$

$$\overline{V}_{mm} \overset{n=m}{=} \frac{N_{mm}}{N_{m-1,m-1}} (2m-1) \left\{ \frac{xR_\oplus}{r^2} \overline{V}_{m-1,m-1} - \frac{yR_\oplus}{r^2} \overline{W}_{m-1,m-1} \right\}$$

$$= \begin{cases} \sqrt{\frac{2m+1}{m}} \left\{ \frac{xR_\oplus}{r^2} \overline{V}_{m-1,m-1} - \frac{yR_\oplus}{r^2} \overline{W}_{m-1,m-1} \right\} & m = 1 \\ \sqrt{\frac{2m+1}{2m}} \left\{ \frac{xR_\oplus}{r^2} \overline{V}_{m-1,m-1} - \frac{yR_\oplus}{r^2} \overline{W}_{m-1,m-1} \right\} & m > 1 \end{cases} \tag{2.10}$$

$$\overline{W}_{mm} \overset{n=m}{=} \frac{N_{mm}}{N_{m-1,m-1}} (2m-1) \left\{ \frac{xR_\oplus}{r^2} \overline{V}_{m-1,m-1} + \frac{yR_\oplus}{r^2} \overline{W}_{m-1,m-1} \right\}$$

$$= \begin{cases} \sqrt{\frac{2m+1}{m}} \left\{ \frac{xR_\oplus}{r^2} \overline{V}_{m-1,m-1} + \frac{yR_\oplus}{r^2} \overline{W}_{m-1,m-1} \right\} & m = 1 \\ \sqrt{\frac{2m+1}{2m}} \left\{ \frac{xR_\oplus}{r^2} \overline{V}_{m-1,m-1} + \frac{yR_\oplus}{r^2} \overline{W}_{m-1,m-1} \right\} & m > 1 \end{cases},$$

$$(2.11)$$

$$\overline{V}_{nm} \overset{m\leq n}{=} N_{n,m} \left\{ \left(\frac{2n-1}{n-m} \right) \frac{1}{N_{n-1,m}} \frac{zR_\oplus}{r^2} \overline{V}_{n-1,m} - \left(\frac{n+m-1}{n-m} \right) \frac{1}{N_{n-2,m}} \frac{R_\oplus^2}{r^2} \overline{V}_{n-2,m} \right\}$$

$$= \sqrt{\frac{(2n+1)}{(n+m)(n-m)}} \left\{ \sqrt{(2n-1)} \frac{zR_\oplus}{r^2} \overline{V}_{n-1,m} - \sqrt{\frac{(n-m-1)(n+m-1)}{(2n-3)}} \frac{R_\oplus^2}{r^2} \overline{V}_{n-2,m} \right\},$$

$$(2.12)$$

$$\overline{W}_{nm} \overset{m\leq n}{=} N_{n,m} \left\{ \left(\frac{2n-1}{n-m} \right) \frac{1}{N_{n-1,m}} \frac{zR_\oplus}{r^2} \overline{W}_{n-1,m} - \left(\frac{n+m-1}{n-m} \right) \frac{1}{N_{n-2,m}} \frac{R_\oplus^2}{r^2} \overline{W}_{n-2,m} \right\}$$

$$= \sqrt{\frac{(2n+1)}{(n+m)(n-m)}} \left\{ \sqrt{(2n-1)} \frac{zR_\oplus}{r^2} \overline{W}_{n-1,m} - \sqrt{\frac{(n-m-1)(n+m-1)}{(2n-3)}} \frac{R_\oplus^2}{r^2} \overline{W}_{n-2,m} \right\}.$$

$$(2.13)$$

Suppose $\begin{pmatrix} x & y & z \end{pmatrix}^T = \mathbf{r}$ is the position vector in the Earth-centered Earth-fixed frame (ECEF), and $\begin{pmatrix} \ddot{x} & \ddot{y} & \ddot{z} \end{pmatrix}^T = \mathbf{a}_{eg}$ is the corresponding acceleration vector due to the attraction of the Earth. Then the acceleration vector can be evaluated in Cartesian representation as:

$$\mathbf{a}_{eg} = \nabla V = \sum_{n,m} \ddot{\mathbf{r}}_{nm} = \sum_{n,m} \begin{pmatrix} \ddot{x}_{nm} & \ddot{y}_{nm} & \ddot{z}_{nm} \end{pmatrix}^T$$

$$\ddot{x}_{n0} = \frac{GM_\oplus}{R_\oplus^2} \cdot \left\{ -\overline{C}_{n0} \overline{V}_{n+1,1} \right\} \sqrt{\frac{(2n+1)(n+2)(n+1)}{2(2n+3)}}$$

$$\ddot{x}_{nm} \overset{m=1}{=} \frac{GM_\oplus}{R_\oplus^2} \cdot \frac{1}{2} \left\{ \sqrt{\frac{(2n+1)(n+3)(n+2)}{(2n+3)}} \left(-\overline{C}_{nm} \overline{V}_{n+1,m+1} - \overline{S}_{nm} \overline{W}_{n+1,m+1} \right) \right.$$
$$\left. + \sqrt{\frac{2(2n+1)}{(2n+3)(n+1)n}} \left(\overline{C}_{nm} \overline{V}_{n+1,m-1} + \overline{S}_{nm} \overline{W}_{n+1,m-1} \right) \right\}$$

$$\ddot{x}_{nm} \overset{m\geq 1}{=} \frac{GM_\oplus}{R_\oplus^2} \cdot \frac{1}{2} \left\{ \sqrt{\frac{(2n+1)(n+m+2)(n+m+1)}{(2n+3)}} \left(-\overline{C}_{nm} \overline{V}_{n+1,m+1} - \overline{S}_{nm} \overline{W}_{n+1,m+1} \right) \right.$$
$$\left. + \sqrt{\frac{(2n+1)}{(2n+3)(n-m+2)(n-m+1)}} \left(\overline{C}_{nm} \overline{V}_{n+1,m-1} + \overline{S}_{nm} \overline{W}_{n+1,m-1} \right) \right\}$$

$$\ddot{y}_{n0} = \frac{GM_\oplus}{R_\oplus^2} \cdot \left\{ -\overline{C}_{n0} \overline{W}_{n+1,1} \right\} \sqrt{\frac{(2n+1)(n+2)(n+1)}{2(2n+3)}}$$

$$\ddot{y}_{nm} \overset{m=1}{=} \frac{GM_\oplus}{R_\oplus^2} \cdot \frac{1}{2} \left\{ \sqrt{\frac{(2n+1)(n+3)(n+2)}{(2n+3)}} \left(-\overline{C}_{nm} \overline{W}_{n+1,m+1} + \overline{S}_{nm} \overline{V}_{n+1,m+1} \right) \right.$$
$$\left. + \sqrt{\frac{2(2n+1)}{(2n+3)(n+1)n}} \left(-\overline{C}_{nm} \overline{W}_{n+1,m-1} + \overline{S}_{nm} \overline{V}_{n+1,m-1} \right) \right\}$$

$$\ddot{y}_{nm} \overset{m\geq 1}{=} \frac{GM_\oplus}{R_\oplus^2} \cdot \frac{1}{2} \left\{ \sqrt{\frac{(2n+1)(n+m+2)(n+m+1)}{(2n+3)}} \left(-\overline{C}_{nm} \overline{W}_{n+1,m+1} + \overline{S}_{nm} \overline{V}_{n+1,m+1} \right) \right.$$
$$\left. + \sqrt{\frac{(2n+1)}{(2n+3)(n-m+2)(n-m+1)}} \left(-\overline{C}_{nm} \overline{W}_{n+1,m-1} + \overline{S}_{nm} \overline{V}_{n+1,m-1} \right) \right\}$$

$$\ddot{z}_{nm} = \frac{GM_\oplus}{R_\oplus^2} \cdot \left\{ \sqrt{\frac{(2n+1)(n+m+1)(n-m+1)}{(2n+3)}} \left(-\overline{C}_{nm} \overline{V}_{n+1,m} - \overline{S}_{nm} \overline{W}_{n+1,m} \right) \right\}.$$

$$(2.14)$$

The partial derivatives of the acceleration with respect to the normalized coefficients $\overline{C}_{nm}$ and

$\overline{S}_{nm}$ are

$$\frac{\partial \ddot{x}_{n0}}{\partial \overline{C}_{n0}} = -\sqrt{\frac{(2n+1)(n+2)(n+1)}{2(2n+3)}} \frac{GM_\oplus}{R_\oplus^2} \overline{V}_{n+1,1}$$

$$\frac{\partial \ddot{x}_{nm}}{\partial \overline{C}_{nm}} \overset{m=1}{=} \frac{GM_\oplus}{R_\oplus^2} \cdot \frac{1}{2} \sqrt{\frac{(2n+1)}{(2n+3)}} \left(-\sqrt{(n+3)(n+2)} \overline{V}_{n+1,m+1} + \sqrt{\frac{2}{(n+1)n}} \overline{V}_{n+1,m-1} \right)$$

$$\frac{\partial \ddot{x}_{nm}}{\partial \overline{C}_{nm}} \overset{m \geq 1}{=} \frac{GM_\oplus}{R_\oplus^2} \cdot \frac{1}{2} \sqrt{\frac{(2n+1)}{(2n+3)}} \left(-\sqrt{(n+m+2)(n+m+1)} \overline{V}_{n+1,m+1} \right.$$
$$\left. + \sqrt{\frac{1}{(n-m+2)(n-m+1)}} \overline{V}_{n+1,m-1} \right)$$

$$\frac{\partial \ddot{x}_{nm}}{\partial \overline{S}_{nm}} \overset{m=1}{=} \frac{GM_\oplus}{R_\oplus^2} \cdot \frac{1}{2} \sqrt{\frac{(2n+1)}{(2n+3)}} \left(-\sqrt{(n+3)(n+2)} \overline{W}_{n+1,m+1} + \sqrt{\frac{2}{(n+1)n}} \overline{W}_{n+1,m-1} \right)$$

$$\frac{\partial \ddot{x}_{nm}}{\partial \overline{S}_{nm}} \overset{m \geq 1}{=} \frac{GM_\oplus}{R_\oplus^2} \cdot \frac{1}{2} \sqrt{\frac{(2n+1)}{(2n+3)}} \left(-\sqrt{(n+m+2)(n+m+1)} \overline{W}_{n+1,m+1} \right.$$
$$\left. + \sqrt{\frac{1}{(n-m+2)(n-m+1)}} \overline{W}_{n+1,m-1} \right)$$

$$\frac{\partial \ddot{y}_{n0}}{\partial \overline{C}_{n0}} = -\sqrt{\frac{(2n+1)(n+2)(n+1)}{2(2n+3)}} \frac{GM_\oplus}{R_\oplus^2} \overline{W}_{n+1,1} \tag{2.15}$$

$$\frac{\partial \ddot{y}_{nm}}{\partial \overline{C}_{nm}} \overset{m=1}{=} \frac{GM_\oplus}{R_\oplus^2} \cdot \frac{1}{2} \sqrt{\frac{(2n+1)}{(2n+3)}} \left(-\sqrt{(n+3)(n+2)} \overline{W}_{n+1,m+1} - \sqrt{\frac{2}{(n+1)n}} \overline{W}_{n+1,m-1} \right)$$

$$\frac{\partial \ddot{y}_{nm}}{\partial \overline{C}_{nm}} \overset{m \geq 1}{=} \frac{GM_\oplus}{R_\oplus^2} \cdot \frac{1}{2} \sqrt{\frac{(2n+1)}{(2n+3)}} \left(-\sqrt{(n+m+2)(n+m+1)} \overline{W}_{n+1,m+1} \right.$$
$$\left. - \sqrt{\frac{1}{(n-m+2)(n-m+1)}} \overline{W}_{n+1,m-1} \right)$$

$$\frac{\partial \ddot{y}_{nm}}{\partial \overline{S}_{nm}} \overset{m=1}{=} \frac{GM_\oplus}{R_\oplus^2} \cdot \frac{1}{2} \sqrt{\frac{(2n+1)}{(2n+3)}} \left(\sqrt{(n+3)(n+2)} \overline{V}_{n+1,m+1} + \sqrt{\frac{2}{(n+1)n}} \overline{V}_{n+1,m-1} \right)$$

$$\frac{\partial \ddot{y}_{nm}}{\partial \overline{S}_{nm}} \overset{m \geq 1}{=} \frac{GM_\oplus}{R_\oplus^2} \cdot \frac{1}{2} \sqrt{\frac{(2n+1)}{(2n+3)}} \left(\sqrt{(n+m+2)(n+m+1)} \overline{V}_{n+1,m+1} \right.$$
$$\left. + \sqrt{\frac{1}{(n-m+2)(n-m+1)}} \overline{V}_{n+1,m-1} \right)$$

$$\frac{\partial \ddot{z}_{nm}}{\partial \overline{C}_{nm}} = -\frac{GM_\oplus}{R_\oplus^2} \sqrt{\frac{(2n+1)(n+m+1)(n-m+1)}{(2n+3)}} \overline{V}_{n+1,m}$$

$$\frac{\partial \ddot{z}_{nm}}{\partial \overline{S}_{nm}} = -\frac{GM_\oplus}{R_\oplus^2} \sqrt{\frac{(2n+1)(n+m+1)(n-m+1)}{(2n+3)}} \overline{W}_{n+1,m}.$$

The partial derivatives of the unnormalized coefficients w.r.t. normalized coefficients can be obtained as

$$\left. \begin{array}{c} \frac{\partial \overline{C}_{nm}}{\partial C_{nm}} \\ \frac{\partial \overline{S}_{nm}}{\partial S_{nm}} \end{array} \right\} = \frac{1}{N_{nm}} = \sqrt{\frac{(n+m)!}{(2-\delta_{0m})(2n+1)(n-m)!}} \qquad \delta_{0m} = \left\{ \begin{array}{cc} 0 & m \neq 0 \\ 1 & m = 0 \end{array} \right. .$$

The derivatives of the gravitational acceleration w.r.t. the position vector are needed in perturbation theory for solving the variational equations. Their derivation will be presented in Chapter 5. Since the gravitational acceleration is independent of velocity, its derivative w.r.t. velocity is zero.

2.2.2 N-Body Perturbation (Direct Tide)

The acceleration due to the attraction of celestial bodies relative to the Earth's center of mass can be represented as

$$\mathbf{a}_{\mathrm{nb}} = \sum_{i=1}^{N} GM_i \left(-\frac{\mathbf{r} - \mathbf{r}_i}{|\mathbf{r} - \mathbf{r}_i|^3} - \frac{\mathbf{r}_i}{r_i^3} \right), \tag{2.16}$$

where N is the total number of the perturbation bodies; M_i is the mass of the ith body; G is the

Newtonian gravitational constant, its nominal value is 6.67428×10^{-11} m^{3}kg^{-1}s^{-2}, see (Petit and Luzum, 2010); $\mathbf{r}$ and $\mathbf{r_i}$ are the position vectors of the satellite and the ith perturbation body, respectively.

The partial derivative of the acceleration w.r.t. the position vector of the satellite is

$$\frac{\partial \mathbf{a}_{\mathrm{nb}}}{\partial \mathbf{r}} = \sum_{i=1}^{N} GM_i \left(-\frac{1}{|\mathbf{r}-\mathbf{r}_i|^3} \mathbf{I_{3 \times 3}} + 3\frac{(\mathbf{r}-\mathbf{r}_i)(\mathbf{r}-\mathbf{r}_i)^T}{|\mathbf{r}-\mathbf{r}_i|^5} \right), \qquad (2.17)$$

where $(\mathbf{r}-\mathbf{r}_i)(\mathbf{r}-\mathbf{r}_i)^T$ is the dyadic product of the two vectors $(\mathbf{r}-\mathbf{r}_i)$ and $(\mathbf{r}-\mathbf{r}_i)^T$. $\mathbf{I_{3 \times 3}}$ represents the 3-by-3 unit matrix.

2.2.3 Solid Earth Tides

Because the Earth is not a rigid body, the attraction of third bodies (in particular moon and sun) deforms the solid Earth. As a result the gravitational field of the Earth slightly changes, which has an effect on the motion of the satellite.

The acceleration due to the second degree solid Earth tides is written as (Montenbruck and Gill, 2000)

$$\mathbf{a}_{\mathrm{et}} = \frac{k_2}{2} \sum_{j=s,m} \frac{GM_j}{r_j^3} \frac{R_\oplus^5}{r^4} \left(\left(3 - 15 \left(\frac{\mathbf{r}_j \cdot \mathbf{r}}{|\mathbf{r}_j||\mathbf{r}|} \right)^2 \right) \frac{\mathbf{r}}{|\mathbf{r}|} + 6 \left(\frac{\mathbf{r}_j \cdot \mathbf{r}}{|\mathbf{r}_j||\mathbf{r}|} \right) \frac{\mathbf{r}_j}{|\mathbf{r}_j|} \right). \qquad (2.18)$$

where s and m in the summation symbol j denote the sun and moon, r is the distance from the satellite to the geocenter, $R_\oplus$ is the radius of the Earth, k_2 is the Love number (≈ 0.3; it can be estimated as a parameter), and r_j is the distance of the third body from the geocenter.

This second degree approximation is sufficient in many cases. If a more precise model is necessary, the variation of the gravitational coefficients of the Earth due to solid Earth tides can be presented as (Montenbruck and Gill, 2000; Tapley, 1989)

$$\left\{ \begin{array}{c} \Delta \overline{C}_{n,m}^j \\ \Delta \overline{S}_{n,m}^j \end{array} \right\} = 4k_n \left(\frac{GM_j}{GM_\oplus} \right) \left(\frac{R_\oplus}{r_j} \right)^{n+1} \sqrt{(n+2) \cdot \left[\frac{(n-m)!}{(n+m)!} \right]^3} \overline{P}_{nm}(\sin\phi_j) \left\{ \begin{array}{c} \cos(m\lambda_j) \\ \sin(m\lambda_j) \end{array} \right\}, \qquad (2.19)$$

where k_n are the Love numbers of degree n; M_j and r_j are the mass and geocentric distance of the tide-generating body, in particular the moon and sun, and some other planets as well; ϕ_j and λ_j are Earth-fixed latitude and longitude of the disturbing bodies. The disturbing accelerations due to solid tides can be computed with Eq. (2.14) by substituting the disturbing gravitational coefficients of Eq. (2.19).

2.2.4 Ocean Tides

The ocean tides are the rise and fall of sea level caused by the combined effects of the gravitational forces exerted by the moon and sun and the rotation of the Earth. This redistribution of the mass in the ocean changes the gravitational field. Similar to solid tides, ocean tides can be represented by gravitational coefficient corrections (variations), which are expressed as (McCarthy and Petit 2004; Montenbruck and Gill 2000; Tapley 1989)

$$
\left\{ \begin{array}{c} \Delta \overline{C}_{n,m} \\ \Delta \overline{S}_{n,m} \end{array} \right\} = \frac{4\pi G R_\oplus^2 \rho_w}{N_{nm} G M_\oplus} \frac{1+k'_n}{2n+1} \left\{ \begin{array}{c} \sum\limits_{s(n,m)} (C_{snm}^+ + C_{snm}^-)\cos\theta_s + (S_{snm}^+ + S_{snm}^-)\sin\theta_s \\ \sum\limits_{s(n,m)} (S_{snm}^+ - S_{snm}^-)\cos\theta_s - (C_{snm}^+ - C_{snm}^-)\sin\theta_s \end{array} \right\}, \quad (2.20)
$$

where ρ_w is the density of the seawater; k'_n are the load-deformation coefficients; $C_{snm}^\pm$ and $S_{snm}^\pm$ are the ocean tide coefficients in meters for the tide constituents s; θ_s is the weighted combination of the six Doodson variables. Doodson variables denote the fundamental arguments of the sun's and moon's orbits, being closely related to the arguments of the nutation series.

The coefficients k'_n, $C_{snm}^\pm$ and $S_{snm}^\pm$ come from a background model, such as CSR4.0 (Eanes, 2002), FES2004 (Lyard et al., 2006) and EOT08a (Savcenko and Bosch, 2008). With the coefficients, analogously to the solid Earth tides, the acceleration can be computed with Eq. (2.14).

A small motion caused by the Chandler wobble in the Earth's axis of rotation relative to the Earth's surface, generates a very small tide, known as a pole tide. This is also applied in our computation, for more details we refer to McCarthy and Petit (2004, chap. 8).

2.2.5 General Relativistic Effects

According to the general theory of relativity, Newtonian theory of gravitation is just an approximation. Thus, for high precision the motion of the satellite should be formulated in accordance with the theory of general relativity. The acceleration of the satellite can be corrected by a post-Newtonian term, which is (compare also Petit and Luzum, 2010, pg. 155)

$$
\mathbf{a}_{ge} = -\frac{GM_\oplus}{r^2} \left(\left(4\frac{GM_\oplus}{c^2 r} - \frac{v^2}{c^2} \right) \mathbf{e_r} + 4\frac{v^2}{c^2}(\mathbf{e_r} \cdot \mathbf{e_v})\mathbf{e_v} \right), \quad (2.21)
$$

where $\mathbf{e_r}$ and $\mathbf{e_v}$ denote the unit position and velocity vector. For a circular orbit, with $v^2 = \frac{GM_\oplus}{r}$ and the velocity perpendicular to the radius vector, the relativistic correction of the acceleration

$$
\mathbf{a}_{ge} = -\frac{GM_\oplus}{r^2} \left(3\frac{v^2}{c^2} \right), \quad (2.22)
$$

is equal to the product of the Newtonian acceleration and a factor of $3\frac{v^2}{c^2}$, which is about 3×10^{-10} for a medium Earth orbiting (MEO) satellite velocity of about 3 km/s. For a LEO satellite, such

as GOCE, not only the velocity is large (up to 7.7 km/s), but the semi-major axis of the satellite orbit is small to about 6749.431 km (corresponding to an altitude of 371 km, by subtracting the semi-major of the Earth ellipsoid from the semi-major of the orbit). Thus, the correction is approximately 2×10^{-8} m/s^2.

2.2.6 Air drag

The most difficult effect to be modeled is air drag. Fortunately, the GOCE satellite orbits the Earth in drag-free motion, although only in flight direction. The model described in this section is not applied for data processing, but only for simulations.

The satellite will experience air drag due to the residual atmosphere. It can be modeled as

$$\mathbf{a}_{\text{drag}} = -0.5 \cdot C_{\text{d}} \cdot \left(\frac{A}{M}\right) \rho \left|\mathbf{v}_{\text{rel}}\right| \mathbf{v}_{\text{rel}}, \tag{2.23}$$

where $\mathbf{v}_{rel}$ is the velocity vector of the satellite relative to the atmosphere; C_d is the drag coefficient of the satellite; A and M are the cross area and the mass of the satellite, respectively; ρ is the density of the atmosphere, which can be taken from atmosphere models such as Harris-Priester or Jacchia-Roberts, compare (Montenbruck and Gill 2000), see also (Beutler, 2004; Frommknecht, 2008).

The atmospheric relative velocity of the satellite, i.e. $\mathbf{v}_{rel}$, can be evaluated as

$$\mathbf{v}_{\text{rel}} = \mathbf{v} - \boldsymbol{\omega} \times \mathbf{r}, \tag{2.24}$$

where the angular velocity of the Earth rotation is $\boldsymbol{\omega} = \begin{bmatrix} 0 & 0 & \omega_e \end{bmatrix}^T$, with the nominal value of $\omega_e = 7.2921151467 \times 10^{-5}$ rad/s.

Air drag is the largest non-gravitational perturbation for LEO satellites. But the physical characteristics of the atmosphere especially at altitudes higher than 180 km are not known in much detail. Furthermore, the interaction between the neutral and ionized atmosphere and the surface of satellites still needs some investigation. Thus, it is difficult to model the air dynamics with mathematical models very accurately. In Eq. (2.23) the drag coefficient depends on the shape and the material of the satellite surface, and it changes with time due to the changes of the satellite's attitude w.r.t. the direction of $\mathbf{v}_{rel}$. Its value varies from 1.5 to 3.0. In general, it is estimated during the orbit determination procedure, in order to compensate the overall atmosphere model error.

The derivatives of the acceleration w.r.t. the drag coefficient can be written as

$$\frac{d\mathbf{a}_{\text{drag}}}{dC_{\text{d}}} = -0.5 \cdot \left(\frac{A}{M}\right) \rho \left|\mathbf{v}_{\text{rel}}\right| \mathbf{v}_{\text{rel}}. \tag{2.25}$$

The partial derivatives of the acceleration w.r.t. the drag coefficient can be evaluated explicitly. However, the partial derivatives of the position vector and velocity vector with respect to the drag

coefficient can only be computed by numerical integration of Eq. (2.25). Based on Eq. (2.23), the partial derivatives of the air drag acceleration w.r.t. the position vector can be formulated as

$$
\begin{aligned}
\frac{\partial \mathbf{a}_{\text{drag}}}{\partial \mathbf{r}} = & -0.5 \cdot C_{\text{d}} \cdot \left(\frac{A}{M} \right) |\mathbf{v}_{\text{rel}}| \mathbf{v}_{\text{rel}} \frac{\partial \rho}{\partial \mathbf{r}} \\
& + 0.5 \cdot C_{\text{d}} \cdot \left(\frac{A}{M} \right) \rho \left(\frac{\mathbf{v}_{\text{rel}} \mathbf{v}_{\text{rel}}^T}{|\mathbf{v}_{\text{rel}}|} + |\mathbf{v}_{\text{rel}}| \mathbf{I}_{3 \times 3} \right) \Omega,
\end{aligned}
\tag{2.26}
$$

where

$$
\Omega = \begin{pmatrix} 0 & -\omega_e & 0 \\ \omega_e & 0 & 0 \\ 0 & 0 & 0 \end{pmatrix} .
$$

The density of the upper atmosphere changes very smoothly and slow with respect to the position vector. Due to the complexity of the atmospheric models, the computation of the partial derivatives of the density w.r.t. the position vector cannot be formulated analytically. In general, one can compute them by numerical differentiation, compare (Bae, 2006; Montenbruck and Gill, 2000).

The partial derivatives of the acceleration with respect to the velocity can be derived as

$$
\frac{\partial \mathbf{a}_{\text{drag}}}{\partial \mathbf{v}} = 0.5 \cdot C_{\text{d}} \cdot \left(\frac{A}{M} \right) \rho \left(\frac{\mathbf{v}_{\text{rel}} \mathbf{v}_{\text{rel}}^T}{|\mathbf{v}_{\text{rel}}|} + |\mathbf{v}_{\text{rel}}| \mathbf{I}_{3 \times 3} \right) .
\tag{2.27}
$$

2.2.7 Solar radiation

The power supply on GOCE satellite comes from solar radiation. Due to the radiation of the sun, the satellite will experience an acceleration, which is modeled as

$$
\mathbf{a}_{\text{srp}} = C_{\text{r}} \left(\frac{A}{M} \right) P_0 R_0^2 \frac{\mathbf{r} - \mathbf{r}_{\text{s}}}{|\mathbf{r} - \mathbf{r}_{\text{s}}|^3} ,
\tag{2.28}
$$

where C_r is the radiation coefficient; the A and M are the area and the mass of the satellite, respectively; the R_0 is the length of one astronomical unit (AU), which is the mean distance between the Earth and the sun, i.e. 149597870 km (IAU 1976); the P_0 is solar radiation pressure constant at 1 AU, which is 4.5605E-6 Nm^{-2} (IERS 1996); the $\mathbf{r}_{\text{s}}$ is the position vector of the sun; the $\mathbf{r}$ is the position vector of the satellite.

The partial derivatives of the solar radiation pressure acceleration is approximated from Eq. (2.28) as

$$
\frac{d\mathbf{a}_{\text{srp}}}{dC_{\text{r}}} = \left(\frac{A}{M} \right) P_0 R_0^2 \frac{\mathbf{r} - \mathbf{r}_{\text{s}}}{|\mathbf{r} - \mathbf{r}_{\text{s}}|^3} .
\tag{2.29}
$$

The gradient $\frac{d\mathbf{a}_{\mathrm{srp}}}{d\mathbf{r}}$ is evaluated as

$$\frac{d\mathbf{a}_{\mathrm{srp}}}{d\mathbf{r}} = C_{\mathrm{r}} \left(\frac{A}{M} \right) P_0 R_0^2 \left(\frac{\mathbf{I}_{3\times 3}}{|\mathbf{r} - \mathbf{r}_{\mathrm{s}}|^3} - 3 \frac{(\mathbf{r} - \mathbf{r}_{\mathrm{s}})(\mathbf{r} - \mathbf{r}_{\mathrm{s}})^T}{|\mathbf{r} - \mathbf{r}_{\mathrm{s}}|^5} \right), \tag{2.30}$$

which is very small and negligible.

2.2.8 Earth Radiation Pressure (Albedo)

An Earth-orbiting satellite will experience a force caused by the back-radiation of the Earth. It is smaller than the direct solar radiation for GOCE satellite and therefore not applied in SHA. It is just presented for completeness. Earth back radiation has two components: the short-wavelength optical radiation and the long-wavelength infrared radiation. In both cases, the force on the satellite decreases with increasing altitude, following the inverse square law of the emitted radiation pressure. The amplitude of the typical albedo force for low-Earth satellites is 10% to 35% of the force due to direct solar radiation pressure (Knocke et al. 1988).

The complexity of Earth radiation pressure is due to the diversity of the reflectivity of the Earth's surface. The Earth's surface and troposphere have different characteristics of reflection and emission. In order to calculate the Earth's radiation pressure, the Earth's surface is divided into elements; each element can be considered as a particular radiation source. By superposition the total force due to Earth radiation pressure can be computed as

$$\mathbf{a}_{\mathrm{erp}} = \sum_{j=1}^{N} C_{\mathrm{r}} \left(a_j v_j \cos \theta_j^E + \frac{1}{4} \xi_j \right) P_0 \frac{A}{m} \cos \theta_j^s \frac{dA_j}{\pi \cdot r_j^2} \mathbf{e}_j, \tag{2.31}$$

where v_j denotes the Earth element shadow functions and θ_j^E and θ_j^s are the angles of the Earth's surface or satellite surface normal, respectively to the incident radiation. The unit vector $\mathbf{e}_j$ points from the Earth surface element to the satellite, while the distance is r_j. The average emissivity ξ_j is approximately 0.68. It is reduced by a factor of 4 due to the ratio of the irradiated Earth cross-section $\pi R_\oplus^2$ to the total radiating Earth surface $4\pi R_\oplus^2$.

The radiation pressure of the Earth acting on GPS satellites is less than 2% of the pressure of the sun. For the GOCE satellite, this effect becomes larger by about 10% to 35% comparing to the direction radiation of the sun, since it is closer to the Earth. The force due to albedo can be approximated as

$$\mathbf{a}_{\mathrm{erp}} = v P_{\mathrm{e}} C_{\mathrm{r}} \frac{A}{m} \frac{R_\oplus^2}{r^3} \mathbf{r}, \tag{2.32}$$

where the variables are the same as in Eq. (2.31), except P_{e} which is now an Earth surface radiation pressure constant, which is equal to $\xi P_0 / 4$.

2.2.9 Empirical Accelerations

For a LEO satellite such as GOCE, the perturbation forces to be considered are the Earth's non-spherical gravitation, direct tide due to the moon and the sun, solid Earth tides and ocean tides, atmosphere drag, solar radiation and Earth radiation as well as relativistic effects. The considered non-gravitational forces are not modelled with their explicit force models, but by introducing some empirical parameters. Model errors limit the dynamic strategies. They result in systematic errors growing with the arc length. Introducing empirical parameters, e.g., 1-cpr parameters or stochastic pulses, in the parameter estimation process allows to minimize these errors and to absorb the non-gravitational forces. This is the key element of the reduced-dynamic strategies. Empirical parameters reduce the influence of possible deficiencies of the dynamical models on the estimated orbit. Lower orbits require more empirical parameters than higher ones because it is virtually impossible to apply adequate models for the atmospheric drag and for the complete Earth's gravitational field (at least initially).

Based on a highly precise force model, small unmodelled forces may be accounted for by using the concept of empirical accelerations. Much of the mis-modelling occurs at a frequency of once per revolution (1-cpr). Accordingly, constant and 1-cpr empirical forces

$$\mathbf{f} = \mathbf{E}(\mathbf{a}_0 + \mathbf{a}_1 \sin v + \mathbf{a}_2 \cos v), \tag{2.33}$$

are employed to accommodate the effect. Here, $\mathbf{a_0}$ is a constant acceleration bias vector, while $\mathbf{a_1}$ and $\mathbf{a_2}$ are the 1-cpr coefficient vectors and v is the true anomaly (for a near-circular orbit, one can use the mean anomaly for simplicity). A linear term is also sometimes applied. The vector of empirical acceleration is commonly specified in the local orbital frame, with axes in the along-track (S), cross-track (T), and approximately radial (W) direction, which is then transformed to the inertial system by a transformation matrix $\mathbf{E}$. In order to provide an optimum compensation of unmodelled forces, the empirical acceleration coefficients have to be adjusted along with other parameters during orbit determination (see Montenbruck and Gill, 2000).

For a given state vector, i.e. position vector $\mathbf{r}$ and velocity vector $\mathbf{v}$, the matrix $\mathbf{E}$ can be determined by three unit vectors (which are column vectors here), i.e.

$$\begin{aligned} \mathbf{e}_S &= \frac{\mathbf{v}}{|\mathbf{v}|} \\ \mathbf{e}_T &= \frac{\mathbf{r} \times \mathbf{v}}{|\mathbf{r} \times \mathbf{v}|} \\ \mathbf{e}_W &= \mathbf{e}_S \times \mathbf{e}_T. \end{aligned} \tag{2.34}$$

The $\mathbf{E}$ matrix is then written as

$$\mathbf{E} = \begin{bmatrix} \mathbf{e}_S & \mathbf{e}_T & \mathbf{e}_W \end{bmatrix}. \tag{2.35}$$

However, the mis-modelling error or unmodelled effects may change rapidly; therefore, the empirical parameters hold only for a short period, somewhere from 10 to 30 minutes. The nine

parameters in Eq. (2.33), i.e. vectors $\mathbf{a}_0$, $\mathbf{a}_1$ and $\mathbf{a}_2$ are estimated based on the measurements inside this short interval. For the next time period, another set of empirical parameters is introduced, in order to absorb the time-varying behavior of the mis-modelling error there. One will find that these parameters are time dependent (depending on the measurements in the short interval).

2.3 Variational Equations

In order to formulate the observation equations for SST measurements, the partial derivatives of the satellite orbits with respect to dynamic force parameters such as gravity coefficients have to be evaluated. These partial derivatives are computed by solving variational equations.

When the vector of position and velocity representing the state of the orbit, it is referred to as state vector. Variational equations are ordinary differential equations of the partial derivatives of the state vector of the satellite w.r.t. the dynamic force coefficients to be estimated. They can be solved by orbit integration.

Suppose

$$\boldsymbol{\beta} = \begin{bmatrix} \overline{C}_{00} & \overline{C}_{10} & \overline{C}_{11} & \overline{S}_{11} & \overline{C}_{20} & \overline{C}_{21} & \overline{S}_{21} & \cdots \end{bmatrix}^T, \tag{2.36}$$

is the vector of coefficients, then the partial derivatives of acceleration w.r.t. $\boldsymbol{\beta}$, i.e. $\frac{\partial \ddot{\mathbf{r}}}{\partial \boldsymbol{\beta}}$, can be evaluated using Eq. (2.15). The partial derivatives of the orbit w.r.t. other parameters such as drag coefficients and/or radiation coefficients is computed from corresponding formulas given in the previous sections.

The partial derivatives $\frac{\partial \ddot{\mathbf{r}}}{\partial \boldsymbol{\beta}}$ evaluated in Eq. (2.14) have to be transformed to the inertial coordinate system, i.e.

$$\frac{\partial \ddot{\mathbf{r}}_i}{\partial \boldsymbol{\beta}} = \frac{\partial \left(\mathbf{C}_e^i \ddot{\mathbf{r}}_e \right)}{\partial \boldsymbol{\beta}} = \mathbf{C}_e^i \frac{\partial \ddot{\mathbf{r}}_e}{\partial \boldsymbol{\beta}}, \tag{2.37}$$

in which $\frac{\partial \ddot{\mathbf{r}}_e}{\partial \boldsymbol{\beta}}$ is what we obtain from Eq. (2.14), and $\mathbf{C}_e^i$ is the rotation matrix from the Earth-fixed frame to the space-fixed frame; $\frac{\partial \ddot{\mathbf{r}}_i}{\partial \boldsymbol{\beta}}$ are the partial derivatives in the inertial frame; they are integrated with a numerical integrator.

In order to formulate variational equations, we introduce $\mathbf{S}$, denoting the sensitivity matrix

$$\mathbf{S} = \begin{pmatrix} \frac{\partial \mathbf{r}}{\partial \boldsymbol{\beta}} \\ \\ \frac{\partial \dot{\mathbf{r}}}{\partial \boldsymbol{\beta}} \end{pmatrix}. \tag{2.38}$$

Then the time derivative of the sensitivity matrix is

$$\dot{\mathbf{S}} = \mathbf{F} \cdot \mathbf{S} + \begin{pmatrix} \mathbf{0} \\ \\ \frac{\partial \ddot{\mathbf{r}}}{\partial \boldsymbol{\beta}} \end{pmatrix}, \tag{2.39}$$

where $\mathbf{F} = \begin{pmatrix} \mathbf{0} & \mathbf{I}_{3 \times 3} \\ \frac{\partial \ddot{\mathbf{r}}}{\partial \mathbf{r}} & \frac{\partial \ddot{\mathbf{r}}}{\partial \dot{\mathbf{r}}} \end{pmatrix}$, with initial value $\mathbf{S}_0 = \mathbf{0}$.

The partial derivatives of position and velocity w.r.t. the initial state vector are used to estimate the orbit by means of dynamical orbit determination. They can be presented in the form of a state transition matrix

$$\boldsymbol{\Phi}(t, t_0) = \begin{pmatrix} \frac{\partial \mathbf{r}}{\partial \mathbf{r}_0} & \frac{\partial \mathbf{r}}{\partial \dot{\mathbf{r}}_0} \\ \frac{\partial \dot{\mathbf{r}}}{\partial \mathbf{r}_0} & \frac{\partial \dot{\mathbf{r}}}{\partial \dot{\mathbf{r}}_0} \end{pmatrix}. \tag{2.40}$$

It is computed by solving the following differential equation:

$$\dot{\boldsymbol{\Phi}}(t, t_0) = \mathbf{F} \cdot \boldsymbol{\Phi}(t, t_0). \tag{2.41}$$

where dotted symbols $\dot{\boldsymbol{\Phi}}$ denote derivatives with respect to time t.

Thereby the initial value of the transition matrix is $\boldsymbol{\Phi}(t_0, t_0) = \mathbf{I_{6 \times 6}}$, with $\mathbf{I_{6 \times 6}}$ a 6-by-6 unit matrix.

Equations (2.39) and (2.41) are called variational equations. By solving these differential equations, the partial derivatives of the state vector w.r.t. the dynamic coefficients are obtained. Thus the derivatives of the geometric measurements such as range or range rate w.r.t. the dynamic coefficients to be estimated are derived. The variational equation can be solved by either numerical integration (Montenbruck and Gill, 2000) or a variational of constants approach (Beutler, 2004).

2.4 Orbit Integration

A highly accurate satellite orbit can only be obtained by means of numerical integration of the equations of motion. A variety of methods has been developed for the numerical integration of ordinary differential equations and many of them have successfully been applied in the field of celestial mechanics. The most frequently used approaches are firstly Runge-Kutta methods that are particularly easy to use and may be applied to a wide range of problems, and can be easily implemented due to their simplicity. But the evaluations of the functions are expensive. The Runge-Kutta method is usually time-consuming. The second one is the multistep methods, which provide a high efficiency but requires a storage of past data points.

The multistep method is used in our computation. The n-dimensional differential equation to be solved is in general

$$\dot{\mathbf{y}} = \mathbf{f}(t, \mathbf{y}) \qquad \mathbf{y}, \ \dot{\mathbf{y}}, \mathbf{f} \in \mathfrak{R}^n, \tag{2.42}$$

where dotted symbols $\dot{\mathbf{y}}$ denote derivatives with respect to time t. The equation of satellite motion

is often written as

$$\ddot{\mathbf{r}} = \mathbf{a}(t, \mathbf{r}, \dot{\mathbf{r}}). \tag{2.43}$$

The state vector of the satellite is composed of the position vector $\mathbf{r}$ and velocity vector $\dot{\mathbf{r}}$, thus we have

$$\mathbf{y} = \begin{pmatrix} \mathbf{r} \\ \dot{\mathbf{r}} \end{pmatrix}, \tag{2.44}$$

to satisfy

$$\dot{\mathbf{y}} = \mathbf{f}(t, \mathbf{y}) = \begin{pmatrix} \dot{\mathbf{r}} \\ \ddot{\mathbf{r}} \end{pmatrix}. \tag{2.45}$$

Suppose the approximate value of the solution $\mathbf{y}(t_j)$ is obtained and represented by η_j at equidistant times $t_j = t_0 + j \cdot h$ for $j = 0, 1, \cdots, i$. Integrating both sides of the differential equation with respect to t from t_i to t_{i+1}, the equivalent expression is

$$\mathbf{y}(t_{i+1}) = \mathbf{y}(t_i) + \int_{t_i}^{t_{i+1}} \mathbf{f}(t, \mathbf{y}) dt. \tag{2.46}$$

The integral cannot be evaluated explicitly, since it depends on the unknown solution $\mathbf{y}(t)$ of the differential equation. The function is therefore replaced by interpolation using a polynomial $\mathbf{p}(t)$ through the values

$$\mathbf{f}_j = \mathbf{f}(t_j, \boldsymbol{\eta}_j), \tag{2.47}$$

at previous times t_j that are already known according to the initial assumption. This results in

$$\boldsymbol{\eta}_{i+1} = \boldsymbol{\eta}_i + \int_{t_i}^{t_i+h} \mathbf{p}(t) dt. \tag{2.48}$$

The increment function of a multistep method is therefore given by

$$\boldsymbol{\Psi} = \frac{1}{h} \int_{t_i}^{t_i+h} \mathbf{p}(t) dt, \tag{2.49}$$

where $h = t_{i+1} - t_i$ is the stepsize, and we arrive at the approximate solution

$$\boldsymbol{\eta}_{i+1} = \boldsymbol{\eta}_i + h\boldsymbol{\Psi}. \tag{2.50}$$

With m points $(t_{i-m+1}, \mathbf{f_{i-m+1}}), \cdots, (t_i, \mathbf{f_i})$, we can use Newton's formula to formulate a poly-

2. THEORY ABOUT ORBIT PERTURBATIONS AND CASE STUDY

nomial of order $m-1$ with equidistant nodes t_i. The polynomial is given by the compact expression

$$\mathbf{p}_m^i(t) = \mathbf{p}_m^i(t_i + \sigma h) = \sum_{j=0}^{m-1} (-1)^j \binom{-\sigma}{j} \nabla^j \mathbf{f}_i, \tag{2.51}$$

where the binomial coefficient is

$$\binom{-\sigma}{j} = \frac{(-\sigma)(-\sigma-1)\cdots(-\sigma-j+1)}{j!}, \tag{2.52}$$

for $j > 0$ and is equal to 1 for j=0. The backward differences of $\mathbf{f_i}$ are recursively computed from

$$\begin{aligned}
\nabla^0 \mathbf{f}_i &= \mathbf{f}_i \\
\nabla^1 \mathbf{f}_i &= \mathbf{f}_i - \mathbf{f}_{i-1} \\
\nabla^n \mathbf{f}_i &= \nabla^{n-1} \mathbf{f}_i - \nabla^{n-1} \mathbf{f}_{i-1}.
\end{aligned} \tag{2.53}$$

With the above notation the increment function of the mth-order Adams-Bashforth multistep method can be denoted as

$$\boldsymbol{\Psi}_{ABm} = \frac{1}{h} \int_{t_i}^{t_i+h} \mathbf{p}_m^i(t) dt = \sum_{j=0}^{m-1} \gamma_j \nabla^j \mathbf{f}_i, \tag{2.54}$$

with stepsize-independent coefficients from a recursive relation (Shampine and Gordon, 1975)

$$\gamma_j = 1 - \sum_{k=0}^{j-1} \frac{1}{j+1-k} \gamma_k \quad . \tag{2.55}$$

Inserting the definition of backward differences into Eq. (2.54), the increment function may also be written in terms of the function values $\mathbf{f_j}$:

$$\boldsymbol{\Psi}_{ABm} = \beta_{m1} \mathbf{f}_{i-m+1} + \beta_{m2} \mathbf{f}_{i-m+2} + \cdots + \beta_{mm} \mathbf{f}_i = \sum_{j=1}^{m} \beta_{mj} \mathbf{f}_{i-m+j} \quad . \tag{2.56}$$

The coefficients β_{mj}, which now depend on the order m, are computed from the following relation

$$\beta_{mj} = (-1)^{m-j} \sum_{l=m-j}^{m-1} \gamma_j \binom{l}{m-j}, \tag{2.57}$$

for $j = 1, \cdots, m$.

In the mth-order Adams-Bashforth method the polynomial $\mathbf{p(t)}$ is defined by m function values up to and including $\mathbf{f_i}$ at time t_i. However, the integration is performed over the subsequent interval $t_i \dots t_{i+1}$ where the approximation is less accurate due to the low accuracy of extrapolation.

Another type of multistep method, known as the Adams-Moulton method, therefore uses the

polynomial $\mathbf{p}_m^{i+1}(t)$ which interpolates m function values at time steps t_{i-m+2} and t_{i+1}:

$$\mathbf{p}_m^{i+1}(t) = \mathbf{p}_m^{i+1}(t_i + \sigma h) = \sum_{j=0}^{m-1} (-1)^j \begin{pmatrix} -\sigma+1 \\ j \end{pmatrix} \nabla^j \mathbf{f}_{i+1}. \tag{2.58}$$

The Adams-Moulton formula is derived from

$$\mathbf{\Psi}_{ABm} = \frac{1}{h} \int_{t_i}^{t_i+h} \mathbf{p}_m^{i+1}(t) dt = \sum_{j=0}^{m-1} \gamma_j^* \cdot \nabla^j \mathbf{f}_{i+1}. \tag{2.59}$$

The coefficients γ_j are evaluated with

$$\gamma_j^* = -\sum_{k=0}^{j-1} \frac{1}{j+1-k} \gamma_k^*. \tag{2.60}$$

The local truncation error of the Adams-Moulton method is smaller than that of the Adams-Bashforth method, see Montenbruck and Gill (2000).

There is another method named collocation method, which is applied in the Bernese software (Dach et al., 2007). For more details the reader is referred to Beutler (2004).

2.5 Case Study for GOCE

In order to investigate how the perturbation forces affect the orbit and on the magnitude of the accelerations due to different perturbations, the orbits are simulated in each perturbation condition and compared to the Kepler orbit. Also the accelerations are computed along the simulated orbits. The approach we will apply for SST uses short arcs with a length of 10 to 30 minutes. The precision of the kinematic orbit is 2 cm (Visser et al., 2010). The simulation can tell us which effect can disturb the orbits by more than 2 cm within 10 to 30 minutes. Effects with orbit disturbances less than the precision of the kinematic orbits can be neglected, since they are beyond the sensitivity of the GPS measurements. In other words, our assumption is that with the precision of the kinematic orbit, the coefficients which disturb the orbit less than the precision of the orbit in short arcs cannot be identified.

The starting elements of the GOCE satellite are

semi-major	6720.495728 km	right ascension	277.2480°
eccentricity	0.014770802	arg. of perigee	95.3014°
inclination	96.66465°	mean anomaly	358.8249°

The mass of the satellite is 1050 kg; the cross-section is 1 m^2. The ocean tide model used in this simulation is EOT08a. The atmospheric density is computed based on the Harris-Priester Density Model. For Earth rotation, the package of Standards Of Fundamental Astronomy (SOFA) is used. The SOFA software is a collection of Fortran 77 subprograms that implement official IAU algorithms for fundamental-astronomy computations, (IAU SOFA Board, 2010). The gravitational

field model used in this simulation is EGM2008 (Pavlis et al., 2008). The perturbation due to disturbing forces are shown in Figs. 2.5 to 2.13, with the left panel containing the disturbance of the orbit, and right panel the disturbing acceleration, respectively, for each perturbation source.

(a) Orbit   **(b)** Acceleration
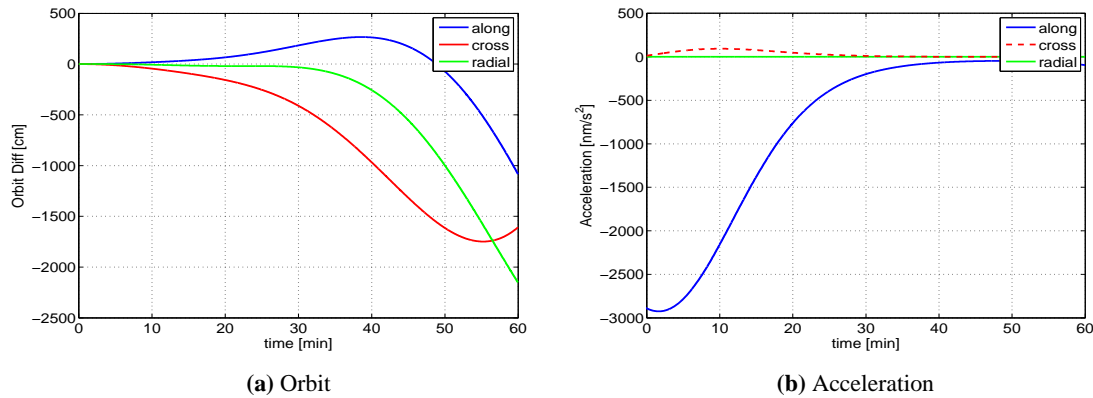
Figure 2.5: Time series of the perturbation of the orbit and the acceleration caused by air drag

(a) Orbit   **(b)** Acceleration
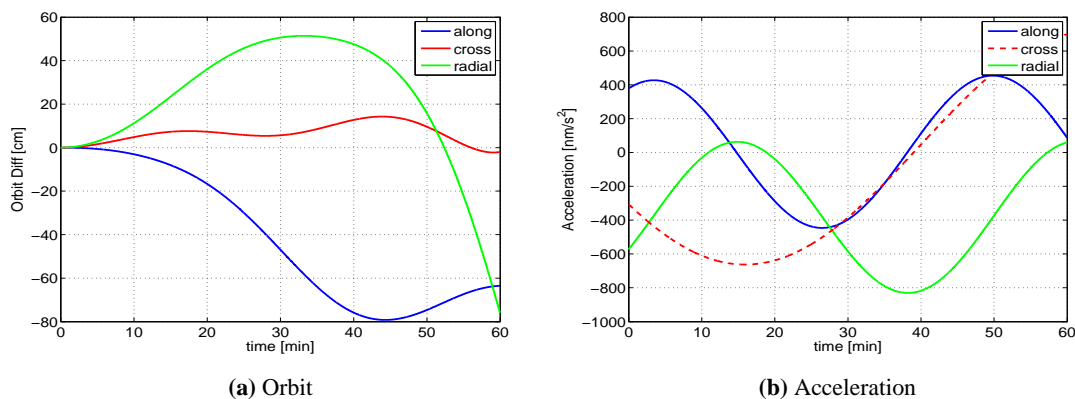
Figure 2.6: Time series of the perturbation of the orbit and the acceleration caused by the direct attraction of sun and moon

The simulation demonstrates that all the perturbations caused by the planets in the solar system can be neglected; only the perturbations of sun and moon are considered since the orbit differences reach more than 10 cm in about 10 minutes. The solar radiation and albedo disturbance can reach the 1-cm level in about one and half hours, which is a bit smaller than the orbit accuracy. Moreover, since empirical parameters given in Eq. (2.33) will be applied, and are able to absorb most of the disturbing accelerations, these two effects are not modelled in SST with their explicit force model, but are expected to be taken care of by the empirical accelerations.

The total of 241 coefficients of the Earth's gravitational field of degree 120 can disturb the GOCE orbit by less than 1 cm in 60 minutes. This means the influence of the coefficients at degree 120 of the gravitational field is less than the noise of the kinematic orbit. From this point of view, one might say degree and order 120 is beyond or at the limit of the capability of GOCE

(a) Orbit   **(b)** Acceleration
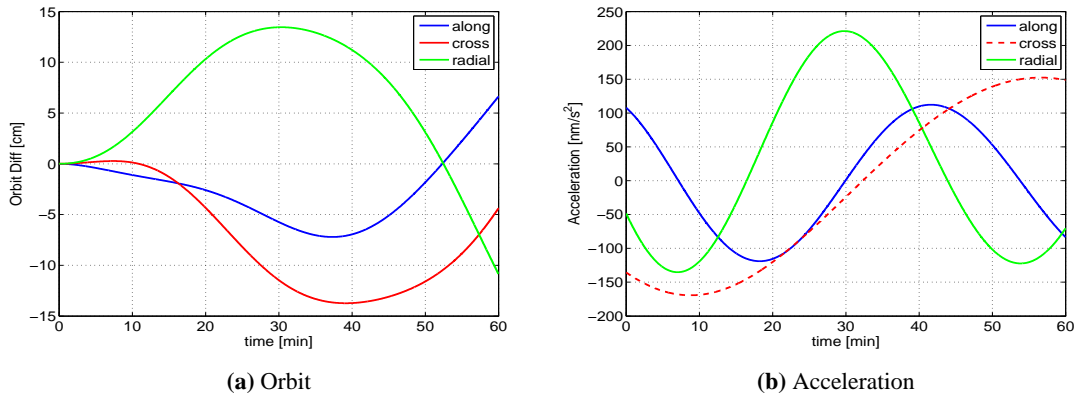
Figure 2.7: Time series of the perturbation of the orbit and the acceleration caused by solid Earth tide

(a) Orbit   **(b)** Acceleration
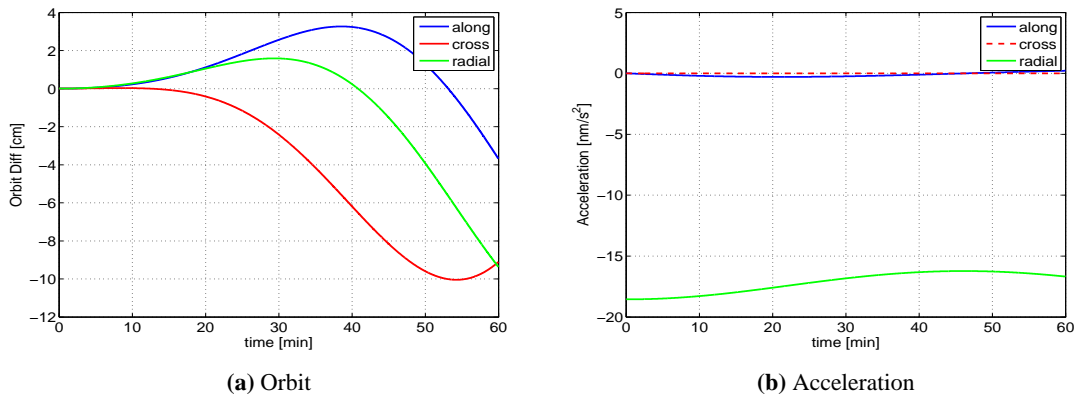
Figure 2.8: Time series of the perturbation of the orbit and the acceleration caused by general relativity

(a) Orbit   **(b)** Acceleration
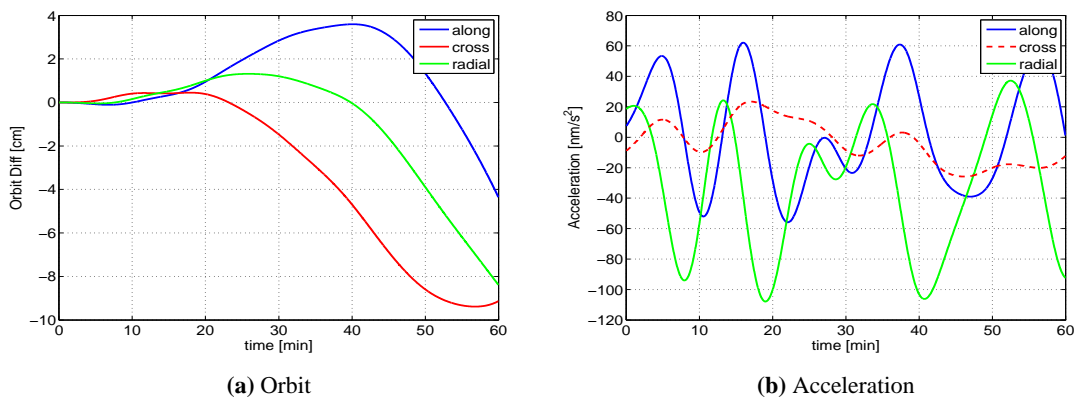
Figure 2.9: Time series of the perturbation of the orbit and the acceleration caused by ocean tide

(a) Orbit
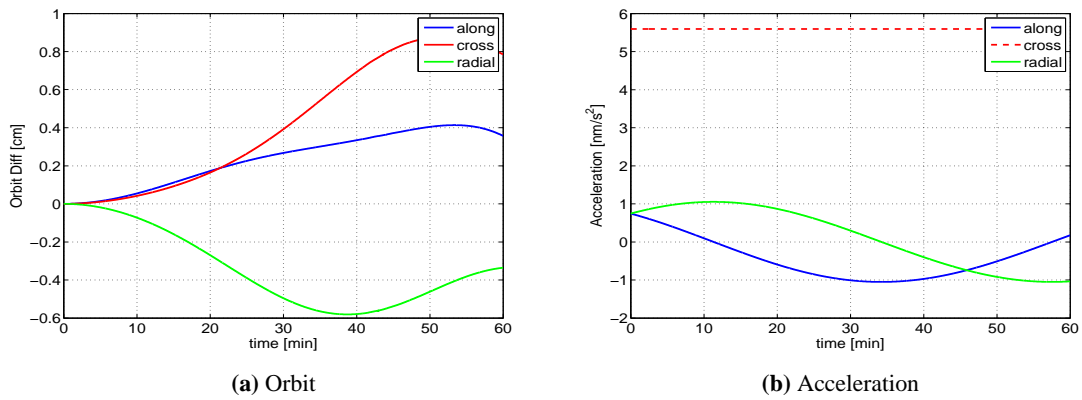
(b) Acceleration

Figure 2.10: Time series of the perturbation of the orbit and the acceleration caused by solar radiation

(a) Orbit
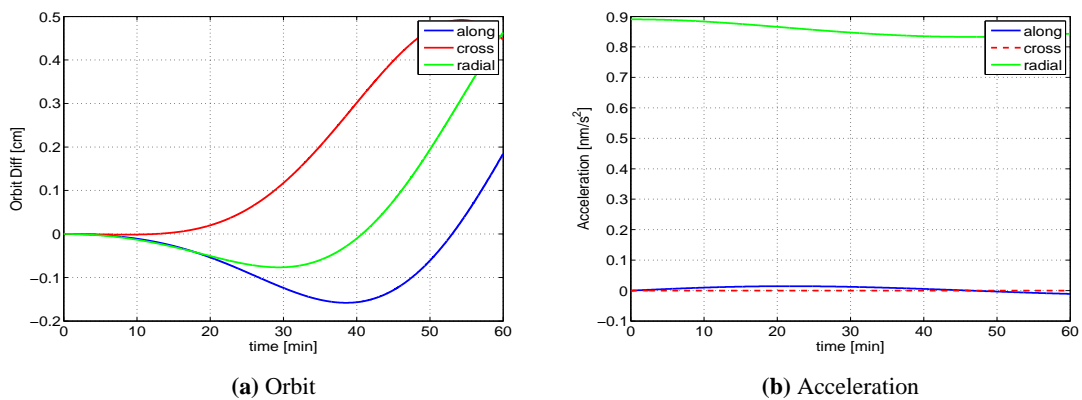
(b) Acceleration

Figure 2.11: Time series of the perturbation of the orbit and the acceleration caused by albedo

(a) Orbit
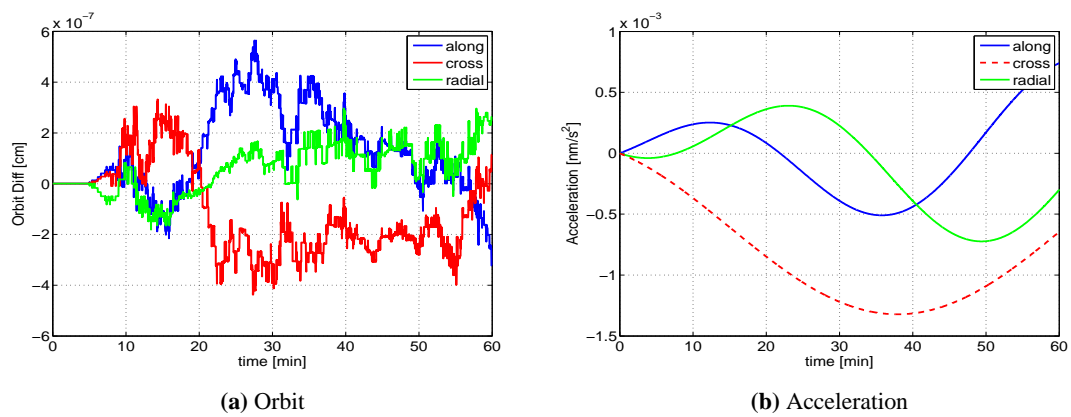
(b) Acceleration

Figure 2.12: Time series of the perturbation of the orbit and the acceleration caused by all the planets

(a) Orbit
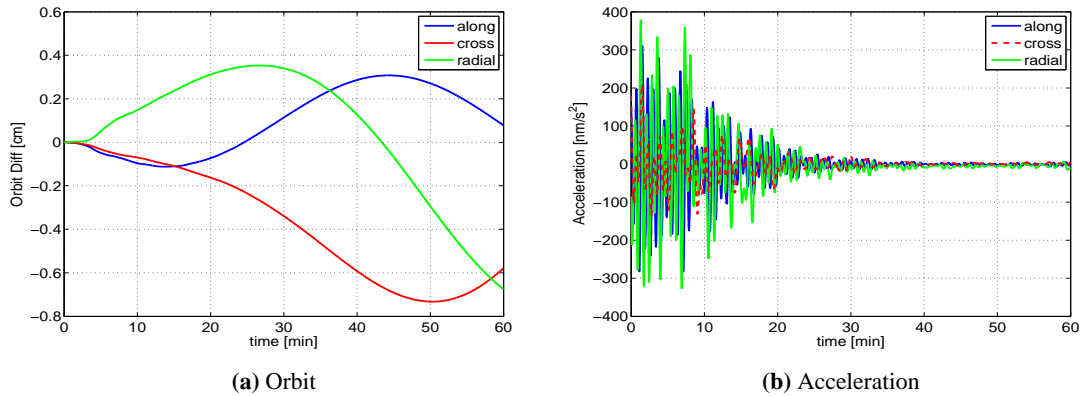
(b) Acceleration

Figure 2.13: Time series of the perturbation of the orbit and the acceleration caused by all the degree 120 coefficients of the gravitational field

orbit sensitivity for parameter estimation. However, the cumulative effect of the gravitational field coefficients of degrees higher than 120 is higher than the 2 cm in 10 to 30 minutes (see Table 2.1); thus it is suitable to set up the SH coefficient solution even higher than 120. The gravity field signal is systematic, in principle, whereas the noise is stochastic. With more and more data used in parameter estimation, the signal-to-noise ratio (SNR) can be accordingly increased. Nevertheless, this is only a rough analysis. The highest d/o one can solve for depends on the precision of the measurements, but also on the word length of the computer, the algorithm used for parameter estimation and the stability of the problem itself, etc. The real performance can only be found from the resulting model after an SST solution has been obtained.

In Table 2.1, the magnitude of the orbit deviations due to sets of gravitational field coefficients is given. The disturbance from d/o 120-130 is already larger than the precision of the kinematic orbits. For all the other d/o in the table the perturbations are smaller than the precision. These are cumulative effects from a group of gravitational field coefficients. Another important point is that the magnitude of the signals corresponding to different coefficients varies significantly. It is cumbersome to reconstruct weak signals which are part of a large strong signal.

Table 2.1: Orbit perturbations (the length in three directions) caused by different gravitational field coefficients over different time periods [cm]

	d/o 120-130	d/o 130-140	d/o 140-150	d/o 150-181
10 min	2.03	0.53	0.27	0.10
20 min	6.28	0.97	0.71	0.62
30 min	11.42	1.30	1.35	1.06
40 min	15.39	1.99	1.98	1.34

The air drag is the largest non-gravitational source of disturbance. For GOCE, it is com-

pensated in flight direction by ion thrusting with a magnitude from a level of 10^{-6} m/s^{-2} to 10^{-8} m/s^{-2}, i.e. two to three orders of magnitude of the drag in flight direction are eliminated, see (Floberghagen et al., 2011). Thus, only the residual of the air drag acceleration and the full drag in cross-track and radial direction need to be modelled or measured.

The perturbation of radiation pressure and albedo is smaller than 2 cm within 40 minutes. They are therefore neglected and hopefully compensated with the empirical accelerations.

The effects of solid Earth tides, ocean tides together with pole tides, as well as general relativity are considered for gravity field recovery, since all these effects disturb the orbit by more than 2 cm in 30 minutes.

2.6   Summary

In this section, the basic theory of the satellite orbit analysis for the case of GOCE is presented. All computations related to orbit perturbation for SST in Chapter 4, and the correction for the disturbance in the measured GGT, are based on this part.

The normalized Cunningham approach for spherical harmonic computation has been derived. It is given in the Cartesian coordinate system. It has no singularity; therefore, it is chosen for the computation in this study. For the gravitational gradient analysis, the derivation will be presented in Chapter 5.

The perturbation forces acting on the GOCE satellite and the resulting orbit perturbation are discussed. The main effect is due to the gravitational field of the Earth as expressed by a series of SH coefficients. The results show that the gravitational forces caused by the direct attraction of the moon and sun, solid Earth tides, ocean tides and general relativity must be included in the parameter estimation procedure. The direct effect of planets is negligible. The effect of the so-called pole tides is considered and incorporated in the computation of solid Earth tides. The perturbation of general relativity is not small; therefore, it has to be considered.

The air drag experienced by GOCE satellite reduces to the level of the precision of the drag-compensation actuators, i.e. the ion thrusters. The residual acceleration after compensation by the ion thruster can be either modelled with empirical accelerations, or removed with the information from the common mode accelerations. The perturbations due to radiation pressure and albedo are smaller than the precision of the kinematic orbit within 40 minutes. They are not modelled in the parameter estimation process explicitly but hopefully compensated by the empirical parameters implicitly.

Based on our case study (Table 2.1), it is reasonable to set up the SH coefficients at least up to d/o 140 to 150. The cumulative effect of the gravity field coefficients higher than d/o 150 on GOCE orbits is likely beyond the capability as determined by the kinematic orbit precision.

3

Least Squares and Data Adjustment for GOCE Data Processing

In modern geodesy, the amount of observations can reach millions or even billions. The handling of such a large amount of observations with a huge amount of unknown parameters is a challenge. It is therefore important to discuss some elements of the theory of parameter estimation, which are then used for SHA in the later chapters for the processing of GOCE measurements.

The large least squares problem is introduced in the first section. The second section presents the idea of regularization, and emphasizes the concept developed in this study. The third section is about contribution analysis, i.e. an approach of evaluating the individual contribution of different data sources. The fourth section is dedicated to data weighting and decorrelation. The fifth section presents the concepts of parameter pre-elimination. And, last but not least, the final section gives the summary of this chapter.

3.1 Least Squares Adjustment and Combination of Different Observation Types

The method of least squares has been widely used to solve overdetermined systems since Gauss and Legendre developed the fundamentals of the basis for least squares analysis. Least squares adjustment can be interpreted as a method of fitting a linear model to (stochastic) observations. The observations are collected under randomly varying conditions. This makes the observations stochastic. The best fit in the least-squares sense is when the sum of squared residuals between observations and modelled values attains its least value. It corresponds to the maximum likelihood criterion if the experimental errors have a normal distribution and can also be derived as a method of moments estimator, cf. Teunissen (2009).

The observation equation of a parameter model can be represented by

$$E\left\{\tilde{\mathbf{L}}\right\} = F(\mathbf{x}) , \qquad (3.1)$$

where

$E\{\}$	operator of expectation
$\tilde{\mathbf{L}}$	vector of stochastic observations
$\mathbf{L}$	expectation or estimate of the observation vector
$\mathbf{x}$	parameter vector to be estimated
F	mapping function .

The stochastic observations are composed of their expectation (true value) and stochastic error $\tilde{\mathbf{v}}$ with expectation zero (tilde "~" meaning stochastic), i.e.

$$\tilde{\mathbf{L}} = \mathbf{L} + \tilde{\mathbf{v}} \,, \tag{3.2}$$

with $E\{\tilde{\mathbf{L}}\} = \mathbf{L}$ and $E\{\tilde{\mathbf{v}}\} = 0$. In case of a non-linear model, linearization is needed. After linearization, Eq. (3.1) is written as

$$E\{\tilde{\mathbf{L}}\} = F(\mathbf{x}_{01}) + \left.\frac{\partial F}{\partial \mathbf{x}}\right|_{\mathbf{x}=\mathbf{x}_{01}} \delta\mathbf{x}. \tag{3.3}$$

with $\delta\mathbf{x}$ the correction of the parameter vector w.r.t. the initial or approximate values $\mathbf{x}_{01}$. Even in case of a linear situation, the initial values $\mathbf{x}_{01}$ are often used to make the right-hand side smaller to reduce computer (both round-off and truncation) error.

Let us define

$$\mathbf{A} = \left.\frac{\partial F}{\partial \mathbf{x}}\right|_{\mathbf{x}=\mathbf{x}_0} \,, \quad \text{and} \quad \tilde{\mathbf{d}} = \tilde{\mathbf{L}} - F(\mathbf{x}_{01}) \,, \tag{3.4}$$

then we arrive at

$$\tilde{\mathbf{v}} = \mathbf{A} \cdot \delta\mathbf{x} - \tilde{\mathbf{d}} \,, \tag{3.5a}$$

$$\text{and} \quad D\{\tilde{\mathbf{d}}\} = D\{\tilde{\mathbf{L}}\} = \boldsymbol{\Sigma} = \sigma_0^2 \mathbf{P}^{-1} = E\{\tilde{\mathbf{v}}\tilde{\mathbf{v}}^T\} \,, \tag{3.5b}$$

where

$\tilde{\mathbf{v}}$	$n \times 1$ misclosure vector, its estimate $\hat{\mathbf{v}}$ is the residual vector
$\mathbf{A}$	$n \times m$ design matrix (coefficient matrix)
$\delta\mathbf{x}$	$m \times 1$ vector of parameter correction
$\tilde{\mathbf{d}}$	$n \times 1$ vector of observed minus computed (OMC)
$D\{\}$	operator of dispersion
$\boldsymbol{\Sigma}$	$n \times n$ variance-covariance matrix (VCM) of observations (or misclosures)
σ_0^2	variance of unit weight (variance factor or variance component)
$\mathbf{P}$	$n \times n$ weight matrix

Since the differences between $\tilde{\mathbf{d}}$ and $\tilde{\mathbf{L}}$ is a deterministic, i.e. non-stochastic vector (the initial parameter mapping into the measurement space), their VCMs are the same. We sometimes say $\tilde{\mathbf{d}}$ is observation vector when it does not cause any confusion. Based on the principle of the least

squares adjustment, i.e.

$$\tilde{\mathbf{v}}^T \mathbf{P} \tilde{\mathbf{v}} = \min, \tag{3.6}$$

we obtain the system of normal equations (NEQs)

$$\mathbf{A}^T \mathbf{P} \mathbf{A} \delta \hat{\mathbf{x}} = \mathbf{A}^T \mathbf{P} \tilde{\mathbf{d}}, \quad \text{or} \quad \mathbf{N} \delta \hat{\mathbf{x}} = \mathbf{U} \tag{3.7}$$

and the following solution equations (Teunissen, 2009; Teunissen and Amiri-Simkooei, 2008)

$$\delta \hat{\mathbf{x}} = \left(\mathbf{A}^T \mathbf{P} \mathbf{A} \right)^{-1} \left(\mathbf{A}^T \mathbf{P} \tilde{\mathbf{d}} \right) = \mathbf{N}^{-1} \mathbf{U}, \tag{3.8a}$$

$$\hat{\mathbf{v}} = \mathbf{A} \delta \hat{\mathbf{x}} - \tilde{\mathbf{d}}, \tag{3.8b}$$

$$\hat{\sigma}_0^2 = \hat{\mathbf{v}}^T \mathbf{P} \hat{\mathbf{v}} / (n - m), \tag{3.8c}$$

$$D\{\delta \hat{\mathbf{x}}\} = \boldsymbol{\Sigma}_{\hat{\mathbf{x}}} = \hat{\sigma}_0^2 \left(\mathbf{A}^T \mathbf{P} \mathbf{A} \right)^{-1}, \tag{3.8d}$$

with n the total number of the observations and m the total number of the unknowns; $\mathbf{N} = \left(\mathbf{A^T P A} \right)$ the normal matrix and $\mathbf{U} = \mathbf{A^T P \tilde{d}}$ the right-hand side which will be used later on. The hat symbol above variables represents their estimates. For example, the residual vector $\hat{\mathbf{v}}$ is the estimate of the noise vector $\tilde{\mathbf{v}}$. Eq. (3.8a) gives us the estimates of the parameters. With them the estimates of the residuals can be obtained from Eq. (3.8b). Eqs. (3.8c) and (3.8d) are the estimates of the variance of unit weight and variance covariance matrix of the estimated parameters, respectively.

In case the amount of the observations is large, e.g., more than one hundred thousand or even millions, the dimension of the design matrix $\mathbf{A}$ will become so large that the memory of the computer is not sufficient to store it. This problem can be solved using the sequential least squares adjustment approach, in which the design matrix is removed from computer memory after it is accumulated to the normal matrix.

Let us suppose the observations can be divided into two stochastic independent parts, i.e. $\tilde{\mathbf{d}}_1$ and $\tilde{\mathbf{d}}_2$. This leads to the design matrix $\mathbf{A}$ to be divided into two parts, too

$$\begin{bmatrix} \tilde{\mathbf{v}}_1 \\ \tilde{\mathbf{v}}_2 \end{bmatrix} = \begin{bmatrix} \mathbf{A}_1 \\ \mathbf{A}_2 \end{bmatrix} \cdot \delta \mathbf{x} - \begin{bmatrix} \tilde{\mathbf{d}}_1 \\ \tilde{\mathbf{d}}_2 \end{bmatrix} \quad , \quad D\left\{ \begin{matrix} \tilde{\mathbf{d}}_1 \\ \tilde{\mathbf{d}}_2 \end{matrix} \right\} = \sigma_0^2 \begin{bmatrix} \mathbf{P}_1^{-1} & \mathbf{0} \\ \mathbf{0} & \mathbf{P}_2^{-1} \end{bmatrix}. \tag{3.9}$$

This holds under the assumption that the observations $\tilde{\mathbf{d}}_1$ and $\tilde{\mathbf{d}}_2$ are independent, i.e., the correlation between these two observation vectors is zero, as presented in the variance covariance matrix of Eq. (3.9).

Based on the principle of least squares, the parameter vector is derived with sequential least squares

$$\delta \hat{\mathbf{x}} = \left(\mathbf{A}_1^T \mathbf{P}_1 \mathbf{A}_1 + \mathbf{A}_2^T \mathbf{P}_2 \mathbf{A}_2\right)^{-1} \left(\mathbf{A}_1^T \mathbf{P}_1 \tilde{\mathbf{d}}_1 + \mathbf{A}_2^T \mathbf{P}_2 \tilde{\mathbf{d}}_2\right) , \tag{3.10a}$$

$$\hat{\sigma}_0^2 = \left(\hat{\mathbf{v}}_1^T \mathbf{P}_1 \hat{\mathbf{v}}_1 + \hat{\mathbf{v}}_2^T \mathbf{P}_2 \hat{\mathbf{v}}_2\right)/(n-m) , \tag{3.10b}$$

$$D\{\delta \hat{\mathbf{x}}\} = \mathbf{\Sigma}_{\hat{\mathbf{x}}} = \hat{\sigma}_0^2 \left(\mathbf{A}_1^T \mathbf{P}_1 \mathbf{A}_1 + \mathbf{A}_2^T \mathbf{P}_2 \mathbf{A}_2\right)^{-1} . \tag{3.10c}$$

It is seen that the combination of NEQs is by adding the two normal matrices and the two right-hand sides, respectively, to form a new system of NEQs. The estimate of the parameter vector can be solved from this new system of normal equations, as one can see in Eq. (3.10a). The estimates of the variance of unit weight and of the variance-covariance matrix are obtained from Eq. (3.10b) and (3.10c). With this idea, the large amount of observations can be decomposed into two or many smaller problems.

In Eq. (3.10), the weights of the two observation groups may not be perfect. Therefore, it is worthwhile to use the posterior estimate of the variance components, as given in Eq. (3.8c), to re-combine the normal equations as (Koch and Kusche, 2002)

$$\left(\frac{1}{\hat{\sigma}_1^2} \mathbf{A}_1^T \mathbf{P}_1 \mathbf{A}_1 + \frac{1}{\hat{\sigma}_2^2} \mathbf{A}_2^T \mathbf{P}_2 \mathbf{A}_2\right) \delta \hat{\mathbf{x}} = \left(\frac{1}{\hat{\sigma}_1^2} \mathbf{A}_1^T \mathbf{P}_1 \tilde{\mathbf{d}}_1 + \frac{1}{\hat{\sigma}_2^2} \mathbf{A}_2^T \mathbf{P}_2 \tilde{\mathbf{d}}_2\right) , \tag{3.11}$$

where the variance factors $\hat{\sigma}_1^2$ and $\hat{\sigma}_2^2$ are computed according to Eq. 3.8c.

It is similar to sequential least squares, see Eq. (3.10), except that the variance factor is introduced in Eq. (3.11) to guarantee the two normal equations to be weighted based on their variance factors. Also the size (length) and/or the sequence of the parameters in the vector may be different. One may have to reorder these parameters during the combination.

The a priori estimate of the variance component is useful for weighting the corresponding observation group in the first combination. It can be determined with OMC values based on a priori information. The a priori estimate of the variance components for an observation type is approximated based on theory of statistics

$$\hat{\sigma}^{2(-)} = \frac{\tilde{\mathbf{d}}^T \mathbf{P} \tilde{\mathbf{d}}}{n} - \left(\frac{1}{n} \sum_{k=1}^{n} \tilde{d}_k \sqrt{P_k}\right)^2 , \tag{3.12}$$

with n the number of the observations and P_k the weight of the kth observation.

3.2 Regularization

The system of normal equations in the least squares estimation problem is ill-posed in the case of GOCE due to several reasons, in particular the existence of polar gaps (non-polar orbits) and an inhomogeneous data distribution (Metzler, 2007); also one of the observation types may contain less information, e.g., one component of the gradient tensor may not be equally sensitive to

the whole gravity field; also the downward continuation will contribute to the instability. The introduced stochastic model of the measurements can be a cause for ill-posed normal equations (Sneeuw, 2000).

In case of ill-posed normal equations, the condition number (the ratio of the maximum eigenvalue to the minimum eigenvalue) of the normal matrix $\mathbf{N}$ is very large. This makes the solution of the system of normal equations unstable. There are two categories of approaches to solve this problem, one is to manipulate the eigenvalues by singular value decomposition (SVD), such as ridge estimation and principal component estimation. The other is to introduce some external or a-priori information to stabilize the normal equations. Since there is a-priori information of the gravity field available, the latter type of the regularization is chosen here for the SHA.

There are several methods of regularization available, such as regularization using Kaula's rule of thumb or first- and second-order Tikhonov regularization. These methods add some "information" to the diagonal elements of the normal matrix according to some rules and criteria (Kusche, 2002; Kusche and Klees, 2002), based on the criterion of a combined minimization residuals and of the gravity potential or its functionals on the sphere of the Earth.

The idea of regularization is to find the balance between the minimum norm of the residuals and that of the vector of unknown parameters relative to some a-priori values. Similar to Eq. (3.6), we minimize now

$$\tilde{\mathbf{v}}^T \mathbf{P} \tilde{\mathbf{v}} + \alpha (\mathbf{x} - \mathbf{x}_0)^T \mathbf{P}_{\mathbf{x}_0} (\mathbf{x} - \mathbf{x}_0) = \min . \tag{3.13}$$

The first term in Eq. (3.13) causes the model to fit the data, the second term constrains the parameters to a-priori values. It will stabilize the normal equations. The regularization factor α plays thereby an important role. It is a tradeoff between observations and a-priori information. Let us assume α to be 1 or incorporated in $\mathbf{P}_{\mathbf{x}_0}$. By taking the derivative on both sides of Eq. (3.13) and re-arranging, the modified estimator becomes:

$$\delta \hat{\mathbf{x}} = \left(\mathbf{A}^T \mathbf{P} \mathbf{A} + \mathbf{P}_{\mathbf{x}_0} \right)^{-1} \left(\mathbf{A}^T \mathbf{P} \tilde{\mathbf{d}} + \mathbf{P}_{\mathbf{x}_0} (\mathbf{x}_0 - \mathbf{x}_{01}) \right) . \tag{3.14}$$

Here $\mathbf{x}_{01}$ is the vector initial values as in Eq. (3.3). It does not necessarily have to be the same as $\mathbf{x}_0$, since one may set up the observation equation with some initial values; later on one may decide to constrain the parameters to some other a-priori values.

Since the inclination of the GOCE orbit is about $96.7°$, there is no GOCE data in both polar areas with a radius of about $6.7°$ around the poles, see Fig. 1.3. Therefore, a gravity field without constraint (regularization) over the polar gap will exhibit large oscillations in the gravity signals such as geoid heights and/or gravity anomalies in these areas. Since the estimator has no information there, it will produce arbitrary values in the polar gap areas, as long as the condition (target function), i.e. Eq. (3.6), is satisfied. For the North Pole, there are terrestrial data available. One

may therefore stabilize the problem with these terrestrial data. For the South Pole, not much terrestrial data have been collected. Thus, regularization must be applied. Metzler and Pail (2005) introduced the so-called Spherical Cap Regularization Approach (SCRA), which will reduce the oscillation of the resulting gravity field signal caused by the polar gaps.

A modified approach is applied in this study. It is to generate pseudo-observations based on a-priori information in the polar gap areas. This information is used to constrain the geoid of the gravity field to be estimated to, for example, EGM2008 or any other appropriate prior information. The assumed precision level is chosen according to a realistic assumption, i.e. a precision of the a-priori information at the polar areas. With the discrete geoid values to constrain the polar areas for the stabilization of the solution, this approach of regularization is different to the SCRA approach, which applies analytical function on the polar gap to reduce the oscillation behavior in the polar areas in the resulting gravity field models.

With the idea of pseudo observations on a $1° \times 1°$ equal angular grid in the polar areas, a normal matrix is generated as shown in Fig. 3.1. The SH coefficients are sorted order-wise (the order of the gravitational field coefficients increases from 0 to the maximum value from the upper left to the bottom right), one can see that the lower order coefficients (close to the upper left in the matrix) are regularized with large values, whereas the high order coefficients (close to the bottom right) are hardly affected by this regularization.
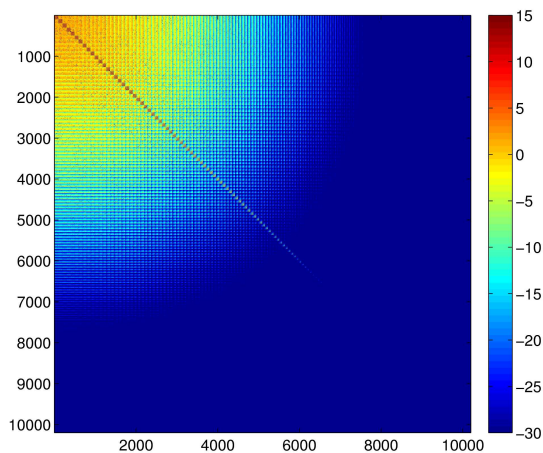
Figure 3.1: Normal matrix of regularization for polar gap (in m^2 and log10 scaled)

The goal of our regularization is that the final result should not be affected too much by the applied method of stabilization. However, since spherical harmonic coefficients are base functions with a global support but data are missing only at the poles, the estimated coefficients in general get correlated, see (Boxhammer and Schuh, 2006). Therefore, the regularization will definitely affect the estimated parameters. Thus, one should make the constraint as loosely as possible, in order to make sure that the $\tilde{\mathbf{v}}^T \mathbf{P} \tilde{\mathbf{v}}$ part in Eq. (3.13) is dominant. In other words, the actual GOCE observations should be given a weight as high as possible.

3.3   Combination and Contribution Analysis

The parameter estimation for GOCE is a combination of various components. It is of interest to know their relative contributions. Let us consider the combination of the orbit and gradiometer observations from the GOCE satellite. It is the combination of the SST and SGG part (the three diagonal components V_{xx}, V_{yy} and V_{zz}), as well as of the a-priori information for polar gap stabilization. In accordance with Eq. (3.11), they are combined as

$$
\begin{aligned}
\mathbf{N}\delta\hat{\mathbf{x}} &= \left(\frac{1}{\sigma_{sst}^2}\mathbf{N}_{sst} + \frac{1}{\sigma_{xx}^2}\mathbf{N}_{xx} + \frac{1}{\sigma_{yy}^2}\mathbf{N}_{yy} + \frac{1}{\sigma_{zz}^2}\mathbf{N}_{zz} + \frac{1}{\sigma_{reg}^2}\mathbf{N}_{reg} \right)\delta\hat{\mathbf{x}} \\
&= \frac{1}{\sigma_{sst}^2}\mathbf{A}_{sst}^T\mathbf{P}_{sst}\tilde{\mathbf{d}}_{sst} + \frac{1}{\sigma_{xx}^2}\mathbf{A}_{xx}^T\mathbf{P}_{xx}\tilde{\mathbf{d}}_{xx} + \frac{1}{\sigma_{yy}^2}\mathbf{A}_{yy}^T\mathbf{P}_{yy}\tilde{\mathbf{d}}_{yy} \\
&\quad + \frac{1}{\sigma_{zz}^2}\mathbf{A}_{zz}^T\mathbf{P}_{zz}\tilde{\mathbf{d}}_{zz} + \frac{1}{\sigma_{reg}^2}\mathbf{A}_{reg}^T\mathbf{P}_{reg}\tilde{\mathbf{d}}_{reg} \, .
\end{aligned}
\tag{3.15}
$$

In order to analyze the individual contribution from the different data sources (observation types) and from regularization, we look into the combined normal matrix of Eq. (3.15)

$$
\mathbf{N} = \frac{1}{\sigma_{sst}^2}\mathbf{N}_{sst} + \frac{1}{\sigma_{xx}^2}\mathbf{N}_{xx} + \frac{1}{\sigma_{yy}^2}\mathbf{N}_{yy} + \frac{1}{\sigma_{zz}^2}\mathbf{N}_{zz} + \frac{1}{\sigma_{reg}^2}\mathbf{N}_{reg} \, .
\tag{3.16}
$$

With the following definitions

$$
\begin{aligned}
\mathbf{R}_{sst} &= \frac{1}{\sigma_{sst}^2}\mathbf{N}^{-1}\mathbf{N}_{sst}, & \mathbf{R}_{xx} &= \frac{1}{\sigma_{xx}^2}\mathbf{N}^{-1}\mathbf{N}_{xx}, \\
\mathbf{R}_{yy} &= \frac{1}{\sigma_{yy}^2}\mathbf{N}^{-1}\mathbf{N}_{yy}, & \mathbf{R}_{zz} &= \frac{1}{\sigma_{zz}^2}\mathbf{N}^{-1}\mathbf{N}_{zz}, \\
\mathbf{R}_{reg} &= \frac{1}{\sigma_{reg}^2}\mathbf{N}^{-1}\mathbf{N}_{reg} \, ,
\end{aligned}
\tag{3.17}
$$

we define so-called *resolution matrices*. All the resolution matrices in the least squares system add up to an unit matrix (Sneeuw, 2000), i.e.,

$$
\mathbf{R}_1 + \mathbf{R}_2 + \cdots + \mathbf{R}_I = \mathbf{I} \, ,
\tag{3.18}
$$

with $\mathbf{I}$ the unit matrix. With $E\left\{\tilde{\mathbf{d}}_i\right\} = \mathbf{A}_i\delta\mathbf{x}$, by taking expectation and multiplying $\mathbf{N}^{-1}$ on both sides of Eq. 3.15, We find

$$
E\left\{\delta\hat{\mathbf{x}}\right\} = (\mathbf{R}_{sst} + \mathbf{R}_{xx} + \mathbf{R}_{yy} + \mathbf{R}_{zz} + \mathbf{R}_{reg})\, E\left\{\delta\hat{\mathbf{x}}\right\} = \delta\mathbf{x}.
\tag{3.19}
$$

The resolution matrices are a measure of the relative contributions of different observation types. They behave as filters through which the vector $\delta\mathbf{x}$ passes to yield the estimator $\delta\hat{\mathbf{x}}$, see (Bouman, 1998; Sneeuw, 2000). Also the amount of the contribution from a-priori information can be evaluated. One should note that the resolution matrices are computed from the normal matrices only, without any information from the measurements or a-priori values themselves. Therefore, it

is an important and reliable tool to identify how much contribution comes from the included data sources and a-priori information.

The main diagonal elements of the resolution matrices in Eq. (3.17) give the contribution measure for individual parameters. For the ith parameter, the contributions from the various data sources are

$$
\begin{aligned}
r_{sst_i} &= [\mathbf{R}_{sst}]_{ii}, & r_{xx_i} &= [\mathbf{R}_{xx}]_{ii}, \\
r_{yy_i} &= [\mathbf{R}_{yy}]_{ii}, & r_{zz_i} &= [\mathbf{R}_{zz}]_{ii}, \\
r_{reg_i} &= [\mathbf{R}_{reg}]_{ii}.
\end{aligned}
\tag{3.20}
$$

They are independent of the correlation between the individual parameters.

Theoretically, the value of the relative contribution $r_{i(k)}$ is between 0 and 1. In computation, it can be slightly larger than 1 or smaller than 0, due to the numerical error or instability of a observation model (e.g. some observation model is of rank deficiency). From Eq. 3.19, it can be found that the parameter vector $\delta\mathbf{x}$ is the sum of its projection by all the resolution matrices. Each resolution matrix maps $\delta\mathbf{x}$ into parameter space. The off-diagonal elements $[\mathbf{R}_i]_{kj}$ gives the contribution of how much information is projected from the kth to j^{th} parameter, or vice versa, in case that the solution is computed based only on observation type i.

3.4 Data Weighting and Filtering

The VCM of the kinematic orbits (in forms of band matrix) is provided as SST_PSO_2I product. It can be used directly in Eq. (3.5) and (3.8) for parameter estimation. The sequence of gradiometer observations, however, is highly correlated and their VCM is not available. Therefore, the observation time series should be decorrelated either by filtering or using the weight matrix derived from additional information. We apply a filter to both the time series of the observations and the design matrix due to the efficiency of the method. In some studies the auto-correlation function of the residual vector is computed from the iteration process during parameter estimation as the inversion of the weight matrix, see Koch et al. (2010); Schuh (2002).

The power spectrum density (PSD) of a signal $x(t)$ is defined as

$$
\text{PSD}(f) = X(f) \cdot X^*(f),
\tag{3.21}
$$

where $X(f) = \int_{-\infty}^{+\infty} x(t)w(t)e^{-j2\pi ft}$ is the Fourier transform of the signal $x(t)$ and $w(t)$ is a window function; $X^*(f)$ is the complex conjugate of $X(f)$. For a discrete signal $x(n)$ with data length N, the Discrete Fourier Transform (DFT) is

$$
X(k) = \sum_{n=0}^{N-1} x(n)w(n)e^{-\frac{j2\pi kn}{N}}, \quad k = 0, \cdots, N-1, \quad n = 0, \cdots, N-1.
\tag{3.22}
$$

The PSD of the discrete signal $x(n)$ is

$$\mathrm{PSD(k)} = \mathrm{X(k)} \cdot \mathrm{X}^*(\mathrm{k}). \tag{3.23}$$

With matrix notation, the DFT of the noise is

$$\tilde{\boldsymbol{\upsilon}} = \frac{1}{\sqrt{N}} \mathbf{F}\tilde{\mathbf{v}}, \tag{3.24}$$

where the Fourier Transform matrix element is

$$\{\mathbf{F}\}_{kn} = e^{-ikn\frac{2\pi}{N}} \quad k,n = 0,1,\cdots,N-1 \ . \tag{3.25}$$

The PSD of the vector $\tilde{\mathbf{v}}$ becomes

$$\mathbf{p} = \begin{bmatrix} \upsilon_0\tilde{\upsilon}_0^* & \upsilon_1\tilde{\upsilon}_1^* & \cdots & \upsilon_{N-1}\tilde{\upsilon}_{N-1}^* \end{bmatrix}^T, \tag{3.26}$$

where $\tilde{\boldsymbol{\upsilon}}^*$ is the complex conjugate of $\tilde{\boldsymbol{\upsilon}}$.

The frequency response of the whitening filter should be the reciprocal of the square root of the PSD of the noise, i.e.

$$\mathbf{H} = \begin{bmatrix} \frac{\alpha}{\sqrt{p_0}} & 0 & \cdots & 0 \\ 0 & \frac{\alpha}{\sqrt{p_1}} & 0 & \cdots \\ \vdots & \vdots & \vdots & \vdots \\ 0 & \cdots & 0 & \frac{\alpha}{\sqrt{p_{N-1}}} \end{bmatrix}, \tag{3.27}$$

where α is the scale factor which is used to make sure that the signal magnitude and physical dimension is the same before and after filtering. The values of p_i, $i = 0,\cdots,N-1$ are the elements of the the PSD of the instruments and provided by industry based on various tests. The noise can then be transformed to be white with the information provided in Eq. (3.27) as

$$\tilde{\mathbf{v}}' = \frac{1}{N}\mathbf{F}^*\mathbf{H}\mathbf{F}\tilde{\mathbf{v}} = \mathbf{G}\tilde{\mathbf{v}}, \tag{3.28}$$

where

$$\mathbf{G} = \frac{1}{N}\mathbf{F}^*\mathbf{H}\mathbf{F}, \tag{3.29}$$

is the filter matrix, and $\mathbf{F}^*$ is the complex conjugate transpose of $\mathbf{F}$. The weight matrix can be derived from

$$\begin{aligned} \mathbf{P} &= \mathbf{G}^*\mathbf{G} = \frac{1}{N^2}\mathbf{F}^*\mathbf{H}\mathbf{F}\mathbf{F}^*\mathbf{H}\mathbf{F} \\ &= \frac{1}{N}\mathbf{F}^*\mathbf{H}\mathbf{H}\mathbf{F}, \end{aligned} \tag{3.30}$$

with $\mathbf{F}\mathbf{F}^* = \mathbf{F}^*\mathbf{F} = N\mathbf{I}$.

3. LEAST SQUARES AND DATA ADJUSTMENT FOR GOCE DATA PROCESSING

The observation equation (3.5) becomes

$$\tilde{\mathbf{v}}' = \mathbf{A}' \cdot \delta \mathbf{x} - \tilde{\mathbf{d}}' \quad , \quad D\{\tilde{\mathbf{d}}'\} = \mathbf{\Sigma}' = \sigma_0^2 \mathbf{P}'^{-1}. \tag{3.31}$$

where $\mathbf{A}' = \mathbf{GA}$ and $\tilde{\mathbf{d}}' = \mathbf{G}\tilde{\mathbf{d}}$. $\mathbf{G}$ acts like a filter that transforms the noise to be white. If the matrix $\mathbf{G}$ is capable of perfectly whitening the noise, the weight matrix of $\tilde{\mathbf{d}}'$ (i.e. filtered $\tilde{\mathbf{d}}$) becomes a unit matrix, i.e. $\mathbf{P}' = \mathbf{I}$.

The VCM in Eq. (3.5) follows from the PSD of the noise, analogously to Eq. (3.30)

$$\mathbf{\Sigma} = \frac{1}{N}\mathbf{F}^*\mathbf{H}'\mathbf{F}, \tag{3.32}$$

where

$$\mathbf{H}' = \begin{bmatrix} p_0 & 0 & \cdots & 0 \\ 0 & p_1 & 0 & \cdots \\ \vdots & \vdots & \vdots & \vdots \\ 0 & \cdots & 0 & p_{N-1} \end{bmatrix}. \tag{3.33}$$

From the derivations above, one can see the connection between the PSD of the noise and the VCM. The coefficients of the filter can be derived from the $((N+1)/2)$th row in the center of the filter matrix $\mathbf{G}$.

The VCM based on the error PSD as shown in Fig. 3.2a is displayed in Fig. 3.2b. The smallest error level of the PSD is achieved in the measurement bandwidth (MBW), which is an ESA jargon for the frequency range [5 100] mHz (in some literature, measurement band (MB) is also used for this frequency range). This means the measurements contain the smallest error level in this MB. One can see that $\mathbf{G}$ is a circulant matrix. The values of diagonal and near-diagonal elements are large due to the high correlation of the measurement noise, corresponding to the high power in the low-frequency band in Fig. 3.2a.

The filter derived from $\mathbf{G}$ is a finite impulse response (FIR) filter, of which the length needs to be large to achieve good performance. Therefore, it is time-consuming to filter the observations and especially the design matrix. It can be approximated, however, by an infinite impulse response (IIR) filter, significantly reducing the computational load (Pail et al., 2011a; Schuh, 2002). During the parameter estimation, the filter is applied to the data and the design matrix, instead of making use of the full weight matrix.

In this study, FIR and IIR filter are both applied, but for different purposes. A FIR filter is applied when analyzing the observation for direct applications in the space domain, since the computational load is not critical for data filtering, and the FIR filter can be designed so as to produce no phase shift. The IIR filter is used for parameter estimation, in order to reduce the computational load. In that case since the filter is applied to both the design matrix and the observations, and

(a) Assumed PSD$^{1/2}$

(b) Variance covariance matrix derived in logarithm scale
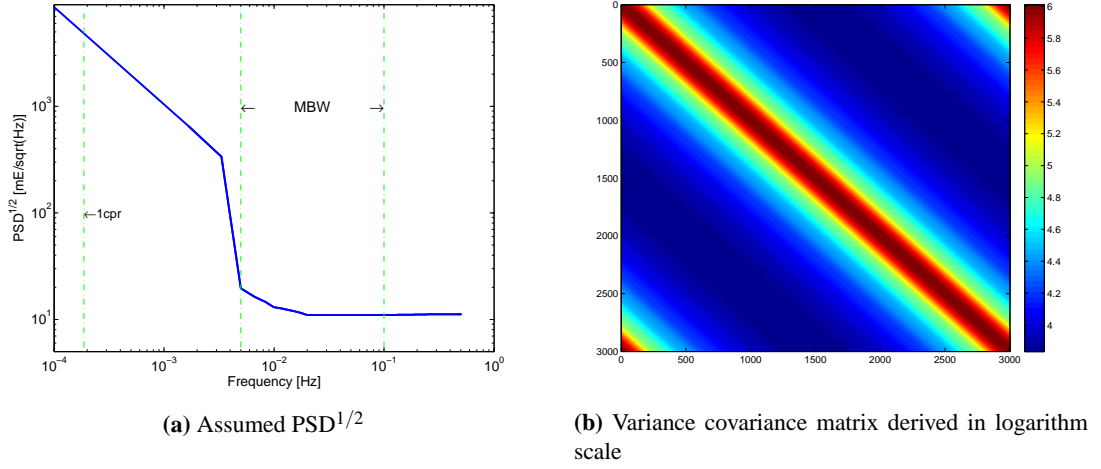
Figure 3.2: An example of PSD$^{1/2}$ and the corresponding variance-covariance matrix

moreover, since

$$\mathbf{G}^* \mathbf{G} = |\mathbf{G}|^{\mathbf{2}} \,, \tag{3.34}$$

is independent of phase when assembling both sides of NEQ. Therefore, the phase shift has no effect on the final results.

3.5 Parameter Pre-elimination

Some parameters may only be needed at an intermediate stage and not be necessary for the final solution; they can be pre-eliminated before solving the normal equations. Suppose two sets of parameters $\delta\mathbf{x_1}$ and $\delta\mathbf{x_2}$ in the following normal equations

$$\begin{bmatrix} \mathbf{N}_{11} & \mathbf{N}_{12} \\ \mathbf{N}_{21} & \mathbf{N}_{22} \end{bmatrix} \begin{bmatrix} \delta\mathbf{x}_1 \\ \delta\mathbf{x}_2 \end{bmatrix} = \begin{bmatrix} \mathbf{U}_1 \\ \mathbf{U}_2 \end{bmatrix} . \tag{3.35}$$

One gets

$$\delta\mathbf{x}_1 = \mathbf{N}_{11}^{-1} \left(\mathbf{U}_1 - \mathbf{N}_{12}\delta\mathbf{x}_2 \right) , \tag{3.36}$$

from the first part of Eq. (3.35). Inserting Eq. (3.36) into the second part of (3.35), yields

$$\left(\mathbf{N}_{22} - \mathbf{N}_{21}\mathbf{N}_{11}^{-1}\mathbf{N}_{12} \right) \delta\mathbf{x}_2 = \left(\mathbf{U}_2 - \mathbf{N}_{21}\mathbf{N}_{11}^{-1}\mathbf{U}_1 \right) . \tag{3.37}$$

Thus the parameters $\delta\mathbf{x_1}$ are pre-eliminated. The normal equations reduce to that of the size of $\mathbf{N}_{22}$. The parameters $\delta\mathbf{x_2}$ can be solved with this reduced normal equations, and the results are still exactly the same.

The pre-elimination is important and useful for large systems of equations. For example, the parameters $\delta\mathbf{x_1}$ could be orbit parameters and empirical accelerations described in section 4.3, while the $\delta\mathbf{x_2}$ could be the vector of gravity field coefficients. One refers to $\delta\mathbf{x_1}$ as local parameters and $\delta\mathbf{x_2}$ as global parameters. In this case the total number of the parameters $\delta\mathbf{x_1}$ is quite large; they are pre-eliminated in order to reduce the size of the system of the normal equations. Thus, the normal equations are reduced to only containing gravitational field coefficients. During the data processing in this study, a system of normal equations is constructed from each day's observations. The pre-elimination is applied to the normal equations constructed from daily observations, before the combination of all the desired normal equations is carried out. After the global parameters $\delta\mathbf{x_2}$ are obtained, the local parameters $\delta\mathbf{x_1}$ are reconstructed by back-substitution. Since the local parameters can be determined with short interval (e.g., less than one day's) measurements, the back-substitution is realized with ease.

3.6 Summary

For a large system of equations, parallelization must be applied. In this study, the observations are separated into daily segments. The normal equations computed from each day's observations are stored on computer disk and combined with a subroutine named **CombineNeq**.

The reciprocal of the variance of unit weight is used as the relative weight for the combination of different observation types. The normal equations to be combined are dimensionless after applying the relative weight.

The regularization is important for SHA based only on GOCE data. Spherical harmonics are global base functions. Without information in the geographical areas of the polar gap, the zonal and near-zonal coefficients are highly correlated and less well determined. This correlation causes that the gravitational field signal recovered only from GOCE observation to exhibit large oscillations in the polar gap areas. Thus, ultimately a constraint in the polar gap areas must be applied, to decorrelate the zonal and near-zonal coefficients.

The contribution from various observation types can be evaluated with resolution matrices. Because only the normal matrices are involved in contribution analysis, the contribution of each individual observation type is explicitly independent of the observations. However, since the relative weights for combination are dependent on the precision of the observation types, implicitly the contribution analysis depends on the quality of the observed data.

With Fourier transformation, the relationship between the PSD of the noise and the VCM of the observations can be established. The error VCM is the Fourier transform of the PSD of the noise, both being quadratic forms. The weight matrix can therefore be derived from the reciprocal of the PSD of the noise. From the reciprocal of the square root of the noise PSD and an appropriate scale factor, a filter matrix is derived. The coefficients of a FIR filter can be found taken from the center row of the filter matrix.

Parameter pre-elimination is necessary and appropriate when the number of unknown parameters is very large, and some parameter sets are only "local". These local parameters, referring to orbit arcs, are only valid in short periods. They are pre-eliminated in order to reduce the size of normal equations. After pre-elimination, only gravitational parameters remain to be solved for. The local parameters are then reconstructed by back-substitution after the global parameters are obtained.

4

GOCE Gravity Field Determination from Satellite-to-satellite Tracking

The idea of the GOCE mission is to combine the SST and SGG techniques for the purpose of the determination of a high-accuracy and high-resolution gravity field. The SST observations are particularly sensitive to long-wavelength gravity field coefficients, and the SGG observations are sensitive to short-wavelength coefficients. The ideas of the SST approach as we apply it to the GOCE mission is presented in this section.

Possible approaches which can be used for gravity field recovery based on GOCE orbit measurements are primarily the following:

i. Semi-analytical method (Sneeuw, 2000), which applies Hill theory, by rotating the spherical harmonic expansion to the orbit plane; the orbit is represented as the superposition of periodical functions. Thus, the observation model can be formulated with ease. But due to the assumptions underlying this approach, in particular that of a circular orbit, without precession, it is only an approximate. It is useful however for pre-mission analysis or quick-look solutions;

ii. Energy balance method (Gerlach et al., 2003; Han, 2003), is based on the idea of conservation of energy. It assumes the kinetic energy, derived from the velocities, and the potential energy, which is a function of the position and the gravity field coefficients, to be constant. In this approach, a 3D-observation is projected to a scalar quantity (potential) per observation epoch. This leads to somewhat degradation of the resulted gravity field model. Moreover, this method needs the velocities of the satellite as observables. The velocities are derived by numerical differentiation of the positions of the satellite orbit. Therefore, the precision of the velocities is somewhat degraded;

iii. Celestial mechanics approach (see Jäggi et al., 2010a), which evaluates the partial derivatives of the orbit w.r.t. the force parameters (gravity field coefficients) by solving the variational equations. This method does not need to use velocities, but it is rather time-consuming

to solve the variational equations if the number of the dynamic (e.g., gravitational field co-efficients) parameters is very large. The underlying model of this approach is nonlinear. One may question whether iteration should be applied. This approach is very flexible and applicable to any observation type, such as SLR and Doppler measurements, which usually may not have equally sampled observations;

iv. Integral equation approach (Eicker et al., 2006; Mayer-Gürr, 2006). Based on Newton's equation of motion, the orbit of the satellite can be formulated as a boundary value problem in the form of a Fredholm-type integral equation. This method is linear and does not need to solve variational equations. It can be faster than the celestial mechanics approach;

v. Acceleration approach (Liu, 2008; Reubelt, 2009). By differentiating twice the position vector derived from GPS measurements, the acceleration of the satellite can be computed and used as a measurement to formulate observation equations.

The idea of the integral equation approach has been proposed as a general method for or-bit determination by Schneider (1968) and modified for gravity field determination by Schneider (1969). Later Ilk and Klose (1984) applied this method for simulation of satellite-to-satellite track-ing analysis. More recently Mayer-Gürr used this method to process the real data from CHAMP (Eicker et al., 2006; Mayer-Gürr, 2006), which was the first and very successful real data applica-tion of this method, and since 2006 he has applied it to GRACE, which resulted in one of the most precise gravitational field models from satellite only data. Solutions are the gravity model ITG-Grace03s (Mayer-Gürr, 2007) and later ITG-Grace2010s (Mayer-Gürr et al., 2010). The idea of this method is to divide the orbit into short arcs, and parameterize gravity field coefficients as well as the boundary parameters of each arc. The boundary parameters can be pre-eliminated before the formation of the normal matrix.

The advantages of the integral equation approach are the following: First, it is linear, thus the a-priori information has almost no effect on the recovered field; second, it is directly based on the (kinematic) orbit positions; this avoids any numerical error due to differentiation. Last, but not least, the variation can be solved in parallel for the all orbit components, i.e. the three elements of the position vector in the variational equations are computed independently of each other. This increases the speed of the computation. Because of these advantages, the integral equation approach is here used for spherical harmonic analysis.

In order to show the functionality of the method, in the computations and analyses of this chapter, we use the kinematic orbit from November 1st to December 31st in 2009. This gives us a full coverage of the Earth with a 61-day repeat orbit. For the combination with SGG in Chapter 6, observations of kinematic orbits of longer period, from November 1st 2009 to April 30th in 2011, will be used for gravity field determination.

4.1 Observation model

The acceleration of a satellite can be represented as

$$\ddot{\mathbf{r}}(t) = \mathbf{f}(t, \mathbf{r}, \dot{\mathbf{r}}, \boldsymbol{\beta}, \boldsymbol{\beta}'), \tag{4.1}$$

with t time and $\mathbf{r}$, $\dot{\mathbf{r}}$ position and velocity vectors, respectively, $\boldsymbol{\beta}$ the vector of parameters to be estimated as defined in section 2.1, and $\boldsymbol{\beta}'$ empirical accelerations as described in Eq. (2.34).

As shown in Fig. 4.1, the satellite passes point A and point B at times t_A and t_B, respectively. The dots are the orbit position vectors derived by GPS.

We define

$$\tau = \frac{t - t_A}{T} \qquad \text{and} \qquad \tau' = \frac{t' - t_A}{T} \tag{4.2}$$

which are the normalized times ranging from 0 to 1, where $T = t_B - t_A$.

Now the goal is to formulate the relationship between the position vector inside the arc and the position vectors at the boundary points, i.e. $\mathbf{r}(t_A) = \mathbf{r}_A$ and $\mathbf{r}(t_B) = \mathbf{r}_B$, as well as the parameters of the force model

Figure 4.1: The trajectory of the satellite over an arc AB

to be estimated, such as gravity field coefficients or the air drag coefficient. Therefore, we define three categories of parameters. With the short arc in Fig. 4.1 as an example, they are orbit parameters, i.e., the position vector $\mathbf{r}_A$ and $\mathbf{r}_B$, empirical parameters (such as empirical accelerations in our study, sometimes perhaps some other parameters such as drag coefficients, radiation coefficients) as presented in subsection 2.2.9 for compensating the mis-modelled or unmodelled accelerations, and the gravitational field coefficients $\overline{C}_{nm}$ and $\overline{S}_{nm}$. A second concept of classification is dividing the parameters into local parameters (or nuisance parameters as described by Ditmar and Klees (2002); they are orbit parameters and empirical parameters which are valid only for a short period) and global parameters (e.g., gravitational field coefficients). A third concept of definition is geometric (orbit) parameters and dynamic parameters (e.g., empirical accelerations, gravitational field coefficients and air drag coefficients, etc., which are incorporated in some force models).

After integrating Eq. (4.1) twice, the position vector can be written as

$$\mathbf{r}(t) = \mathbf{r}(t_A) + \dot{\mathbf{r}}(t_A) \cdot (t - t_A) + \int_{t_A}^{t} \int_{t_A}^{t'} \mathbf{f}(t'', \mathbf{r}, \dot{\mathbf{r}}, \boldsymbol{\beta}, \boldsymbol{\beta}') dt'' dt'. \tag{4.3}$$

With the rule of integration by parts, Eq. (4.3) becomes

$$\mathbf{r}(t) = \mathbf{r}(t_A) + \dot{\mathbf{r}}(t_A) \cdot (t - t_A) + \int\limits_{t_A}^{t} (t - t')\mathbf{f}(t', \mathbf{r}, \dot{\mathbf{r}}, \boldsymbol{\beta}, \boldsymbol{\beta}')dt' \qquad (4.4)$$

Introducing normalized time as given in Eq. (4.2), Eq. (4.3) can be rewritten as

$$\mathbf{r}(\tau) = \mathbf{r}_A + \dot{\mathbf{r}}_A T \tau + T^2 \int\limits_{0}^{\tau} (\tau - \tau')\mathbf{f}(\tau', \mathbf{r}, \dot{\mathbf{r}}, \boldsymbol{\beta}, \boldsymbol{\beta}')d\tau', \qquad (4.5)$$

and we obtain the position at time epoch t_B as

$$\mathbf{r}_B = \mathbf{r}(1) = \mathbf{r}_A + \dot{\mathbf{r}}_A T + T^2 \int\limits_{0}^{1} (1 - \tau')\mathbf{f}(\tau', \mathbf{r}, \dot{\mathbf{r}}, \boldsymbol{\beta}, \boldsymbol{\beta}')d\tau'. \qquad (4.6)$$

Combination of Eq. (4.5) and (4.6), yields

$$\begin{aligned}
\mathbf{r}(\tau) =& \mathbf{r}_A + \left(\mathbf{r}_B - \mathbf{r}_A - T^2 \int\limits_{0}^{1} (1 - \tau')\mathbf{f}(\tau', \mathbf{r}, \dot{\mathbf{r}}, \boldsymbol{\beta}, \boldsymbol{\beta}')d\tau' \right) \tau + T^2 \int\limits_{0}^{\tau} (\tau - \tau')\mathbf{f}(\tau', \mathbf{r}, \dot{\mathbf{r}}, \boldsymbol{\beta}, \boldsymbol{\beta}')d\tau' \\
=& \mathbf{r}_A(1 - \tau) + \mathbf{r}_B \tau - T^2 \tau \int\limits_{0}^{1} (1 - \tau')\mathbf{f}(\tau', \mathbf{r}, \dot{\mathbf{r}}, \boldsymbol{\beta}, \boldsymbol{\beta}')d\tau' + T^2 \int\limits_{0}^{\tau} (\tau - \tau')\mathbf{f}(\tau', \mathbf{r}, \dot{\mathbf{r}}, \boldsymbol{\beta}, \boldsymbol{\beta}')d\tau' \\
=& \mathbf{r}_A(1 - \tau) + \mathbf{r}_B \tau - T^2 \int\limits_{0}^{1} K(\tau, \tau')\mathbf{f}(\tau', \mathbf{r}, \dot{\mathbf{r}}, \boldsymbol{\beta}, \boldsymbol{\beta}')d\tau',
\end{aligned}$$

$$(4.7)$$

where the integral kernel function is

$$K(\tau, \tau') = \left\{ \begin{array}{ll} \tau'(1 - \tau) & \tau' < \tau \\ \tau(1 - \tau') & \tau < \tau'. \end{array} \right.$$

The velocity of the satellite can be computed by differentiation of Eq. (4.7)

$$\dot{\mathbf{r}}(\tau) = \frac{\mathbf{r}_B - \mathbf{r}_A}{T} - T \int\limits_{0}^{1} \frac{\partial K(\tau, \tau')}{\partial \tau}\mathbf{f}(\tau', \mathbf{r}, \dot{\mathbf{r}}, \boldsymbol{\beta}, \boldsymbol{\beta}')d\tau'. \qquad (4.8)$$

The integrals in Eq. (4.7) and (4.8) are convolutions of the acceleration vector with the kernel functions. They can be converted to a matrix multiplication. For details refer to (Mayer-Gürr, 2006; Yi, 2007).

After the kernel matrix $\mathbf{K}$ is evaluated, the observation model can be written as

$$\mathbf{r}(\tau) = \mathbf{r}_A(1 - \tau) + \mathbf{r}_B \tau + \mathbf{K}\mathbf{f}(\tau, \mathbf{r}, \dot{\mathbf{r}}, \boldsymbol{\beta}, \boldsymbol{\beta}'). \qquad (4.9)$$

4. GOCE GRAVITY FIELD DETERMINATION FROM SATELLITE-TO-SATELLITE TRACKING

The velocity vector yields

$$\dot{\mathbf{r}}(\tau) = \frac{\mathbf{r}_B - \mathbf{r}_A}{T} + \dot{\mathbf{K}}\mathbf{f}(\tau, \mathbf{r}, \dot{\mathbf{r}}, \boldsymbol{\beta}, \boldsymbol{\beta}'), \tag{4.10}$$

where $\mathbf{K} = -T^2 \int_0^1 K(\tau, \tau') \cdot d\tau'$ and $\dot{\mathbf{K}} = -T \int_0^1 \frac{\partial K(\tau, \tau')}{\partial \tau} \cdot d\tau'$, are the matrices converted from the convolution with the two different kernel functions. The symbol $\cdot$ in the integrals means the operation to any function. The matrix-vector multiplication in Eq. 4.9 and 4.10 is realized by multiplying each component of the force vector $\mathbf{f}$ which is a time series inside a short arc for three directions.

The structure of the matrices $\mathbf{K}$ and $\dot{\mathbf{K}}$ is shown in Fig. 4.2. In the matrices $\mathbf{K}$ and $\dot{\mathbf{K}}$, each row corresponds to the time epoch of a value to be computed, i.e., τ, while each column corresponds to the integral variable τ'. The maximum values of every row in the matrix $\mathbf{K}$ appear along the diagonal, and the value of the diagonal reaches its maximum at the center of the matrix, see Fig. 4.2a. This is due to the fact that the maximum deviation of the orbit from the line of sight between the two boundary points happens at the middle of the arc. There is a boundary between the upper triangle and lower triangle in the matrix $\dot{\mathbf{K}}$. The values in the upper triangle are positive and in the lower triangle they are negative, see Fig. 4.2b.
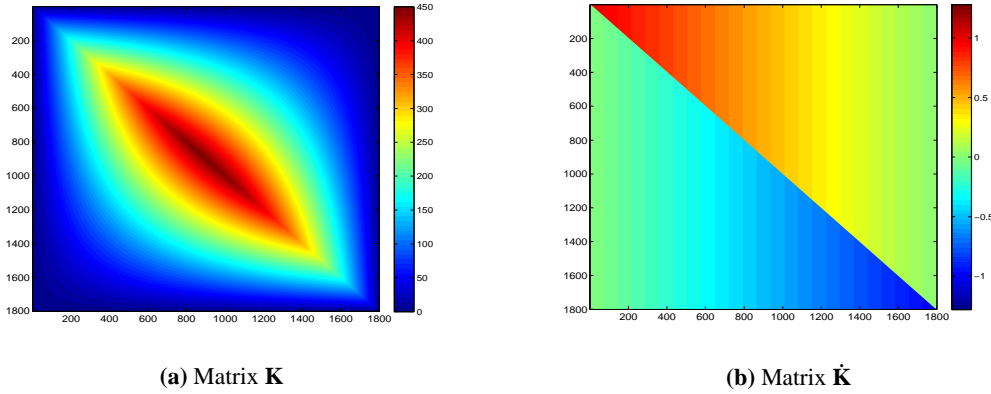
(a) Matrix $\mathbf{K}$ (b) Matrix $\dot{\mathbf{K}}$

Figure 4.2: An overview of the matrix $\mathbf{K}$ and $\dot{\mathbf{K}}$

The acceleration due to the Earth's gravity field and empirical parameters can be evaluated using Eq. (2.5). It is a linear function of the gravity field coefficients and empirical parameters. For example, at epoch i of the arc, it is

$$\mathbf{f}(\tau_i, \mathbf{r}_i, \dot{\mathbf{r}}_i, \boldsymbol{\beta}, \boldsymbol{\beta}') = \begin{bmatrix} \ddot{x}_i \\ \ddot{y}_i \\ \ddot{z}_i \end{bmatrix}$$

$$= \mathbf{G_i}\boldsymbol{\beta} + \mathbf{G'_i}\boldsymbol{\beta}' = \begin{bmatrix} \mathbf{G}_{xi} \\ \mathbf{G}_{yi} \\ \mathbf{G}_{zi} \end{bmatrix}\boldsymbol{\beta} + \begin{bmatrix} \mathbf{G}'_{xi} \\ \mathbf{G}'_{yi} \\ \mathbf{G}'_{zi} \end{bmatrix}\boldsymbol{\beta}', \tag{4.11}$$

where $\mathbf{G_i}$ contains the partials of the acceleration w.r.t. the gravitational field coefficients at epoch i, and $\mathbf{G'_i}$ the partials of the acceleration w.r.t. the empirical accelerations. Thus, the partials of $\mathbf{G_i}$ for the whole arc can be written as

$$
\mathbf{G}_x = \begin{bmatrix} \frac{\partial \ddot{x}_0}{\partial \beta_0} & \frac{\partial \ddot{x}_0}{\partial \beta_1} & \cdots & \frac{\partial \ddot{x}_0}{\partial \beta_{M-1}} \\ \frac{\partial \ddot{x}_1}{\partial \beta_0} & \frac{\partial \ddot{x}_1}{\partial \beta_1} & \cdots & \frac{\partial \ddot{x}_1}{\partial \beta_{M-1}} \\ \vdots & \vdots & \ddots & \vdots \\ \frac{\partial \ddot{x}_{N-1}}{\partial \beta_0} & \frac{\partial \ddot{x}_{N-1}}{\partial \beta_1} & \cdots & \frac{\partial \ddot{x}_{N-1}}{\partial \beta_{M-1}} \end{bmatrix}, \quad \mathbf{G}_y = \begin{bmatrix} \frac{\partial \ddot{y}_0}{\partial \beta_0} & \frac{\partial \ddot{y}_0}{\partial \beta_1} & \cdots & \frac{\partial \ddot{y}_0}{\partial \beta_{M-1}} \\ \frac{\partial \ddot{y}_1}{\partial \beta_0} & \frac{\partial \ddot{y}_1}{\partial \beta_1} & \cdots & \frac{\partial \ddot{y}_1}{\partial \beta_{M-1}} \\ \vdots & \vdots & \ddots & \vdots \\ \frac{\partial \ddot{y}_{N-1}}{\partial \beta_0} & \frac{\partial \ddot{y}_{N-1}}{\partial \beta_1} & \cdots & \frac{\partial \ddot{y}_{N-1}}{\partial \beta_{M-1}} \end{bmatrix},
$$

$$
\mathbf{G}_z = \begin{bmatrix} \frac{\partial \ddot{z}_0}{\partial \beta_0} & \frac{\partial \ddot{z}_0}{\partial \beta_1} & \cdots & \frac{\partial \ddot{z}_0}{\partial \beta_{M-1}} \\ \frac{\partial \ddot{z}_1}{\partial \beta_0} & \frac{\partial \ddot{z}_1}{\partial \beta_1} & \cdots & \frac{\partial \ddot{z}_1}{\partial \beta_{M-1}} \\ \vdots & \vdots & \ddots & \vdots \\ \frac{\partial \ddot{z}_{N-1}}{\partial \beta_0} & \frac{\partial \ddot{z}_{N-1}}{\partial \beta_1} & \cdots & \frac{\partial \ddot{z}_{N-1}}{\partial \beta_{M-1}} \end{bmatrix}.
\tag{4.12}
$$

Similarly to Eq. (2.37), the partial derivatives of the accelerations w.r.t. dynamic parameters are transformed to the inertial frame before multiplication with the kernel matrix, since the integration can be carried out easily in the inertial frame.

The partials $\mathbf{G'_i}$ are transform matrices like Eq. (2.35), multiplied with the constant terms and 1 cpr. They are

$$
\mathbf{G'}_x = \begin{bmatrix} \mathbf{E}_0^{(1,:)} & \mathbf{E}_0^{(1,:)}s_0 & \mathbf{E}_0^{(1,:)}c_0 \\ \mathbf{E}_1^{(1,:)} & \mathbf{E}_1^{(1,:)}s_1 & \mathbf{E}_1^{(1,:)}c_1 \\ \vdots & \vdots & \vdots \\ \mathbf{E}_{(N-1)}^{(1,:)} & \mathbf{E}_{(N-1)}^{(1,:)}s_{N-1} & \mathbf{E}_{(N-1)}^{(1,:)}c_{N-1} \end{bmatrix}, \mathbf{G'}_y = \begin{bmatrix} \mathbf{E}_0^{(2,:)} & \mathbf{E}_0^{(2,:)}s_0 & \mathbf{E}_0^{(2,:)}c_0 \\ \mathbf{E}_1^{(2,:)} & \mathbf{E}_1^{(2,:)}s_1 & \mathbf{E}_1^{(2,:)}c_1 \\ \vdots & \vdots & \vdots \\ \mathbf{E}_{(N-1)}^{(2,:)} & \mathbf{E}_{(N-1)}^{(2,:)}s_{N-1} & \mathbf{E}_{(N-1)}^{(2,:)}c_{N-1} \end{bmatrix},
$$

$$
\mathbf{G'}_z = \begin{bmatrix} \mathbf{E}_0^{(3,:)} & \mathbf{E}_0^{(3,:)}s_0 & \mathbf{E}_0^{(3,:)}c_0 \\ \mathbf{E}_1^{(3,:)} & \mathbf{E}_1^{(3,:)}s_1 & \mathbf{E}_1^{(3,:)}c_1 \\ \vdots & \vdots & \vdots \\ \mathbf{E}_{(N-1)}^{(3,:)} & \mathbf{E}_{(N-1)}^{(3,:)}s_{N-1} & \mathbf{E}_{(N-1)}^{(3,:)}c_{N-1} \end{bmatrix},
\tag{4.13}
$$

where $\mathbf{E}_i^{(j,:)}$ means the jth row of the matrix $\mathbf{E}$ derived with Eq. (2.35) at epoch i. s_i and c_i are $\sin v_i$ and $\cos v_i$, respectively, with v_i the true anomaly at epoch i.

To evaluate the partials of the position vector w.r.t. the dynamic parameters in inertial frame, the convolution of Eqs. (4.7) is performed by multiplying the kernel matrix $\mathbf{K}$ with the partials in Eq. (4.12), i.e.

$$
\mathbf{H}_x = \mathbf{K}\mathbf{G}_x, \qquad \mathbf{H}_y = \mathbf{K}\mathbf{G}_y, \qquad \mathbf{H}_z = \mathbf{K}\mathbf{G}_z.
\tag{4.14}
$$

The matrices $\mathbf{H}_x$, $\mathbf{H}_y$ and $\mathbf{H}_z$ are now establishing the link between satellite position and po-

4. GOCE GRAVITY FIELD DETERMINATION FROM SATELLITE-TO-SATELLITE TRACKING

tential coefficients:

$$
\mathbf{H}_x = \begin{bmatrix} \frac{\partial x_0}{\partial \beta_0} & \frac{\partial x_0}{\partial \beta_1} & \cdots & \frac{\partial x_0}{\partial \beta_{M-1}} \\ \frac{\partial x_1}{\partial \beta_0} & \frac{\partial x_1}{\partial \beta_1} & \cdots & \frac{\partial x_1}{\partial \beta_{M-1}} \\ \vdots & \vdots & \ddots & \vdots \\ \frac{\partial x_{N-1}}{\partial \beta_0} & \frac{\partial x_{N-1}}{\partial \beta_1} & \cdots & \frac{\partial x_{N-1}}{\partial \beta_{M-1}} \end{bmatrix}, \qquad \mathbf{H}_y = \begin{bmatrix} \frac{\partial y_0}{\partial \beta_0} & \frac{\partial y_0}{\partial \beta_1} & \cdots & \frac{\partial y_0}{\partial \beta_{M-1}} \\ \frac{\partial y_1}{\partial \beta_0} & \frac{\partial y_1}{\partial \beta_1} & \cdots & \frac{\partial y_1}{\partial \beta_{M-1}} \\ \vdots & \vdots & \ddots & \vdots \\ \frac{\partial y_{N-1}}{\partial \beta_0} & \frac{\partial y_{N-1}}{\partial \beta_1} & \cdots & \frac{\partial y_{N-1}}{\partial \beta_{M-1}} \end{bmatrix},
$$

$$
\mathbf{H}_z = \begin{bmatrix} \frac{\partial z_0}{\partial \beta_0} & \frac{\partial z_0}{\partial \beta_1} & \cdots & \frac{\partial z_0}{\partial \beta_{M-1}} \\ \frac{\partial z_1}{\partial \beta_0} & \frac{\partial z_1}{\partial \beta_1} & \cdots & \frac{\partial z_1}{\partial \beta_{M-1}} \\ \vdots & \vdots & \ddots & \vdots \\ \frac{\partial z_{N-1}}{\partial \beta_0} & \frac{\partial z_{N-1}}{\partial \beta_1} & \cdots & \frac{\partial z_{N-1}}{\partial \beta_{M-1}} \end{bmatrix}. \tag{4.15}
$$

Similarly to Eq.(4.14), the partials of the position vector w.r.t. the empirical accelerations $\mathbf{H}'_z$, $\mathbf{H}'_y$ and $\mathbf{H}'_z$ are derived by multiplying the kernel matrix $\mathbf{K}$ with $\mathbf{G}'_x$, $\mathbf{G}'_y$ and $\mathbf{G}'_z$, respectively.

We see that the variational equations are solved by this matrix multiplication. They are implemented in parallel since the three components in Eq. (4.14) are independent. This improves computation speed. The *Open Multi-Processing (OpenMP)* interface is used for this kind of parallelization.

Back to Eq. (4.9), the observation equations for epoch i in the arc are formulated as

$$
\begin{bmatrix} 1-\tau_i & 0 & 0 & \tau_i & 0 & 0 \\ 0 & 1-\tau_i & 0 & 0 & \tau_i & 0 \\ 0 & 0 & 1-\tau_i & 0 & 0 & \tau_i \end{bmatrix} \begin{bmatrix} x_A \\ y_A \\ z_A \\ x_B \\ y_B \\ z_B \end{bmatrix} + \begin{bmatrix} \mathbf{H}'_{xi} \\ \mathbf{H}'_{yi} \\ \mathbf{H}'_{zi} \end{bmatrix} \delta\beta' + \begin{bmatrix} \mathbf{H}_{xi} \\ \mathbf{H}_{yi} \\ \mathbf{H}_{zi} \end{bmatrix} \delta\beta
$$

$$
= \begin{bmatrix} \tilde{x}_i \\ \tilde{y}_i \\ \tilde{z}_i \end{bmatrix} - \begin{bmatrix} x_{0i} \\ y_{0i} \\ z_{0i} \end{bmatrix}, \tag{4.16}
$$

where $\tilde{x}_i$, $\tilde{y}_i$ $\tilde{z}_i$ are the position elements of the kinematic orbit in the inertial frame at epoch i. The elements x_{0i}, y_{0i} and z_{0i} are reference values derived from initial conditions. The a-priori information is introduced only for the purpose of reducing the numerical error, making the right-hand side smaller in order to reduce computer (both round-off and truncation) error. It has no effect on the final results since the observation model is linear. As a demonstration serves Fig. 4.3, which shows the geoid differences of two models recovered, one based on EGM2008 and one based on EGM96 (Lemoine et al., 1998), with the same other conditions. The comparison includes the polar gap areas. The maximum value of the differences is 5.3×10^{-3} cm, and the STD value is 5.5×10^{-4} cm. Both values are very small and negligible.
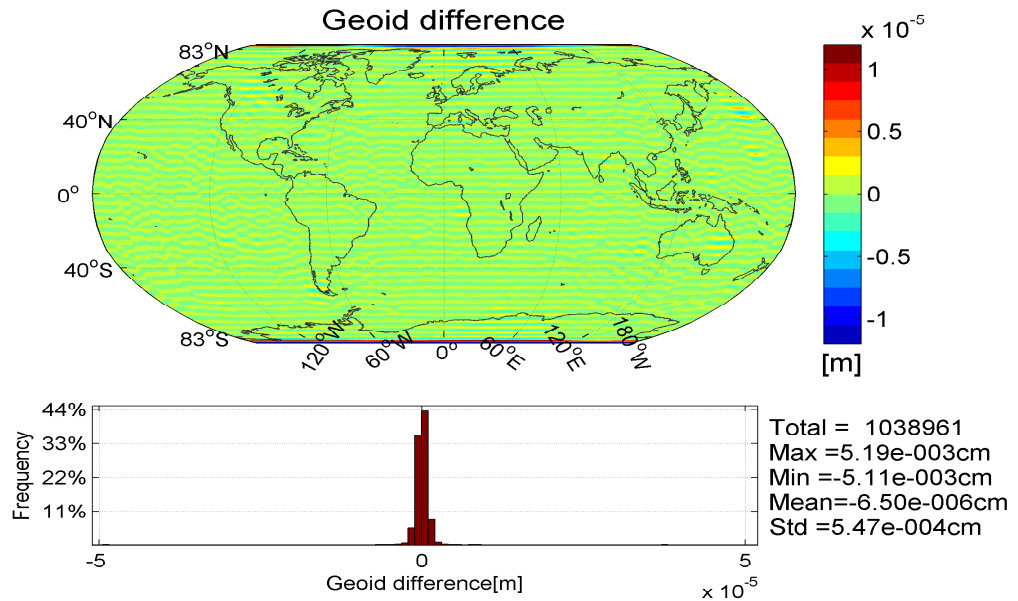
Figure 4.3: Geoid difference with EGM2008 and EGM96 as a-priori values

4.2 Reduction of the forces

As stated in Chapter 2, the forces can be divided into two categories: gravitational and non-gravitational forces. Besides the gravitational acceleration from the Earth, they include third-body attraction, solid Earth tides, ocean tides, and non-tidal variations of the gravitational field due to atmosphere and ocean. Non-gravitational accelerations include air drag or residual of air drag, solar radiation pressure and albedo. In this work the non-gravitational accelerations are not modelled with their explicit functions, but with empirical acceleration parameters.

4.2.1 Gravitational forces

All the models of gravitational forces have been presented in section 2.2 except the short-term variations due to atmosphere and oceans (A&O). In the geodetic literature they are referred to as atmosphere and ocean de-aliasing (AOD), see (Flechtner, 2007). Since the atmosphere and ocean are fluids, they change rapidly with changes in solar radiation, pressure, temperature, etc. This leads to mass redistribution and therefore tiny variations of the Earth's gravitational field. The numerical models for these variations of the gravitational field are derived based on the data from weather services and barotropic ocean models, again see (Flechtner, 2007). The SH coefficients of the variations are provided every six hours and the products, which are named atmosphere and ocean de-aliasing level 1B data (AOD1B), are available to the users. The variations at any time epoch are obtained by interpolating between two neighboring epochs. The acceleration due to AOD is then computed with Eq. (2.14).

As an example, Fig. 4.4 shows the magnitude of different gravitational accelerations using the orbit of GOCE on November 1st, 2009. The direct attraction of the moon is the largest. The magnitude of the attraction of the sun is at the same level as the Earth tides. The effects of ocean tides are smaller than those of the Earth tides, but much more irregular. The acceleration due to AOD is the smallest, with a magnitude of about 10^{-8} m/s^2.
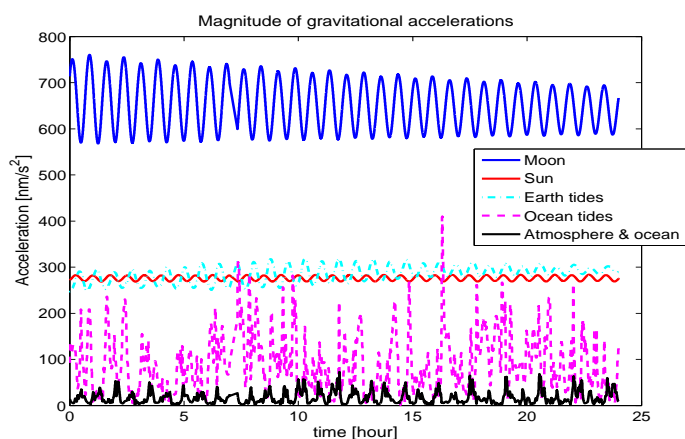
Figure 4.4: Magnitude of time varying gravitational accelerations

These accelerations are modelled and the perturbation of the orbit due to them is removed from the observations in Eq. (4.16), i.e., the reference values x_{0i}, y_{0i} and z_{0i} are computed by taking these accelerations into account. Although these accelerations can be computed with well-known models, the error of the models or mismodeling, such as of ocean tides, inaccurate Love number, etc., can cause small deviations from the true orbit. The effect of the background model is therefore worthwhile to be investigated.

4.2.2 Non-gravitational accelerations measured by GOCE accelerometers

Non-gravitational accelerations are accelerations caused by forces acting on the surface of the satellite. They are therefore called *surface* or *skin forces*.

As stated in Chapter 2, the largest part of the non-gravitational acceleration is due to air drag. In the case of GOCE the air drag is compensated in flight direction by the ion thrusters. The residuals after this compensation are quite small and can be measured as common mode accelerations (CMA) by the accelerometers. The drag-free compensation started on September 14th, 2009. In Fig. 4.5, the left panel shows the CMA sensed by the three accelerometer pairs when no drag-free compensation is applied, see Fig. 4.5a. The right panel is the CMA output from the accelerometers in drag free motion, see Fig. 4.5b. Since the *x*-direction is approximately pointing in the along-track direction, the largest part of the air drag would be measured by the accelerometers in this component. When the satellite is not in drag-free motion, the magnitude of the accelerometer output in the *x*-direction can reach 3000 nm/s^2, and the RMS value is approximately 600 to 700 nm/s^2. When the drag free compensation is applied, these values decrease to 200 nm/s^2 (without correction of the constant offset) and 2 nm/s^2, respectively. After drag-free compensation,

both the RMS values of the accelerometer data in the *x*- and *y*-direction decrease, but the RMS value in the *x*-direction (approximately pointing to the Earth's center) increases from 8.9 nm/s^2 to 22.7 nm/s^2. This is likely due to some forces from the ion thrusters projected into the *z*-direction.

(a) Not in drag-free motion

(b) In drag-free motion
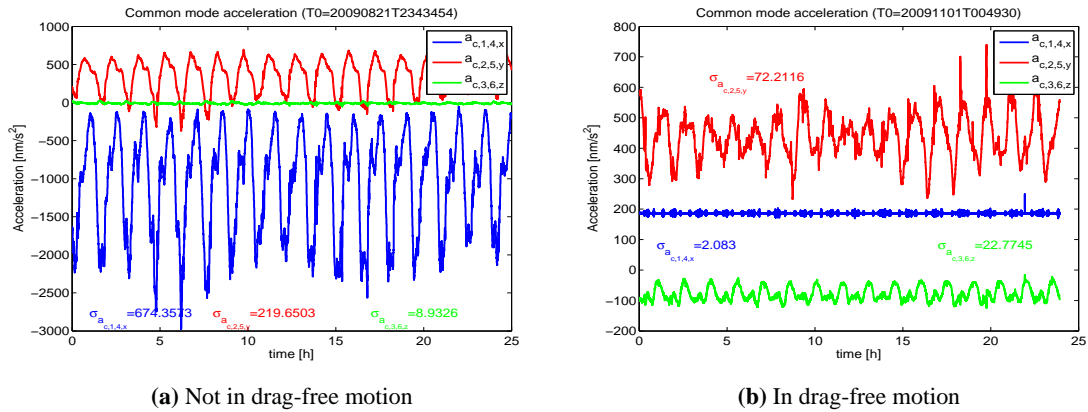
Figure 4.5: Accelerations in common mode sensed by the accelerometers

The CMA in the *x*-direction in drag free mode is presented as a global map in Fig. 4.6, based on the EGG_CCD_2C product in November 2009. It is shown for both ascending and descending tracks and gives primarily the effect of orbit altitude and atmospheric composition.

(a) Ascending

(b) Descending
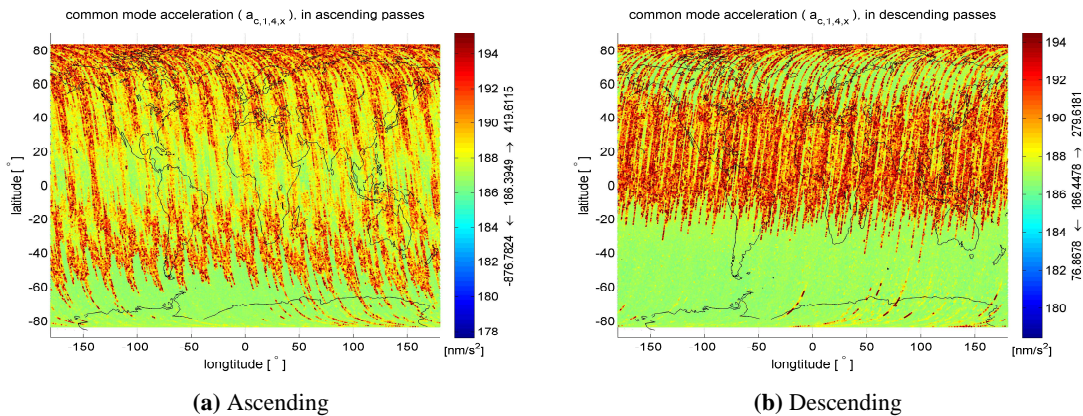
Figure 4.6: CMA shown geographically in November 2009 when drag free compensation was applied

The accelerometer data can be used to correct for surface forces in the process of orbit determination and gravity field reconstruction. Since the measurements contain colored noise, they need to be filtered and calibrated, cf. (Visser, 2009). Another option is to try to absorb non-gravitational accelerations by empirical parameters, see (Jäggi et al., 2010a).

Since all of the time during the operation phase of the mission the satellite is in drag-free motion, we use empirical parameters to determine the unmodelled or mis-modelled effects as well as the residuals of the air drag and other non-gravitational accelerations. The CMA data are not used for gravitational field determination. After the gravity field model is obtained, the empirical

accelerations are reconstructed and compared to the measured common mode accelerations.

4.3 Spherical harmonic analysis from the kinematic orbit

Level-2 orbit products are provided in the context of the Level-2 processing of the HPF by the AIUB Bern and DEOS Delft (Bock et al., 2011; GOCE HPF, 2009). The so-called Rapid Science Orbit (RSO) is computed in Delft using Geodyn (Putney et al., 1990; Rowlands et al., 1995) and GHOST software (Montenbruck et al., 2005a,b) with a latency of 1 day. The Precise Science Orbit (PSO) is computed in Bern with the Bernese software (Dach et al., 2007), with a latency of 1 week. Both kinds of products consist of kinematic orbits and reduced dynamic orbits, as well as variance-covariance matrices and rotation matrices.

With the available orbits, one can choose between the reduced dynamic orbits and kinematic orbits as measurements for gravitational field determination. Unlike the reduced dynamic orbits which make use of a-priori models, the kinematic orbits are derived purely geometrically, without information from any a-priori gravitational field models. Therefore, we use the kinematic orbits as input.

4.3.1 Outlier detection

In Fig. 4.7, the differences between the kinematic orbits and reduced dynamic orbits are presented as global maps and histogram, for all three components, based on the data of November and December, 2009. As shown in Fig. 4.7c, 4.7f and 4.7i, the standard deviations (STD) of these differences in all the three components are less than 1.1 cm. We choose 6 cm as the threshold value for outlier detection. The differences between the kinematic orbits and reduced dynamic orbit larger than 6 cm are considered as outliers. These data are not used for parameter estimation.

As one can see from both ascending and descending tracks, large differences can be found in areas close to the North and South Poles. This can be due to the fact that the observation geometry between GPS satellites and GOCE satellite is poor at high latitudes or it may be caused by an ionosphere effect linked to the Earth's magnetic field. Therefore, the kinematic orbits in these locations are less accurate than at low latitudes. The precision of the recovered gravitational field model at these latitudes is expected to be degraded.

The precision of the kinematic orbit is supposed to be better than 2 cm, cf. (Visser et al., 2010). The weight of an observation is computed with

$$P(\Delta) = \begin{cases} 1, & |\Delta| \leq \beta \\ \left(\frac{\alpha - |\Delta|}{\alpha - \beta}\right)^4, & \beta \leq |\Delta| \leq \alpha \\ 0, & \alpha \leq |\Delta| \end{cases}, \tag{4.17}$$

where Δ is the difference between the kinematic orbit and the reduced dynamic orbit. α and β are 6 cm and 3 cm, respectively. For observations with Δ value inside $[\beta, \alpha]$, the computed weight
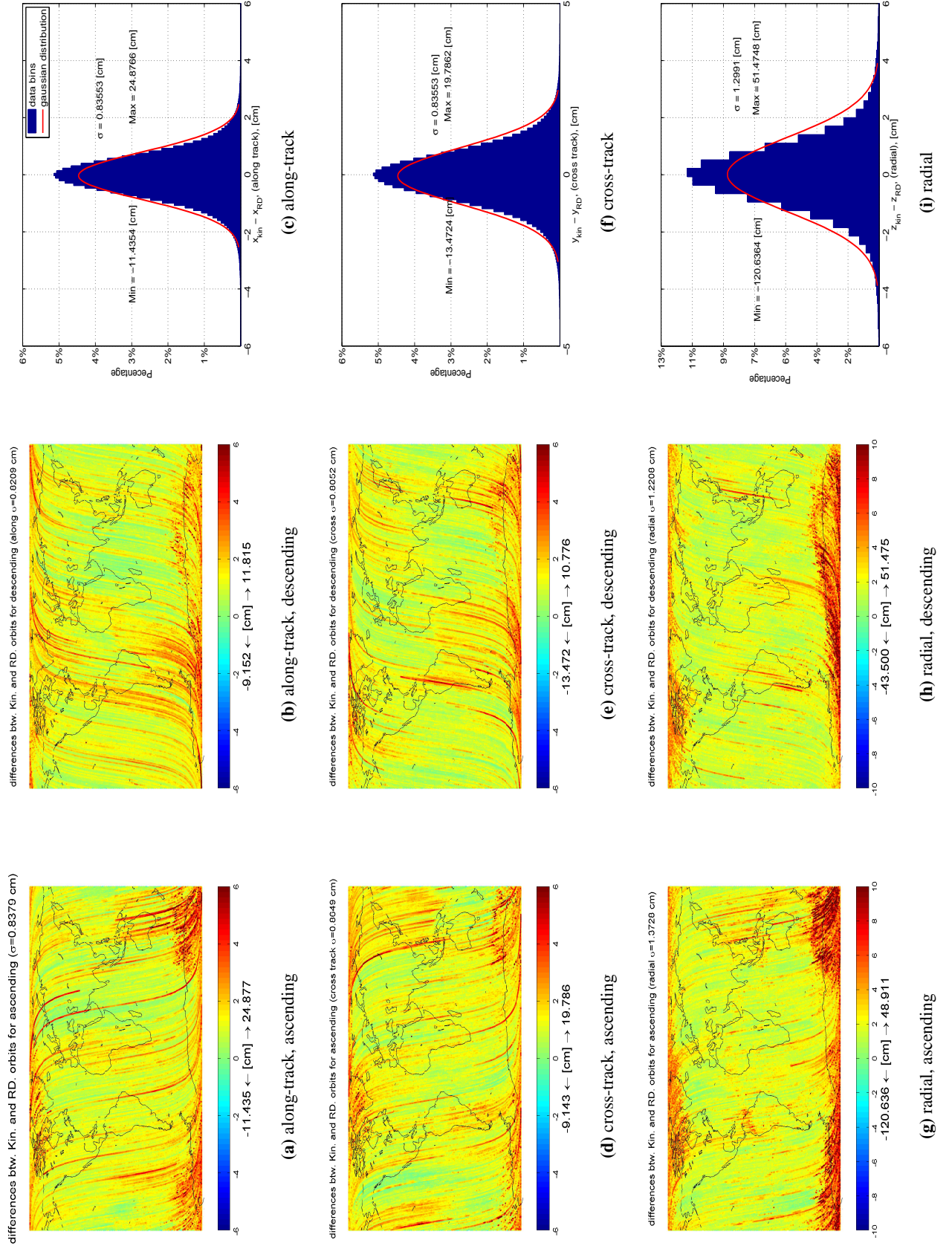
Figure 4.7: differences between kinematic orbit and reduced dynamic orbit, with the data in November and December 2009, 16,212,480 observations for all the three components

decreases with increasing Δ. The curve of the weight function is presented in Fig. 4.8. As the curve shows, if Δ is larger than 3 cm, the observation is weighted down, based on Eq. (4.17).
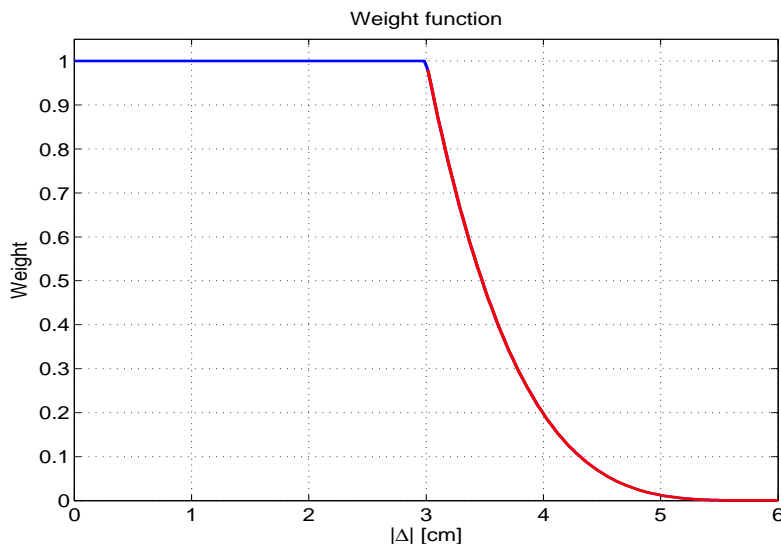
Figure 4.8: Weight function of the kinematic orbit

Based on this idea, with the data over November and December 2009, 23,056 out of 16,212,480 observations are detected as containing outliers, which is about 0.1422% of the total amount of observations. Most of the outliers are located in the areas close to the North Pole and even more to the South Pole, see the global maps of Fig. 4.7.

4.3.2 Arc length and parameterization

The approach applied in this study requires the orbit to be sampled without interruption. Whenever a data gap appears the arc will be terminated and a new arc will be started after this gap. As shown in Fig. 4.9, the neighboring short arcs are distinguished with colors blue and red, and they are connected to the same node point which is the end of one short arc and the beginning of the next one. The node points are marked with black triangles in the figure. Since the two neighboring arcs share the same node point, the orbit is continuous but not smooth (i.e. its time derivative is not continuous at the node points). The position vectors at the node points are set up as unknown parameters (namely the orbit parameters, $\mathbf{r_A}$ and $\mathbf{r_B}$ in Eq. (4.9)), and estimated after the gravity field model is obtained. Since the continuity of the orbit is guaranteed, this approach is slightly different from the short arc approach as applied by Mayer-Gürr (2006) or Eicker et al. (2006), nevertheless the principle is the same.

The long arc in this study is defined as a continuous orbit without data gap or clock jump of the GPS receiver on board. It can be as long as 1 day and as short as minimally three short arcs. The short arc is the orbit segment of which two boundary positions are estimated together with the
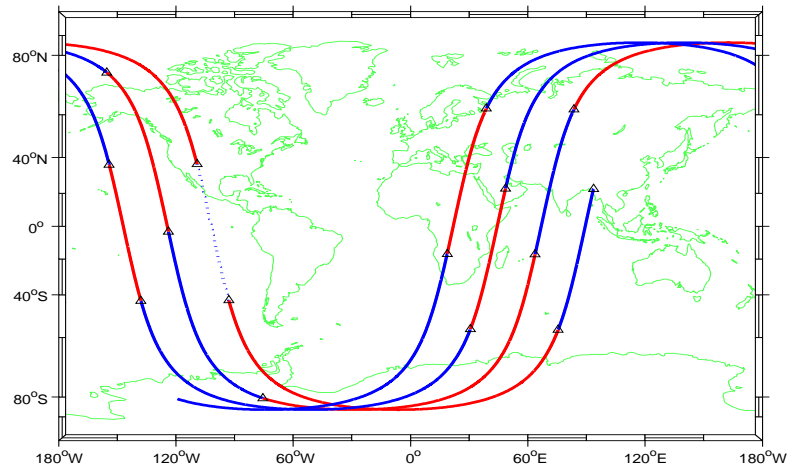
Figure 4.9: 20 minutes segments of short arcs

other parameters such as gravity field coefficients. It is 20 minutes long in this study. The whole curve in blue and red in Fig. 4.9 is a long arc. Long arcs are plotted between two circle dots, since there is no data gap. In the figure, the black dots represent a data gap or a clock jump; after these black dots a new long arc starts with the initial point marked with a black circle, as one can see the new arc in magenta and cyan. The short arc is the orbit between two triangle marks, or a triangle mark and a circle.

As mentioned in section 4.1, the parameters for SST can be divided into three categories: *orbit parameters*, *empirical parameters* and *global parameters*. The orbit parameters are the corrections of the positions of the node points. For a long arc, the total number of the orbit parameters is $3 \cdot (n_{arc} + 1)$, with n_{arc} the number of short arcs. The empirical parameters are the 1 cpr accelerations for the whole long arc, and constant values for each short arc. The total number of the empirical parameters per long arc is $6 + 3 \cdot n_{arc}$. These two kinds of parameters are called *local parameters* since they are arc-dependent. Global parameters are gravity coefficients; they are independent of the arcs.

Once the observation equations of long arc are obtained, they can be accumulated to the normal equations, following Eqs. (3.9) and (3.10). The position vectors at the boundary location and the gravity field coefficients are estimated together with the empirical accelerations, as stated in subsection 2.2.9, by simply applying the convolution to the partials computed according to Eq. (2.33). As an example, in Fig. 4.10 the normal matrix is shown from seven continuous short arcs. There are 24 orbit parameters, 27 parameters for empirical accelerations, and gravitational field coefficients. The correlation between the local parameters and the global parameters can be found in the off-diagonal parts in the inverse of the normal matrix.
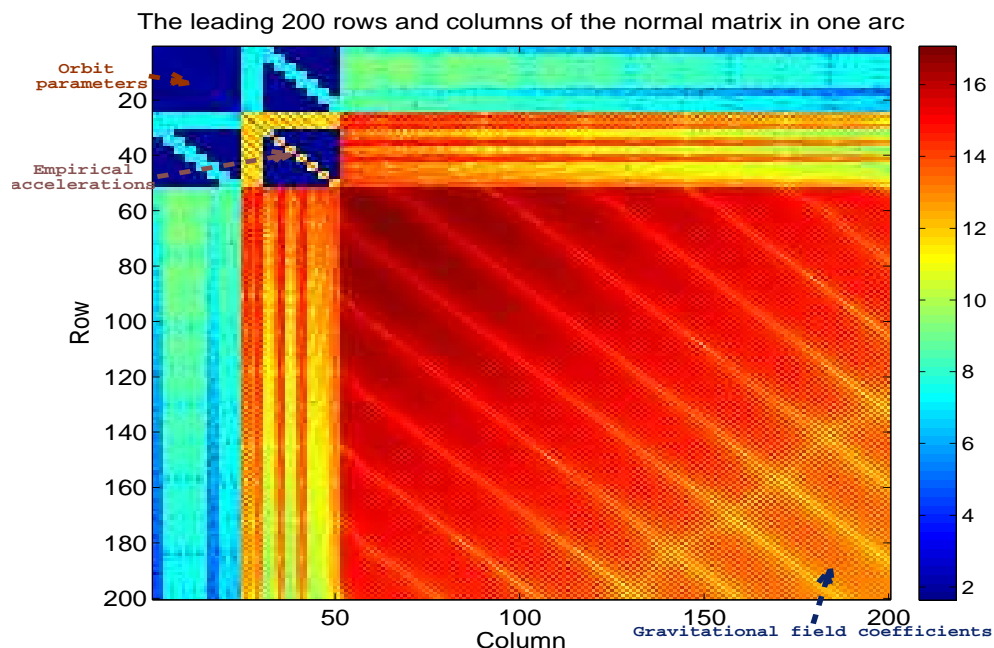
Figure 4.10: Normal matrix with orbit parameters, empirical accelerations and gravitational coefficients for seven consequentive arcs (in m^2 and log10 scaled)

The number of the local parameters can be very large, even much higher than the number of the gravitational field coefficients. For instance, there are more than 20 thousand local parameters for two months of observations. The longer the time period of data used for parameter estimation, the more local parameters have to be taken into account. Therefore, the size of the whole normal equations will become very large for years of observation data. Since these local parameters are arc dependent, they can be pre-eliminated before combination of the normal equations as discussed in section 3.5. After the global parameters, i.e. the gravitational field coefficients, are solved for from the combined normal equations, the local parameters are reconstructed arc by arc by re-substitution.

4.3.3 Results and analysis

We use the kinematic orbit from the PSO product of the period of November 1st to December 31st in 2009. A gravity field model up to d/o 150 is recovered. More observations are processed and combined with SGG for GOCE gravity field solutions presented in Chapter 6.

The estimated coefficients can be compared to the reference values in terms of degree RMS, similar to Eq. (2.4), computed as

$$\sigma_n = \sqrt{\frac{1}{2n+1}\sum_{m=0}^{n}\left(\overline{C}_{nm} - \overline{C}_{nm}^{ref}\right)^2 + \left(\overline{S}_{nm} - \overline{S}_{nm}^{ref}\right)^2}, \qquad (4.18)$$

for degree n. The $\overline{C}_{nm}$ and $\overline{S}_{nm}$ are the estimated coefficients, whereas $\overline{C}_{nm}^{ref}$ and $\overline{S}_{nm}^{ref}$ are the reference values of degree n order m. One can also compare two fields in terms of degree median, which is obtained from the median value for each degree.

The degree RMS values of the estimated gravitational field models with various arc lengths compared to ITG-Grace2010s are presented in Fig. 4.11. Based on our experiments, the short arc with a length of 20 minutes is chosen for SHA, due to its good trade-off between smoothness of the orbit and adequate description of the actual variation of the unmodelled (non-gravitational) accelerations with the empirical parameters.
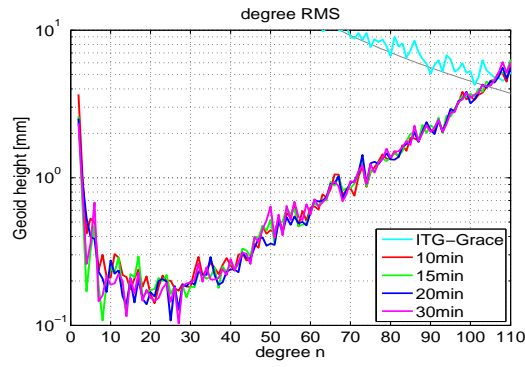
Figure 4.11: The degree RMS of the results estimated with different arc length.

Figure 4.12 shows the degree RMS and degree median. The gravitational field model ITG-Grace2010s is used as a reference for comparison. TUMYGSST is defined as the result without constraint in the polar gap; TUMYGSSTpgr means the result with constraining the geoid height in the polar gap to be consistent to that of EGM2008 with an STD of 20 cm. We use a $1° \times 1°$ grid over the polar gap defined at latitudes [-90° -83°] and [83° 90°]. These are the areas the satellite orbit does not reach due to its inclination of 96.7°. The solid curves in red and in blue are the differences of the ITG-Grace2010s to the unconstrained solution and constrained solution, respectively. The dashed curves in red and in blue are formal errors of the unconstrained and constrained solutions, respectively. The zig-zag behavior in the degree RMS of unconstrained results is due to the polar gap. After the constraint is applied, this behavior disappears. The degree medians of both the unconstrained and constrained solution are similarly close to ITG-Grace2010s. The shape of the formal error shows good consistency of the difference of the coefficients to the reference model. The signal-to-noise ratio (SNR) is one at approximately degree 105. This is the upper limit one can achieve with only two months of orbit data. The analysis in Chapter 2 about the maximum d/o to be recovered, which states that the degree up to 120 was beyond the sensitivity of GOCE SST, is therefore confirmed by the real data analysis.

The daily variation of atmosphere and ocean in terms of SH coefficients is also included (in magenta). This contribution is modelled and subtracted from the observations. In the degree median in Fig. 4.12b one can see the deviations of the estimated coefficients from the reference

4. GOCE GRAVITY FIELD DETERMINATION FROM SATELLITE-TO-SATELLITE TRACKING

(a) Degree RMS
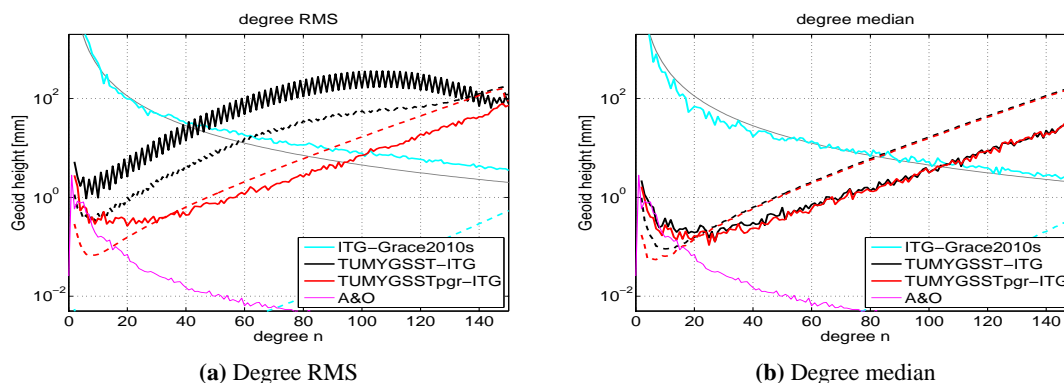
(b) Degree median

Figure 4.12: Degree RMS and degree median of the models

model, ITG-Grace2010s. They are smaller than or at same level of magnitude as the AOD signal, up to degree 8. This shows that the AOD correction should be applied during the parameter estimation.

The coefficient differences of the SST solution w.r.t. ITG-Grace2010s and formal errors of the solutions are presented in Fig. 4.13, with the arrangement of the coefficients as in Fig. 2.1. The coefficients of higher order and less than degree 100 are estimated with good accuracy. This can be seen from the coefficient differences and formal error for both the unconstrained case and constrained case. The zonal and near-zonal coefficients are determined with less accuracy due to the polar gap. After the constraint is applied, the zonal and near-zonal coefficients are determined with the a similar level of accuracy as the other coefficients, compare Fig. 4.13c and 4.13d to Fig. 4.13a and 4.13b.

The geoid height can be computed from the estimated SH coefficients using Eq. (2.2). The differences between two models represent their spatial deviations. In Fig. 4.14 the geoid differences in the latitude range [-83° 83°] between unconstrained solution and ITG-Grace2010s and between constrained solution and ITG-Grace2010s are displayed on a $0.25° \times 0.25°$ grid. The latitude band is restricted in order to eliminate the polar areas where no data is collected by GOCE.

In Fig. 4.14a, the geoid differences between the unconstrained solution and ITG-Grace2010s up to d/o 100 display large values in the high-latitude areas. The STD value (11.14 m) is even larger than that of the geoid differences for the case of up to d/o 150 (4.25 cm), see Fig. 4.14b. This is the truncation effect due to the correlation of the zonal and near zonal coefficients, and this coefficient correlation is due to the existence of the polar gap. Due to this correlation, the high degree coefficients contain information of the long-wavelength signal of the gravity field. If one truncates the model at a certain degree and order, some long-wavelength signal is removed from the model and large differences appear in its differences to the reference gravity field model.

The geoid differences between the constrained solution and ITG-Grace2010s are displayed in Fig. 4.14c and 4.14d, for the situations of up to d/o 100 and 150, respectively. After the constraint over the polar gap is applied, this truncation effect disappears. This is because the correlation in
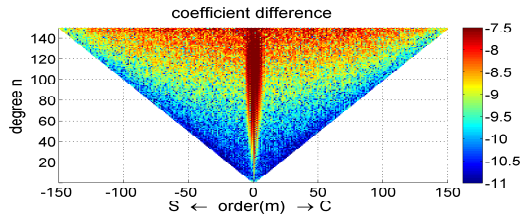
(a) Coefficient differences, unconstrained at polar gap
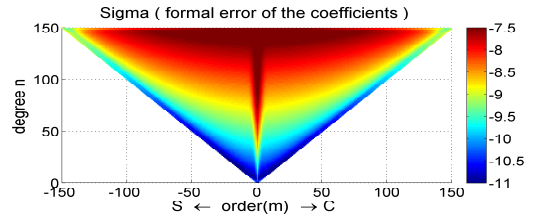
(b) Formal error, unconstrained at polar gap
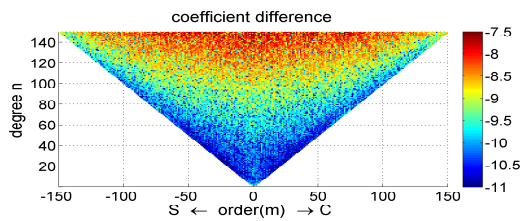
(c) Coefficient differences, constrained at polar gap
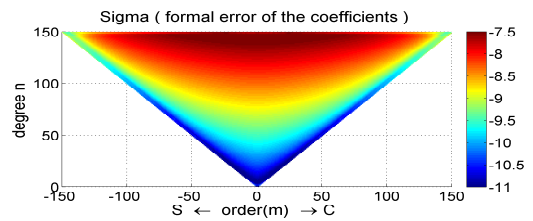
(d) Formal error, constrained at polar gap

Figure 4.13: coefficient differences of SST solution w.r.t. ITG-Grace2010s and formal error of the solution (log10 scale)
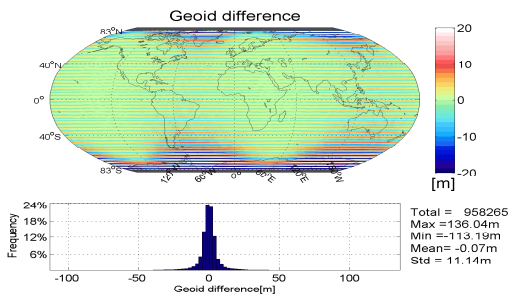
(a) Unconstrained at polar gap, d/o 100
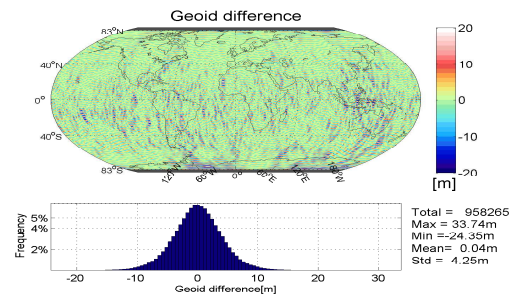
(b) Unconstrained at polar gap, d/o 150
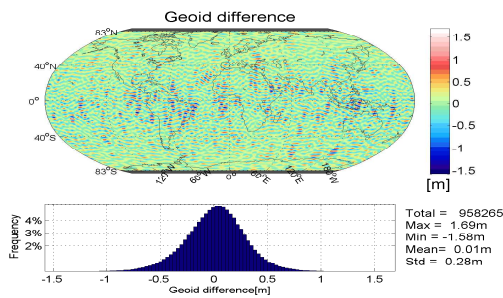
(c) Constrained at polar gap, up to d/o 100
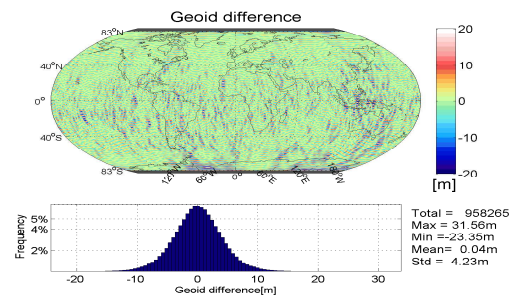
(d) Constrained at polar gap, up to d/o 150

Figure 4.14: Geoid differences of SST solution w.r.t. ITG-Grace2010s, up to d/o 100 and 150

63

the zonal and near-zonal coefficients due to the polar gap is largely taken care of by the introduced polar gap constraint (regularization).

Since the orbit of GOCE is lower than that of CHAMP, its sensitivity to the gravitational field is higher than that of CHAMP. As shown in Fig. 4.15, two months of GOCE data can provide a result more close to ITG-Grace2010s than that with one year of CHAMP data. The CHAMP solution is from the model AIUB-CHAMP01S (Jäggi et al., 2011) up to d/o 70. It was computed based on the CHAMP orbits over the period from March 2002 through March 2003. The STD values of the geoid differences between ITG-Grace2010s and the constrained solution with 61 days of GOCE orbit (model TUMYGSSTpgr) are 4.09 cm and 7.34 cm for up to d/o 50 and 70, respectively. However, the STD values of the geoid differences between ITG-Grace2010s and AIUB-CHAMP01S are 7.3 cm and 28 cm, for up to d/o 50 and 70, respectively, much higher than the comparison between TUMYGSSTpgr and ITG-Grace2010s. The ITG-Grace2010s is very accurate at long and medium wavelength. It is a precise model to be used as reference model. This indicates that two months of GOCE data can provide a result which is more accurate than that with one year of CHAMP data.

(a) Result from 1 year CHAMP, d/o 50

(b) Result from 1 year CHAMP, d/o 70

(c) Result from 2 months GOCE, d/o 50

(d) Result from 2 months GOCE, d/o 70
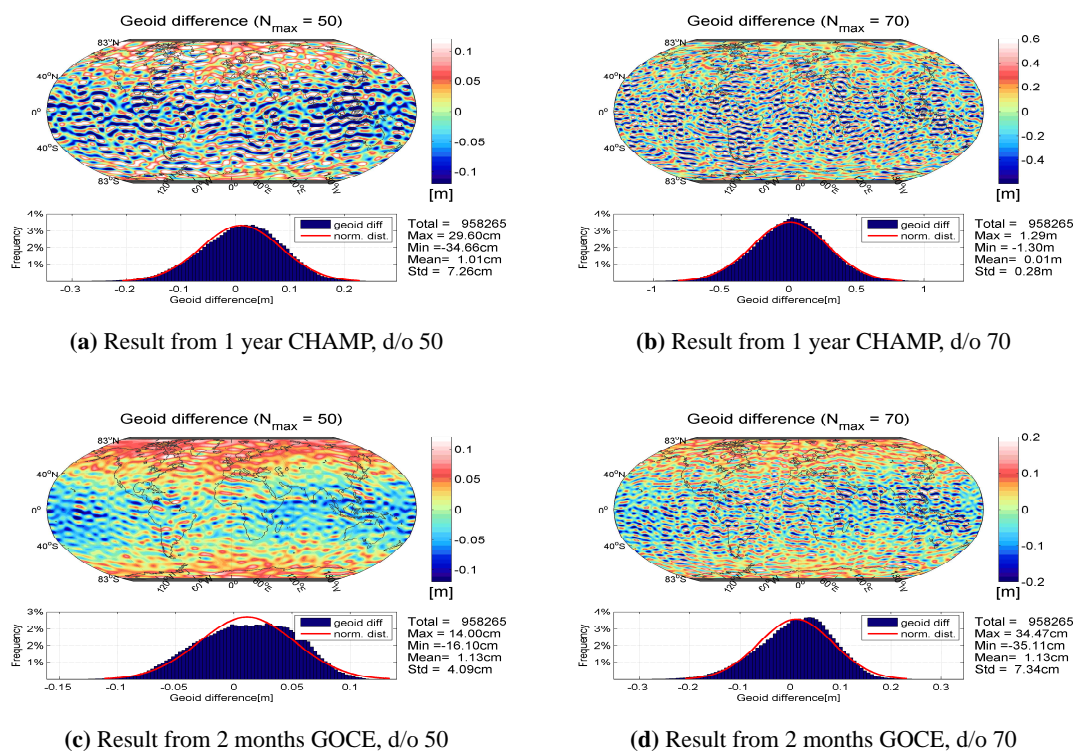
Figure 4.15: Geoid differences of SST solution w.r.t. ITG-Grace2010s, up to d/o 50 and 70

The geoid differences for both CHAMP and GOCE w.r.t. ITG-GRACE2010s are not normally distributed. Large values in high latitudes are likely due to the fact that the accuracy of the GOCE orbits is not globally homogeneous, compare Fig. 4.7. As a result $\overline{C}_{20}$ and other low degree coefficients are affected by this kind of behavior. Two options can be taken to overcome this issue,

one is fixing $\overline{C}_{20}$ and other low degree coefficients to some a-priori information, disregarding any correlation with other coefficients, the other one is combining GOCE SST with other observation types such as K-band ranging of GRACE and/or satellite laser ranging (SLR) to LAGEOS, which are more sensitive to $\overline{C}_{20}$ and other low degree coefficients than GOCE.

4.3.4 Contribution of Regularization

The contribution of observations (GOCE kinematic orbit) and pseudo-observations (the grid values for the constraint (stabilization) in the polar gap) can be computed with their normal matrices based on the theory presented in section 3.3. As shown in Fig. 4.16, the contribution from regularization is less than one percent, if the geoid of the polar gap is constrained at a 20-cm level to an a-priori model, such as in our case EGM2008. The upper right and lower left panels in Figs. 4.16a and 4.16a display the contribution per degree and per order, respectively. The contribution analysis of the regularization is explicitly independent of the chosen a-priori model, because it is computed from the normal matrices only, without "knowledge" of the observations and the a-priori values.

(a) From kinematic orbits

(b) From regularization
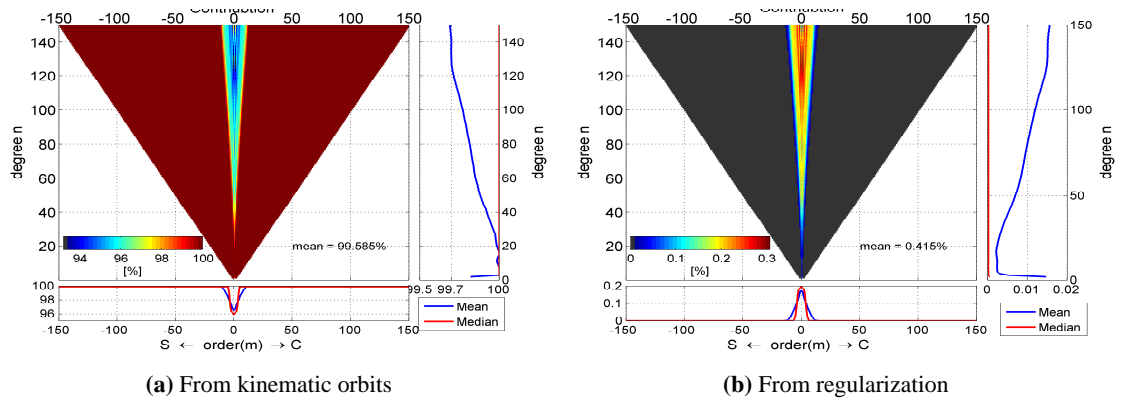
Figure 4.16: Contribution from SST observations and pseudo-observations in polar gaps

From the contribution analysis, one can find that zonal and near-zonal coefficients get information from the regularization (constraint), and the higher the degree, the more contribution comes from the a-priori information. The average value of the contribution the polar stabilization is as small as 0.415%. This means the information of the a-priori field for regularization is very small. However, it is important for GOCE, since it largely de-correlates the zonal and near-zonal coefficients caused by the existence of the polar gap, and it stabilizes the solution.

There is a dilemma when regularization is applied. On the one hand, it is hoped to obtain results without regularization in order to avoid any dependency on the applied a-priori information. On the other hand, it is hoped to combine the good available a-priori information with the observations to get an optimal solution. With the contribution analysis, insight is gained into how much information comes from the actual observations, and how much from regularization.

4.3.5 Reconstructed Accelerations

Apart from the quality of the global parameters, we look into that of the local parameters. The
empirical accelerations can be reconstructed after the global parameters are solved. As shown in
Fig. 4.17, the full normal equations (FNEQ) are constructed from observations of each day. By
applying pre-elimination as described in section 3.5, all orbit parameters and empirical accelera-
tions can be pre-eliminated, and the system of full normal equations reduces to the so-called re-
duced normal equations (RDNEQ). As the parameters in the RDNEQ are only gravitational field
coefficients, they can be combined applying the appropriate weighting. The gravitational field
coefficients are obtained by solving the combined normal equations. Introducing the estimated
coefficients into the observation equations, which contain now only orbit parameters and empir-
ical parameters, for each arc the local parameters can be obtained by solving these observation
equations by least squares estimation.
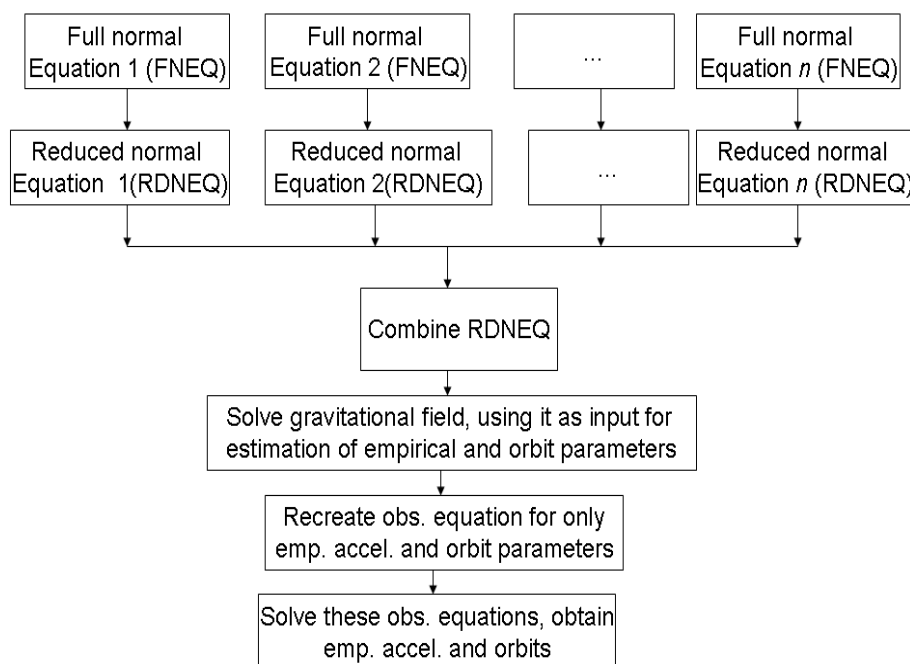
Figure 4.17: Diagram of SST data processing

The reconstructed accelerations are shown in Fig. 4.18 during the transition time period from
non-drag-free to drag-free motion. The values over the period of November and December 2009
are presented in Fig. 4.19. In the upper panel of Fig. 4.18, from 00:00 to about 14:40 the magni-
tude in the along-track direction is larger than the other two. This shows that the air drag is not
compensated by ion thrusting. After 14:40 both the reconstructed and the observed accelerations
decrease significantly. The reconstructed accelerations follow the observed ones but are not the
same as the observed ones. On the one hand, there are offsets and scale factors in the observed
values; on the other hand, the reconstructed values contain not only non-gravitational forces, but
some model errors from the gravitational forces.
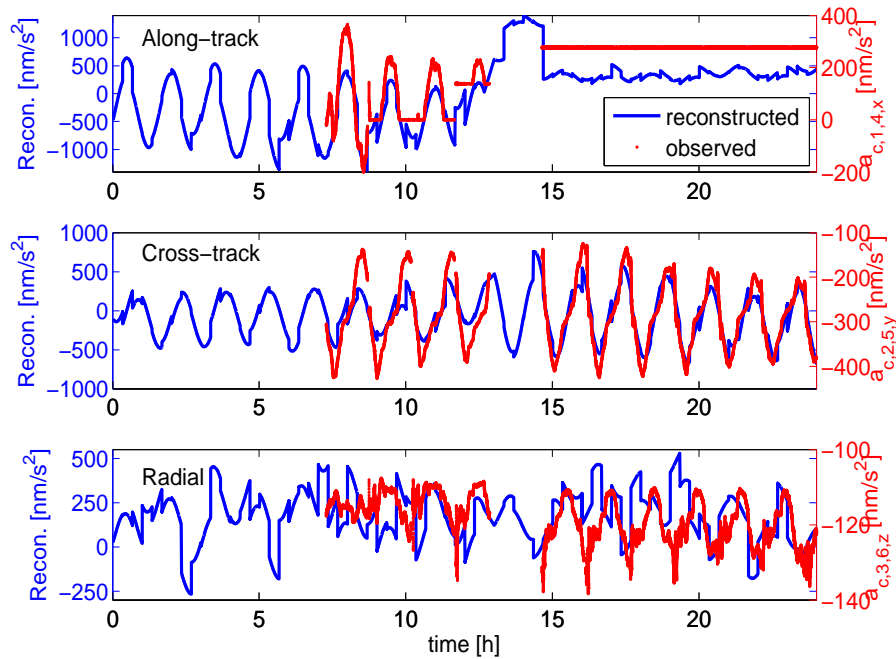
Figure 4.18: Empirical accelerations vs. observed accelerations on May 7th, 2009; at about 14:41 GOCE transits from non-drag-free to drag-free mode, a similar behavior can be found in (Jäggi et al., 2010b)

The reconstructed accelerations in the cross-track direction are more consistent with the measured accelerations than the other two components. In radial direction, the differences between the reconstructed and the observed accelerations are larger than those in along- and cross-track directions. The possible reason is that the unmodelled and/or mis-modelling effects in radial direction are larger than in the other two directions, and/or some information from along-track direction might be absorbed by the radial direction due to the theoretical coupling between along-track and radial directions (Sneeuw, 2000).

This comparison holds only approximately, since the reconstructed accelerations are given in the local orbital reference frame (LORF), whereas the measured values are given in the gradiometer reference frame (GRF), (see Gruber, 2010). If the empirical parameters were modelled in the GRF, this information could be used to estimate the biases and scale factors of the six individual accelerometers, as done in (Visser, 2009).

In Fig. 4.19 some correlation can be found when comparing the reconstructed accelerations and the differences between the kinematic orbits and reduced dynamic orbits presented in Fig. 4.7. The magnitude of the reconstructed accelerations in the along-track direction is smaller than those in the cross-track and radial directions, due to the drag-free compensation in flight direction. Correlation can be found between the reconstructed cross-track acceleration and the yaw angle of the transformation between GRF to LORF, if one compares Fig. 4.19 to the attitude angles between the GRF and LORF presented in Fig. 5.6 in the next chapter. The differences between the σ values in

Fig. 4.19 and in 4.5b is large, the reasons are first, the scale differences between the measured and
reconstructed accelerations exist, as shown in Fig. 4.18; second, these two types of accelerations
are defined in two slightly different coordinate systems; and third, the reconstructed accelerations
contain not only the non-gravitational accelerations, but also some mis-model error.

(a) along-track, ascending

(b) along-track, descending

(c) cross-track, ascending

(d) cross-track, descending

(e) radial, ascending

(f) radial, descending
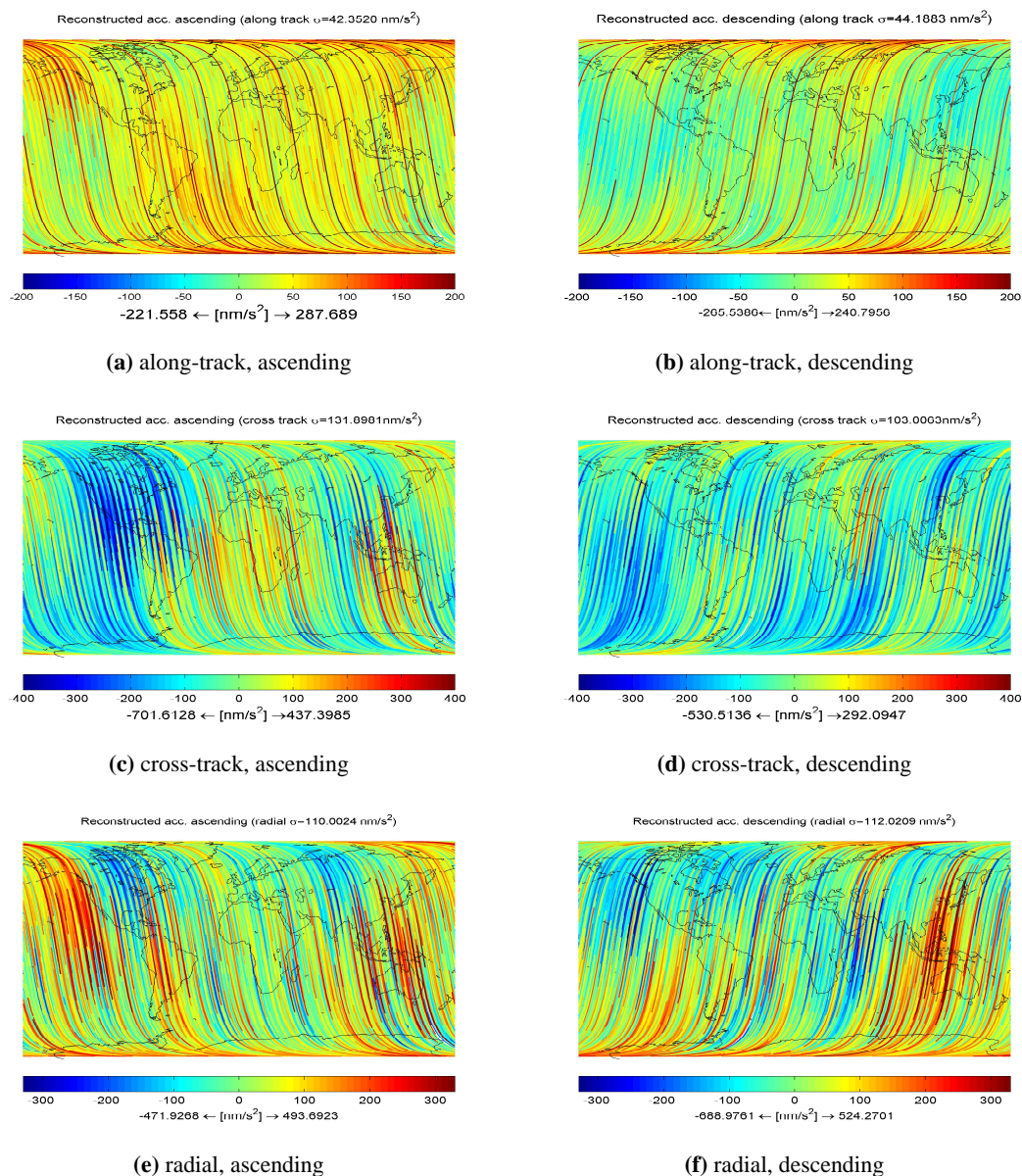
Figure 4.19: Reconstructed acceleration over the period of November and December 2009

4.3.6 Reconstructed Orbits and Residual Analysis

Using Eq. (4.9), the orbits can be reconstructed from the resulting gravitational field together with
the solved boundary position $\mathbf{r_A}$, $\mathbf{r_B}$ and the empirical accelerations. The reconstructed orbits are
reduced dynamic orbits, since the empirical accelerations are introduced during the parameter es-

timation. As we used the kinematic orbits as observations, the differences between the kinematic orbits and the reconstructed orbits are the residuals. In Fig. 4.20 the residuals are presented geographically. Large values of the residuals can be found at high latitudes. As pointed out earlier the kinematic orbits in these regions are less accurate, compare Fig. 4.7. Compared to the reduced dynamic orbits in SST_PRD_2I sub-products computed at AIUB, the reconstructed orbits in this study are closer to the kinematic orbit, since a gravitational field model derived from the kinematic orbits is used to reconstruct the orbits, cf. the right column of Fig. 4.20. Since the precision of orbits at high latitudes is poorer than that at lower latitudes, the recovered gravitational field model is expected also to be less accurate towards the poles. This can be found in Fig. 4.15 by comparing our results to ITG-Grace2010s. However, the formal errors of the geoid of the estimated model at high latitudes are smaller than at low latitudes, due to the fact that the number of the observations is much higher towards the poles. With more and more observations used for parameter estimation, the high latitude areas will result better precision, benefited from the high density of the measurements there.

The standard deviations of the differences between the reconstructed orbits to the kinematic orbits are smaller than those of the difference between the kinematic orbits to the reduced dynamic orbits, compare the right column of Fig. 4.20 and 4.7. One can see that the residuals satisfy a Gaussian distribution (with 95% confidence based on a Kolmogorov-Smirnov test, see (Massey, 1951)). This proves that the estimated parameters are really well adjusted to the kinematic orbits.

4.4   Summary

Based on the integral equation approach, a gravitational field model up to d/o 150 is recovered from the observations in November and December 2009. The signal-to-noise ratio (SNR) is close to one at about d/o 105. Due to the linearity of the method, the results show hardly any correlation with the applied a-priori gravitational field (initial values).

The disturbances from solid Earth tides, ocean tides, direct attraction from the moon and the sun, the effect of general relativity as well as mass redistribution due to the variation of atmosphere and ocean are modelled and removed from the orbit. Since these accelerations can be modelled reasonably well, a potential mis-modelling error of gravitational forces should be quite small. However, if there are some errors in the models, such as uncertainties of the ocean tide model, or atmosphere/ocean, it can lead to deviations. The empirical parameters are useful to compensate for such mis-modelling.

The non-gravitational forces are modelled by introducing empirical parameters, which are 1-cpr sine/cosine parameters for a whole continuous long arc, and constant accelerations for each short arc, all in all three directions. They are modelled in the LORF, as discussed in subsection 2.2.9. Comparing the reconstructed empirical accelerations to the CMA measured by the accelerometers on board shows clear similarities. The gravitational field signal does not have the

differences btw. Kin. and Reconstructed orbits for descending (along υ=0.3600 cm)

(a) along-track, ascending
-6.641 ← [cm] → 7.641

differences btw. Kin. and Reconstructed orbits for descending (cross υ=0.3915 cm)

(d) cross-track, ascending
-5.497 ← [cm] → 6.628

differences btw. Kin. and Reconstructed orbits for ascending (radial υ=0.7810 cm)

(g) radial, ascending
-5.167 ← [cm] → 6.152

differences btw. Kin. and Reconstructed orbits for descending (along υ=0.3590 cm)

(b) along-track, descending
-9.137 ← [cm] → 6.077

differences btw. Kin. and Reconstructed orbits for descending (cross υ=0.5620 cm)

(e) cross-track, descending
-6.359 ← [cm] → 5.928

differences btw. Kin. and Reconstructed orbits for descending (radial υ=0.7463 cm)

(h) radial, descending
-5.703 ← [cm] → 6.381

Pecentage

Min = −9.137 [cm]

x_Kin − x_Rec (along track) [cm]

(c) along-track
σ = 0.37383 [cm]

Max = 7.6409 [cm]

Pecentage

Min = −6.3585 [cm]

x_Kin − y_Rec (cross track) [cm]

(f) cross-track
σ = 0.37699 [cm]

Max = 6.6279 [cm]

Pecentage

Min = −5.7031 [cm]

z_Kin − z_Rec (radial) [cm]

(i) radial
σ = 0.76379 [cm]

Max = 6.3809 [cm]

Figure 4.20: differences between kinematic orbit and reconstructed orbit

70

behavior of a constant (in the time period of a short arc) and 1-cpr, theoretically the empirical parameters are expected to absorb little signal of the gravitational field.

The reconstructed orbits are very close to the kinematic orbits, compared to the differences between the reduced dynamic orbits and the kinematic orbits from the SST_PSO_2I product. This indicates that the recovered gravitational field fits the kinematic orbit more than the a-priori field used for deriving the reduced dynamic orbit in the SST_PSO_2I product. The radial direction is slightly less accurate than the other two components obviously due to the observing geometry between GPS satellites and GOCE satellite, as expected.

The recovered gravitational field from GOCE kinematic orbits based on two months of data seems to fit better to the very accurate gravity field model ITG-Grace2010s than that based on one year of CHAMP data. This is due to the low altitude of GOCE orbits, which makes them more sensitive to the higher end of the long-wavelength part of the Earth's gravitational field. The geoid heights derived from the gravity field model recovered with GOCE kinematic orbits have an accuracy of 7.34 cm RMS up to d/o 70, when compared to ITG-Grace2010s. The coefficients $\overline{C}_{20}$ and some other low degree ones are less accurately determined, due to the fact that GOCE's orbits in this two-month period are less accurate at high latitudes.

Pseudo-observations in the polar areas are used to stabilize the computation and de-correlate the zonal and near-zonal coefficients. Their contribution is very small, but important. As one can see in Fig. 4.14, after the pseudo-observations are applied, the truncation effect is reduced, or even disappears.

5

GOCE Gravitational Gradiometry and Spherical Harmonic Analysis

GOCE is the first mission with a gradiometer on board. The gradiometer measures some components of the gravitational gradients, which are the second derivatives of the gravitational potential. The gravitational gradients serve as the primary observations for gravity field determination. This chapter focuses on the analysis of the gradiometer data, and the spherical harmonic analysis based on these data. The introduction of the gravitational gradiometry and the derivation of the GGT are discussed in section 5.1. The observation model is presented in section 5.2. Section 5.3 presents an analysis of the gradiometer data regarding various aspects. Section 5.4 focuses on spherical harmonic analysis. Section 5.5 summarizes the methodology and results.

5.1   GOCE gravitational gradiometry

The gradiometer is made of three orthogonally arranged one-axis gradiometers. Each of them consists of two ultra-sensitive three-dimensional accelerometers mounted at the end points of a half-meter baseline. Each accelerometer contains a test mass of Rhodium-Platinum, weight 320 g and $4 \times 4 \times 1$ cm^3 in size. The test mass is kept levitated by an electrostatic feedback system inside a chamber with eight pairs of electrodes. The center of the three gradiometer axes coincides closely with the satellite's center of mass, compare Fig. 5.1. Thus, the components of the gravitational gradient tensor are approximated by the finite acceleration difference over the corresponding baseline (Rummel et al., 2011).

Because functional testing of the accelerometers is done in the laboratory on ground and requires levitation of the test mass under the influence of gravity, this leads to each accelerometer being ultra-precise along two orthogonal directions but much less sensitive along its third axis, see also Floberghagen et al. (2011); Rummel et al. (2011). Thus the ultimate sensitivity can only be attained along two axes, while the third is made less sensitive. The configuration shown in Fig. 5.2 was decided for the GOCE gradiometer.
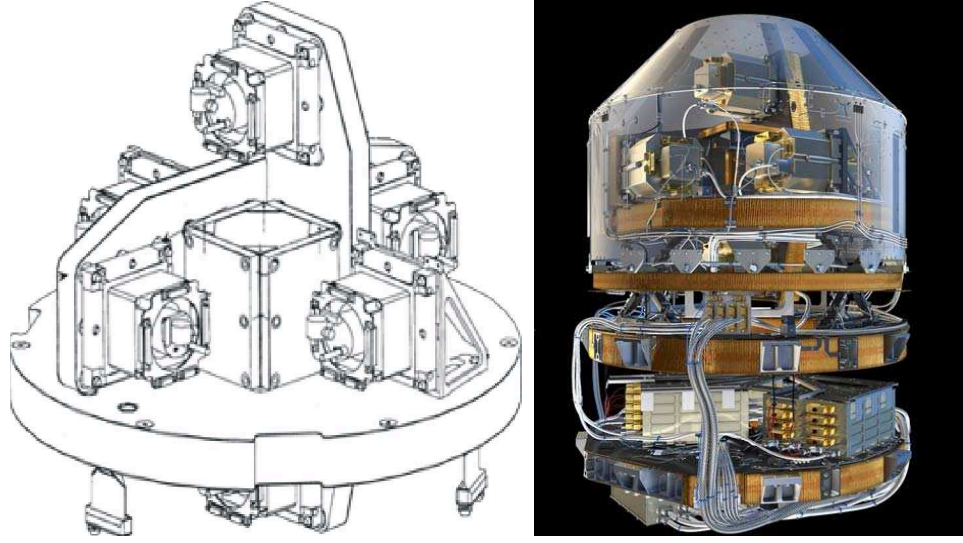
Figure 5.1: GOCE gravitational gradiometer consisting of three orthogonal one-axis gradiometers, each 50 cm long and with two accelerometers; technical drawing (left) and actual instrument (right) (source: ESA)

The difference between accelerations measured by each set of two accelerometers (which are about 50 cm apart, see Fig. 5.2), i.e., the so-called differential mode acceleration (DMA), in the direction joining them contains the basic gradiometric information. After removing the angular motion from the DMA, the gravitational gradients (GG) are derived in the gradiometer reference frame (GRF), see (European Space Agency, 2006; Gruber, 2010; van Hees et al., 2008; Rummel, 1986).

Gravitational gradiometry is the measurement of the second derivatives of the gravitational potential V. It is referred to as gradiometry because the gradients of the components of the gravitational acceleration vector $\boldsymbol{a}$ are measured. The gravitational gradients form a second-order tensor field with 3×3 components, the so-called gravitational gradient tensor (GGT) (Rummel et al., 2011). The tensor is denoted as $\boldsymbol{V}$. In an arbitrarily chosen local Cartesian coordinate system at location O, it is defined as

$$\boldsymbol{V}(O) = \nabla \otimes \boldsymbol{a} = \begin{bmatrix} V_{xx} & V_{xy} & V_{xz} \\ V_{yx} & V_{yy} & V_{yz} \\ V_{zx} & V_{zy} & V_{zz} \end{bmatrix} . \tag{5.1}$$

The acceleration at location of accelerometer i is

$$\mathbf{a}(i) = \mathbf{a}(O) + \boldsymbol{V} \Delta \mathbf{r_i} + \left(o^2 \right) , \tag{5.2}$$

with $\Delta \boldsymbol{r}_i = \boldsymbol{r}_i - \boldsymbol{r}_o$. The omitted quadratic and higher order terms contain the third-, fourth- and higher-order derivative tensors of V. We assume the components of $\boldsymbol{a}$ to be measured by an
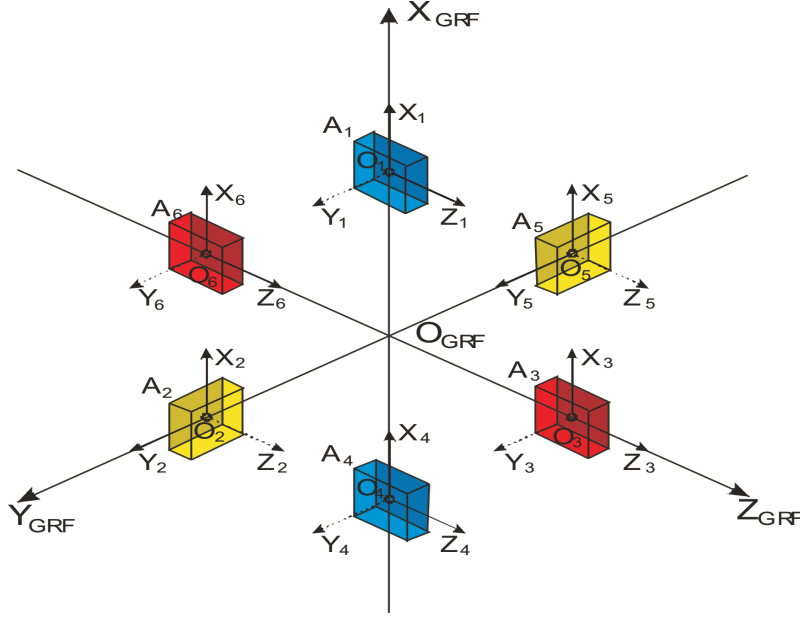
Figure 5.2: Location of the 6 accelerometers, denoted A_i, $i = 1, 2, \cdots, 6$ in the gradiometer reference frame (GRF). The *solid arrows* at each of the accelerometer triads show the ultra-sensitive axes, the *dashed arrows* the less sensitive axes.

accelerometer at i and a second device at a point j exactly symmetric to i relative to O. Then the acceleration difference between i and j gives

$$\boldsymbol{a}(j) - \boldsymbol{a}(i) = \boldsymbol{V}(O)\Delta\boldsymbol{r}_{ij} + \left(o^3\right), \tag{5.3}$$

where $\Delta\boldsymbol{r}_{ij} = \boldsymbol{r}_j - \boldsymbol{r}_i$.

The even terms drop out because of the symmetry of the Taylor series. The cubic and all higher-degree terms are negligibly small, at least for gradiometers of laboratory size. Thus, the nine components of $\boldsymbol{V}$ are derived from measured acceleration differences over baseline lengths, e.g., the component V_{xy} is derived from the difference of the x-components of the two accelerometers of the y-axis, divided by the baseline length Δy:

$$\boldsymbol{V} = \begin{pmatrix} V_{xx} & V_{xy} & V_{xz} \\ V_{yx} & V_{yy} & V_{yz} \\ V_{zx} & V_{zy} & V_{zz} \end{pmatrix} = \begin{pmatrix} \frac{\Delta a_{1,4,x}}{\Delta x} & \frac{\Delta a_{2,5,x}}{\Delta y} & \frac{\Delta a_{3,6,x}}{\Delta z} \\ \frac{\Delta a_{1,4,y}}{\Delta x} & \frac{\Delta a_{2,5,y}}{\Delta y} & \frac{\Delta a_{3,6,y}}{\Delta z} \\ \frac{\Delta a_{1,4,z}}{\Delta x} & \frac{\Delta a_{2,5,z}}{\Delta y} & \frac{\Delta a_{3,6,z}}{\Delta z} \end{pmatrix} + \left(o^3\right)$$

$$= \boldsymbol{D} + \left(o^3\right), \tag{5.4}$$

where Δx, Δy and Δz are the distance between the accelerometer pairs 1-4, 2-5 and 3-6, respectively. $\Delta a_{i,j,x} = a_{i,x} - a_{j,x}$ is the x-component of the difference between the accelerations at the centers of accelerometers i and j.

The gradiometer rigidly mounted into the spacecraft rotates in space with the main angular velocity about the y-axis. Thus, in the GRF the accelerometers pick up any rotational motion, in

addition to the gravitational signal

$$\boldsymbol{a}'(i) = \boldsymbol{a}(i) + \boldsymbol{\Omega}\,\boldsymbol{\Omega}\Delta\boldsymbol{r}_i + \dot{\boldsymbol{\Omega}}\Delta\boldsymbol{r}_i,$$
(5.5)

with $\boldsymbol{a}'$ the accelerations measured in the rotating GRF, and with the well-known expressions for centrifugal and Euler accelerations, where

$$\boldsymbol{\Omega} = \begin{pmatrix} 0 & -\omega_z & \omega_y \\ \omega_z & 0 & -\omega_x \\ -\omega_y & \omega_x & 0 \end{pmatrix} \quad \text{and}$$
(5.6a)

$$\dot{\boldsymbol{\Omega}} = \begin{pmatrix} 0 & -\dot{\omega}_z & \dot{\omega}_y \\ \dot{\omega}_z & 0 & -\dot{\omega}_x \\ -\dot{\omega}_y & \dot{\omega}_x & 0 \end{pmatrix}.$$
(5.6b)

Thereby it is assumed that the test masses of all six accelerometers are kept "still" and levitated. The differential accelerations in the rotating frame become

$$
\begin{aligned}
\boldsymbol{D} &= \begin{pmatrix} D_{xx} & D_{xy} & D_{xz} \\ D_{yx} & D_{yy} & D_{yz} \\ D_{zx} & D_{zy} & D_{zz} \end{pmatrix} = \begin{pmatrix} V_{xx} & V_{xy} & V_{xz} \\ V_{yx} & V_{yy} & V_{yz} \\ V_{zx} & V_{zy} & V_{zz} \end{pmatrix} \\
&+ \begin{pmatrix} -(\omega_y^2 + \omega_z^2) & \omega_x\omega_y & \omega_x\omega_z \\ \omega_y\omega_x & -(\omega_z^2 + \omega_x^2) & \omega_y\omega_z \\ \omega_z\omega_x & \omega_z\omega_y & -(\omega_x^2 + \omega_y^2) \end{pmatrix} \\
&+ \begin{pmatrix} 0 & -\dot{\omega}_z & \dot{\omega}_y \\ \dot{\omega}_z & 0 & -\dot{\omega}_x \\ -\dot{\omega}_y & \dot{\omega}_x & 0 \end{pmatrix} \\
&= \boldsymbol{V} + \boldsymbol{\Omega}\,\boldsymbol{\Omega} + \dot{\boldsymbol{\Omega}}.
\end{aligned}
$$
(5.7)

In Eq. (5.7), the left-hand side contains the measured acceleration differences per baseline length with, e.g., $D_{xy} = \frac{\Delta a_{2,5,x}}{\Delta y}$, $D_{yx} = \frac{\Delta a_{1,4,y}}{\Delta x}$, compare Eq. (5.4). The right-hand side is the sum of gravitational gradients and centrifugal terms with angular velocity products as well as a matrix containing angular accelerations. Symmetry of $\boldsymbol{V}$ and $\boldsymbol{\Omega}\,\boldsymbol{\Omega}$ versus skew-symmetry of $\dot{\boldsymbol{\Omega}}$ allows separation and therefore "isolation" of the angular accelerations:

$$\dot{\boldsymbol{\Omega}} = \frac{1}{2}\left(\boldsymbol{D} - \boldsymbol{D}^T\right),$$
(5.8a)

$$\boldsymbol{V} + \boldsymbol{\Omega}\,\boldsymbol{\Omega} = \frac{1}{2}\left(\boldsymbol{D} + \boldsymbol{D}^T\right).$$
(5.8b)

Angular velocities are obtained by integration of the angular accelerations; with the elements of $\boldsymbol{\Omega}\,\boldsymbol{\Omega}$ known, the gravitational gradients in $\boldsymbol{V}$ can be determined. In fact, the angular velocities are derived from an optimized combination of these angular accelerations and angular rates derived from the star tracker (Rummel et al., 2011; Stummer et al., 2011).

5. GOCE GRAVITATIONAL GRADIOMETRY AND SPHERICAL HARMONIC ANALYSIS

It is unavoidable to use some less accurate components for the separation of GGT and angular motion. With the configuration of Fig. 5.2, the GGT is derived based on Eq. (5.7) as

$$
\begin{pmatrix} V_{xx} & \tilde{V}_{xy} & V_{xz} \\ \tilde{V}_{yx} & V_{yy} & \tilde{V}_{yz} \\ V_{zx} & \tilde{V}_{zy} & V_{zz} \end{pmatrix} = \begin{pmatrix} D_{xx} & D_{xy} & D_{xz} \\ \tilde{D}_{yx} & D_{yy} & \tilde{D}_{yz} \\ D_{zx} & \tilde{D}_{zy} & D_{zz} \end{pmatrix}
$$
$$
- \begin{pmatrix} -(\omega_y^2 + \tilde{\omega}_z^2) & \tilde{\omega}_x \omega_y & \tilde{\omega}_x \tilde{\omega}_z \\ \omega_y \tilde{\omega}_x & -(\tilde{\omega}_z^2 + \tilde{\omega}_x^2) & \omega_y \tilde{\omega}_z \\ \tilde{\omega}_z \tilde{\omega}_x & \tilde{\omega}_z \omega_y & -(\tilde{\omega}_x^2 + \omega_y^2) \end{pmatrix} \qquad (5.9)
$$
$$
- \begin{pmatrix} 0 & -\tilde{\dot{\omega}}_z & \dot{\omega}_y \\ \tilde{\dot{\omega}}_z & 0 & -\tilde{\dot{\omega}}_x \\ -\dot{\omega}_y & \tilde{\dot{\omega}}_x & 0 \end{pmatrix}.
$$

The less sensitive elements are indicated with tilde above the variables. This choice ensures that $\dot{\omega}_y$ can be determined with high precision, and after integration ω_y as well. This is important when determining the angular rates, because it holds $\omega_y \gg \omega_x$ or ω_z. Essentially the four gradiometer components V_{xx}, V_{yy}, V_{zz}, and V_{xz} are resolvable with high precision.

The observations from GOCE gradiometer are in general correlated, i.e. statistically not independent. The PSD of their noise is frequency dependent. This kind of noise is called colored noise. A very powerful test of the performance of the gradiometer is the Laplace condition, which says that the sum of the three diagonal components of the GGT, i.e. its trace, is theoretically zero. For the output of the gradiometer, the trace of the measured GGT is the noise of the measurement. As shown in Fig. 5.3 based on (Cesare, 2008), the requirements of square root of the GGT trace error PSD in the MB is displayed in blue. The expected square root of the trace error PSD in the low-frequency band (LFB) is in dashed black and in the higher-frequency band (HFB) is given in red. The requirements of the square root of the GGT trace error PSD are approximately the noise PSD of the measurements, which are frequency dependent as shown in Fig. 5.3. In the MB from 5 to 100 mHz, the noise level is smaller than that at the frequencies outside of this range, and at 5 mHz it increases with $1/f$ towards the lower frequencies. The higher noise outside of this frequency range (especially the frequencies lower than 5 mHz, i.e. LFB) can either be filtered out or modelled with empirical parameters before data analysis.
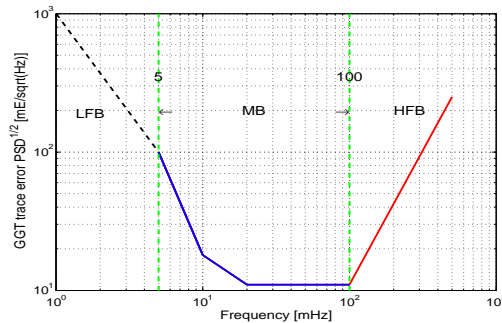
Figure 5.3: Square-root of the power spectrum density of the GGT trace

With the GGT measurements, the following approaches can be applied to gradiometer data for SHA:

i. Semi-analytical approach based on Hill's theory, (Sneeuw, 2000). The time series of the gradiometer observations are transformed to the spectral domain, the observation equations are formulated in the spectral domain as well. From the assumption of circular orbit, the normal matrix can be reduced to be block diagonal. Therefore, it can be computed very fast and with a rather small computer memory;

ii. Direct approach (DIR): Analysis based on the information inside the measurement band (MB) only. The information outside of the MB is bandpass filtered. Gradiometry is introduced directly as new type of observable into the existing GINS software (Marty et al., 2005). GINS has been used for the series of EIGEN models produced by GFZ and GRGS;

iii. Time-wise approach (TIM): Data decorrelated over the entire spectrum (Pail et al., 2011a; Schuh, 2002). The residuals for the observations are analyzed and a filter is constructed based on the residuals. The idea is, after the residuals pass the dedicated filter as inputs, the output behaves like white noise. The essence is: the data are treated as a time series along the orbit;

iv. Space-wise approach (SPW): Collocation approach after applying Wiener filter (Migliaccio et al., 2004; Tscherning, 1993). By exploiting the spatial correlation of the Earth gravity field, a gravitational field model can be estimated from the measurements gridded at mean satellite altitude. The essence is: the data are treated as observations in the space domain on a sphere.

In addition, there is a quick look solution. Similar to semi-analytical approach, it is computed based on the approximations that the orbit must be circular, and without precession. It is useful for quality check and data cleaning (Pail et al., 2007). Recently, a few models, such as TIM1, DIR1, SPW1 (Pail et al., 2011a) and TIM2 (Pail et al., 2011b), DIR2 (Bruinsma et al., 2010), SPW2(Migliaccio et al., 2011), have been published based on DIR, TIM and SPW approaches. The method for SGG data processing in this study is similar to a time-wise approach. Applying a filter at both sides of the observation equations, the colored noise outside of the MB is transformed to a white noise situation and the information inside the MB is preserved and extracted by SHA.

5.2   Observation model

The GGT measured by GOCE gradiometer is given in GRF, as seen in Eq. (5.9). The gravity field is, in general, computed in the Earth fixed frame. The GGT computed from the gravity field model

5. GOCE GRAVITATIONAL GRADIOMETRY AND SPHERICAL HARMONIC ANALYSIS

is given in the ECEF frame as

$$\mathbf{V}_{ECEF} = \begin{bmatrix} V_{xx} & V_{xy} & V_{xz} \\ V_{yx} & V_{yy} & V_{yz} \\ V_{zx} & V_{zy} & V_{zz} \end{bmatrix}_{ECEF}, \tag{5.10}$$

where $V_{ij} = \sum\limits_{n=0}^{N_{max}} \sum\limits_{n=0}^{n} V_{ij}^{nm}$, and $i,j = x,y,z$. V_{ij}^{nm} are computed with Eqs. (5.11) to (5.16). Starting with Eqs. (2.1) or (2.6), the second derivatives of the gravitational potential are computed referring to ECEF frame. They are gradient of the gravitational accelerations, which are computed with Eq. (2.14). The derivation can be found in Métris et al. (1999); Montenbruck and Gill (2000). Here we modify the formulas into fully normalized form, again, in order to avoid the overflow and/or underflow which can happen in unnormalized cases. With the notation given in Eq. 2.7 in page 14, the elements of gravitational gradient matrix in terms of spherical harmonics are

$$V_{xx}^{n0} = \frac{\partial \ddot{x}_{n0}}{\partial x} = \frac{GM_\oplus}{R_\oplus^3} \cdot \frac{1}{2} \left\{ \sqrt{\frac{(2n+1)}{(2n+5)}} \left(\sqrt{\frac{(n+4)!}{2n!}} \overline{V}_{n+2,2} - \frac{(n+2)!}{n!} \overline{V}_{n+2,0} \right) \overline{C}_{n0} \right\}$$

$$V_{xx}^{n1} = \frac{\partial \ddot{x}_{n1}}{\partial x} = \frac{GM_\oplus}{R_\oplus^3} \cdot \frac{1}{4} \left\{ \sqrt{\frac{(2n+1)(n+5)!}{(2n+5)(n+1)!}} \left(\overline{C}_{n1} \overline{V}_{n+2,3} + \overline{S}_{n1} \overline{W}_{n+2,3} \right) \right.$$

$$\left. + \sqrt{\frac{(2n+1)(n+3)(n+2)}{(2n+5)}} \left(-3\overline{C}_{n1} \overline{V}_{n+2,1} - S_{n1} \overline{W}_{n+2,1} \right) \right\}$$

$$V_{xx}^{n2} = \frac{\partial \ddot{x}_{n2}}{\partial x} = \frac{GM_\oplus}{R_\oplus^3} \cdot \frac{1}{4} \left\{ \sqrt{\frac{(2n+1)(n+6)!}{(2n+5)(n+2)!}} \left(\overline{C}_{n2} \overline{V}_{n+2,4} + \overline{S}_{n2} \overline{W}_{n+2,4} \right) \right.$$

$$+ 2\sqrt{\frac{(2n+1)(n+4)!n!}{(2n+5)(n+2)!(n-2)!}} \left(-\overline{C}_{n2} \overline{V}_{n+2,2} - \overline{S}_{n2} \overline{W}_{n+2,2} \right) \tag{5.11}$$

$$\left. + \sqrt{\frac{2(2n+1)(n+2)!}{(2n+5)(n-2)!}} \left(\overline{C}_{n2} \overline{V}_{n+2,0} + \overline{S}_{n2} \overline{W}_{n+2,0} \right) \right\}$$

$$V_{xx}^{nm} \stackrel{m \geq 2}{=} \frac{\partial \ddot{x}_{nm}}{\partial x} = \frac{GM_\oplus}{R_\oplus^3} \cdot \frac{1}{4} \left\{ \sqrt{\frac{(2n+1)(n+m+4)!}{(2n+5)(n+m)!}} \left(\overline{C}_{nm} \overline{V}_{n+2,m+2} + \overline{S}_{nm} \overline{W}_{n+2,m+2} \right) \right.$$

$$+ 2\sqrt{\frac{(2n+1)(n+m+2)!(n-m+2)!}{(2n+5)(n+m)!(n-m)!}} \left(-\overline{C}_{nm} \overline{V}_{n+2,m} - \overline{S}_{nm} \overline{W}_{n+2,m} \right)$$

$$\left. + \sqrt{\frac{(2n+1)(n-m+4)!}{(2n+5)(n-m)!}} \left(\overline{C}_{nm} \overline{V}_{n+2,m-2} + \overline{S}_{nm} \overline{W}_{n+2,m-2} \right) \right\},$$

$$V_{xy}^{n0} = \frac{\partial \ddot{x}_{n0}}{\partial y} = \frac{GM_\oplus}{R_\oplus^3} \cdot \frac{1}{2} \left\{ \left(\overline{C}_{n0} \overline{W}_{n+2,2} \right) \sqrt{\frac{(2n+1)(n+4)!}{2(2n+5)n!}} \right\}$$

$$V_{xy}^{n1} = \frac{\partial \ddot{x}_{n1}}{\partial y} = \frac{GM_\oplus}{R_\oplus^3} \cdot \frac{1}{4} \left\{ \sqrt{\frac{(2n+1)(n+5)!}{(2n+5)(n+1)!}} \left(\overline{C}_{n1} \overline{W}_{n+2,3} - \overline{S}_{n1} \overline{V}_{n+2,3} \right) \right.$$

$$\left. + \frac{(n+1)!}{(n-1)!} \sqrt{\frac{(2n+1)(n+3)!}{(2n+5)(n+1)!}} \left(-\overline{C}_{n1} \overline{W}_{n+2,1} - \overline{S}_{n1} \overline{V}_{n+2,1} \right) \right\}$$

$$V_{xy}^{n2} = \frac{\partial \ddot{x}_{n2}}{\partial y} = \frac{GM_\oplus}{R_\oplus^3} \cdot \frac{1}{4} \left\{ \sqrt{\frac{(2n+1)(n+6)!}{(2n+5)(n+2)!}} \left(\overline{C}_{n2} \overline{W}_{n+2,4} - \overline{S}_{n2} \overline{V}_{n+2,4} \right) \right. \qquad (5.12)$$

$$\left. + \sqrt{\frac{(2n+1)(n+2)!}{(2n+5)(n-2)!}} \left(-\overline{C}_{n2} \overline{W}_{n+2,0} + \overline{S}_{n2} \overline{V}_{n+2,0} \right) \right\}$$

$$V_{xy}^{nm} \overset{m \geq 2}{=} \frac{\partial \ddot{x}_{nm}}{\partial y} = \frac{GM_\oplus}{R_\oplus^3} \cdot \frac{1}{4} \left\{ \sqrt{\frac{(2n+1)(n+m+4)!}{(2n+5)(n+m)!}} \left(\overline{C}_{nm} \overline{W}_{n+2,m+2} - \overline{S}_{nm} \overline{V}_{n+2,m+2} \right) \right.$$

$$\left. + \sqrt{\frac{2(2n+1)(n-m+4)!}{(2n+5)(n-m)!}} \left(-\overline{C}_{nm} \overline{W}_{n+2,m-2} + \overline{S}_{nm} \overline{V}_{n+2,m-2} \right) \right\},$$

$$V_{xz}^{n0} = \frac{\partial \ddot{x}_{n0}}{\partial z} = \frac{GM_\oplus}{R_\oplus^3} \cdot \left\{ (n+1) \sqrt{\frac{(2n+1)(n+3)(n+2)}{2(2n+5)}} \left(\overline{C}_{n0} \overline{V}_{n+2,1} \right) \right\}$$

$$, V_{xz}^{n1} = \frac{\partial \ddot{x}_{n1}}{\partial z} = \frac{GM_\oplus}{R_\oplus^3} \cdot \left\{ \frac{n}{2} \sqrt{\frac{(2n+1)(n+4)!}{(2n+5)n(n+1)!}} \left(\overline{C}_{n1} \overline{V}_{n+2,2} + \overline{S}_{n2} \overline{W}_{n+2,2} \right) \right.$$

$$\left. + \frac{(n+2)!}{2(n-1)!} \sqrt{\frac{2(2n+1)}{(2n+5)(n+1)n}} \left(-\overline{C}_{n1} \overline{V}_{n+2,0} - \overline{S}_{n1} \overline{W}_{n+2,0} \right) \right\}$$

$$V_{xz}^{n1} \overset{m \geq 1}{=} \frac{\partial \ddot{x}_{n1}}{\partial z} = \frac{GM_\oplus}{R_\oplus^3} \cdot \left\{ \frac{1}{2} \sqrt{\frac{(2n+1)(n-m+1)(n+m+3)!}{(2n+5)(n+m)!}} \left(\overline{C}_{nm} \overline{V}_{n+2,m+1} + \overline{S}_{nm} \overline{W}_{n+2,m+1} \right) \right.$$

$$\left. + \frac{1}{2} \sqrt{\frac{(2n+1)(n+m+1)(n-m+3)!}{(2n+5)(n-m)!}} \left(-\overline{C}_{nm} \overline{V}_{n+2,m-1} - \overline{S}_{nm} \overline{W}_{n+2,m-1} \right) \right\},$$

$$(5.13)$$

5. GOCE GRAVITATIONAL GRADIOMETRY AND SPHERICAL HARMONIC ANALYSIS

$$V_{yy}^{n0} = \frac{\partial \ddot{y}_{n0}}{\partial y} = \frac{GM_\oplus}{R_\oplus^3} \cdot \frac{1}{2} \left\{ \sqrt{\frac{(2n+1)}{(2n+5)}} \left(-\sqrt{\frac{(n+4)!}{2n!}} \overline{V}_{n+2,2} - \frac{(n+2)!}{n!} \overline{V}_{n+2,0} \right) \overline{C}_{n0} \right\}$$

$$V_{yy}^{n1} = \frac{\partial \ddot{y}_{n1}}{\partial y} = \frac{GM_\oplus}{R_\oplus^3} \cdot \frac{1}{4} \left\{ \sqrt{\frac{(2n+1)(n+5)!}{(2n+5)(n+1)!}} \left(-\overline{C}_{n1} \overline{V}_{n+2,3} - \overline{S}_{n1} \overline{W}_{n+2,3} \right) \right.$$

$$\left. + \frac{(n+1)!}{(n-1)!} \sqrt{\frac{(2n+1)(n+3)(n+2)}{(2n+5)(n+1)n}} \left(-\overline{C}_{n1} \overline{V}_{n+2,1} - 3\overline{S}_{n1} \overline{W}_{n+2,1} \right) \right\}$$

$$V_{yy}^{n2} = \frac{\partial \ddot{y}_{n2}}{\partial y} = \frac{GM_\oplus}{R_\oplus^3} \cdot \frac{1}{4} \left\{ \sqrt{\frac{(2n+1)(n+6)!}{(2n+5)(n+2)!}} \left(-\overline{C}_{n2} \overline{V}_{n+2,4} - \overline{S}_{n2} \overline{W}_{n+2,4} \right) \right.$$

$$+ 2\sqrt{\frac{(2n+1)(n+4)!(n)!}{(2n+5)(n+2)!(n-2)!}} \left(-\overline{C}_{n2} \overline{V}_{n+2,2} - \overline{S}_{n2} \overline{W}_{n+2,2} \right) \tag{5.14}$$

$$\left. + \sqrt{\frac{2(2n+1)(n+2)!}{(2n+5)(n-2)!}} \left(-\overline{C}_{n2} \overline{V}_{n+2,0} - \overline{S}_{n2} \overline{W}_{n+2,0} \right) \right\}$$

$$V_{yy}^{nm \, m\geq 2} = \frac{\partial \ddot{y}_{n2}}{\partial y} = \frac{GM_\oplus}{R_\oplus^3} \cdot \frac{1}{4} \left\{ \sqrt{\frac{(2n+1)(n+m+4)!}{(2n+5)(n+m)!}} \left(-\overline{C}_{nm} \overline{V}_{n+2,m+2} - \overline{S}_{nm} \overline{W}_{n+2,m+2} \right) \right.$$

$$+ 2\sqrt{\frac{(2n+1)(n+m+2)!(n-m+2)!}{(2n+5)(n+m)!(n-m)!}} \left(-\overline{C}_{nm} \overline{V}_{n+2,m} - \overline{S}_{nm} \overline{W}_{n+2,m} \right)$$

$$\left. + \sqrt{\frac{(2n+1)(n-m+4)!}{(2n+5)(n-m)!}} \left(-\overline{C}_{nm} \overline{V}_{n+2,m-2} - \overline{S}_{nm} \overline{W}_{n+2,m-2} \right) \right\},$$

$$V_{yz}^{n0} = \frac{\partial \ddot{y}_{n0}}{\partial z} = \frac{GM_\oplus}{R_\oplus^3} \cdot \frac{1}{2} \left\{ (n+1)\sqrt{\frac{(2n+1)(n+3)(n+2)}{2(2n+5)}} \left(\overline{C}_{n0} \overline{W}_{n+2,1} \right) \right\}$$

$$V_{yz}^{n1} = \frac{\partial \ddot{y}_{n1}}{\partial z} = \frac{GM_\oplus}{R_\oplus^3} \cdot \left\{ \frac{1}{2}\sqrt{\frac{(2n+1)(n)(n+4)!}{(2n+5)(n+1)!}} \left(\overline{C}_{n1} \overline{W}_{n+2,2} - \overline{S}_{n1} \overline{V}_{n+2,2} \right) \right.$$

$$\left. + \frac{1}{2}\sqrt{\frac{2(2n+1)(n+2)(n+2)!}{(2n+5)(n-1)!}} \left(\overline{C}_{n1} \overline{W}_{n+2,0} - \overline{S}_{n1} \overline{V}_{n+2,0} \right) \right\}$$

$$V_{yz}^{nm \, m\geq 1} = \frac{\partial \ddot{y}_{nm}}{\partial z} = \frac{GM_\oplus}{R_\oplus^3} \cdot \left\{ \frac{1}{2}\sqrt{\frac{(2n+1)(n-m+1)(n+m+3)!}{(2n+5)(n+m)!}} \left(\overline{C}_{nm} \overline{W}_{n+2,m+1} - \overline{S}_{nm} \overline{V}_{n+2,m+1} \right) \right.$$

$$\left. + \frac{1}{2}\sqrt{\frac{(2n+1)(n+m+1)(n-m+3)!}{(2n+5)(n-m)!}} \left(\overline{C}_{nm} \overline{W}_{n+2,m-1} - \overline{S}_{nm} \overline{V}_{n+2,m-1} \right) \right\} \tag{5.15}$$

$$V_{zz}^{nm} = \frac{\partial \ddot{z}_{nm}}{\partial z} = \frac{GM_\oplus}{R_\oplus^3} \cdot \left\{ \sqrt{\frac{(2n+1)(n+m+2)!(n-m+2)!}{(2n+5)(n+m)!(n-m)!}} \left(\overline{C}_{nm} \overline{V}_{n+2,m} + \overline{S}_{nm} \overline{W}_{n+2,m} \right) \right\} . \tag{5.16}$$

Similar to Eq. (2.15), the partial derivatives of the gradients w.r.t. the gravitational field coef-

ficients are obtained based on Eqs. (5.11) to (5.16) and are represented as

$$
\frac{\partial \mathbf{V}_{ECEF}}{\partial \boldsymbol{\beta}} = \begin{bmatrix} \frac{\partial V_{xx}}{\partial \boldsymbol{\beta}} & \frac{\partial V_{xy}}{\partial \boldsymbol{\beta}} & \frac{\partial V_{xz}}{\partial \boldsymbol{\beta}} \\ \frac{\partial V_{yx}}{\partial \boldsymbol{\beta}} & \frac{\partial V_{yy}}{\partial \boldsymbol{\beta}} & \frac{\partial V_{yz}}{\partial \boldsymbol{\beta}} \\ \frac{\partial V_{zx}}{\partial \boldsymbol{\beta}} & \frac{\partial V_{zy}}{\partial \boldsymbol{\beta}} & \frac{\partial V_{zz}}{\partial \boldsymbol{\beta}} \end{bmatrix}_{ECEF} . \tag{5.17}
$$

Since the measurements of the V_{xy} and V_{yz} components are less accurate, the measured GGT from the GOCE gradiometer is an incomplete tensor. It must be avoided to transform the incomplete GGT from the GRF to ECEF or any other Earth-fixed frame, otherwise the highly accurate components will be degraded by the less accurate ones. Moreover, the rotation of the measurements will lead to a correlation between different components. Therefore, the observation equations are directly formulated in the GRF. This means, the partial derivatives of the GGT to each individual coefficient and the reference values of the GGT computed from a-priori model are rotated into the GRF. The rotation is done by

$$
\begin{aligned}
\mathbf{V}_{\mathrm{GRF}} &= \mathbf{C}_{\mathrm{GRF}}^i \mathbf{C}_i^e \mathbf{V}_{\mathrm{ECEF}} \left(\mathbf{C}_{\mathrm{GRF}}^i \mathbf{C}_i^e \right)^T \\
\Rightarrow \frac{\partial \mathbf{V}_{\mathrm{GRF}}}{\partial \boldsymbol{\beta}} &= \mathbf{C}_{\mathrm{GRF}}^i \mathbf{C}_i^e \frac{\partial \mathbf{V}_{\mathrm{ECEF}}}{\partial \boldsymbol{\beta}} \left(\mathbf{C}_{\mathrm{GRF}}^i \mathbf{C}_i^e \right)^T ,
\end{aligned} \tag{5.18}
$$

where $\mathbf{C}_i^e$ is the rotation matrix from the ECEF to the inertial frame, and $\mathbf{C}_{\mathrm{GRF}}^i$ is the rotation matrix from the inertial frame to the GRF. The $\mathbf{C}_i^e$ can be evaluated using the SST_PRM_2I sub-product or using IERS conventions (McCarthy and Petit, 2004) with a dedicated software package, such as SOFA, (see IAU SOFA Board, 2010). The $\mathbf{C}_{\mathrm{GRF}}^i$ is obtained from the EGG_IAQ_2C product.

With the above derivations, the observation equations become:

$$
\tilde{\mathbf{v}} = \frac{\partial \mathbf{V}_{\mathrm{GRF}}}{\partial \boldsymbol{\beta}} \delta \boldsymbol{\beta} - \left(\tilde{\mathbf{V}}_{\mathrm{GRF}} - \mathbf{V}_{\mathrm{GRF}}^0 \right) , \tag{5.19}
$$

with $\tilde{\mathbf{V}}_{\mathrm{GRF}}$ the measured GGT and $\mathbf{V}_{\mathrm{GRF}}^0$ the reference values from an a-priori model. Compared to Eq. (3.5), $\tilde{\mathbf{V}}_{\mathrm{GRF}} - \mathbf{V}_{\mathrm{GRF}}^0 = \tilde{\mathbf{d}}$ is the observed minus computed part; the parameters in vector $\boldsymbol{\beta}$ can be therefore estimated based on Eq. (3.8) with appropriate weighting, as described in section 3.4.

5.3 Reductions of the Gravitational Gradient

Like the orbit perturbations, compare sect. 4.2, also the output from the gradiometer onboard the satellite contains a contribution from the gravitational gradients due to the attraction of the moon and sun, Earth solid tides and ocean tides as well as short-term variations from the atmosphere and ocean. The gradients due to the direct attraction of the moon and sun are computed with Eq. (2.17), and those due to solid Earth tides, ocean tides and atmosphere and ocean are computed from Eqs. (5.11) to (5.16) using the corresponding coefficients of these models.

5. GOCE GRAVITATIONAL GRADIOMETRY AND SPHERICAL HARMONIC ANALYSIS

The GGT has nine elements, and is symmetric. Thus, disregarding Laplace condition, there are six independent components. We define the signal magnitude of a GGT by six elements

$$|\mathbf{V}| = \sqrt{V_{xx}^2 + V_{yy}^2 + V_{zz}^2 + V_{xy}^2 + V_{xz}^2 + V_{yz}^2} \quad . \tag{5.20}$$

In Fig. 5.4, the magnitude of the computed values from models is shown on the left and $\mathrm{PSD}^{1/2}$ on the right. From the magnitude shown in Fig. 5.4a with μ representing mean values, the largest effect is due to solid Earth tides, different from Fig. 4.4 where the direct tidal attraction of the moon is the largest effect. This can be explained by the fact that the magnitude of the acceleration due to the direct attraction of the moon and the sun is larger than that due to the Earth tides, but its variation (gradient) is smaller than that due to the Earth tides and ocean tides.
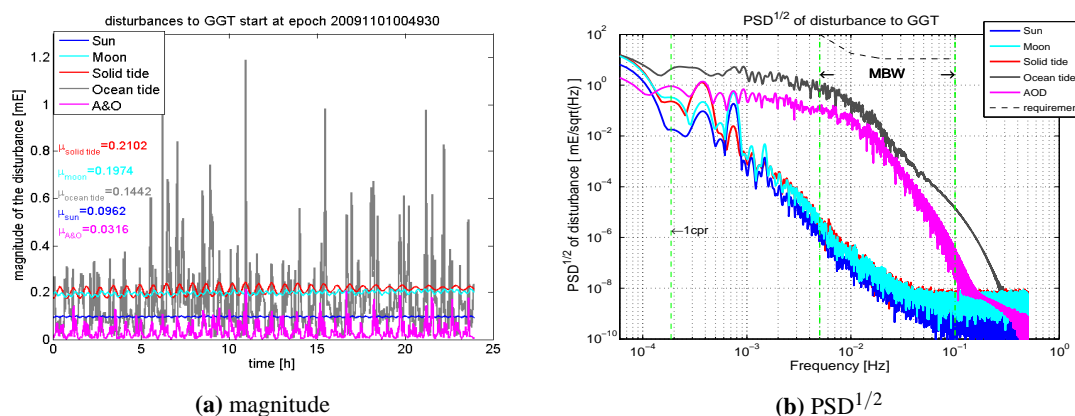
Figure 5.4: Magnitude (left) and $\mathrm{PSD}^{1/2}$ (right) of the corrections to GGT

In Fig. 5.4b, the specified requirements represent the expected noise level of the GOCE gradiometer. They are shown as black dashed line. In the MB and below, the magnitudes of all the time-varying signals are significantly below the requirements. This may explain why the GOCE gradiometer cannot really sense the time-varying signal in the GGT. Nevertheless, since models are available for the time-varying signals, and since in some regions the signal strength could be higher, they are removed from the measurements. Gradiometer instruments with even higher performance may be able to measure these time-varying signals.

Of all the above effects, ocean tide models are the least accurate. This is due to their non-linear behavior, in particular in shelf waters. As shown in Fig. 5.4b, the ocean tides vary rapidly and may have large values in some coastal regions. In order to look more closely into their effect, the modelled gradient values for the time span November and December 2009 are computed along the orbit and interpolated onto a $20' \times 20'$ grid, as presented in Fig. 5.5. In Fig. 5.5a the values computed with model EOT2008a are presented. The largest effects can be found in coastal areas. However, they are still smaller than $11/\sqrt{3} \frac{\mathrm{mE}}{\sqrt{\mathrm{Hz}}}$, with 11 mE the requirement value of the trace in the MB and $\sqrt{3}$ expressing the average contribution of each individual component of the three diagonal

elements to the trace of the tensor, according to the rule of error propagation. The differences between EOT2008a and a second ocean tide model Fes2004 are presented in Fig. 5.5b. Large discrepancies exist in some coastal areas such as Cape of Good Hope, Labrador Sea and Hudson Bay, etc. The EOT2008a model is derived from only satellite altimetry data, whereas Fes2004 model was computed from the assimilation of altimetry into a hydrodynamic ocean model.
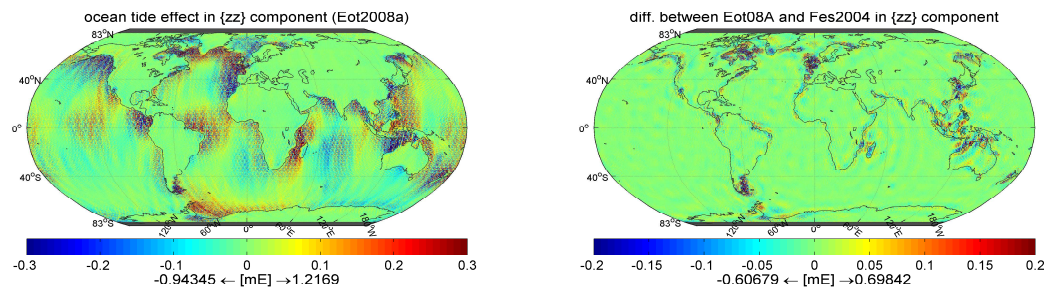
(a) V_{zz} computed using ocean tide model Eot2008a   (b) Differences between Eot2008a and Fes2004 in V_{zz}

Figure 5.5: V_{zz} computed from the ocean tide model EOT08A (left) and the differences between the values computed from Eot2008a and Fes2004

With the above computation, we can say that the values of V_{zz} computed using an ocean tide model are smaller than the sensitivity level of the gradiometer. The magnitude of the signal of V_{zz} from an ocean tide model (Fig. 5.5a) is high in coastal areas. The uncertainty (see the differences between two models in Fig. 5.5b) shows that the two ocean models are not perfectly consistent with each other in shelf waters (coastal areas), but these differences are even lower than the model values themselves.

5.4 Data Analysis before Spherical Harmonic Analysis

In order to understand the behavior of the data, we analyze the orientation of the satellite and the quality of the gradiometer data before SHA. This is part of the pre-processing, and is important for the assessment of the data. Some findings are useful for SHA.

5.4.1 Attitude Data Analysis

Apart from the gradiometer there are three star trackers on board. The star trackers measure the orientation of the satellite in inertial space. Their output is combined with the gradiometer data, resulting in a product named EGG_IAQ_2C, in which precise orientation data of the satellite are given (European Space Agency, 2006; Stummer et al., 2011).

We analyze the angular motion of the satellite w.r.t. the LORF. This gives us a hint about how well the GRF can follow the LORF. As stated in (Sechi et al., 2006), the requirements of the

angular motion control between GRF and LORF are in roll and yaw less than 8.6 ° and in pitch less than 3.5 °.

The *x*-direction of LORF is the same as the direction of the velocity vector; the *z*-direction is approximately upwards from the Earth center; and the *y*-direction of LORF is in the direction of the angular momentum vector of the orbit, forming a right-handed system. The direction of the *z*-axis of GRF approximately points downwards to the Earth's center; and the *y*-direction is in the opposite direction of angular momentum vector. Therefore, there is approximately a $180°$ difference in the directions of the *y*- and *z*-axes of GRF and LORF by definition. We define a new system LORF′, with its *x*-direction the same as that of LORF, but with the *y*- and *z*-axes in the opposite direction of those of LORF.

Slightly different from Eq. (2.34), one gets the following unit vectors with the position and velocity vectors given in the inertial frame:

$$
\begin{aligned}
\mathbf{e}_S' &= \frac{\mathbf{v}}{|\mathbf{v}|} \\
\mathbf{e}_T' &= -\frac{\mathbf{r}\times\mathbf{v}}{|\mathbf{r}\times\mathbf{v}|} \\
\mathbf{e}_W' &= -\mathbf{e}_S' \times \mathbf{e}_T'.
\end{aligned}
\tag{5.21}
$$

Then similar to Eq. (2.35) we have

$$
\mathbf{C}_{\text{LORF}'}^{\text{Inertial}} = \begin{bmatrix} \mathbf{e}_S' & \mathbf{e}_T' & \mathbf{e}_W'. \end{bmatrix}^T
\tag{5.22}
$$

The transformation matrix from the GRF to the inertial frame is computed with the quaternions of the EGG_IAQ_2C product as

$$
\mathbf{C}_{\text{Inertial}}^{\text{GRF}} = \begin{bmatrix}
q_0^2+q_1^2-q_2^2-q_3^2 & 2(q_1q_2-q_3q_0) & 2(q_1q_3+q_2q_0) \\
2(q_1q_2+q_3q_0) & q_0^2-q_1^2+q_2^2-q_3^2 & 2(q_2q_3-q_1q_0) \\
2(q_1q_3-q_2q_0) & 2(q_2q_3+q_1q_0) & q_0^2-q_1^2-q_2^2+q_3^2,
\end{bmatrix}
\tag{5.23}
$$

where q_0, q_1, q_2 and q_3 are the elements of the quaternion with q_0 being the scalar part. Suppose the rotation matrix is defined by the three Euler angles, i.e., roll angle φ, pitch angle θ, and yaw ψ, then we find

$$
\begin{aligned}
\mathbf{C}_{\text{LORF}'}^{\text{GRF}} &= \mathbf{R}_z(\psi)\mathbf{R}_y(\theta)\mathbf{R}_x(\varphi) \\
&= \begin{bmatrix}
\cos\theta\cos\psi & \cos\varphi\sin\psi+\sin\varphi\sin\theta\cos\psi & \sin\varphi\sin\psi-\cos\varphi\sin\theta\cos\psi \\
-\cos\theta\sin\psi & \cos\varphi\cos\psi-\sin\varphi\sin\theta\sin\psi & \sin\varphi\cos\psi+\cos\varphi\sin\theta\sin\psi \\
\sin\theta & -\sin\varphi\cos\theta & \cos\varphi\cos\theta
\end{bmatrix}.
\end{aligned}
\tag{5.24}
$$

By multiplying the two matrices in Eq. (5.22) and (5.23), the transformation matrix from GRF to LORF′ is obtained as

$$
\mathbf{C}_{\text{LORF}'}^{\text{GRF}} = \mathbf{C}_{\text{LORF}'}^{\text{Inertial}}\mathbf{C}_{\text{Inertial}}^{\text{GRF}}.
\tag{5.25}
$$

The three rotation angles can therefore be computed from the rotation matrix and are presented in Fig. 5.6. It is

$$
\begin{aligned}
\varphi &= \arctan\left(-\frac{C_{3,2}^{\mathrm{GRF}\to\mathrm{LORF}'}}{C_{3,3}^{\mathrm{GRF}\to\mathrm{LORF}'}}\right) \\
\theta &= \arctan\left(\frac{C_{3,1}^{\mathrm{GRF}\to\mathrm{LORF}'}}{\sqrt{C_{3,2}^{\mathrm{GRF}\to\mathrm{LORF}'\,2}+C_{3,3}^{\mathrm{GRF}\to\mathrm{LORF}'\,2}}}\right) , \\
\psi &= \arctan\left(-\frac{C_{2,1}^{\mathrm{GRF}\to\mathrm{LORF}'}}{C_{1,1}^{\mathrm{GRF}\to\mathrm{LORF}'}}\right)
\end{aligned}
\tag{5.26}
$$

with e.g. $C_{2,1}^{\mathrm{GRF}\to\mathrm{LORF}'}$ the element in the second row and first column of the rotation matrix $\mathbf{C}_{\mathrm{LORF}'}^{\mathrm{GRF}}$.

As one can see, the pitch angles correlate strongly with the magnetic equator and have some large oscillation when the satellite passes close to these areas. This is due to the fact that attitude control is done by magnetic torquing. This also implies that orientation with respect to the field lines of the magnetic field leaves undetermined one degree of freedom at any moment. The amplitude of the yaw angle, which is the largest of all the three Euler angles, is about 3 degree, which tells us that GRF is close to LORF$'$.

Correlation can be found between the yaw angles in Fig. 5.6 and the reconstructed accelerations in the cross-track direction, see Figs. 4.19c and 4.19d. The actual propulsion of the ion thrusters is given in the x-direction in GRF. Its projection in the direction of the velocity vector has to be kept the same as the actual air drag experienced by the satellite in the direction of the velocity vector, for the purpose of drag free motion. However, due to the Euler angles not being zero, the magnitude of the actual propulsion of the ion thrusters has to be higher than the magnitude of the actual air drag, in order to fulfill this purpose. Some part of air drag compensation projects to the cross-track direction and is visible in the reconstructed empirical accelerations. The pitch and roll angles are small compared to yaw; therefore the correlation of the pitch and roll angles to the reconstructed acceleration is smaller than that of the yaw angles.

5.4.2 Gradiometer Data Analysis

The gradiometer data are the primary observations of the GOCE mission for the determination of the short-wavelength part of the gravity field. It is therefore very important to understand their characteristics and performance. We conduct an analysis of the data in the time domain, frequency domain and space domain. In this subsection, the observations in the period from November and December 2009 are analyzed.

5.4.2.1 Outlier Detection

Outlier detection is one of the most important steps of the pre-processing. If the outliers were not identified and removed from the data, they might contaminate the parameters to be estimated. The

(a) Ascending

(b) Descending

(c) Ascending

(d) Descending

(e) Ascending
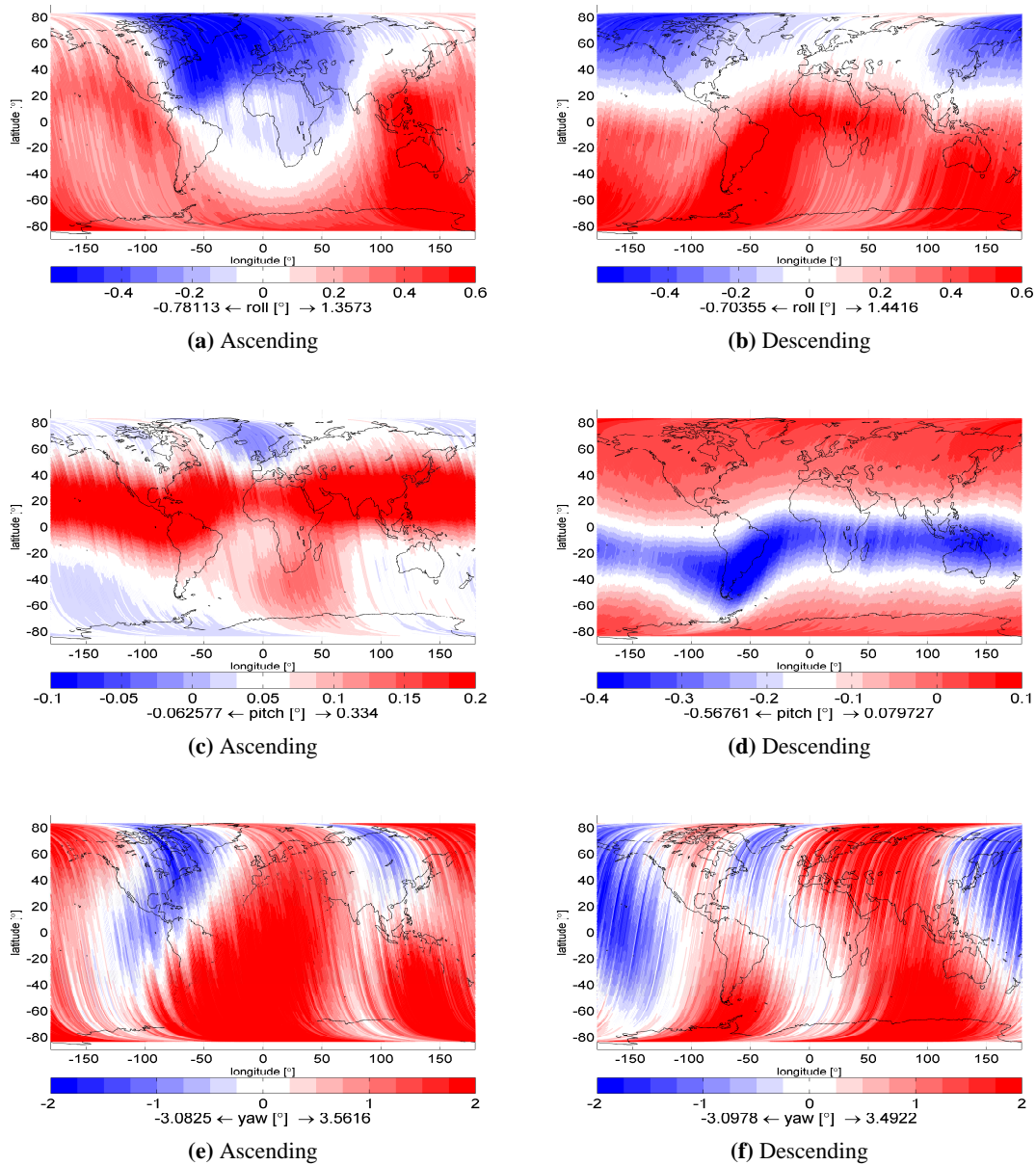
(f) Descending

Figure 5.6: Global map of variations of attitude angles roll, pitch and yaw of ascending (left) and
descending (right) tracks in November and December, 2009

outliers can be identified based on the measurements themselves, before the actual data analysis, or can be removed iteratively based on the residuals of the least squares adjustment. The advantage of outlier detection based on the residuals is that the results are more sensitive to outliers. The disadvantage is time-consuming due to iteration. In this study, we do not apply iteration for outlier detection.

In our data processing, a method is presented for outlier detection that looks into the standard deviation of short and long series of OMC (observed minus computed) and the trace of the GGT. In the presence of outliers, special attention has to be paid to the robustness and the efficiency of the algorithm. The principle of our approach is to compute the standard deviation of each short segment (e.g., 30 seconds) of the time series; if it is larger than a threshold value, the segment of data are assumed to contain outliers.

An exact definition of an outlier often depends on assumptions regarding the random behavior of the noise in the data and the applied detection method. Hawkins (1980) defined an outlier as an observation that deviates so much from other observations as to arise the suspicion that it was generated by a different mechanism. Barnett and Lewis (1994) said that an outlying observation, or outlier, is one that appears to deviate markedly from other members of the sample in which it occurs, similarly, Johnson and Wichern (2001) defined an outlier as an observation in a data set which appears to be inconsistent with the remainder of that set of data. All in all, these definitions are similar. In the case of the GOCE gradiometer data, since the gradiometer signal changes with time, we define as outlier that the OMC value deviates markedly from the adjacent OMCs, with the computed values are obtained from the EGM2008 (Pavlis et al., 2008) up to degree and order 215. In addition, since the noise in the gradiometer data is not white, i.e., depends on frequency, we introduce two criteria, long-period outlier and short-period outlier. A long-period outlier is the one detected with the data longer than or equal to half an orbit revolution. A short-period outlier is detected locally, with data of about 31 seconds.

We use two quantities for outlier detection, one is the OMC value, another one is the trace of the GGT with zero expectation. If the value of either of them deviates from their mean value greater than a threshold value (e.g., 3 times the STD), the observation at this epoch is assumed an outlier.

With the GGT trace as an example, the long-period outliers are identified by comparing the difference of the trace minus its mean value to the 3σ, where σ is the standard deviation of the trace and μ the mean value of $V_{xx} + V_{yy} + V_{zz}$, i.e.

$$|V_{xx} + V_{yy} + V_{zz} - \mu| = \begin{cases} > 3\sigma & \text{outlier} \\ \leq 3\sigma & \text{not outlier}, \end{cases} \tag{5.27}$$

where μ and σ are computed based on the measurements. This criterion is also applied to the OMC values.

Theoretically the OMC value and the trace should change slowly. But sometimes an outlier occurs inside the range of 3σ. It cannot be detected with the algorithm as described in Eq. (5.27). We introduce therefore a second kind of outlier detector. Similar to the terminology of moving average, a moving standard deviation is used to find the short-period outlier by computing the standard deviation of every short interval of the trace and OMC (in our case the length is 31 seconds). If it is larger than the threshold value (e.g., 60 mE, considering the noise level of the trace in the MB to be about 20 mE), the measurements in this interval are assumed to contain outliers.

In Fig. 5.7, the long period outliers are presented in the left panel and the short ones are in the right panel. In the upper panel of Fig. 5.7a, at epoch between hour 0 to 1 on the horizontal axis, the values of the trace deviate from the mean value of the whole day larger than 3σ; therefore, the measurements in this interval are assumed to contain outliers, based on the criterion of the long period outlier detection. In Fig. 5.7b, at epoch 1.5 hours there are large oscillations. However, the magnitude of the oscillations is inside the range of 3σ and cannot be detected by Eq. (5.27). In the lower panel of Fig. 5.7b, the moving STD at about hour 1.5 is larger than the threshold value (60 mE in this example), which means the anomalous behavior at hour 1.5 on the horizontal axis is detected with our second criterion. Therefore, the two strategies are complementary. Both the long-period outliers and the short-period outliers are identified with this approach.

(a) long-period outlier

(b) short-period outlier
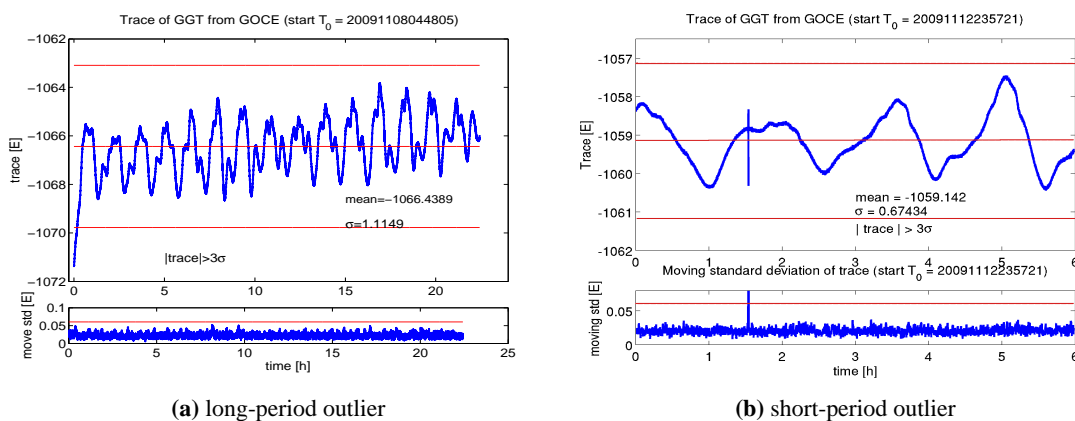
Figure 5.7: Outlier in long-period (left) and short-period (right); the two criteria are complementary

Once the outliers are identified, they are removed from the measurements and not used for parameter estimation. The outliers detected for the data from November 1 to December 31, 2009 are shown in Fig. 5.8. The long-period outliers in this period are plotted in red, with 603 epochs. The short-period outliers are given in blue, with 152 epochs.

5.4.2.2 Gradiometer Data in the Time Domain

The gradiometer data can be presented as a time series in the time domain as shown in Fig. 5.9. In Figs. 5.9a and 5.9b a gradiometeric profile of V_{zz} is shown for a time span of two orbit revolutions.
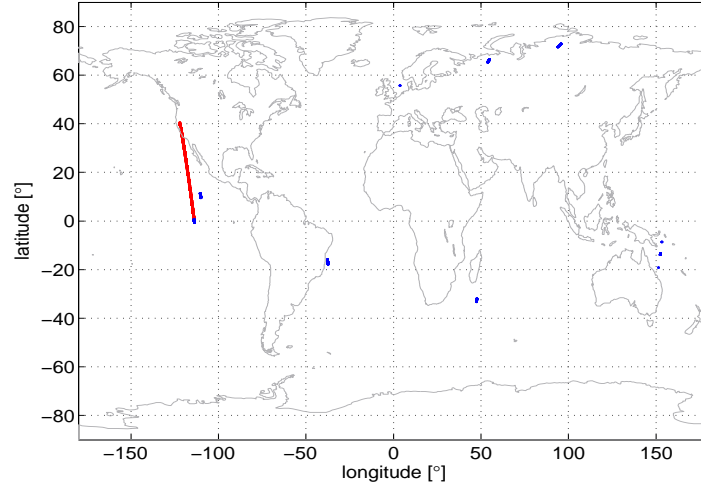
Figure 5.8: Outliers detected for the data from November 1 to December 31, 2009; Long-period outliers are given in red and short-period ones are given in blue

For comparison also the reference values from EGM2008 are included.

(a) Unfiltered
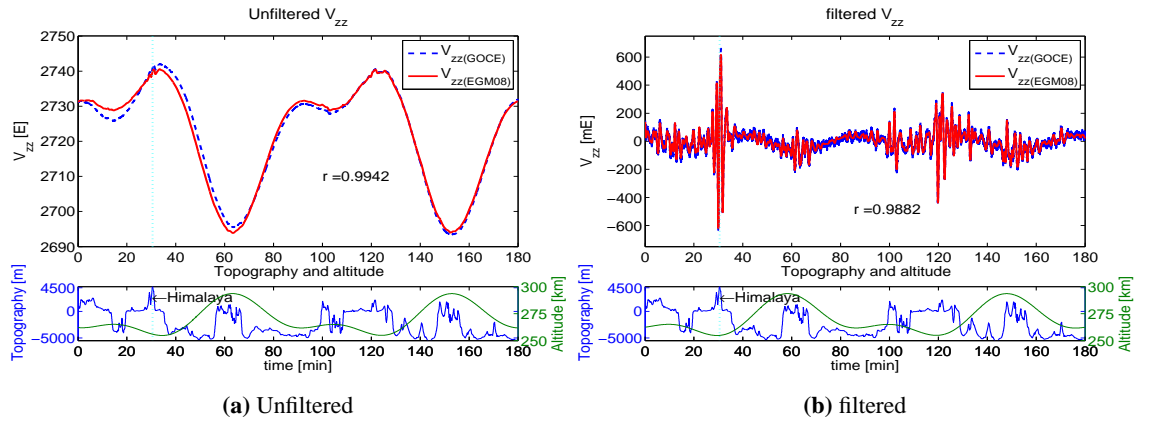
(b) filtered

Figure 5.9: Time series covering two orbit revolutions of the GOCE gradient component V_{zz} and of the corresponding values computed from EGM2008; unfiltered (left) and filtered (right); also included is the correlation between the two profiles; the lower panel shows the topographic profile along the ground track and the ellipsoidal height of the orbit (smooth curve)

The lower panel in Fig. 5.9 shows the topographic profile along this track and a smooth curve with the ellipsoidal height of the orbit. In Fig. 5.9a the unfiltered values are given. There is a small systematic difference between GOCE and EGM2008 which is caused by the gradiometer drift or the so-called colored noise. One can also recognize the signature of the Himalayas. The overall trend of both curves is anti-correlated with orbit altitude. The correlation between them is $r = 0.9942$. In order to show the detailed signal in the MB, the data is filtered with a bandpass FIR filter. The coefficients of the filter are obtained from the $((N+1)/2)$th row of a matrix $\mathbf{G}$ in Eq. (3.29), with N the length of the filter (in our case it is 5383). In order to suppress the noise at the low-frequency band, the $\sqrt{psd(f_i)}$ outside the MB is kept zero, while inside the MB the values are set to 1. A Hanning window with length 10 is applied to $\sqrt{psd(f_i)}$, before

the computation of **G**, in order to make the transition band of the filter short. In Fig. 5.9b the analysis is repeated for filtered values. Now strong signal oscillations can be observed both in the measured and computed gradients and a correlation of $r = 0.9882$ between them. A higher correlation can be found with the topographic features underneath. This behavior is also found in the other gradiometeric components.

The correlation between measured values and computed values from EGM2008 shows that the signal contains information of the Earth's gravitational field. The differences between them, namely observed minus computed values, are expected to contain the improvements of GOCE above EGM2008.

5.4.2.3 Gradiometer Data in the Frequency Domain

In order to quantify the signal content in a chosen frequency range, say from f_1 to f_2, the signal ratio (SR) is defined in our study as

$$SR(f_1, f_2) = \frac{\sum\limits_{k=\lfloor Nf_1 \rfloor}^{\lfloor Nf_2 \rfloor} \sqrt{PSD(k)}}{\sum\limits_{k=0}^{N-1} \sqrt{PSD(k)}} \tag{5.28}$$

with $\lfloor * \rfloor$ the operator of rounding to the nearest integers towards minus infinity.

The behavior of the signal in the frequency domain is important for us to know. In Fig. 5.10 the PSDs of the three diagonal gravitational gradients are shown together with their trace, based on the data from November 1st to December 31st, 2009. The MB and engineering requirements are included as well. As shown in Fig. 5.10a the white noise level is approximately 10 $\frac{\text{mE}}{\sqrt{\text{Hz}}}$ for V_{xx} and V_{yy} and 20 $\frac{\text{mE}}{\sqrt{\text{Hz}}}$ for V_{zz}. It is visible for frequencies above approximately $3.8 \cdot 10^{-2}$ Hz. We see the strong gradiometric signal power in the range from 10^{-3} Hz to $3 \cdot 10^{-2}$ Hz, towards the low frequencies more and more superimposed by the $1/f$-instrument noise, and more significantly, by orbit- and attitude-induced periodic distortions at one cpr and multiples of one cpr. A very powerful test of the instrument performance is the Laplace condition, i.e., the trace of the GGT theoretically to be zero. As shown in Fig. 5.10c the trace of the GGT is generated from the computed values at the same location and orientation based on EGM2008 up to d/o 360. It is theoretically zero and actually at the level of computer round-off and truncation error. In the measured GGT it shows the noise level of the sum of the measured diagonal gravitational gradients. The engineering requirement of the trace, based on a pre-launch analysis of the sensor performance, is 11 $\frac{\text{mE}}{\sqrt{\text{Hz}}}$ in the upper part of the MB; the actual trace is about 20 $\frac{\text{mE}}{\sqrt{\text{Hz}}}$ mainly due to the higher noise level of V_{zz}, see Fig. 5.10a. It also shows the $1/f$ increase and periodic distortions at frequencies below 5 mHz. In Fig. 5.10c, the signal ratios of the reference values are computed and shown. They are divided into three frequency ranges: 0 to 5 mHz, 5 to 100 mHz, and 100 to 1000 mHz, denoted LFB, MB, and HFB together with the SR values outside the MB in red text,

and inside MB in black or green. With the period of the orbit being 5384 seconds, the upper limit of the signal content of a coefficient of degree N in frequency is $N/5384$. Most of the signal is concentrated in the LFB, as the SRs of the four components in the LFB are larger than 96%. By comparing the measured and observed values in the frequency domain, see Fig. 5.10d, it can be found that noise dominates the signal at about $3.8 \cdot 10^{-2}$ Hz. This corresponds to a maximum d/o of a spherical harmonic expansion of about $n \approx 205$. However, this does not mean GOCE can only achieve d/o 205. Since the gravity field coefficients of high d/o contain low-frequency signal as well, high degree coefficients can be recovered with GOCE measurements by making use of their information at frequencies below $3.8 \cdot 10^{-2}$ Hz.

(a) of measurements

(b) the same confined to the MB

(c) of modelled values

(d) Comparison of measured and EGM2008 PSD$^{1/2}$s for V_{xx} and V_{zz}
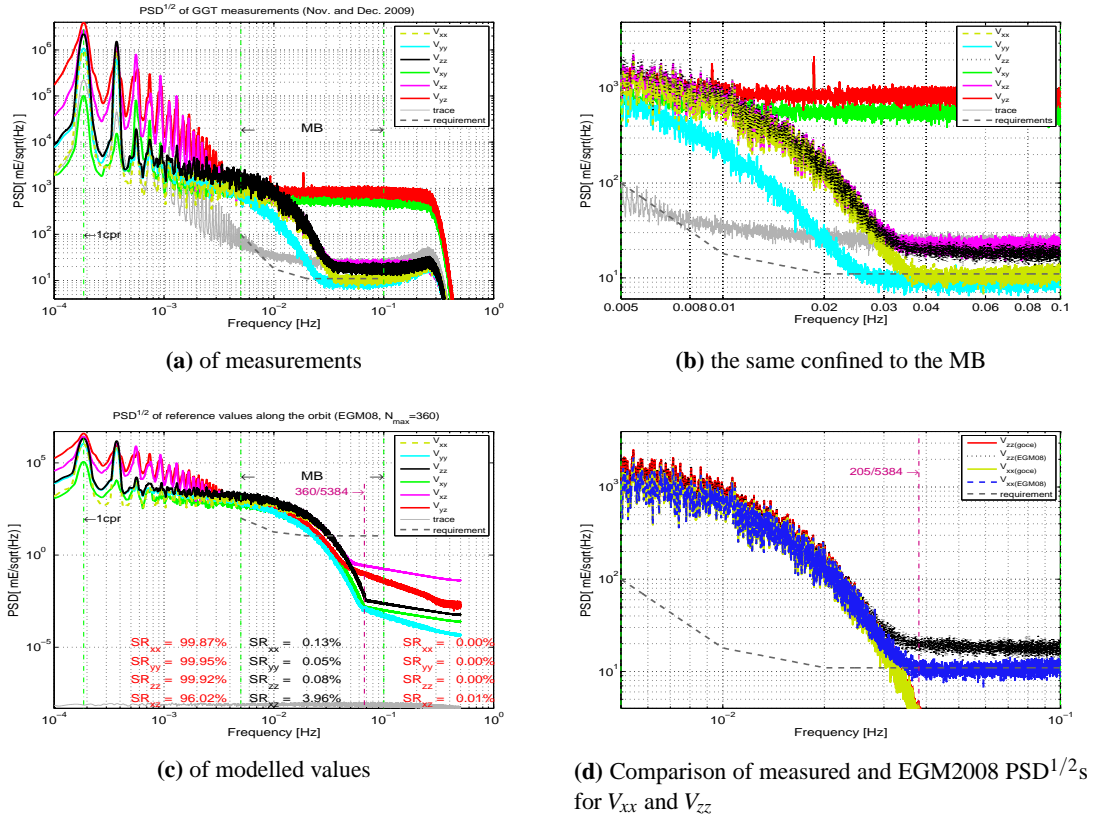
Figure 5.10: PSD$^{1/2}$s from 2 months of data of GGT components and the trace values of the GGT; also shown is the engineering requirement for the trace, the MB and the once-per-revolution (cpr) frequency.

As an example to show the SR of individual SH coefficients, in Fig. 5.11, the PSD$^{1/2}$s of the signals from some selected individual coefficients are presented. The values are computed along the orbit and rotated to GRF. The superimposition of the contribution of all gravitational field coefficients results in the gravitational signals as shown in Fig. 5.10c. In addition to the upper limit corresponding to each individual coefficient, three facts can be found: Firstly, there is low-frequency signal coming from the high d/o coefficients. But it is difficult to use because of the complicated colored noise structure at the LFB. Secondly, the magnitude of the signals from

individual d/o coefficients is much smaller than the noise requirement, which is roughly the same as the actual noise level of the gradiometer. Thirdly, as example, the SR for degree 155 and 215 in the MB is greater than that outside of the MB; for degree 25 the SR is concentrated in the LFB. As expected, the signal of lower degree coefficients is concentrated at lower frequencies and outside the MB of the gradiometer.

(a) $C_{155,0}$

(b) $C_{155,155}$ and $S_{155,155}$

(c) $C_{25,0}$

(d) $C_{215,215}$ and $S_{215,215}$
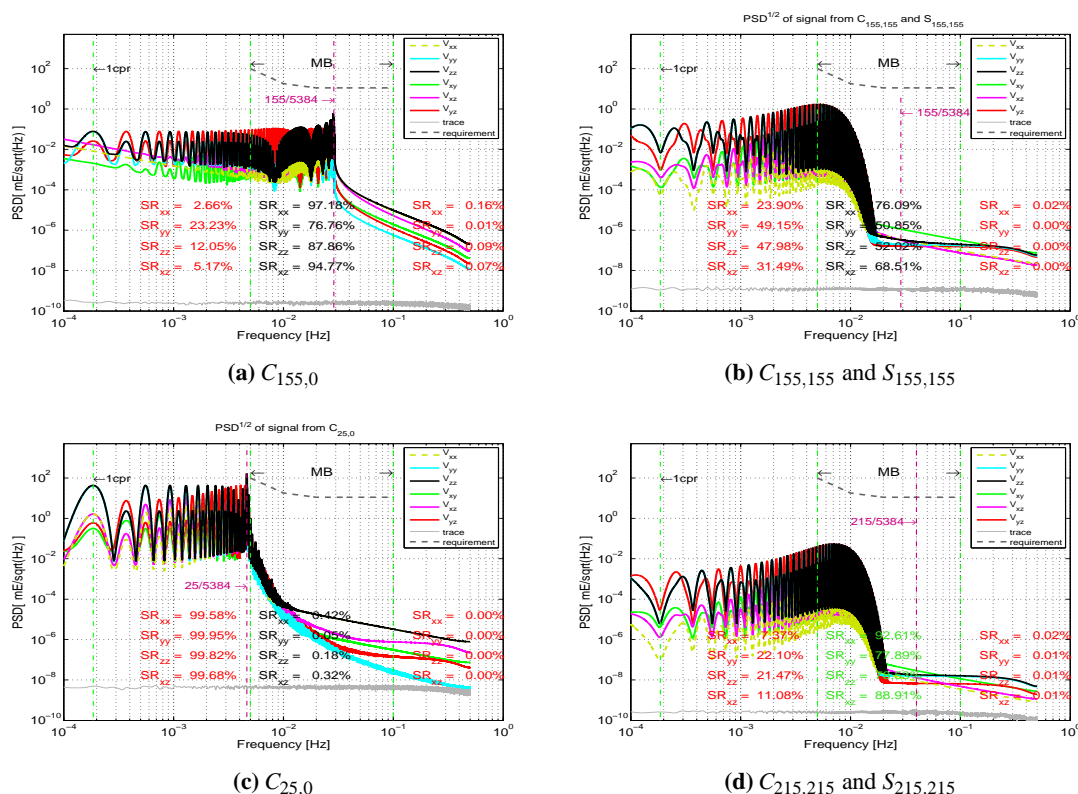
Figure 5.11: PSD$^{1/2}$s computed from the modelled values with signal of individual SH coefficients

5.4.2.4 Gradiometer Data in the Space Domain

In order to look into the data geographically, they need to be geo-located and plotted on a global map. Due to the presence of the noise outside the MB, the data has to be filtered before geo-location. The same filter is applied to all the data as the one used for data analysis in the time domain described in section 5.4.2.2. In Figs. 5.12 to 5.17 all the measured components are shown on global maps.

Each map shows the values on a global grid with a resolution of $15' \times 15'$, interpolated from filtered gradients based on triangle-based linear interpolation (Watson, 1992). The left- and right-hand side of the figures is based on the measurements of the ascending and descending passes, respectively. For V_{xx} and V_{yy} one can see significant differences between ascending and descending, due to the large difference in orientation between ascending and descending tracks, see Fig. 5.12 and 5.13. In the case of V_{zz} the maps of ascending and descending tracks almost coincide, because

the orientation of the z-axis is not so different for the two cases, see Fig. 5.14. V_{xy} and V_{yz} are the weak components. However, after removing the outliers still some characteristic gradient values show up in mountainous regions, as shown in Fig. 5.15 and 5.17. The V_{xz}-component (Fig. 5.16) is the only accurate off-diagonal component. High correlation with tectonic features appears in the gradient maps. Figure 5.18 displays the difference between $V_{zz(GOCE)}$ measured by the GOCE gradiometer and $V_{zz(EGM08)}$ computed from the gravity model EGM2008 up to degree and order 215 for comparison. EGM2008 is a so-called combined gravity field model. It combines the GRACE gravity field model ITG-GRACE03S up to degree and order 180 with carefully selected worldwide terrestrial and altimetric data sets. The global root-mean-square (RMS) of these differences is 6.56 mE. Six regions are marked. Three are known to have good terrestrial gravity data (North America, Europe, Australia), and the RMS values for these regions agree well with the global RMS. Three other regions are known to have partly poor or inconsistent data. The RMS values in these regions are between 8.98 and 12.57 mE at satellite altitude. The same phenomenon can be found in the other components.

(a) Ascending
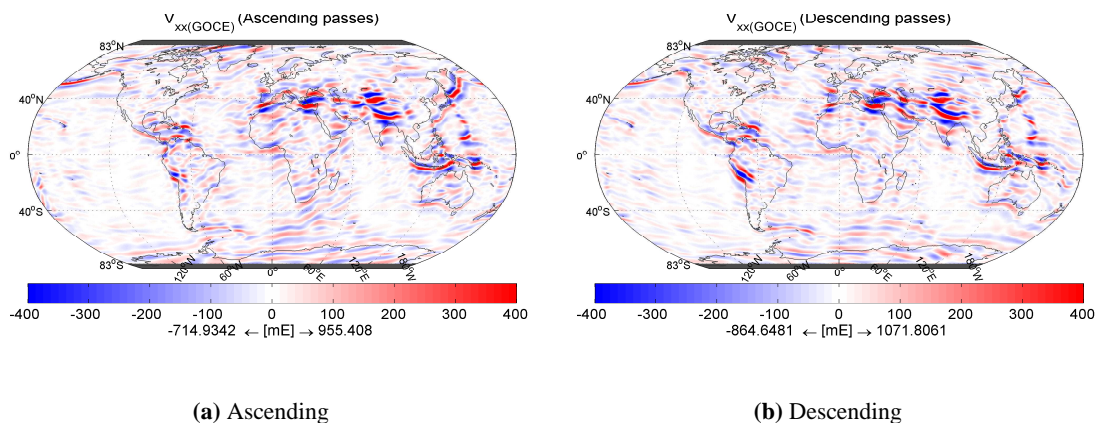
(b) Descending

Figure 5.12: Global map of the gradient component $V_{xx(GOCE)}$: Ascending tracks (left) and descending tracks (right); significant differences are visible due to the different orientation of the x-axis of the GRF for ascending and descending tracks

A check of the Laplace condition is shown in Fig. 5.19. The sum of the three diagonal gradients is taken in every point of the global grid. The values show no larger systematic effects and a standard deviation of about 14 mE.

From the presented results, one can see that GOCE provides gravity information in the MB with good quality. The trace in the MB is globally homogeneous, except for anomalous areas over the North and South Magnetic Poles, as shown in Fig. 5.20.

This anomalous behavior is due to the V_{yy} component (Stummer et al., 2011). It is caused by the strong cross winds (Lühr et al., 2007) over the Magnetic Poles, especially for the ascending tracks. As shown in Fig. 5.21, the Earth rotates from the west to the east and the ascending tracks always correspond to local time at about 6 p.m. The atmosphere and ionosphere move from the hot hemisphere with high solar radiation (day) to the cold hemisphere with no solar radiation (night).

(a) Ascending
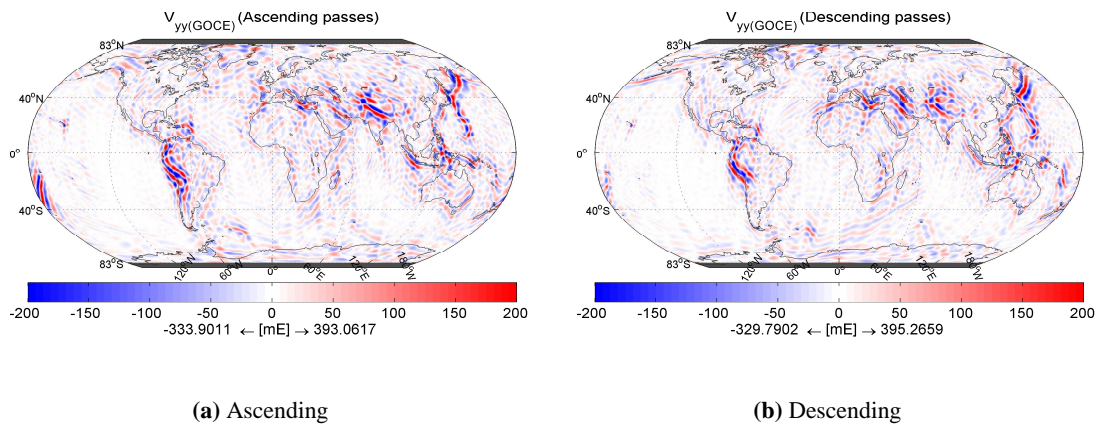
(b) Descending

Figure 5.13: Global map of the gradient component $V_{yy(GOCE)}$: Ascending tracks (left) and descending tracks (right); again significant differences are visible due to the different orientation of the y-axis of the GRF for ascending and descending tracks

(a) Ascending
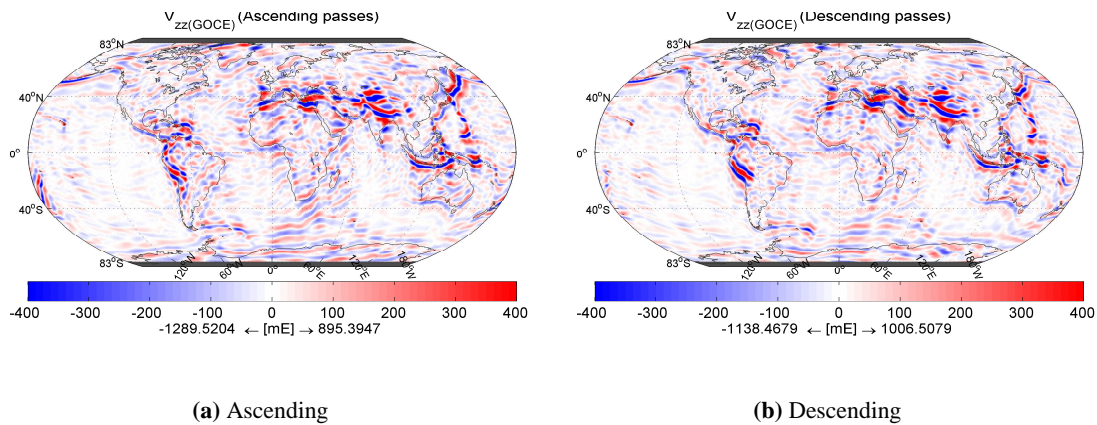
(b) Descending

Figure 5.14: Global map of the almost vertical gradient component $V_{zz(GOCE)}$: Ascending tracks (left) and descending tracks (right) agree well

(a) ascending
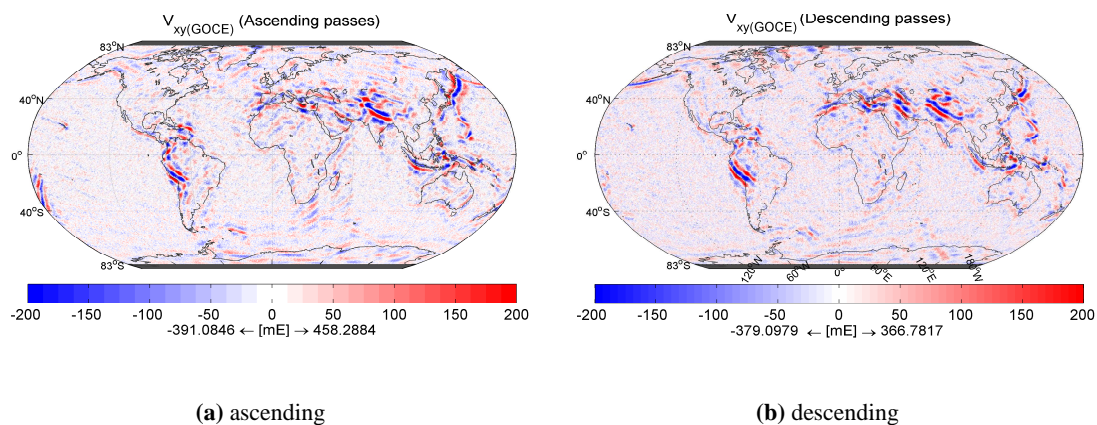
(b) descending

Figure 5.15: Global map of the weak component $V_{xy(GOCE)}$ for ascending (left) and descending (right) tracks; after the removal of outliers signal structures become visible

(a) ascending   **(b)** Descending
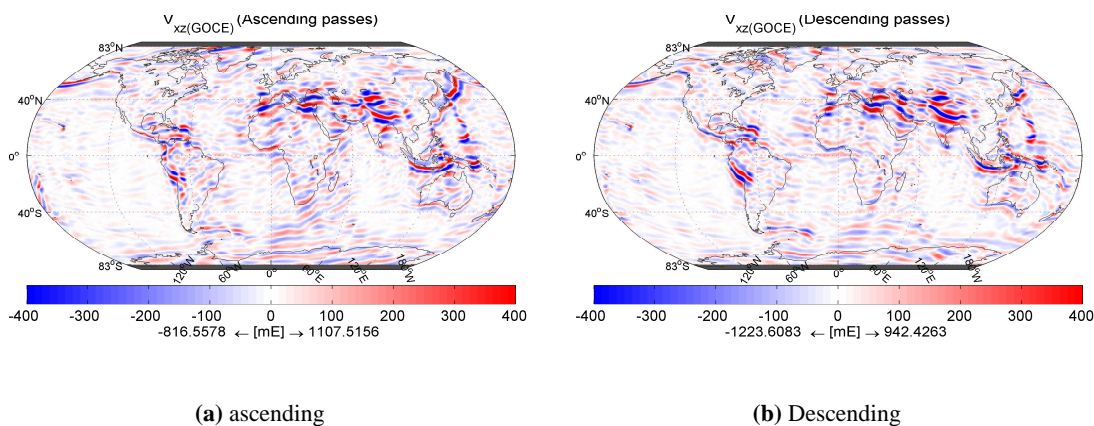
Figure 5.16: Global map of the accurate off-diagonal component $V_{xz(GOCE)}$: Ascending tracks (left) and descending tracks (right)

(a) ascending   **(b)** Descending
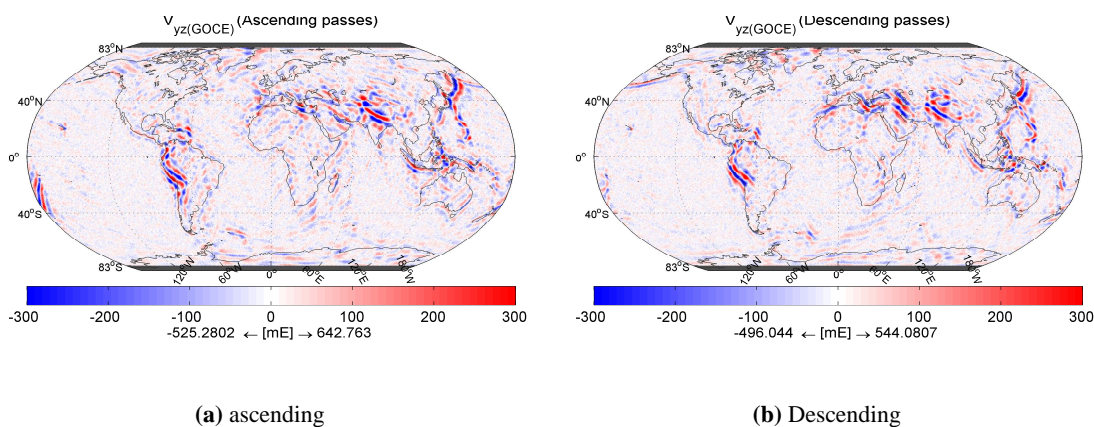
Figure 5.17: Global map of the weak off-diagonal component $V_{yz(GOCE)}$: Ascending tracks (left) and descending tracks (right), after removal of outliers signal structures become visible

(a) ascending   **(b)** descending
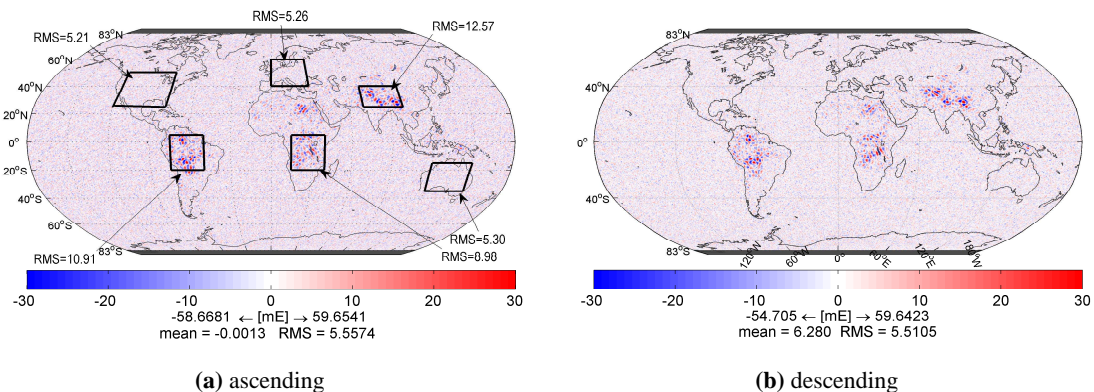
Figure 5.18: Global map of the differences between $V_{zz(GOCE)}$ and $V_{zz(EGM08)}$ for ascending (left) and descending (right) tracks. Also included are 3 areas with good terrestrial gravity and 3 areas with poor terrestrial gravity as well as their RMS differences.

(a) ascending
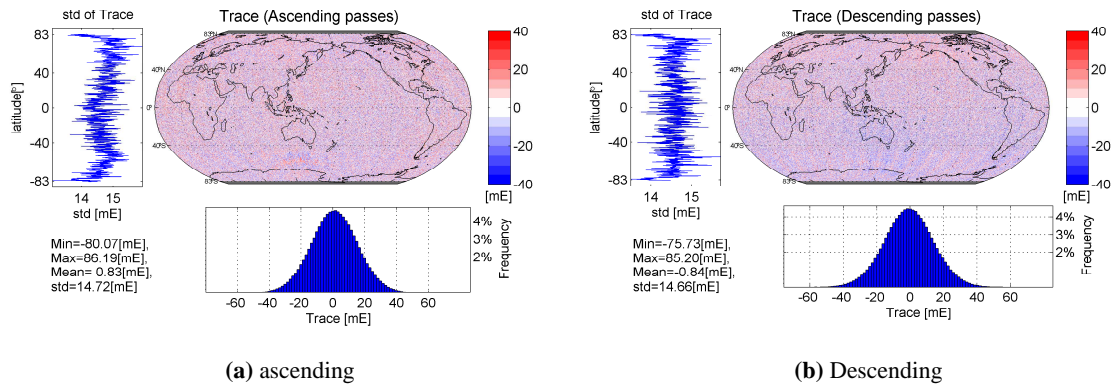
(b) Descending

Figure 5.19: Global map of trace of the measured GGT

(a) North Magnetic Pole (85°N 132°W)

(b) South Magnetic Pole (64°S 137°E)
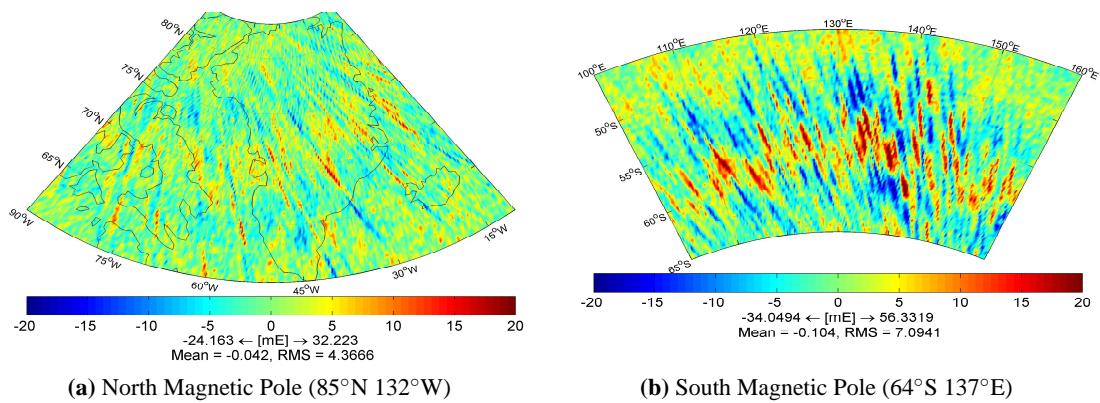
Figure 5.20: Anomalous observation in V_{yy} components over North (a) and South Magnetic Poles (b) for ascending tracks, over the period of November and December 2009.

At the Magnetic Poles the activity of the ionosphere is quite strong, which leads to strong cross winds at these locations. The descending tracks correspond to the local time at about 6 a.m., when the ionosphere rotates from the cold side to the hot side. There the effect is smaller. In case the gradiometer is not perfectly calibrated (not perfectly scaled), the common acceleration on the two accelerometers forming the V_{yy} component is not perfectly eliminated when taking the difference. The effect on V_{yy} is higher because this axis points in the direction of the cross winds. A more detailed discussion can be found in (Peterseim et al., 2011).
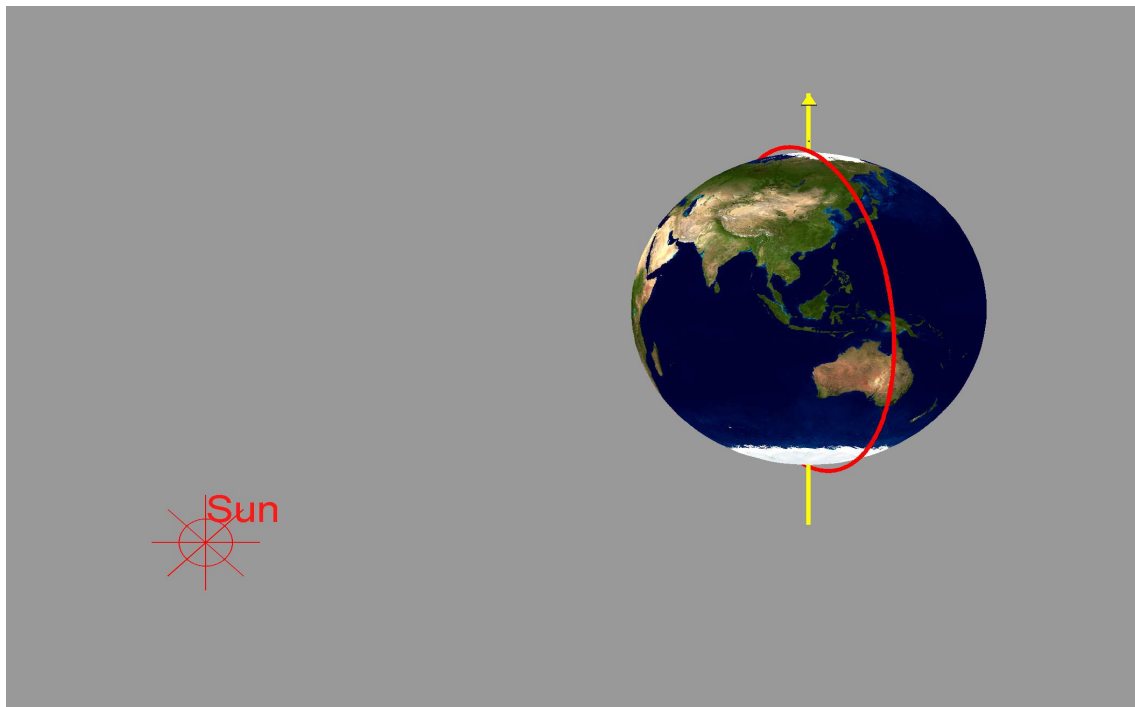
Figure 5.21: Geometry of the GOCE orbit and the sun

5.4.2.5 Modeling the Lower-Frequency Errors

We are now analyzing the gradiometric error behavior at lower frequencies, i.e. below the MB. The noise of the gradiometer comes from, in principle, two categories, the accelerometer noise and the noise from the uncertainties of orientation, angular velocities and angular accelerations. The accelerometers exhibit a typical $1/f$ error behavior, also denoted flicker noise in the literature. In the time domain this $1/f$-behavior is observed as accelerometer drift. The drift behavior is different for each accelerometer. Thus it is not (perfectly) removed when taking the gradiometric difference. The effect of angular motion is required to be precisely removed from the DMA in the MB. However at the LFB, the angular motion (especially the angular velocity or centrifugal part) is not guaranteed to be reconstructed with high accuracy. For more details about the angular velocity of the GOCE accelerometer measurements, we refer to (Rummel et al., 2011; Stummer et al., 2011).

5. GOCE GRAVITATIONAL GRADIOMETRY AND SPHERICAL HARMONIC ANALYSIS

As shown in Fig. 5.22, the observed gradients minus computed values at the same location in the same orientation vary with 1-cpr frequency, modulated by some multiples and at once per day (1-cpd) and multiples of 1-cpd as well. Possible explanations for this behavior are either the modulation due to cyclic orbit and attitude effects of the low-frequency systematic error behavior of each of the gradiometer components and the imperfect removal of the contribution of the angular rates. It is shown in Stummer et al. (2011) that a significant part is produced by the latter effect. One can see that the variation in V_{xx} and V_{zz}, which are derived by removing the rather high angular motion about the y-axis from the DMA in the {xx} and {zz} components, are larger than the variation of V_{yy}, which does not contain high contribution of the angular motion about the y-axis. This gives us a hint that the angular motion, especially the angular velocity, are not determined as precisely in the LFB as in the MB. The low-frequency error contains therefore the lower-frequency noise of the gradiometer as well as the residual of the angular motion which could not be removed from the differential mode accelerations. It is a crucial hint of how to handle the lower-frequency error. It can be either filtered or modelled.
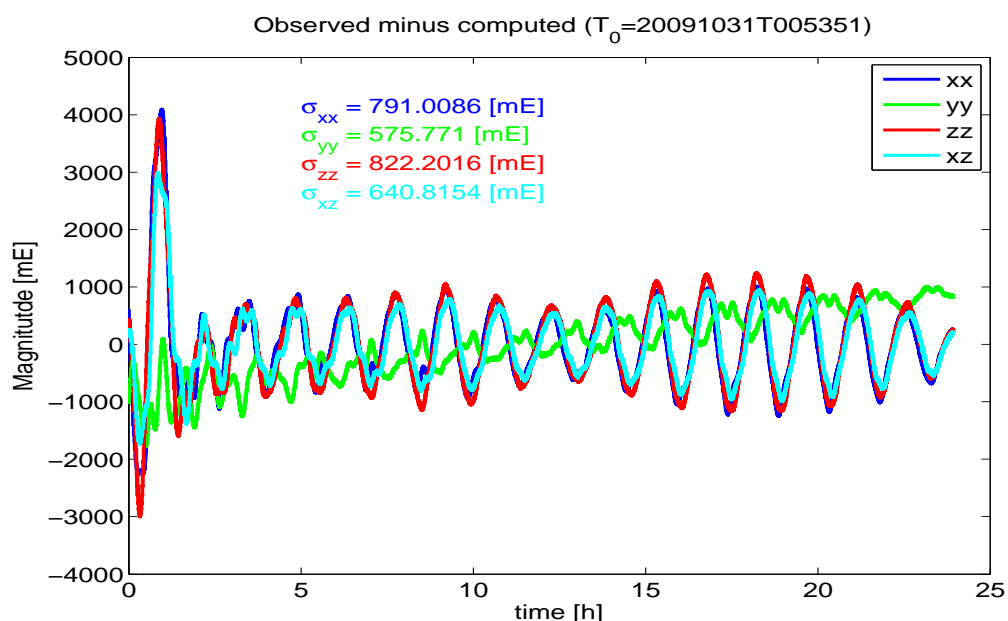
Figure 5.22: observed minus computed values in October 31st, 2009

Two approaches can be applied to model the low frequency error. One is in the time domain, e.g., with piecewise polynomials applied to short segments (e.g., 1 minute to 10 minutes), or in the frequency domain by modelling the low-frequency error by Fourier expansion.

To model the low frequency error with polynomials, the OMC values are parameterized in such a way that for the whole data span, the empirical parameters 1-cpd, 2-cpd, 1-cpr and 2-cpr are introduced, and for each short time interval, in addition a constant and a linear term. The criterion of the lower frequency modelling is that the information in the MB should not be affected

by the modelling parameters. As shown in Fig. 5.23, the $PSD^{1/2}$ of the original OMC values and of the values after removing a piecewise polynomial of varying lengths from the original OMC demonstrates that a polynomial with a time interval of 60 seconds absorbs some information in the MB; with an interval of 180 seconds the result is reasonable, which corresponds to $1/180 \approx 5.5$ mHz, and is more or less at the lower limit of the MB; with longer time intervals the low-frequency part cannot be modelled well enough. When comparing the $PSD^{1/2}$ of the original OMC and the $PSD^{1/2}$ of the residual OMC after removing the modelled signal of a time interval of 300 seconds, 450 and 600 seconds, some distortions can be found in the figure. One must apply some constraint for the smoothness at the boundary epochs for a better performance.
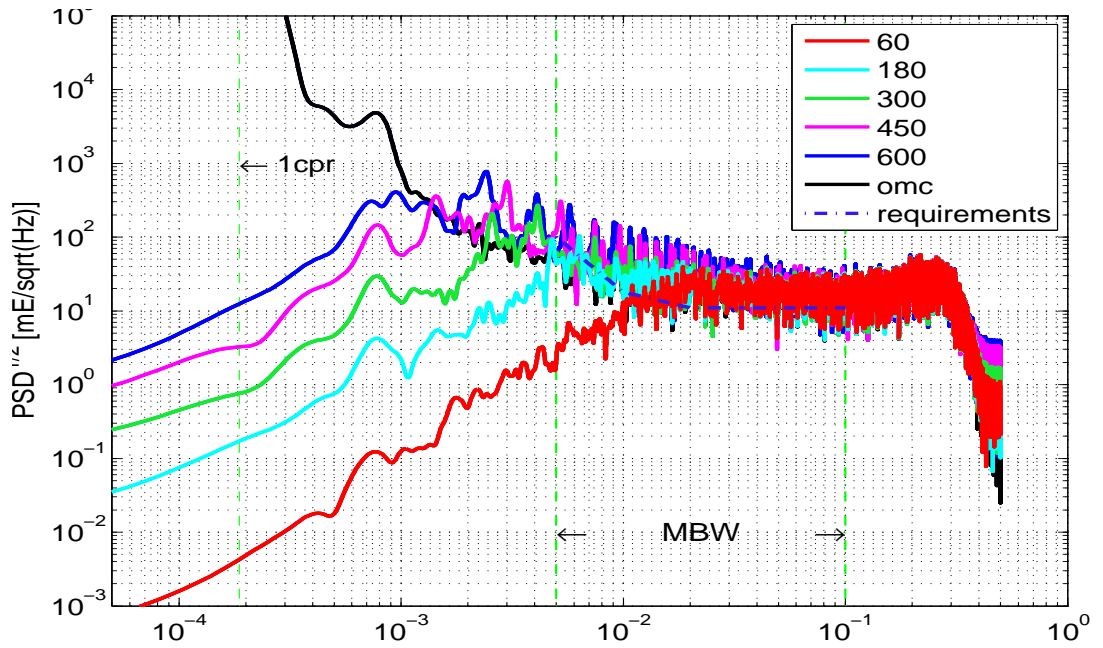
Figure 5.23: $PSD^{1/2}$ of the OMC of V_{zz} after removing the low frequency error with piecewise polynomial modelling, different time periods for a polynomial of order 1 are applied. The unit of the number in legend is second

An alternative to the polynomial is Fourier expansion for the low-frequency error modelling. At least two advantages of the Fourier function for this issue are (1), the continuity of the measurements is maintained and (2) the signal in the MB can be well preserved, by setting no parameter at the frequencies in the MB. In Fig. 5.24, on the left hand side (Fig. 5.24a) the $PSD^{1/2}$ of the original OMC of V_{zz} is shown in red, and after removing the lower-frequency part in blue, and the parameters (in gray cross dot) corresponding to the magnitude of the signal in pre-defined frequencies together with the $PSD^{1/2}$ of the time series reconstructed from the parameters (in cyan); on the upper panel of the right-hand side (Fig. 5.24b) the original OMCs are displayed in red and after modelling as a time series in the time domain they are expressed in blue. As shown in Fig. 5.24a, the frequencies chosen for this purpose are 1-cpd and multiples of 1-cpd, 1-cpr and multiples of 1-cpr, as well as some frequencies close to multiples of 1-cpr, see the gray cross-dots

in the figure. By comparing the curves in blue and red, one can see that the influence of the LFB part is removed. The cyan dashed line is the square root of PSD of the modelled low frequency part. It can be found that it does not absorb any information at the frequencies higher than about 600 mHz. The STD values before and after modelling are 822.2 mE and 13.9 mE, respectively, cf. Fig. 5.24b. Because this procedure is linear, this modelling can be applied directly to the observed and computed values. The lower panel in Fig. 5.24b shows the differences. As one can see, the differences are less than 5×10^{-7} mE. We can therefore conclude that the modelling works with very good accuracy.
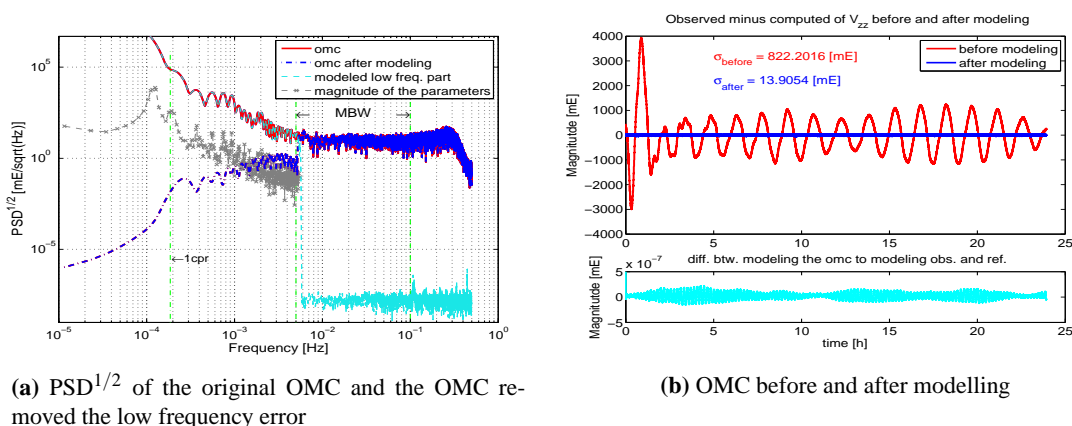
(a) $\text{PSD}^{1/2}$ of the original OMC and the OMC removed the low frequency error

(b) OMC before and after modelling

Figure 5.24: Modeling of low-frequency error presented in the frequency and in the time domain, based on the values in {zz} component of one day

After removing the low-frequency part with the Fourier expansion shown in Fig. 5.24, the short wavelengths of the gravity field signals are pronounced in the gradients. As an example, the V_{zz} component is shown in Fig. 5.25, with ascending tracks on the left (Fig. 5.25a) and descending tracks on the right (Fig. 5.25b). The maximum and minimum values are 1006.96 mE and -1262.9 mE, respectively. The gravity features are very close to the behavior in Fig. 5.14.

From the experiments above, one can see that modelling the lower-frequency part of the data behaves as filtering. The ideal case would be that the mis-behavior of the low-frequency part is eliminated completely, and that the signal in the MB is not affected by this modelling. In a second step, the eliminated part can now be analyzed and interpreted. However, there is also some noise in the HFB. This higher-frequency part is difficult to model with this idea. We do not pursue this idea of modelling but instead we apply filtering in the context of the SHA.

5.5 Spherical Harmonic Analysis from SGG Data

From the analysis of the previous sections, we know already that the gradiometer data do contain gravity field signal. In this section, SHA is applied to the individual gradiometer components and

(a) Ascending
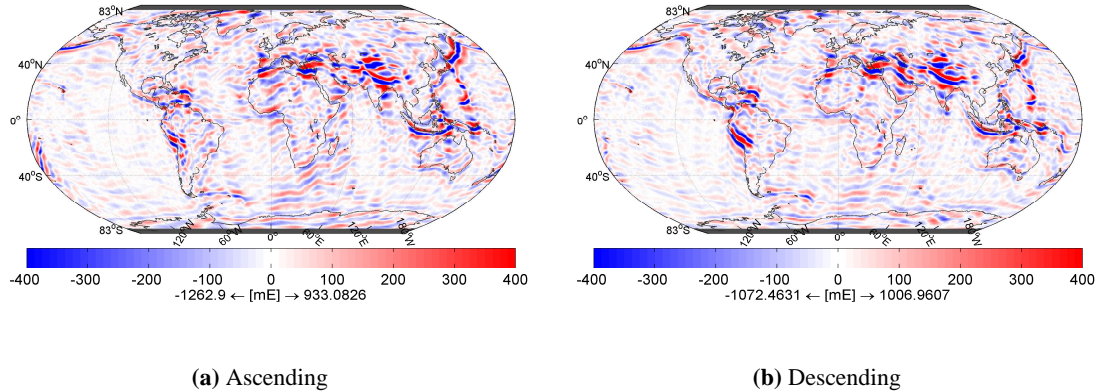
(b) Descending

Figure 5.25: Global map of component $V_{zz(GOCE)}$: Ascending tracks (left) and descending tracks (right); after removing the low-frequency error by modelling with Fourier functions, the similarity can be found by comparing to Fig. 5.14

their combination. The data of the four precise components are used for SHA. Using only individual components and only the gradiometer data, and in the presence of the polar gap, some parts of the coefficients cannot be well recovered. With the intermediate results of individual components, we will analyze degree medians, coefficient differences and formal errors in triangular form in this section. The complete analysis of the solution will be given after combination with SST and after applying some constraint over polar areas in Chapter 6.

We want to see the information content and characteristics of each gradiometer component. The different components in the GGT map the gravity field under different angles. With SHA, the behavior of each component will appear.

Instead of 61 days of data used in the previous section, the measurements of the four precise components over the period from November 1st 2009 to April 30th 2011 are used in this section as input for SHA. The data sampling is one second. The experiment is to estimate gravitational field models up to d/o 215 using a bandpass filter for data de-correlation of each of the accurate gradiometer components and their combination.

5.5.1   Filters used for SHA

If the weight matrix in Eq. (3.5) can be determined precisely, the observations can be decorrelated and an optimal solution be obtained. However, for the present least squares problem, the dimension of the weight matrix is so large that not only the computation cost would be very high, but also the memory space for saving this matrix is not sufficient even with supercomputers. In principle, the weight matrix is not a full matrix, but a band matrix, for a stationary error behavior, see Fig. 3.2b. Thus, a filter with limited length, either finite impulse response (FIR) or infinite impulse response (IIR), can be applied to the data. As described in section 3.4, for filtering the design matrix during parameter estimation, it is desirable to use an IIR filter due to its low computation load, by using not only input values, but also filtered values of the past (in terms of autoregressive).

5. GOCE GRAVITATIONAL GRADIOMETRY AND SPHERICAL HARMONIC ANALYSIS

The filter used in this study for SHA is a bandpass filter, with length 9 for both autoregressive and moving average parts, i.e., an ARMA(9,9) model, and with warming-up time 5400 seconds. In Fig. 5.26, the frequency and phase responses (Oppenheim and Schafer, 2009) of the bandpass filter are displayed. The bandpass filter extracts the signal inside the MB, with its frequency response shown in the figure. The decibel (dB) is given by

$$L_{\text{db}} = 10\log_{10}\left(H(f)\right), \tag{5.29}$$

with $H(f)$ the frequency response of the filter. From the upper panel of Fig. 5.26, it can be seen that the filter suppresses not only the lower-frequency noise outside of the MB, but also the higher-frequency part. The phase response is almost linear for the frequencies from 5 to 100 mHz, as shown in the lower panel of the figure.
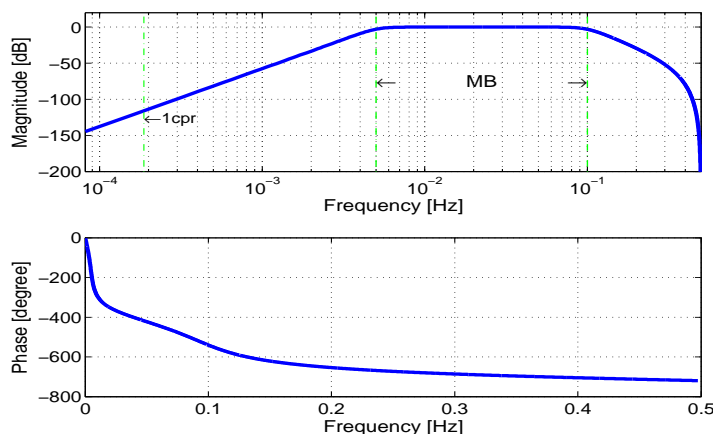
Figure 5.26: Frequency and phase response of the highpass filter applied for SHA.

5.5.2   Result Analysis of SHA

With the available SGG data, based on the observation model, i.e. Eq. (5.19) and filtering the design matrix and the observations as well as the reference values, gravitational field models are computed for different components of the gradiometer by solving the least square problem. After filtering four additional parameters are used to remove the constant offset, linear trend and 1-cpr behaviors from the observation equations for each component per day. In principle, these features of signals or errors are removed by filtering. This consideration serves as a back-up for the case that the filter does not completely remove these behaviors. In our results these parameters are indeed very small and negligible. These four parameters for each component are pre-eliminated before the normal equations are stored and solved. With this consideration and the measurements of the four accurate components, i.e., V_{xx}, V_{yy}, V_{zz} and V_{xz}, four gravitational field models are obtained.

The flow chart of the SHA for one day of GGT data is shown in Fig. 5.27. The geo-location is realized by time synchronization between PSO_PRD_2I and EGG_GGT_2C, the partials of GGT to gravitational field coefficients are computed in the ECEF and then rotated to the GRF, according to Eq. (5.18). Overlapping segments of 5400 seconds are applied for warming-up of the filter, in order to ensure the continuity of filtering. The observation equations are then constructed in the GRF and both the design matrix and the measurements together with the reference values are filtered into the desired frequency range with the same bandpass filter, cf. Fig 5.26. The normal equations, i.e. Eq. (3.7), are computed and saved according to our defined format. By accumulating (or combining) more than one day's normal equations, more and more information is added to the system and the results are obtained by solving the accumulated normal equations.

```
┌─────────────┐  ┌─────────────┐  ┌─────────────┐
│ PSO_PRD_2I  │  │ EGG_GGT_2C  │  │ EGG_IAQ_2C  │
└─────────────┘  └─────────────┘  └─────────────┘
            │            │                │
            ▼            ▼                │
        ┌─────────────────────┐          │
        │   geo-location &    │          │
        │   synchronization   │          │
        └─────────────────────┘          │
                    │                     │
                    ▼                     ▼
        ┌─────────────────────────────────────┐
        │        rotate partials to GRF        │
        └─────────────────────────────────────┘
                    │
                    ▼
        ┌─────────────────────┐
        │ obs. equation &     │
        │ filtering           │
        └─────────────────────┘
                    │
                    ▼
        ┌─────────────────────┐
        │ compute N = AᵀPA    │
        │ & AᵀPd, save        │
        └─────────────────────┘
```
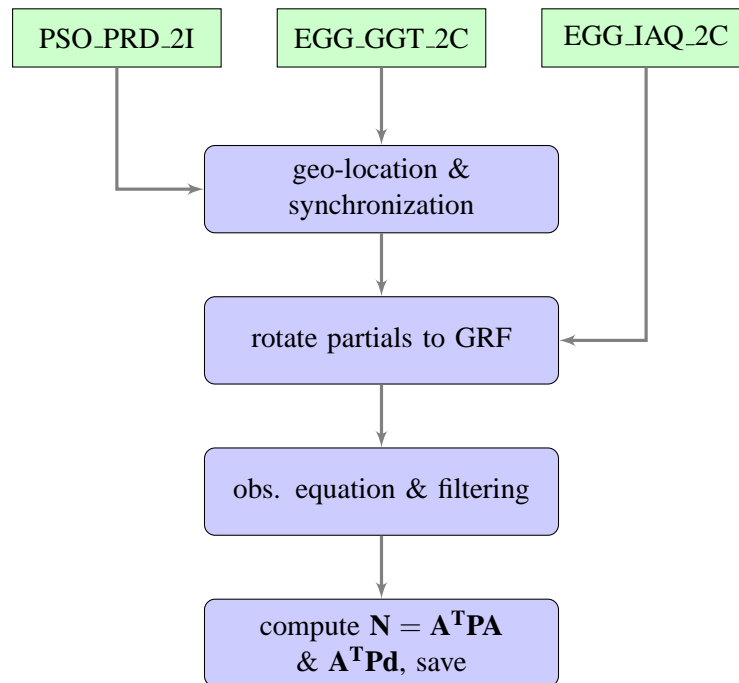
Figure 5.27: Flow chart of SHA with SGG data

The coefficient differences between gravitational field models recovered from the measurements of each individual of the accurate components and EGM2008 are presented in Fig. 5.28 up to d/o 215. Correlations can be seen in the coefficients of order 16 and multiples of 16, which is the number of revolutions of the GOCE orbit per day. Less precision can be found in the low degree coefficients due to the lower sensitivity of the gradiometer there, and in the zonal and near zonal coefficients due to the polar gap. From the coefficient differences and the formal error, one can observe that the lower order coefficients (close to zonal) estimated with the V_{xx} component are more accurate than the higher order ones; the coefficients of higher order (close to sectorial) estimated with V_{yy} component are more accurate than the lower order ones. Thus V_{xx} and V_{yy} are complementary, and their combination will result in the same behavior (i.e. homogeneity) as V_{zz} due to the fact that $V_{xx} + V_{yy} = -V_{zz}$. The result of the V_{zz} component is more homogeneous than

those of V_{xx} and V_{yy}. Due to its z-component, V_{xz} is more isotropic than V_{xx}, but due to its x-component less homogeneous than V_{zz}. For a more detailed description of isotropic combinations, it is referred to (Sneeuw, 2000).

The formal errors of the recovered gravity models in Fig. 5.29 show the characteristics of the individual components. The errors of the lower degree coefficients are quite large, which means gradiometer data are not capable of determining the long wavelength gravity information. The zonal and near-zonal coefficients are not determined with high accuracy due to the existence of the polar gap. This behavior is shown up in Fig. 5.28, too. The homogeneity of V_{zz} and the characteristics of the other three components are similar to the coefficients differences with EGM2008 shown in Fig. 5.28.

(a) V_{xx}

(b) V_{yy}

(c) V_{zz}

(d) V_{xz}
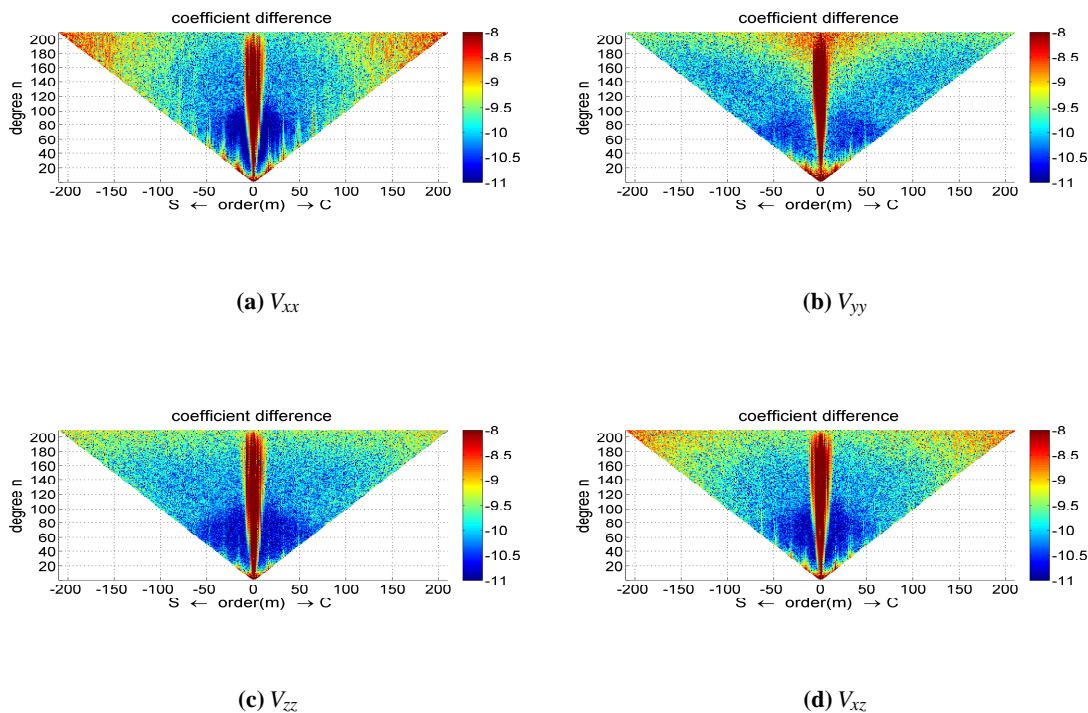
Figure 5.28: Coefficient differences between EGM2008 and recovered models from individual components up to d/o 215 (log10 scale)

The degree median values (Sneeuw, 2000) of these models compared to EGM2008 with each individual component estimated separately are presented in Fig. 5.30. One can find that the component V_{zz} is the most consistent to EGM2008, its formal errors and the deviation from EGM2008 of the coefficients are smaller than those of the other components. At higher degrees the coefficients recovered from V_{yy} are closer to EGM2008 than those from the V_{xx} and V_{xz}, whereas at lower degrees (lower than d/o about 50) V_{yy} is the poorest. The SGG-combined solution (SGG in the figure marked in black) is much closer to EGM2008, and its formal error is, as expected, smaller than that of each of the individual components .

(a) V_{xx}

(b) V_{yy}

(c) V_{zz}

(d) V_{xz}
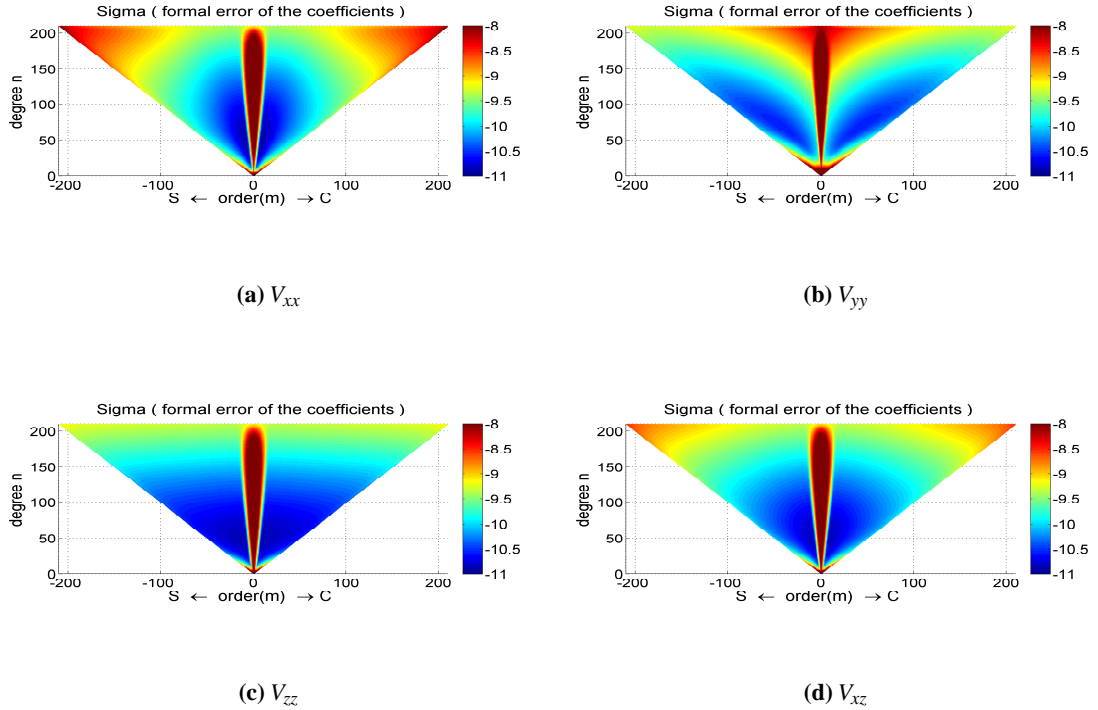
Figure 5.29: Formal errors of the recovered models from individual components up to d/o 215 (log10 scale)
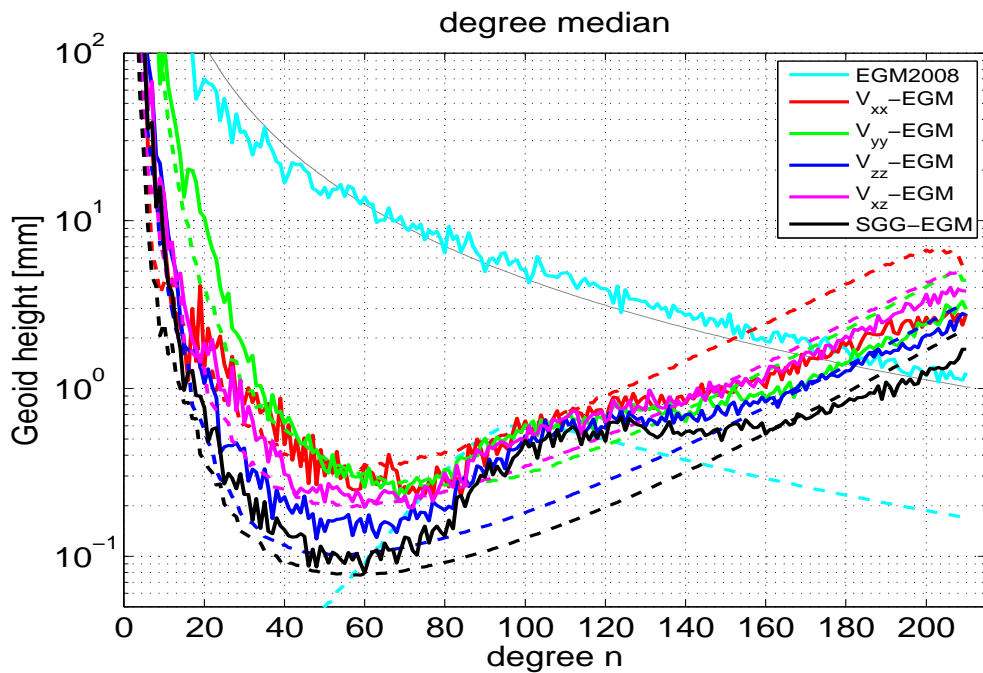
Figure 5.30: Degree median of the models compared to EGM2008, with dashed line the formal errors

The accuracy of the terrestrial data used for determination of EGM2008 is not homogeneous, which leads to some systematic differences when comparing our models to EGM2008, as shown in the coefficients of d/o about from 70 to 150 in Fig. 5.30. In Fig. 5.31, the degree medians of our solutions are compared to ITG-Grace2010s. Again they show good consistency between our solution from d/o about 40 to 150. The large differences in the low degrees show the poor performance of SGG at lower degrees. It can be taken care of by combining with SST. At degrees above 150 GOCE exhibits a lower error level than GRACE by comparing the black and cyan dashed lines in Fig. 5.31. It should be mentioned that in these comparison, the external gravity field (EGM2008 or ITG-GRACE2010s) may be better or worse than GOCE.
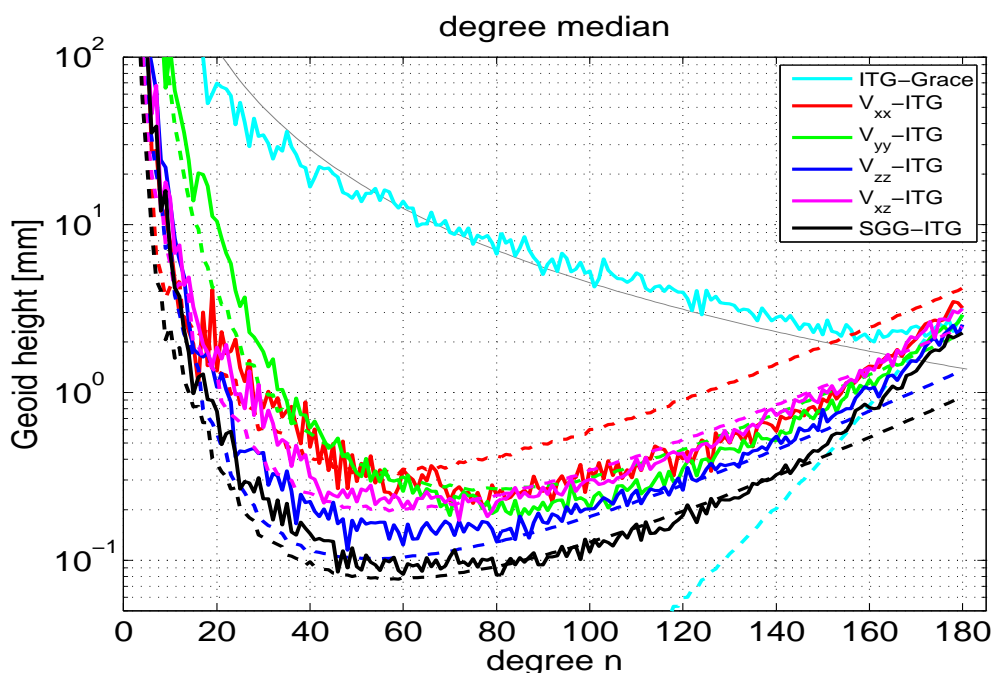
Figure 5.31: Degree median of the models compared to ITG-Grace2010s, with dashed line the formal errors

The intermediate results are obtained from each individual component in GGT. They are not accurate at lower degrees. Apart from that, the polar gaps make the zonal and near-zonal coefficients highly correlated. It is therefore not meaningful to analyze these models in terms of geoid height differences.

5.6 Summary

The observation equations of the measured gravity gradients used for this study are formulated in the GRF. They are connected to the SH expansion in the ECEF by rotating the design matrix and the right hand-side to the GRF based on the EGG_IAQ_2C product and the SOFA package. This avoids rotation of the measurement tensor components and therefore guarantees that the

less sensitive components do not degrade the results. Furthermore, it is possible to analyze each individual component independently.

The magnitude of the time varying signal in gravitational gradients at the location of the GOCE satellite, from large to small, are solid tides, the direct tidal attraction of the moon, ocean tides, the direct tidal attraction of the sun, and short variations of atmosphere and ocean, based on the mean values of these gradients caused by these effects computed along the orbit. The ocean tides and A&O have highest power in the MB, but still much smaller than the requirement. These effects are taken care of by models. In general, the time-varying effects are smaller than the sensitivity of the gradients as measured by GOCE.

The outliers are detected based on two strategies. One is based on the deviations of the trace values and of the OMCs from their mean value. If these deviations are outside of three sigma, they are assumed to be outliers. The second strategy is the computation of the moving STD of the trace and the OMC. If they are larger than the defined threshold values, we assume the measurements involved in the moving STD-computation to contain outliers.

From the $\text{PSD}^{1/2}$s of the signals corresponding to individual d/o coefficients, we showed the high degree coefficients to contain low frequency signal, but no signal at the frequencies higher than the product of degree and orbit frequency (1/5384, with 5384 the orbit period).

High correlations are found between the measurements and the modelled values computed along the GOCE orbit and based on a reference gravitational field model (in our case EGM2008). High signal variations are found in areas of rough topographic changes. In the frequency domain, the $1/f$ behavior of the measurements appears in the $\text{PSD}^{1/2}$ values at frequencies less than 500 mHz down to zero. The signal-to-noise ratio (SNR) equals one at a frequency of about $3 \cdot 10^{-2}$ Hz, which corresponds to degree and order of a spherical harmonic expansion of about $n \approx 205$.

The contributions in the frequency domain varies from component to component. The noise level of the measured V_{zz} component in the MB is 20 mE, higher than those of V_{xx} and V_{yy} (10 mE). However, due to its high signal content, V_{zz} is still the best component, as one can find by comparing the reconstructed models with V_{zz} and the other components.

Two filters are applied to the data. A FIR filter with length 5383 is used to filter the measured gradients to the MB in order to present them in global maps, since FIR filters can be designed without phase shift. For SHA, since it is very time-consuming to filter the design matrix, an IIR filter is applied to both sides of the observation equations, due to the fact that the IIR filters can achieve good performance with small order, and therefore the computational effort can be kept small.

The filtered measurements displayed on global maps show the information contained in the gravitational gradients. Since the orientation of the satellite and therefore also of GRF varies, the measurements are plotted in global maps separately for ascending and descending tracks. Gravitational signal variations can be found even in the weak components. Comparison to EGM2008

shows large differences between GOCE and EGM2008 in areas such as Himalaya, South America and South Africa.

A gravitational field model is obtained from each of the four precise components. The coefficients of order 16 and multiples of 16 are correlated due to the effect of orbit resonance. Each component has its specific error behavior, e.g., the V_{xx} component is sensitive to low order coefficients, V_{yy} to high order ones, and V_{zz} is more homogeneous than the other components. The results of the combined solution become better than those of each of the individual ones. This shows that their complementarity is helpful to estimate a combined solution.

6

Combination of SST and SGG

In order to estimate a complete gravitational field model from GOCE orbits and gravitational gradients, the normal equations of SST and SGG are to be combined in an appropriate way. The performance of the measured gradients is poorer at long wavelengths, while SST performs better there. Therefore, gravity field modelling in the case of GOCE is based on a combination of the SST contribution for the low-wavelength part and on gravitational gradiometry for the spatial details. SST and SGG are two independent techniques. Thus one can do cross checking as done in (Visser, 2007, 2009) with this two kinds of observation types. As presented in the previous chapters, SST can only resolve SH coefficients for lower degree and order, whereas SGG can reach much higher, but performs poorly at degrees from 0 to about 30, especially for higher order coefficients. Therefore, these two methodologies are complementary. With their combination the advantages of SST and SGG are preserved, and their disadvantages are removed or reduced.

The GOCE observations of both SST and SGG used for the combination in this chapter are from November 1st 2009 to April 30th 2011. Considering the outage of the satellite and special events, it is less than one and a half years. After data cleaning, the total amount of gradiometer data of the four accurate components is 127,573,301, and of the observations of the SST part is 95,678,985. The gravity field coefficients are set up from degree 2 to 215 for the SGG part and 150 for the SST part.

Section 6.1 discusses the methodology of combination. Section 6.2 is dedicated to a presentation of the combined solution. Section 6.4 presents the results of a combination of GOCE and GRACE. A summary is given in section 6.4.

6.1   Methodology

If the dimensions of the normal equations to be combined are equal and the gravitational field coefficients are sorted in the same way, the combination can be realized with ease, as explained in Eq. (3.11). However, this is not always the case, since the normal equations of SST are not necessarily set up to the same high degree and order as those of the gradients. For example, the

coefficients of d/o higher than about 120 are beyond the sensitivity of the current GOCE SST so-
lution; and the variational equations are expensive to compute if the amount of parameters is very
large. Thus, in the case of the SST part of GOCE, the gravitational field coefficients are set up
here to d/o not higher than 150. This is higher than the sensitivity of the GOCE SST part, in order
to ensure a smooth transition from coefficients contributed from both SST and SGG to those from
SGG only. However, the SGG part can achieve good accuracy up to d/o more than 200. It is there-
fore an important point of how to optimally combine normal equations with different dimensions
and different locations of the same parameters in the system of normal equations. The procedure
of combination can be found in Fig. 6.1. The daily normal equations from an observation group
(type) are combined into one normal equation. Then the combined normal equations from differ-
ent observation groups are combined to one single system of normal equations. In this step the
variance component (VC, the variance of the unit weight of an observation type) for each obser-
vation group is estimated and combined with the newly estimated VC. The constraint of the polar
gaps are introduced with normal equations which are added to the combined normal equations.
The final solution is then obtained by solving the final combined system of normal equations by
Cholesky decomposition.
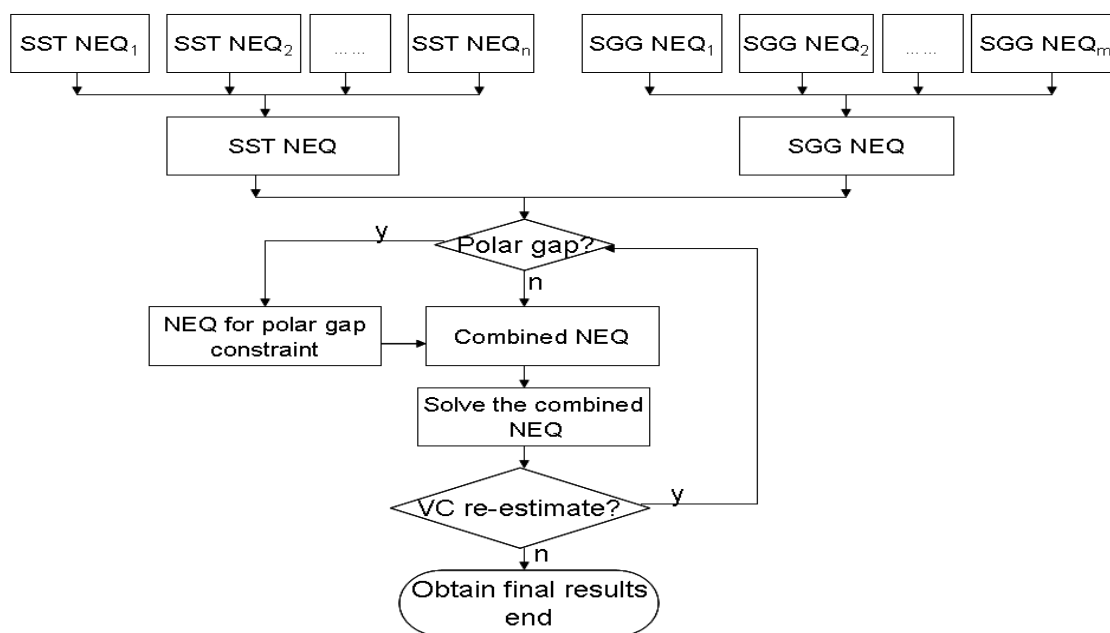
Figure 6.1: Diagram of combination of SST and SGG (The SGG part consists of the four accurate
components)

Taking into account that the gravitational coefficients (as parameters) are sorted differently for
the SST and SGG part, the two normal equations can be combined by adding the corresponding
elements on both the left- and right-hand side according their weight. The variances of unit weight
$\hat{\sigma}_{sst}^2$ and $\hat{\sigma}_{sgg}^2$ are estimated first with Eq. 3.12 and then iteratively with Eq. (3.8c). Their inverses
serve as weights for the combination. Here, we only give the SST and SGG as an example. In

real data processing, the SGG part contains the four precise gradiometer components. Suppose the total number of the parameters of the SST part is N, and the SGG part is M. In addition, we suppose the ith parameter in the normal equations of the SST part corresponds to an SH coefficient which is the kth parameter in the SGG part, and similar for the jth and the lth, then the combined values corresponding to the two above-mentioned parameters can be obtained as

$$\left\{ \frac{1}{\hat{\sigma}_{\text{sst}}^2} \begin{bmatrix} n_{11}^{\text{sst}} & n_{12}^{\text{sst}} & \cdots & \cdots & n_{1N}^{\text{sst}} \\ \vdots & \vdots & \vdots & \vdots & \vdots \\ \cdots & \cdots & n_{ij}^{\text{sst}} & \cdots & \cdots \\ \vdots & \vdots & \vdots & \vdots & \vdots \\ n_{N1}^{\text{sst}} & n_{N2}^{\text{sst}} & \cdots & \cdots & n_{NN}^{\text{sst}} \end{bmatrix} + \frac{1}{\hat{\sigma}_{\text{sgg}}^2} \begin{bmatrix} n_{11}^{\text{sgg}} & n_{12}^{\text{sgg}} & \cdots & \cdots & n_{1M}^{\text{sgg}} \\ \vdots & \vdots & \vdots & \vdots & \vdots \\ \cdots & \cdots & n_{kl}^{\text{sgg}} & \cdots & \cdots \\ \vdots & \vdots & \vdots & \vdots & \vdots \\ n_{M1}^{\text{sgg}} & n_{M2}^{\text{sgg}} & \cdots & \cdots & n_{MM}^{\text{sgg}} \end{bmatrix} \right\} \delta\mathbf{x}$$

$$= \frac{1}{\hat{\sigma}_{\text{sst}}^2} \begin{bmatrix} u_1^{\text{sst}} \\ u_2^{\text{sst}} \\ \vdots \\ u_N^{\text{sst}} \end{bmatrix} + \frac{1}{\hat{\sigma}_{\text{sgg}}^2} \begin{bmatrix} u_1^{\text{sgg}} \\ u_2^{\text{sgg}} \\ \vdots \\ u_M^{\text{sgg}} \end{bmatrix} . \quad (6.1)$$

The combined element $n_{k'l'}^{\text{combined}}$ in the new normal matrix is computed as

$$n_{k'l'}^{\text{combined}} = \frac{1}{\hat{\sigma}_{\text{sst}}^2} n_{ij}^{\text{sst}} + \frac{1}{\hat{\sigma}_{\text{sgg}}^2} n_{kl}^{\text{sgg}} \quad . \qquad (6.2)$$

The right-hand side is combined in an analogous way.

Since all the local parameters, of both SST and SGG, are pre-eliminated before combination, the only parameters left in the normal equations are the gravitational field coefficients. This is very convenient for speeding up the combination since the number of the local parameters can be very large.

All the four accurate components from gradiometry are combined for the final solutions. They are assumed to be independent. One can therefore apply Eq. (3.15) to combine the normal equations computed from SGG data. In principle, the gradiometric components may be correlated due to the angular reconstruction applied in the same way to all the GGT components. Since the magnitude of the angular motion is smaller than that of GGT and differential acceleration in the measurement band (see Rummel et al., 2011), it is reasonable to assume the components of the measured GGT to be independent.

6.2 Analysis of the Solution Derived by Combination of GOCE SST and SGG

In the following a complete GOCE SST and SGG spherical harmonic analysis is described. All preprocessing steps and filtering have been applied as described in the previous chapters. With the integral equation approach on orbit data and the bandpass filter applied to gradiometer data,

the final GOCE solution is obtained after the combination of SST and SGG part, together with the constraint in the polar areas realized by the pseudo-observations on a $1° \times 1°$ resolution grid in terms of geoid heights of an assumed STD 20 cm close to that of EGM2008. The result is expected to be consistent with the other recently developed GOCE only models, such as TIM2 (Pail et al., 2011b) or DIR2 (Bruinsma et al., 2010). The analysis of the solution is conducted in various forms: as errors per degree, coefficient errors in triangular form, geoid differences and gravity anomaly differences w.r.t. other considered models, variance-covariance matrix and error propagation, as well as individual contribution of the three parts, i.e. the SST part and the SGG part together with the polar constraint. The contribution of the four accurate components in the SGG part are also analyzed.

The square root of the variance of the unit weight (variance component) for different observation types are given in Table 6.1. The a prior $\hat{\sigma}^{(-)}$ computed with Eq. (3.12) and the posteriori values with Eq. (3.8c). The posteriori values of the σ of the GGT data are smaller than their a priori values. This means they are underweighted with a priori $\hat{\sigma}^{(-)}$ during the combination, and is updated with the posteriori values. The kinematic orbit of SST is the other way round. It is overweighted during the combination with a priori value of its STD of unit weight, and is updated with the posterior value for a better estimate of the data quality. The posterior estimate of the orbit accuracy is 1.8 cm, which is satisfied with the accuracy requirement for GOCE orbit, i.e. 2 cm. The values of V_{xx}, V_{yy} and V_{zz} are 3.6, 3.6 and 5.9 mE, respectively. The $\hat{\sigma}$ value of V_{zz} component is larger than those of V_{xx}, V_{yy}, due to the high noise in the MB, see (Rummel et al., 2011). The posterior σ value of the V_{xz} component is 7.0 mE, which is the largest among all the four sensitive components. The large STD values of the component V_{xz} is due to its high noise level in the MB, see again (Rummel et al., 2011). The polar areas are constrained with a STD of 20 cm to EGM2008 for combination, based on the fact that the formal error of EGM2008 in terms of cumulative geoid height is 7.2 cm (1σ) up to d/o 200. In our computation, we hope our solution is close to EGM2008 in the polar areas for the values on a $1° \times 1°$ grid with 3σ, which is approximately 20 cm.

Table 6.1: σ of different observation types

Obs. types	a priori $\hat{\sigma}_j^{(-)}$	posterior $\hat{\sigma}_j$
V_{xx} [mE]	3.7	3.6
V_{yy} [mE]	3.8	3.6
V_{zz} [mE]	6.2	5.9
V_{xz} [mE]	7.1	7.0
SST kin. orbit [cm]	1.76	1.85
Polar stabilization (in terms of geoid) [cm]	20	20

6.2.1   Analysis in terms of per Degree Error

In Fig. 6.2 the degree RMS compared to EIGEN-6S (Förste et al., 2011) of the SGG only solution is shown in red, the SST only solution in green, the combined solution in blue and the combined solution with additional constraint in the polar areas in magenta. The model EIGEN-6S is a satellite-only gravity field model computed from GRACE from the time span 1 Jan 2003 till 30 June 2009 and 6.5 years of LAGEOS (SLR) as well as GOCE (satellite gradiometry) data from the time span 1 Nov 2009 till 30 June 2010. We assume that EIGEN-6S is a good model being chosen as a reference for comparison and analysis.
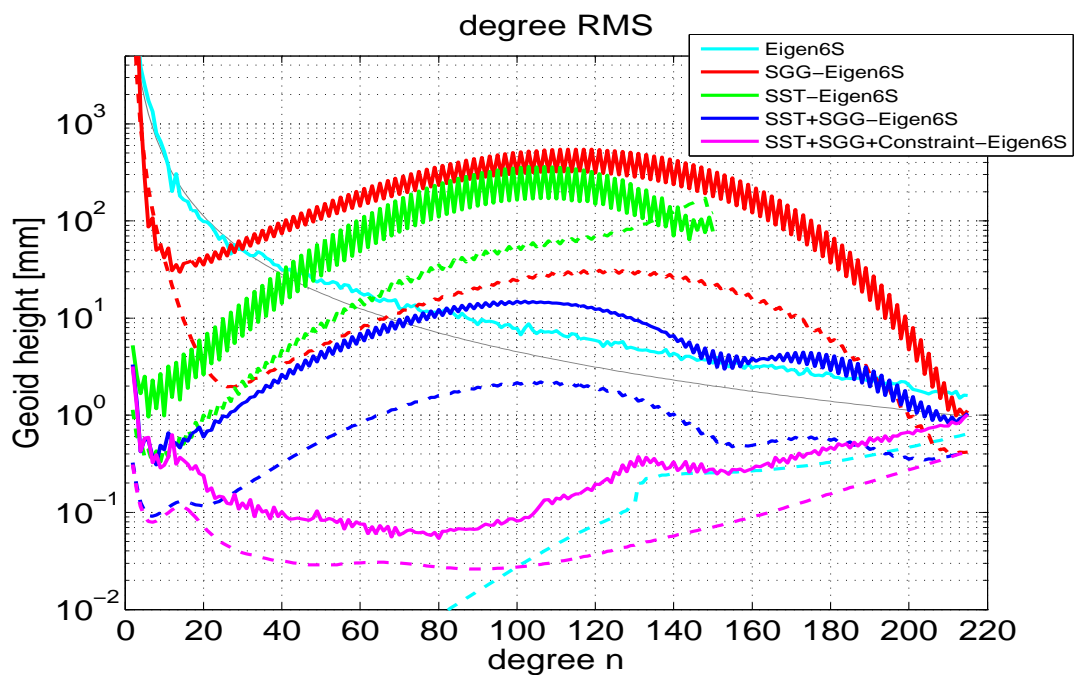
Figure 6.2: The degree RMS comparing to EIGEN-6S. The formal errors for each solution are given in the dashed line with the same color.

The degree RMS of both SGG and SST only solutions oscillate due to the polar gap. The degree RMS is dominated by the large errors of the zonals and near-zonals. After the combination of SST and SGG, the degree RMS (in blue) becomes smaller compared to the SGG and SST only solution. However, due to the polar gap, the zonal and near-zonal coefficients in the combined solution are still correlated and not well determined. After applying the constraint in the polar areas in latitudes [-90° -83°] and [83° 90°] on a $1° \times 1°$ grid with geoid heights from EGM2008 and an assumed STD of 20 cm, the final result is obtained and its degree RMS is shown by the magenta curves. The degree RMS of the combined and constrained solution is the smallest of all solutions. Under the assumption that the model EIGEN-6S is a good reference, the combined solution is seen to be improved and therefore better than any individual solution. This shows the correctness of the combination. The degree RMS is smaller than the signal strength even at d/o

215, as shown by the comparison of the magenta curves (both solid and dashed) to the signal degree RMS in solid cyan. This means that even higher d/o coefficients can be estimated with the data and methodology of this processing scenario.

In order to analyze the quality of our result, we compare our model with TIM2, DIR2 and ITG-Grace2010s all referred to EIGEN-6S. The TIM2 model is estimated with the time-wise approach. It uses the observations in the time span from November 1st 2009 to July 05th, 2010. Kaula regularization is applied in TIM2 to the coefficients starting from degree 181 up to 250. In addition, spherical cap regularization for stabilization of the system is applied. The DIR2 model is derived with the direct approach with the observations in the time span from November 1st 2009 to June 30th, 2010. It takes the ITG-Grace2010s as a reference model for regularization. Both TIM2 and DIR2 use diagonal components of the GOCE GGT for the SGG part. One must keep in mind that the data period for the computation of our model is longer than those for DIR2 and TIM2.

In Fig. 6.3, the degree RMS and cumulative error in terms of geoid height compared to other gravity field models are shown on the left and right panels, respectively. ITG stands for the gravity field model ITG-Grace2010s, which is included here to study the performance differences between GOCE and GRACE. Our gravity field model is named TUMYGSTGpgr in the figure. The solid lines express the differences between the various compared models to the reference model EIGEN-6S, and the dashed lines denote the formal errors of the compared models. Among the GOCE only models, the DIR2 solution is the closest one to EIGEN-6s, simply because the EIGEN-6S model is estimated based on the combination of the DIR2 solution and LAGEOS and GRACE. It is fair to say that the constraint in the polar gap plays an important role for this comparison. The constraint used in TIM2 for the polar gap is less strict, resulting large differences in the low to medium degrees. TIM2 in non-polar areas is very accurate as validated in (Gruber et al., 2011; Pail et al., 2011b). In Fig. 6.3a, our solution is closer to EIGEN-6S than TIM2 at degrees from 0 to about 130. Between degree 130 to 180 TUMYGSTGpgr and TIM2 show more or less the same degree RMS. For degrees higher than 180 the degree RMS of TIM2 is less than that of TUMYGSTGpgr, very likely because TIM2 solution applies Kaula regularization starting at degree 180. At degrees higher than about 205, the degree RMS of the differences between DIR2 and EIGEN-6S is significantly smaller than the others. The reason is that EIGEN-6S adopted a large amount of information from the DIR2 solution in this degree range. In comparison to GRACE, the ITG-GRACE model is better than a GOCE model approximately from degree 0 to 100, above this GOCE shows better accuracy, according to the formal errors of ITG-Grace2010s and TUMYGSTGpgr.

The cumulative geoid error is shown in Fig. 6.3b. Compared to the reference field EIGEN-6S, the geoid differences of TUMYGSTGpgr can reach 8 cm up to d/o 210, whereas those of TIM2 model are about 10 cm. The formal error of TUMYGSTGpgr seems quite optimistic, less than 3 cm up to d/o 200. It is the smallest of all the considered GOCE models. This is because more data is used for model TUMYGSTGpgr.

(a) degree RMS   (b) cumulative geoid error
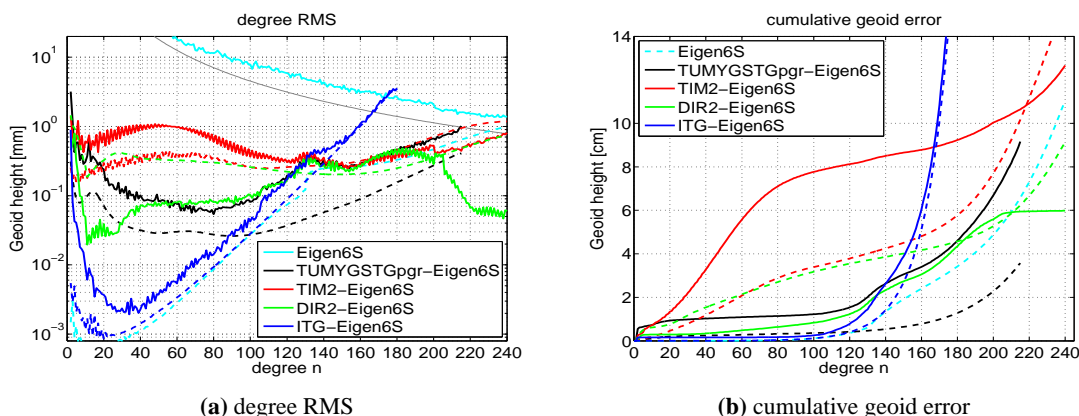
Figure 6.3: degree RMS and cumulative geoid in terms of geoid height error

From the degree error analysis, one can conclude that TUMYGSTGpgr is consistent with TIM2 and DIR2. However, the degree error per degree cannot give information about how accurate individual coefficients are.

6.2.2 Analysis of Coefficient Error in terms of Spherical Harmonic coefficients (Triangular Representation)

The error behavior of TUMYGSTGpgr is displayed in triangular form in Fig. 6.4. The differences between TUMYGSTGpgr and EIGEN-6S in Fig. 6.4a show that these two models are more consistent with each other at lower degrees than at higher ones. However, at degrees 10 to 20 the consistency between the two models is not as good as at degrees from 40 to 100. No large systematic distortion is found between TUMYGSTGpgr and EIGEN-6S. The formal error shown in Fig. 6.4b shows a similar behavior as the coefficient differences in Fig. 6.4a. The coefficients of TUMYGSTGpgr from degree 30 to 120, excluding the zonal and near zonal coefficients are estimated with high precision. The effect of the polar gap shows up in both the coefficient differences and the formal errors.

The models TUMYGSTGpgr and EIGEN-6S are quite close to each other. The error structure shows that the higher degree coefficients are less precise than the lower degree ones, and zonal and near-zonal coefficients are less precise than the higher order ones. One might therefore probably introduce an even stronger constraint in the polar gap areas.

6.2.3 Analysis in terms of Geoid and Gravity Anomaly Differences

There are gravity field models based on measurements from satellite-only, and combined models which are based on satellite and terrestrial data. Both kinds of models are compared to our solutions in this subsection.

(a) coeff. differences (log10 scale) (b) formal error (log10 scale)
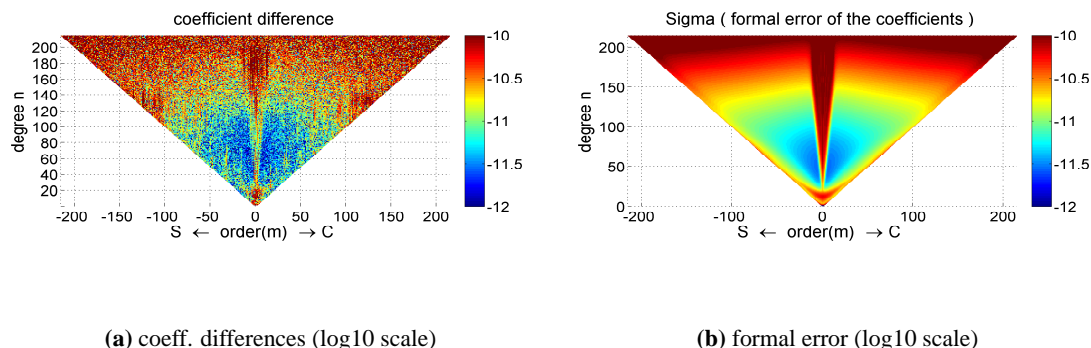
Figure 6.4: coefficient differences between TUMYGSTGpgr to EIGEN-6S and the formal error of SH coefficients of TUMYGSTGpgr

6.2.3.1 Comparison to Satellite-only Models

From the most recent satellite-only gravity field models we choose EIGEN-6S and GOCO02s (Goiginger et al., 2011; Pail et al., 2010) to compare them with TUMYGSTGpgr. GOCO02s is derived by the combination of 8 months of GOCE SGG data, 7 years of GRACE data, 8 years of CHAMP data and 5 years of SLR data (5 satellites). A Kaula regularization is applied starting at degree/order 180. Similar to EIGEN-06S it is therefore very precise in both long- and short-wavelength parts.

The geoid and gravity anomaly differences are important quantities for gravity field model analysis. The error behavior in the space domain can be presented geographically as shown in Fig. 6.5 for the areas from latitude -83° to 83°, with the geoid differences on the upper panel and the gravity anomaly differences on the lower panel. The STD values of geoid differences between TUMYGSTGpgr and EIGEN-6S and those between TUMYGSTGpgr and GOCO02s are 8.2 cm and 7.5 cm, respectively; on the lower panel, the STD values of gravity anomaly differences are 2.42 mgal and 2.27 mgal, respectively. Based on these comparisons, it seems as if TUMYGSTGpgr is closer to GOCO02s than to EIGEN-6s, at least for an expansion up to d/o 215.

The STD values of geoid differences between various models are presented in Table. 6.2, again for the areas from latitude -83° to 83°. When comparing up to d/o 215, TUMYGSTGpgr deviates from the other models due to its larger STD values. There are two reasons for this. Firstly TUMYGSTGpgr is estimated only up to d/o 215. Some information higher than 215 projects into the coefficients close to degree 215 due to an aliasing effect. Secondly, for TUMYGSTGpgr and DIR2 only a polar gap regularization is applied, whereas for TIM2 polar gap and to high degrees Kaula regularization is used.

If these models are compared only up to d/o 200, TUMYGSTGpgr is at the same error level

(a) geoid differences to EIGEN-6S

(b) geoid differences to GOCO02s

(c) gravity anomaly differences to EIGEN-6S

(d) gravity anomaly differences to GOCO02s
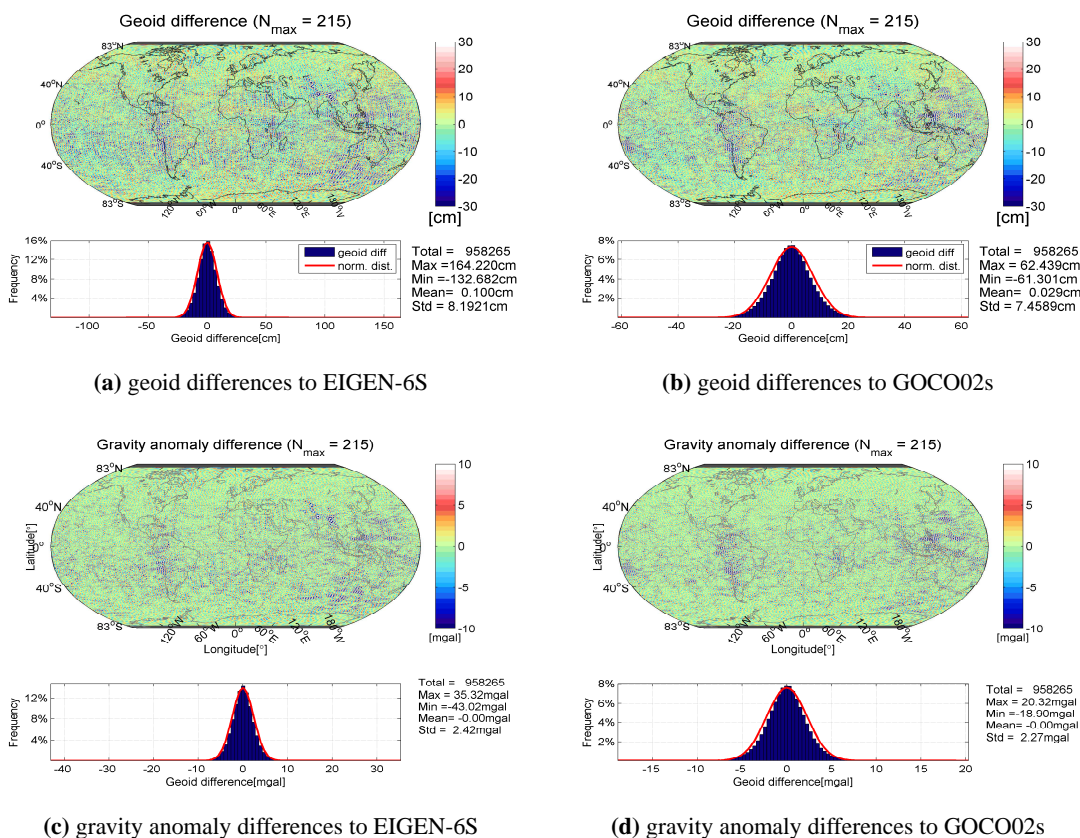
Figure 6.5: geoid differences and gravity anomaly differences between TUMYGSTGpgr and EIGEN-6S, and between TUMYGSTGpgr and GOCO02s

Table 6.2: Comparison of various models up to d/o 215, in terms of the STD values of geoid differences in centimeters (in latitudes [-83° to 83°])

	TUMYGSTGpgr	TIM2	DIR2	EIGEN-6S	GOCO02s
TUMYGSTGpgr	0	7.39	8.04	8.19	7.46
TIM2		0	5.64	5.78	2.00
DIR2			0	3.03	5.82
EIGEN-6S				0	5.82
GOCO02s					0

as the other models, see Table 6.3. Since GOCO02s has partially adopted TIM2, these two models are close to each other, and the same is the case for EIGEN-6S and DIR2. One may notice that the STD value between DIR2 and EIGEN-6S up to d/o 200 is larger than that up to d/o 215. This phenomenon also happens in the case of TIM2 and GOCO02s. It indicates that the zonal and near-zonal coefficients are not ideally decorrelated, since in principle the STD value of geoid difference should be smaller up to lower degrees than up to higher ones. This phenomenon does not exist in the case of TUMYGSTGpgr for this comparison.

Table 6.3: Comparison of various models up to d/o 200, in terms of the STD values of geoid differences in centimeters (in latitudes [-83° to 83°])

	TUMYGSTGpgr	TIM2	DIR2	EIGEN-6S	GOCO02s
TUMYGSTGpgr	0	4.84	5.87	5.88	4.86
TIM2		0	4.69	4.87	2.14
DIR2			0	3.36	4.99
EIGEN-6S				0	4.94
GOCO02s					0

The comparison in terms of geoid differences and gravity anomaly differences shows that the TUMYGSTGpgr is as good as the other recently developed models, such as TIM2, DIR2, EIGEN-6S and GOCE02s, and is closer to TIM2 and GOCE02s than to DIR2 and EIGEN-6S.

6.2.3.2 Comparison to Combined Models

Similar to the comparison with satellite only models, the model TUMYGSTGpgr is compared to EGM2008 and EIGEN-6C (Förste et al., 2011), both of them so-called combined gravity field models with terrestrial data included. In Fig. 6.6, the geoid differences between TUMYGSTGpgr and EGM2008 and between TUMYGSTGpgr and EIGEN-6C are displayed on the left and right, respectively. Large differences in terms of geoid height between TUMYGSTGpgr and EGM2008 are found in Himalaya, Africa, New Guinea, South America and Antarctica, where terrestrial data as used in EGM2008 is less accurate, see Fig. 6.6a. This is also known from the measured gradient analysis, see Fig. 5.18. The STD value between the geoids of TUMYGSTGpgr and EGM2008 is 13.4 cm, up to d/o 215. The comparison with EIGEN-6C shows better consistency with a smaller STD value of 8 cm, see Fig. 6.6b.

These comparisons show a certain inhomogeneity of the combined model (terrestrial data included) relative to TUMYGSTGpgr. Terrestrial data is very useful and important for gravity field modelling, but it is still an open question as to how to optimally combine satellite measurements with terrestrial (surface) data. The terrestrial data are collected under observing conditions which vary from region to region in terms of precision and density; therefore it is a challenge to combine them with optimal weighting.

(a) geoid differences to EGM2008   **(b)** geoid differences to EIGEN-6C

Figure 6.6: geoid differences between TUMYGSTGpgr and EGM2008 and between TUMYGSTGpgr and EIGEN-6C up to d/o 215

The STD values of the geoid differences between TUMYGSTGpgr and the two combined models are given in Table 6.4. Based on the STD values, TUMYGSTGpgr seems more consistent with EIGEN-6C than with EGM2008 for a global comparison.

Table 6.4: STD values of the geoid differences between TUMYGSTGpgr and EGM2008 and between TUMYGSTGpgr and EIGEN-6C in centimeters (in latitudes [-83° to 83°])

up to d/o	215	200	180	150
EGM2008	13.43	11.60	9.90	7.73
EIGEN-6C	8.01	5.39	3.54	2.20

As shown in Fig. 6.7, more north-south stripes are found in the geoid differences between TUMYGSTGpgr and EIGEN-6C (Fig. 6.7b) than between TUMYGSTGpgr and EGM2008 (Fig. 6.7a). The north-south stripes are the typical error behavior of GRACE. It indicates that most of the information in EIGEN-6C up to d/o 150 comes from GRACE, which leads to a dominance of GRACE error characteristics in the geoid differences. Since the terrestrial data contributes to EIGEN-6C starting at d/o 160 (Förste et al., 2011), this can explain these differences between Figs 6.7a and 6.7b.

A global map of geoid height differences between TUMYGSTGpgr and EGM2008 up to d/o 200 is shown in Fig. 6.8. Three regions marked with dark lines in Fig. 6.8 are chosen for comparison. They are in rectangular areas of the given lower left and upper right coordinates [(-120°W 30°N); (-80°W 50°N)] for USA, [(5°E 45°N); (15°E, 55°N)] for Germany and [(120°E -20°S); (145°E -35°S)] for Australia. In these three regions accurate terrestrial data is incorporated in EGM2008.

The short wavelength part of EGM2008 in land areas is based on terrestrial gravimetry data. The three marked in black regions are known to have terrestrial data with high accuracy. As pre-

(a) geoid differences to EGM2008
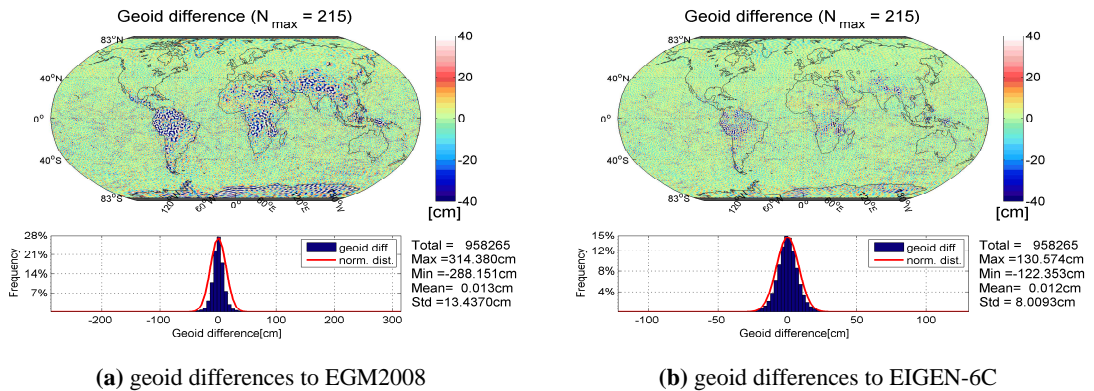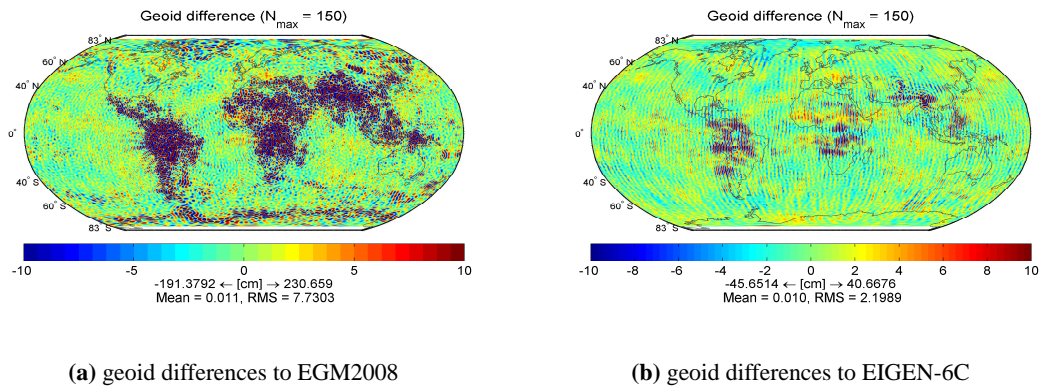
(b) geoid differences to EIGEN-6C

Figure 6.7: geoid differences between TUMYGSTGpgr and EGM2008 and between TUMYGSTGpgr and EIGEN-6C up to d/o 150

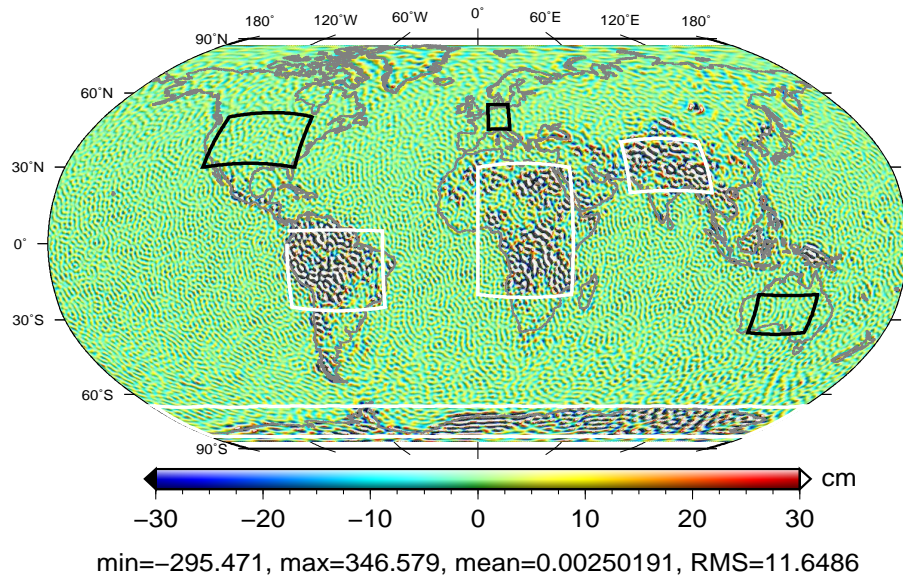**Figure 6.8:** geoid differences between TUMYGSTGpgr and EGM2008 to d/o 200

sented in (Gruber et al., 2011), in these three black marked regions, EGM2008 is very consistent with the GPS-leveling. Therefore, we can just compare the GOCE-based models to EGM2008 in these regions. This comparison can be considered as assessment of the accuracy of the GOCE-based models with terrestrial gravity anomalies. The advantage of this comparison is that the high frequency part of the terrestrial data which is used for the determination of EGM2008 is filtered out by truncating EGM2008 at any desired degree.

In order to show the improvement of GOCE to EGM2008, four regions with weaker gravity data are selected for comparison. They are marked in white rectangles in Fig. 6.8 with the lower left and upper right coordinates [(-80°W -30°S); (-40°W 0°N)] for South America, [(0°E -20°S); (40°E 30°N)] for Africa, [(65°E 20°N); (100°E 40°N)] for Himalaya area, and [(-180°W -80°S); (180°E -65°S)] for Antarctica. The RMS-values of the geoid differences between TUMYGST-Gpgr and EGM2008 in the seven regions are given in Table 6.5.

Table 6.5: RMS-values of the geoid differences between EGM2008 and TUMYGSTGpgr for the selected areas and global RMS; SA is the South America and SE-Asia is the Southeast Asia; unit is centimeter

d/o	Australia	Germany	USA	SA	Africa	SE-Asia	Antarctica	Global RMS
180	3.34	2.45	2.90	33.56	23.41	35.53	11.19	9.90
200	5.34	4.04	4.33	36.35	25.09	37.05	15.50	11.64

It can be seen that the RMS-values in the three regions with precise terrestrial data used for EGM2008 are small and those in the other four regions are very large. With the comparison of TUMYGSTGpgr and EGM2008 in the regions where accurate terrestrial gravimetry data were used for the determination of EGM2008, it can result accuracy assessment of our GOCE model. There are at least two advantages with this idea. First, EGM2008 is very accurate in these regions and can be used as a reference model; second, the omission error is eliminated by truncation of the SH expansion at any desired degree. In this comparison, the GOCE-based models are shown to be consistent with EGM2008 with RMS-values of 4 to 6 cm, for the case of truncation at degree 200. The comparison in regions where terrestrial data of only poorer accuracy was available for EGM2008, shows significant improvements from GOCE observations in the range between degree 100 and 200. In Antarctica where only GRACE observations were used for the determination of EGM2008, the improvements from GOCE are also demonstrated.

6.2.4 Analysis in terms of Formal Error

With Eq. (3.10c), the VCM of the parameter vector is obtained, and shown in Fig. 6.9a for the first 6 thousand rows and columns. Based on the rule of error propagation, i.e.

$$\Sigma_{\hat{\mathbf{y}}} = \mathbf{A}\Sigma_{\hat{\mathbf{x}}}\mathbf{A}^{\mathrm{T}},$$
(6.3)

for $\hat{\mathbf{y}} = \mathbf{A}\hat{\mathbf{x}}$, the VCM can be transformed into the VCM of any other linear gravity functional. In order to look into the error behavior in the space domain, the VCM of the SH coefficients has been transformed to the formal error of gravity quantities on the Earth sphere. With $\hat{\mathbf{y}}$ as geoid height, the matrix $\mathbf{A}$ is computed according to Eq. 2.2, and the formal error in terms of geoid height is obtained with Eq. (6.3) and displayed in Fig. 6.9b. The error is latitude dependent, i.e. larger error at lower latitudes and smaller error at higher latitudes, due to the fact that the ground track density at low latitudes is sparser than at high latitudes. The maximum value of the error is 5.0 cm in polar areas, because there is no information from GOCE in these areas and the constraint from polar stabilization is rather loose (20 cm prior STD in terms of geoid height).

(a) Variance-covariance matrix

(b) Formal error propagated to geoid height up to d/o 215
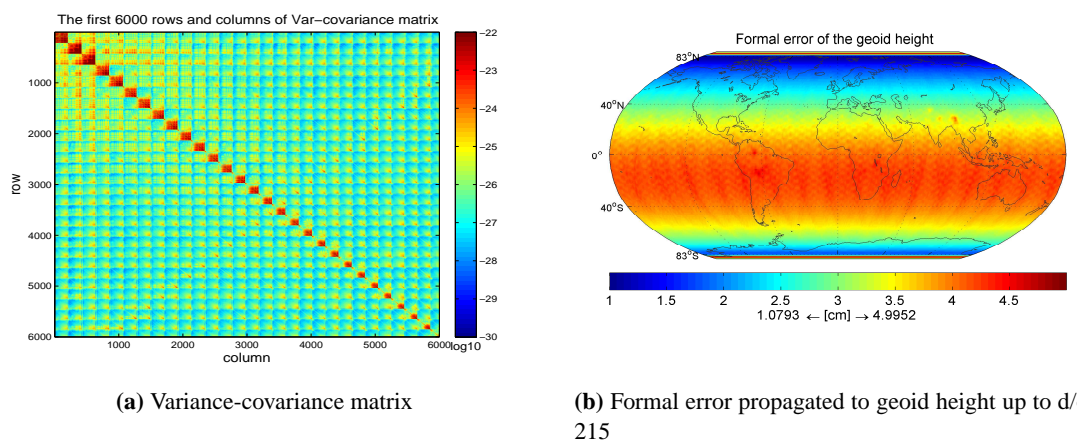
Figure 6.9: Variance-covariance matrix (left) and its propagation to geoid heights (right)

The formal error of the coefficients and the geoid will decrease with more and more data collected. Based on estimation theory, the accuracy of the spherical harmonic coefficients determined from the measured gradients, and to a small extent also the spatial resolution, will increase with an increasing number of measurements.

6.2.5 Analysis in terms of Contribution Analysis

Since the GOCE-only gravity field model is estimated from a number of components such as SST and the four accurate gravitational gradient components, it is interesting to know the contribution of each individual part. Therefore, we conduct such an analysis based on the normal matrices of each individual component and their combination.

6.2.5.1 Contribution Computed by Means of Resolution Matrices

Based on the normal equations and posteriori variance components, the contribution from all the involved data types are computed, as shown in Fig. 6.10. With mean value in blue and median in red, the contribution per degree and per order are given in the upper right panel and lower left

panel, respectively. For each data type the characteristic of its contribution is shown. It can be seen that V_{xx} contributes mainly to the lower order coefficients, and V_{yy} to the higher order ones, and that V_{zz} is rather homogeneous. The maximum contributions are from V_{zz} and V_{xx}, with up to 32.7% and 28.0%, respectively. A bit less comes from V_{yy} with 26.1%, and even less from V_{xz} with 10.9%. SST contributes mostly to the lower degree coefficients, especially in the range of the sectorial and near-sectorial coefficients, with 1.9% mean value. Last but not least, the constraint in the polar areas is important, even though its contribution is only 0.2%.

(a) Contribution from V_{xx}

(b) Contribution from V_{yy}

(c) Contribution from V_{zz}

(d) Contribution from V_{xz}

(e) Contribution from SST

(f) Contribution from pseudo obs.
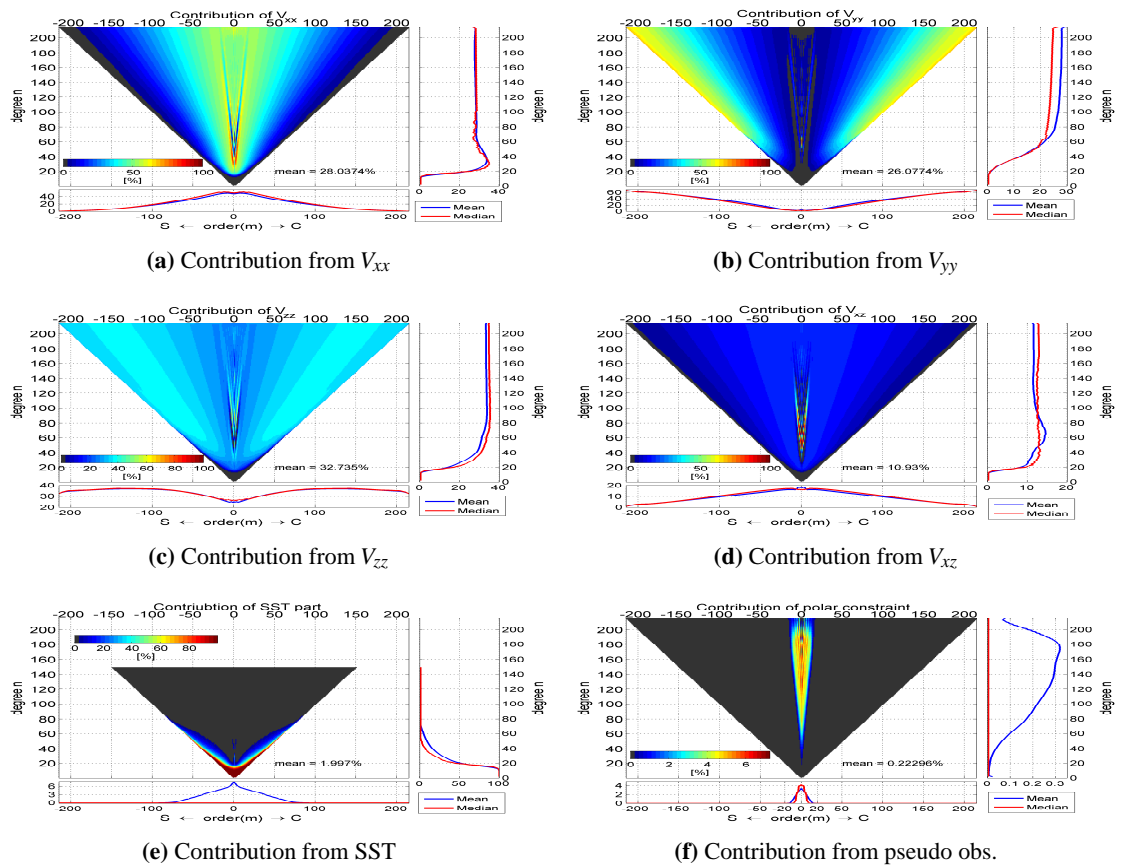
Figure 6.10: Contribution of each individual components (per SH coefficient and percentage)

The contributions of the GOCE gravity gradient components V_{xx}, V_{yy} are complementary, and those of V_{zz} are rather homogeneous. Although the noise in V_{zz} is higher than in the other two, its information content is still the highest. The V_{zz} shows very good consistency to the fully combined solution, due to its good spatial homogeneity. This property reduces the standard deviation of the geoid differences between the partially combined solution of V_{zz} and the fully combined solution and makes it smaller than those of V_{xx}, V_{yy} and V_{xz}. V_{zz} is therefore the most important component. From the analysis in terms of spherical harmonics, the contribution from V_{zz} is the largest, whereas V_{xx} and V_{yy} have a similar magnitude of contribution. Pseudo-observations in the polar areas are used to stabilize the computation and de-correlate the zonal and near-zonal coefficients. They

have, however, less than 1% influence on the final result. SST contributes more information to the lower degree coefficients and especially to the higher orders of the lower degree coefficients.

6.2.5.2 Comparison of individual components to the complete combined solution

The geoid differences between models derived from SST (and pseudo-observations in the polar areas) combined with each of the sensitive components of SGG, individually, with the fully combined solution of all observations are presented in Fig. 6.11. The STD of the difference between the partially combined V_{zz} component and the fully combined solution is less than that of the other three components. This is due to the homogeneity of the V_{zz}, compare Fig. 6.10c. The larger STD for V_{xx} and V_{yy} in Fig. 6.11a and 6.11b is because of the non-isotropic error behavior of the coefficients estimated with these two components, as shown in Fig. 6.10a and 6.10b. One can observe a certain stripe pattern in north-south and east-west direction in the error behavior of the components V_{xx} and V_{yy}, respectively. Since V_{xz} contains both an x and z component, its geoid difference to the fully combined solution also shows the same north-south stripes but with a smaller STD as compared to V_{xx}.

The constraint in the polar gap areas is important for decorrelation of the zonal and near-zonal coefficients of the estimated gravity field model. Nevertheless, it is tried to keep it as small as possible. In addition to the contribution analysis based on the resolution matrix, the differences of the coefficients and geoid heights between the polar-constrained model and polar-unconstrained model are presented in Fig. 6.12. The coefficient differences between these two models are smaller than $10^{-12.5}$ for almost all non-zonal and not near-zonal coefficients, see Fig. 6.12a. This means the polar constraint applied in TUMYGSTGpgr affects only the zonal and near-zonal coefficients. The geoid differences in latitudes [-83° 83°] between the constrained and unconstrained models are shown in Fig. 6.12b. One can find that the geoid differences between the constrained and unconstrained solutions are quite small, with more than 50% of the geoid differences on the global grid being smaller than 0.5 cm. The STD value of the differences is 1.83 cm. Large differences are found only at high-latitude areas close to the polar gaps.

With the contributions of polar constraint, together with the comparison between the constrained solution and unconstrained solution, we conclude that some essential a-priori information enters into the result, but its contribution is kept quite small.

6.2.6 Analysis in terms of External Validations

The geoid undulations can be obtained either by computing the geoid height of a gravity field model relative to an adopted normal ellipsoid, such as WGS84 (Sillard and Boucher, 1996), or by taking the difference between orthometric height derived from leveling surveying and ellipsoidal heights derived from GPS. The latter approach is referred to as "GPS-leveling". Theoretically the
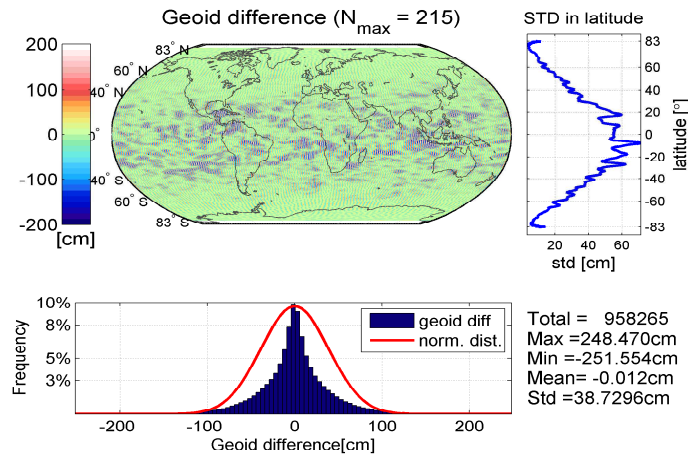
(a) Geoid differences between the V_{xx} (with SST and pseudo-obervations) relative to the fully combined solution
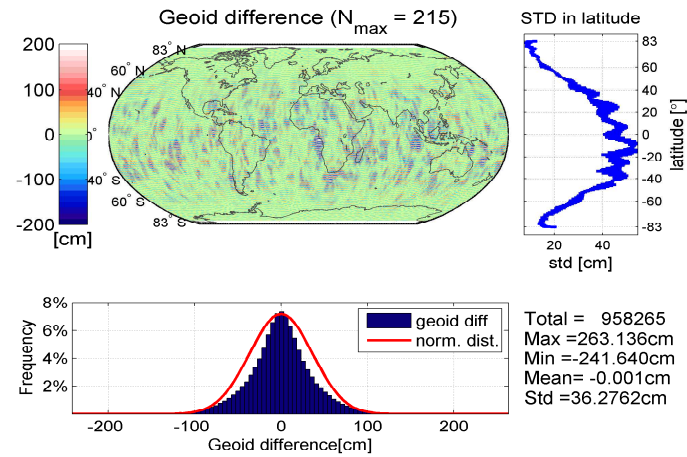
(b) Geoid differences between the V_{yy} (with SST and pseudo-obervations) relative to the fully combined solution
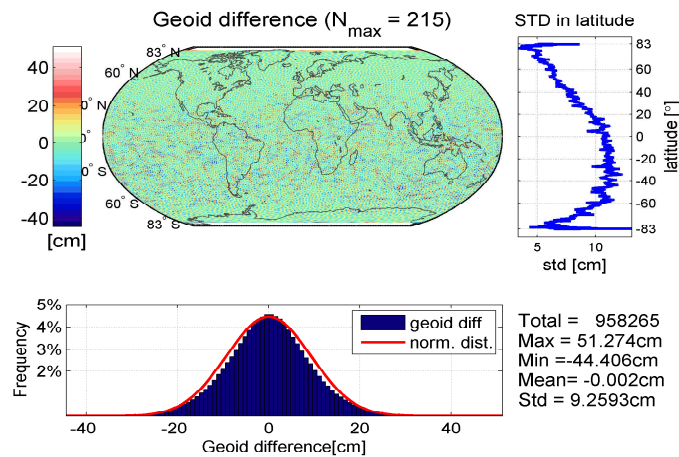
(c) Geoid differences between the V_{zz} (with SST and pseudo-obervations) relative to the fully combined solution
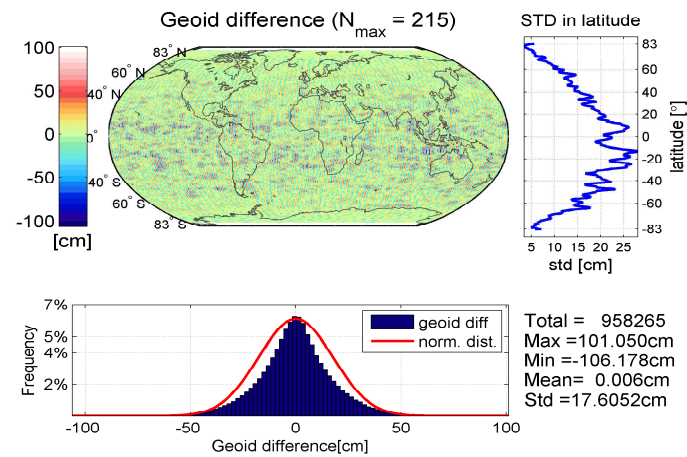
(d) Geoid differences between the V_{xz} (with SST and pseudo-obervations) relative to the fully combined solution

Figure 6.11: Geoid differences of individual components relative to the fully combined solution

(a) coefficient differences between polar-constrained and unconstrained solutions (log10 scale)

(b) geoid differences between polar-constrained and unconstrained solutions
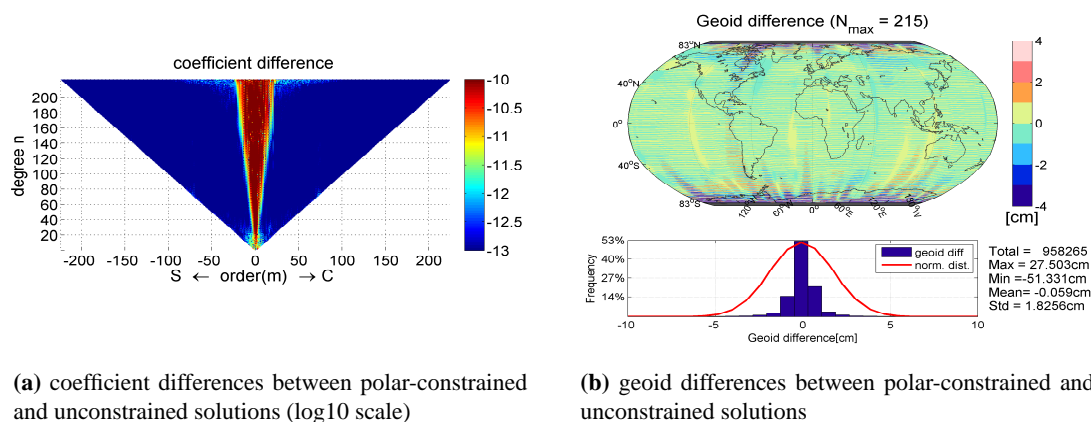
Figure 6.12: comparison between polar-constrained and unconstrained solutions

geoid undulations derived with these two approaches are equivalent. Therefore, a comparison of their values at the same geographical location allows to assess the accuracy of the gravity model.

Our model TUMYGSTGpgr has been validated with the benchmark areas in Australia, Canada, Europe, Germany, Japan and USA by Dr. Thomas Gruber. For the estimation of the omission error we make use of the EGM2008 model, see Gruber et al. (2011). The RMS-values of the geoid heights of the four models to be validated differing to "GPS-leveling" are shown in Fig. 6.13, with a truncation up to d/o 180 on the left, and up to d/o 200 on the right. One can find that the model TUMYGSTGpgr is slightly but consistently closer to the "GPS-leveling" data than the other 3 models. The reason can be that the model TUMYGSTGpgr is based on a longer time span with GOCE data than the others. The GPS-leveling data in Germany are the most accurate among all these data sets used for validation, that is the reason why the RMS-values in this area is the smallest. All the fields are close to the German GPS-leveling data set with about 4-6 cm uncertainty. It is difficult to say whether the GPS-leveling data are more accurate than the gravity field models, or vice versa. However, if the gravity field models are so close to the most accurate GPS-leveling data set, it can be assumed that both the "GPS-leveling" data and our gravity field models TUMYGSTGpgr have an error level of not larger than 6 cm in terms of geoid undulation up to d/o 200, at least for the area of Germany.

Geoid height/anomaly slope differences are more sensitive to mid- to high-frequency variations of the geoid (Gruber et al., 2011). They are the RMS-values of the differences between the geoid of gravity field model and that derived from GPS-leveling and classified according to the distance between all the combinations of any two benchmark point in each region. A closer investigation is taken for German and Japanese data sets. In Fig. 6.14, the relation between the RMS values of the geoid differences and the distance of the points is given, for the regions of Japan (left) and Germany (right). The RMS value of TUMYGSTGpgr is smaller than those of all the other models, for the distance less than 1700 km in the area of Japan, and even much significantly

(a) up to d/o 180   **(b)** up to d/o 200
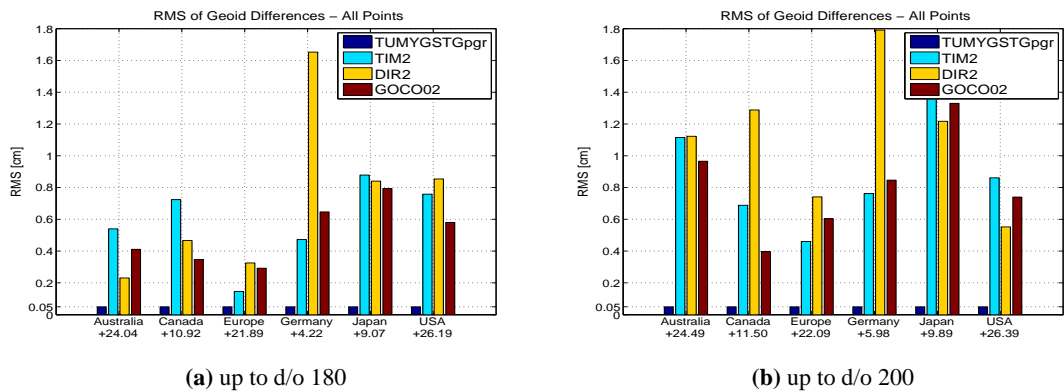
Figure 6.13: RMS of the geoid height differences between the "GPS-leveling" and gravity field models

smaller in the area of Germany. This shows that TUMYGSTGpgr is better consistent with the external validation data, based on this computation in terms of geoid slope differences. For the other data sets similar, but due to the fact that their accuracy is poorer, less pronounced results as presented in Fig. 6.14 were obtained. In the tests truncated in other degrees, TUMYGSTGpgr also shows better consistency with the GPS-leveling data sets.

(a) Japan   **(b)** Germany
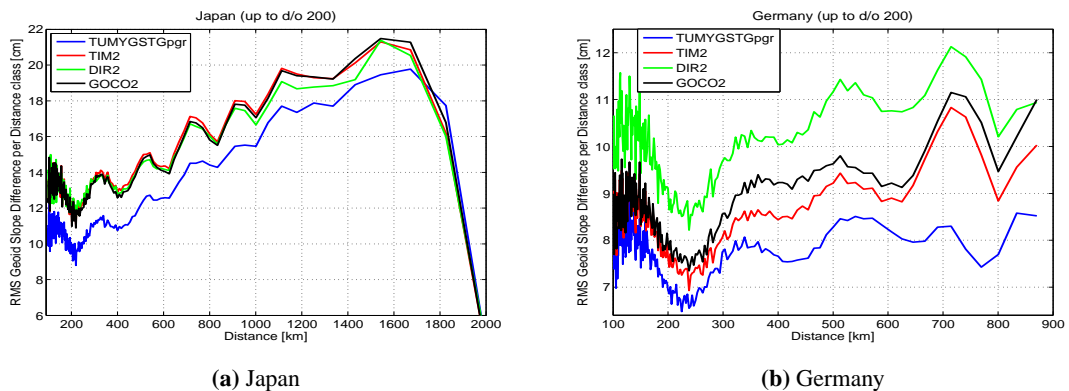
Figure 6.14: RMS geoid height differences for the regions of Japan (left) and Germany (right) classified by distance (d/o 200)

With this external comparison, we conclude that the gravity field model derived in this study is at least as good as the other GOCE models considered in this study. As we stated, the long data time span may be essential for the good quality of TUMYGSTGpgr.

6.3   Analysis of the Solution Derived by Combination of GRACE SST and GOCE SGG

On the one hand, due to the high sensitivity of GGT in the MB, GOCE has a very good performance at higher degrees; on the other hand, GRACE is very accurate at lower degree SH coefficients. They are complementary with each other. It is advantageous and desirable to combine them for a good solution covering both the lower and higher degree coefficients. We combine the normal equations of the SGG part (up to d/o 215) of model TUMYGSTGpgr with the normal equations of the GRACE gravity field model ITG-GRACE2010s (up to d/o 180), which is computed with 7 years of GRACE data from August 2002 to August 2009 (Mayer-Gürr et al., 2010). Even though GRACE contains information in the polar areas, its resolution is not adequate to fully compensate the instability of the combined normal equations caused by the polar gap. Therefore, as for the computation of TUMYGSTGpgr, the constraint in the polar areas is still applied to the linear system of the GRACE-GOCE combination, with a STD of 20 cm to EGM2008 on the $1° \times 1°$ resolution grid. The posteriori estimates of the variance components of the GOCE SGG part in Table 6.1 are used for the combination with GRACE. Based on these considerations, a new model named GOGRA01s has been computed.

The model GOGRA01s is compared with GOCO02s, together with the model TUMYGST-Gpgr, EIGEN-6S and ITG-Grace2010s. In Fig. 6.15 the degree RMS and cumulative geoid error are given on the left and right hand side, respectively. The solid lines represent the differences between the models and the reference model, GOCO02s. The dashed lines represent the corresponding formal error. From Fig. 6.15a one finds that the coefficients of lower degrees are determined very accurately due to GRACE, and that GOCO02s is closer to ITG-Grace2010s than GOGRA01s. This is because different filters are used in GOGRA01s and GOCO02s. The coefficients of degree from 2 to 60 in GOCO02s depend more on GRACE than these in GOGRA01s do. This makes that GOCO02s is closer to GRACE at the lower degree coefficients. Below about degree 105, the curves of ITG-GOCO and GOGRA01s-GOCO are quite close to each other. At degrees higher than 105 the two curves deviate. This may imply that GOCE improves ITG-GRACE2010s starting from degree 150. In Fig. 6.15b, the cumulative error in terms of geoid height show that the model TUMYGSTGpgr is less accurate than GOGRA01s due to the fact that the lower degree coefficients are determined with less accuracy based only on GOCE observations. But at higher degrees its cumulative geoid error is closer and closer to GOGRA01s. Since more data is used for TUMYGSTGpgr and GOGRA01s than for GOCO02s, the formal errors of both GOGRA01s and TUMYGSTGpgr are smaller than those of GOCO02s. From the formal error point of view, up to degree 200, the cumulative geoid errors of TUMYGSTGpgr and GOGRA01s are at the level of 2 to 3 cm (1σ).

The geoid differences between TUMYGSTGpgr and GOGRA01s are displayed in Fig. 6.16. With 1.45 cm STD value up to d/o 215, they are very close to each other. Larger differences are

(a) degree RMS

(b) cumulative geoid error
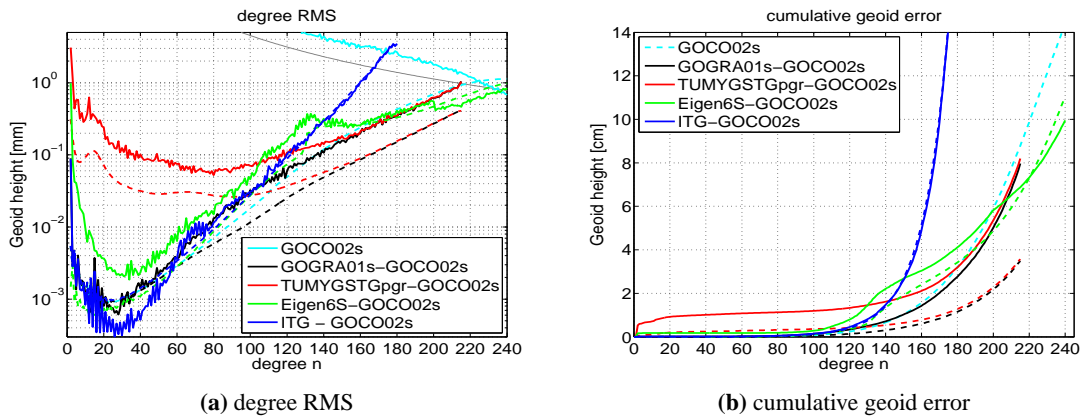
Figure 6.15: degree RMS and cumulative geoid error per degree

located at higher latitudes. More than 50% of the total (958,265) points of the geoid differences is smaller than 1 cm, and in about 90% of the total points the difference is smaller than 2 cm. It can be seen in upper-right panel that the RMS per latitude at the latitude of Himalaya is rather large. Very likely it is due to the differences between GOCE SST solution and GRACE solution.
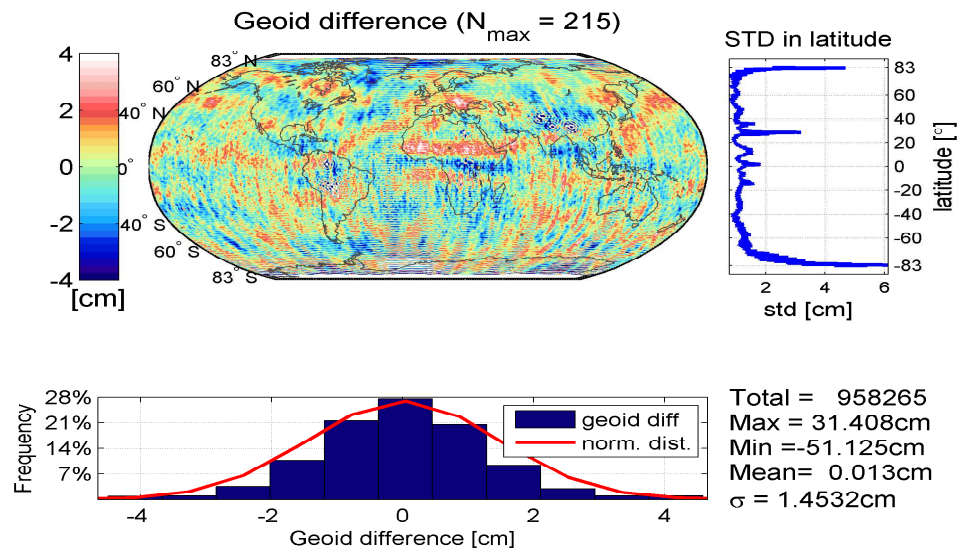
Figure 6.16: Geoid differences between GOGRA01s and TUMYGSTGpgr

As done for model TUMYGSTGpgr, the contribution of GOCE, GRACE and polar area constraints to GOGRA01s is analyzed as well. As shown in Fig. 6.17, the contribution of GOCE is large for the higher degree coefficients and that of GRACE is large for the lower degree coefficients. Even though the same constraints in the polar areas are applied to both GOGRA01s and

TUMYGSTGpgr, the effect is different on them since GRACE contributes some low- and medium-wavelength information to GOGRA01s. This leads to large differences between GOGRA01s and TUMYGSTGpgr in high-latitude areas, see Fig. 6.16. The mean contribution of GOCE and GRACE are 69.9% and 30.06%, respectively. The polar area constraint has a small value of 0.047%. Its contribution starts from about degree 140 to the zonal and near-zonal coefficients. This is different to TUMYGSTGpgr in which all the zonal and near-zonal coefficients get relatively large contribution from the polar constraint. It is reasonable that the contribution of polar constraint to GOGRA01s is smaller than to TUMYGSTGpgr, because below degree 140 the zonal and near-zonal coefficients are determined with good accuracy due to the contribution of GRACE.

(a) GOCE SGG

(b) GRACE

(c) Polar area constraint
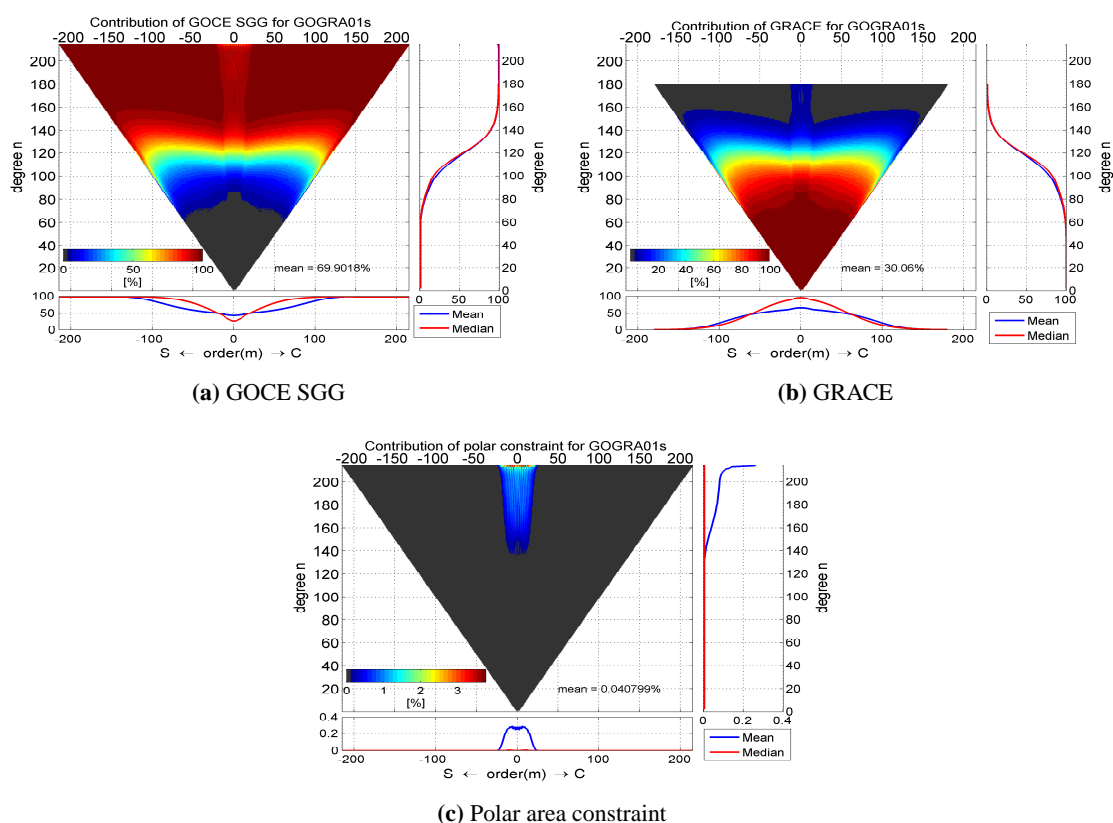
Figure 6.17: Contribution of GOCE SGG (upper left), GRACE (upper right) and polar area constraint (lower center) for GOGRA01s

The contribution analysis for model GOGRA01s demonstrates that GOCE and GRACE are complementary to each other. From the upper right panels of Figs. 6.17a and 6.17a, it is seen that below degree 60, the information from GRACE is dominant in GOGRA01s; From degree 60 increasing to 140, the information of GOCE increases from 0 to be dominant (almost 1); Higher than degree 140, the signal content of GOCE is superior in GOGRA01s. In the lower left panels of Figs. 6.17a and 6.17a, the contribution per order of GOCE is almost 1 for the orders higher than 100; GRACE contributes more information to the lower order coefficients than the higher order

ones. From the lower left and upper right of Fig. 6.17c, we see that the polar constraint inputs some information only to the coefficients of degree higher than 140 and order below about 15.

With the above computation and analysis, we can conclude that the combination of GOCE and GRACE is very useful for an accurate gravity field model in long-, medium- and short-wavelength.

6.4 Summary

A satellite-only combined solution was computed using SST and all four accurate gravitational gradiometry components. The combined normal equations are derived by taking the weighted sum of the normal equations of the various observation types. The weights of the individual components (observation types) are computed from the inverse of their variance components.

The contributions of individual components are computed by means of resolution matrices. Based on the analysis, it is found that the contribution of the V_{zz} component is the largest; the contribution of V_{xx} component is following; that of the V_{yy} and V_{xz} components are the third and fourth, respectively; the SST part is the fifth and its contribution is concentrated on the lower degree coefficients and especially those of higher orders; last but not least, the constraint in the polar areas contributes less than 0.3% to the complete solutions. The SGG part contributes more than 97%. The contribution of the SST part is only about 2%, nevertheless it is essential.

The advantage of the combination of SST and SGG part is demonstrated in our analysis. With the combination, the error curves of individual parts decrease. By comparing the degree RMS, the coefficients and geoid difference maps, it can be seen that our solution is consistent with other newly developed models.

From the triangular representation of the coefficient errors, we conclude that the estimated coefficients are most accurate for degrees from about 30 to 120. The polar gap effect is still existent, even though the constraint in polar areas has largely reduced it.

The geoid differences between TUMYGSTGpgr and other newly developed satellite-only models show that TUMYGSTGpgr agrees better with GOCO02s and TIM2 than with DIR2 and EIGEN-6S. The combined model EIGEN-6C is closer to TUMYGSTGpgr with a lower STD value of geoid differences than EGM2008. Inhomogeneities, probably due to the terrestrial ground data, are found from the geoid differences between TUMYGSTGpgr and combined models.

The VCM of our solution has been transformed into a global geoid error map. Since the ground tracks at high latitudes are denser than that at low latitudes, the formal error in terms of geoid height at high latitudes is smaller than that close to the equator. The estimated model is more precise in the northern hemisphere than in the southern hemisphere, due to the orbit altitude in the northern part being lower than in the southern part of the Earth. This is the effect of the orbit eccentricity and the orientation of the orbit ellipse.

The constraint in the polar gap areas is important for stabilizing the solution and decorrelating the zonal and near-zonal coefficients. According to the differences between the constrained and

unconstrained solution, we see that the constraint in polar areas affects only the zonal and near-zonal coefficients. From a comparison of the geoid differences between polar-constrained and unconstrained solutions, we conclude that very little information from the constraint is projected to the areas outside of the polar gaps.

Based on the validation, we find that TUMYGSTGpgr, together with TIM2, DIR2 and GOCO02s, are close to the "GPS-leveling" data with a precision of about 4 cm up to d/o 180, of 6 cm up to d/o 200, in terms of geoid height on Earth sphere (for the area of Germany), considering that the benchmark in Germany is very precise. Smaller RMS-values of TUMYGSTGpgr to the "GPS-leveling" data than those of the other models are likely due to its longer period of observation time.

The combination of GOCE and GRACE is very useful. The accuracy of the coefficients of lower degrees is greatly improved by including GRACE. The comparison between the GOCE-only model TUMYGSTGpgr and GOGRA01s shows that they are consistent with each other with an STD value of 1.5 cm up to d/o 215. The contribution of GOCE is higher (70%) than that of GRACE (30%) in the case of model GOGRA01s and is dominant at the coefficients above degree 140. The polar area constraint is still important. Since GRACE measurements do not contain information with a resolution as high as GOCE, it is necessary to apply this polar constraint in order to stabilize the equations and compensate the lack of high-resolution information in the polar areas.

7

Concluding Remarks

7.1   Discussion

With the gradiometric measurements collected by the GOCE satellite and the kinematic orbits, a gravity field model TUMYGSTGpgr has been derived using the integral equation approach for the SST part and a bandpass filter applied to the gradiometer data for the SGG part. As stated in the literature and presented in this study, the SST part achieves good accuracy for the lower degree coefficients and the SGG part for the higher degrees and orders.

Based on a forward computation (case study of the GOCE orbit), considering the cumulative effect the kinematic GOCE orbits are sensitive to the Earth's gravity field up to d/o 150. The largest disturbance of the orbit is caused by air drag. Since the air drag in flight direction, which is its largest components, is compensated by ion thrusters, the residual air drag and other mis-modeled and unmodeled perturbation forces are expected to be adequately taken into account by models and by the applied empirical accelerations.

The integral equation approach is efficient for gravity field modeling based on orbit data. It is fast due to the fact that the variational equations are solved by matrix operations, instead of orbit integration. The computation is parallelized with OpenMP interface for the three orthogonal spatial components, by making use of their independence in this approach. The correlation of the results with the used a-priori model is proved to be negligible.

Since the altitude of the orbit is low, the reconstructed models recovered from GOCE's kinematic orbits show good quality when compared to those based on CHAMP. The accuracy of the resulting gravity field model is not homogeneous because the accuracy of the orbit degrades towards high latitudes. In particular in high latitude and in the areas close to the South and North Magnetic Poles the accuracy of the orbit and of the estimated gravity field model is lower than at lower-latitude areas. By residual analysis, it can be shown that the reconstructed orbits are more consistent to the kinematic orbits than the reduced dynamic orbits provided in the product SST_PRD_2I.

7. CONCLUDING REMARKS

The empirical accelerations are derived by re-substitution after the global parameters are obtained. Similarities are found between the reconstructed empirical accelerations and the measured accelerometer data. This shows that the empirical accelerations really absorb a large part of the unmodeled effects. A correlation between the reconstructed accelerations and the Euler angles between GRF and LORF is found in this study. The GRF is kept close to LORF by magnetic torquing. Likely some of the ion thrust in the x-direction in the GRF is projected into the empirical parameters modeled in LORF.

Due to the existence of the polar gap, the normal equations have to be stabilized by a constraint of grid values in the two polar areas using an a-priori model. Since the constraint is set quite loose, the results show that there is little information projected into the areas covered by the GOCE orbits, based on comparison between the constrained and unconstrained solutions. This kind of constraints is helpful of decorrelating the zonal and near-zonal coefficients.

The observation model of the SGG part is derived and formulated in the GRF, by rotating the partials of the GGT w.r.t. the SH coefficients from the Earth-fixed frame to GRF. This avoids the rotation of the measured GGT, therefore the less sensitive components in the measurements do not degrade the results.

Apart from digital filtering, tests were carried out to suppress the noise of the gradiometer data in the LFB by modeling either with polynomials or with Fourier expansion. After the removal of the error in the LFB, the gravity field information can be derived from the gradiometer data. According to our experiments, due to its properties of continuity and preservation of the information inside the MB, a Fourier expansions is more suitable than polynomials.

The analysis of the GGT data (before SHA) shows the nice performance of the gradiometer. This can be seen from the trace as well as the noise floor of the individual components. The major tectonic features are found directly from the measurements. The noise in the frequencies below the MB is larger than that in the MB. In order to suppress this low-frequency noise, two filters are applied to the data. One is a FIR bandpass filter for a global data view in order to guarantee that no phase shift occurs due to filtering. The other one is a IIR bandpass filter for SHA because of its lower computation load.

The combination of SGG with SST shows the improvement of the combined solutions to the individual ones. According to the comparisons, our model TUMYGSTGpgr is quite consistent with other models derived from GOCE measurements. Based on external validation, our results show even better performance likely due to the longer data span used in our case.

Despite of its higher noise in the MB, the information content of V_{zz} is the highest, with a value of 32.7%. The components V_{xx} and V_{yy} contribute 28.04% and 26.08%, respectively. The contribution of the only accurate off-diagonal component V_{xz} is 10.93%, smaller than the three diagonal components, due to its larger STD value resulting in a smaller weight during the combination. V_{xz} shall be used in gravity field determination. The SST part contributes about 2% to the whole

solution. The zonal and near-zonal coefficients are de-correlated by the polar constraint, which contributes very small amount, less than 1%.

The formal error is propagated into geoid height errors on an Earth sphere. Because of the denser orbit coverage, the formal error of the geoid height at higher latitudes is smaller than at the lower ones. Furthermore, because the altitude of the satellite is lower in the northern hemisphere than in the southern hemisphere, the precision of the geoid heights of the estimated gravity field in the northern hemisphere is higher than in the southern hemisphere.

The result of the combination of GOCE SGG and GRACE shows the expected improvements compared to the GOCE-only and GRACE-only solution. It takes the advantages of both GOCE and GRACE. Due to the high sensitivity of GGT in the MB, GOCE shows very good performance at higher SH degrees and orders. GRACE is very accurate at lower degree and order SH coefficients. The two missions are complementary with each other. In our model GOGRA01s, the contribution of GOCE reaches 60.9% and GRACE contributes mainly to lower degree coefficients with an average value of 30.06%. By taking the advantages of both GOCE and GRACE, the model GOGRA01s shows its high accuracy at both lower and higher degree and order coefficients.

Our solution TUMYGSTGpgr achieves an accuracy of about 4 to 6 cm up to d/o 200, according to the formal error of the geoid height and the validation based on external data. With more and more data available, results of even better accuracy are hopefully obtained.

7.2 Outlook

A certain format of normal equations is defined and applied in this study. The normal equations of SST and SGG part are computed from their observation equations, respectively. Each day's normal equations are stored on disk with our defined format and then accumulated. It can be applied to other observation types such as SLR and terrestrial data, too.

In our result, we find that the intersection of the formal error and the signal is above d/o 215. This means that from GOCE data one can determine a gravity field model higher than this value. A new solution up to even higher degree and order is therefore in the planning.

With the software developed in this study, we will process and analyze the continuing stream of GOCE data. It is hopefully used also for some future missions.

Long wavelength gravity field signal can be measured by SLR with high accuracy. It is therefore desirable to combine GOCE and GRACE with SLR for a better performance at the lowest degree coefficients.

It is important for a GOCE solution to handle the polar gaps of the northern and southern hemispheres. One may use terrestrial or airborne gravity data for the northern polar areas. For the southern polar areas, there is no sufficient terrestrial data available. Introducing some other information in these areas for a GOCE solution is therefore unavoidable.

List of Abbreviations

AIUB	Astronomisches Institut der Universität Bern
CHAMP	CHAllenging Minisatellite Payload
CMA	Common mode acceleration
CPR	Cycle per revolution
DEOS	Delft Institute for Earth-Oriented Space research
DIR	Direct approach
DMA	Differential mode acceleration
EGF	Earth gravitational field
ESA	European Space Agency
FFT	Fast Fourier Transform
ECEF	Earth-centered earth-fixed
GRF	Gradiometer reference frame
FIR	Finite impulse response
GINS	Géodésie par Intégrations Numériques Simultanées
GG	Gravitational gradient
GGT	Gravitational gradient tensor
GINS	Géodésie par Intégrations Numériques Simultanées
GOCE	Gravity field and steady-state Ocean Circulation Explorer
GRACE	Gravity Recovery And Climate Experiment
GRGS	Groupe de Recherche de Geodesie Spatiale
IAPG	Institut für Astronomische und Physikalische Geodäsie
IAU	International Astronomical Union
IERS	International Earth Rotation and reference systems Service
IIR	Infinite impulse response
LORF	Local orbital reference frame
MB	Measurement band
MBW	Measurement bandwidth
NEQ	Normal equation
OMC	Observed minus computed
PSD	Power spectral density

RMS	Root mean square
PSO	Precise science orbit
SGG	Satellite gravitational gradiometry
SH	Spherical harmonic
SHA	Spherical harmonic analysis
SHS	Spherical harmonic synthesis
SLR	Satellite laser ranging
RSO	Rapid science orbit
SST	Satellite-to-satellite tracking
STD	Standard deviation
SNR	Signal-to-Noise Ratio
SOFA	Package of standards Of fundamental astronomy
SPW	Spacewise approach
TIM	Timewise approach
VCM	Variance-covariance matrix

References

Bae TS (2006) Near real time precise orbit determination of low earth orbit satellites using an optimal GPS triple-difference technique. PhD Thesis, the Ohio State University

Barnett V, Lewis T (1994) Outliers in Statistical Data, 3rd edn. Wiley

Beutler G (2004) Methods of Celestial Mechanics: Volume I: Physical, Mathematical, and Numerical Principles. Springer, Berlin

Bock H, Jäggi A, Meyer U, Visser P, van den Ijssel J, van Helleputte T, Heinze M, Hugentobler U (2011) GPS-derived orbits for the GOCE satellite. Journal of Geodesy DOI 10.1007/s00190-011-0484-9, tbd: online first

Bouman J (1998) Quality assessment of geopotential models by means of redundancy decomposition. DEOS Progress Letters (98.2):81–89

Boxhammer C, Schuh W (2006) GOCE gravity field modeling: Computational aspects — free kite numbering scheme. In: Flury J, Rummel R, Reigber C, Rothacher M, Boedecker G, Schreiber U (eds.) Observation of the Earth System from Space, Springer-Verlag, Berlin/Heidelberg, pp 209–224, DOI 10.1007/3-540-29522-4_15

Bruinsma S, Marty J, Balmino G, Biancale R, Foerste C, Abrikosov O, Neumayer H (2010) GOCE gravity field recovery by means of the direct numerical method. In: Lacoste-Francis H (ed.) Proceedings of the ESA Living Planet Symposium, ESA Publication, ESA/ESTEC

Burša M, Picha J (1971) Parameters of the normal gravity field deduced from satellite observations. Studia Geophysica et Geodaetica 15(2):124–131, DOI 10.1007/BF01623909

Casotto S, Fantino E (2007) Evaluation of methods for spherical harmonic synthesis of the gravitational potential and its gradients. Advances in Space Research 40(1):69–75, DOI 10.1016/j.asr.2007.01.021

Cesare S (2008) GOCE - Performance requirements and budgets for the gradiometrc mission. project report, ThalesAleniaSpace, Torino

Dach R, Hugentobler U, Fridez P, Meindl M (2007) Bernese GPS Software Version 5.0. Tech. Rep., Astronomical Institute, University of Bern

Ditmar P, Klees R (2002) A Method to Compute the Earths Gravity Field from SGG/SST Data to be Acquired by the GOCE satellite. Tech. Rep., Delft University Technology, Delft, The Netherlands

Eanes R (2002) The CSR4.0 Global Ocean Tide Model. ftp://www.csr.utexas.edu/pub/tide

Eicker A, Mayer-Gürr T, Ilk K (2006) An integrated Global/Regional gravity field determination approach based on GOCE observations. In: Flury J, Rummel R, Reigber C, Rothacher M, Boedecker G, Schreiber U (eds.) Observation of the Earth System from Space, Springer-Verlag, pp 225–237, DOI 10.1007/3-540-29522-4_16

European Space Agency (1999) Gravity field and steady-state ocean circulation mission, report for mission selection of the four candidate earth explorer missions. Tech. Rep., ESA SP-1233(1), ESA publications division, Noordwijk

European Space Agency (2006) GOCE L1b products user handbook. Technical note, SERCO/DATAMAT Consortium

Flechtner F (2007) AOD1B product description document for product releases 01 to 04. Tech. Rep., GeoForschungszentrum Potsdam

Floberghagen R, Fehringer M, Lamarre D, Muzi D, Frommknecht B (2011) Mission design, operation and exploitation of the Gravity field and steady-state Ocean Circulation Explorer. Journal of Geodesy DOI 10.1007/s00190-011-0498-3

Förste C, Bruinsma S, Shako R, Marty JC, Flechtner F, Abrikosov O, Dahle C, Lemoine JM, Neumayer K, Biancale R, Barthelmes F, Knig R, Balmino G (2011) A new combined global gravity field model including GOCE data from the collaboration of GFZ Potsdam and GRGS Toulouse. Presented to EGU-2011, Vienna

Freeden W, Michel V, Nutz H (2008) Satellite-to-Satellite tracking and satellite gravity gradiometry (Advanced techniques for high-resolution geopotential field determination). Journal of Engineering Mathematics 43(1):19–56, DOI 10.1023/A:1016577524288

Frommknecht B (2008) Integrated sensor analysis of the GRACE mission. PhD Thesis, Fakultät für Bauingenieur- und Vermessungswesen, TU München

Gerlach C, Földvary L, Svehla D, Gruber T, Wermuth M, Sneeuw N, Frommknecht B, Oberndorfer H, Peters T, Rothacher M, Rummel R, Steigenberger P (2003) A CHAMP-only gravity field model from kinematic orbits using the energy integral. Geophysical Research Letters 30(20), DOI 10.1029/2003GL018025

GOCE HPF (2009) Product Specification for Level-2 Products and Auxiliary Data Products. GO-ID-HPF-GS-0041, Issue 6.1

Goiginger H, Hoeck E, Rieser D, Mayer-Guerr T, Maier A, Krauss S, Pail R, Fecher T, Gruber T, Brockmann J, Krasbutter I, Schuh WD, Jäggi A, Prange L, Hausleitner W, Baur O, Kusche J (2011) The combined satellite-only global gravity field model GOCO02S, presented at the 2011 General Assembly of the European Geosciences Union, Vienna, Austria

Gruber T (2010) Reference systems and gradiometry. Tech. Rep., European GOCE Gravity Consortium, Muenchen

Gruber T, Visser PNAM, Ackermann C, Hosse M (2011) Validation of GOCE gravity field models by means of orbit residuals and geoid comparisons. Journal of Geodesy DOI 10.1007/s00190-011-0486-7

Han SC (2003) Efficient global gravity determination from satellite-to-satellite tracking (SST). PhD Thesis, the Ohio State University

Hawkins D (1980) Identification of Outliers. Springer

REFERENCES

van Hees R, Bouman J, Koop R, Rispens S, de Witte S (2008) HPF ICD to PDS-DPA. Tech. Rep., GOCE High Level Processing Facility

Hofmann-Wellenhof B, Moritz H (2006) Physical geodesy. Springer

IAU SOFA Board (2010) IAU SOFA software collection. URL http://www.iausofa.org

Ilk K, Klose U (1984) Zur numerischen Quadratur von Integralen im Rahmen der Bestimmung des hochfrequenten Anteils des Gravitationsfeldes. In: Schneider M (ed.) Die Arbeiten des Sonderforschungsbereiches 78 Satellitengeodäsie der Technischen Universität München 1983, Veröffentlichungen der BEK, Astronomisch-Geodätische Arbeiten, 45, Verlag der Bayerischen Akademie der Wissenschaften, pp 173–189

Jäggi A, Beutler G, Mervart L (2010a) GRACE gravity field determination using the celestial mechanics approach first results. In: Mertikas SP (ed.) Gravity, Geoid and Earth Observation, International Association of Geodesy Symposia, vol 135, Springer Berlin Heidelberg, pp 177–184

Jäggi A, Bock H, Prange L, Dach GBR (2010b) Processing LEO Data and Gravity Field Determination at AIUB: A Status Report. International GNSS Service, IGS workshop 2010, 28 June - 2 July 2010, Newcastle upon Tyne

Jäggi A, Bock H, Prange L, Meyer U, Beutler G (2011) GPS-only gravity field recovery with GOCE, CHAMP, and GRACE. Advances in Space Research 47(6):1020–1028, DOI 10.1016/j.asr.2010.11.008

Johannessen JA, Balmino G, Provost CL, Rummel R, Sabadini R, Sünkel H, Tscherning C, Visser P, Woodworth P, Hughes C, Legrand P, Sneeuw N, Perosanz F, Aguirre-Martinez M, Rebhan H, Drinkwater M (2003) The European gravity field and steady-state ocean circulation explorer satellite mission: Its impact on geophysics. Surveys in Geophysics 24(4):339–386, DOI 10.1023/B:GEOP.0000004264.04667.5e

Johnson RA, Wichern DW (2001) Applied Multivariate Statistical Analysis, 5th edn. Prentice Hall

Klees R, Ditmar P, Broersen P (2003) How to handle colored observation noise in large least-squares problems. Journal of Geodesy 76(11-12):629–640, DOI 10.1007/s00190-002-0291-4

Knocke PC, Ries JC, Tapley BD (1988) Earth radiation pressure effects on satellites. AIAA/AAS Astrodynamics Conference, Minneapolis

Koch K, Kusche J (2002) Regularization of geopotential determination from satellite data by variance components. Journal of Geodesy 76(5):259–268, DOI 10.1007/s00190-002-0245-x

Koch KR, Kuhlmann H, Schuh W (2010) Approximating covariance matrices estimated in multivariate models by estimated auto- and cross-covariances. Journal of Geodesy 84:383–397, DOI 10.1007/s00190-010-0375-5

Koop R (1993) Global gravity field modelling using satellite gravity gradiometry. new series 38, Netherlands Geodetic Commission, Delft

Kurtenbach E, Mayer-Gürr T, Eicker A (2009) Deriving daily snapshots of the earth's gravity field from GRACE L1B data using Kalman filtering. Geophysical Research Letters 36(17), DOI 10.1029/2009GL039564

Kusche J (2002) Inverse Probleme bei der Gravitationsfeldbestimmung mittels SST- und SGG-Satellitenmissionen. DGK, Reihe C 548, Habilitationsschrift. Deutsche Geodätische Kommission

Kusche J, Klees R (2002) Regularization of gravity field estimation from satellite gravity gradients. Journal of Geodesy 76(6-7):359–368, DOI 10.1007/s00190-002-0257-6

Lemoine F, Kenyon S, Factor J, Trimmer R, Pavlis N, Chinn D, Cox C, Klosko S, Luthcke S, Torrence M, Wang Y, Williamson R, Pavlis E, Rapp R, Olson T (1998) The Development of the Joint NASA GSFC and the National Imagery and Mapping Agency (NIMA) Geopotential Model EGM96. Tech. Rep., Goddard Space Flight Center, Greenbelt, USA, NASA Technical Paper NASA/TP1998206861

Liu X (2008) Global gravity field recovery from satellite-to-satellite tracking data with the acceleration approach. PhD Thesis, Delft University of Technology

Lühr H, Rentz S, Ritter P, Liu H, Häusler K (2007) Average thermospheric wind patterns over the polar regions, as observed by CHAMP. Ann Geophys 25:1093–1101

Lyard F, Lefevre F, Letellier T, Francis O (2006) Modelling the global ocean tides: modern insights from FES2004. Ocean Dynamics 56(5-6):394–415, DOI 10.1007/s10236-006-0086-x

Marty J, Bruinsma S, Balmino G, Abrikosov O, Foerste C, Rothacher M (2005) Gravity field recovery with simulated GOCE observations. AGU Fall Meeting, San Francisco

Massey FJ (1951) The Kolmogorov-Smirnov test for goodness of fit. Journal of the American Statistical Association 46(253):68–78, DOI 10.2307/2280095

Mayer-Gürr T (2006) Gravitationsfeldbestimmung aus der Analyse kurzer Bahnbögen am Beispiel der Satellitenmissionen CHAMP und GRACE. PhD Thesis, Universität Bonn

Mayer-Gürr T (2007) ITG-Grace03s: The latest GRACE gravity field solution computed in Bonn. presentation at GSTM+SPP, Potsdam

Mayer-Gürr T, Eicker A, Kurtenbach E, Ilk K (2010) ITG-GRACE: global static and temporal gravity field models from GRACE data. In: Flechtner F, Gruber T, Güntner A, Mandea M, Rothacher M, Schöne T, Wickert J (eds.) System Earth via Geodetic-Geophysical Space Techniques, Springer Berlin Heidelberg, Berlin, Heidelberg, pp 159–168, DOI 10.1007/978-3-642-10228-8_13

McCarthy D, Petit G (eds.) (2004) IERS Conventions, Verlag des Bundesamts für Kartographie und Geodäsie

Métris G, Xu J, Wytrzyszczak I (1999) Derivatives of the gravity potential with respect to rectangular coordinates. Celestial Mechanics and Dynamical Astronomy 71(2):137151, DOI 10.1023/A:1008361202235

Metzler B (2007) Spherical cap regularization a spatially restricted regularization method tailored to the polar gap problem. PhD Thesis, Graz University of Technology

Metzler B, Pail R (2005) GOCE data processing: The spherical cap regularization approach. Studia Geophysica et Geodaetica 49(4):441–462, DOI 10.1007/s11200-005-0021-5

Migliaccio F, Reguzzoni M, Sansò F (2004) Space-wise approach to satellite gravity field determination in the presence of coloured noise. Journal of Geodesy 78(4-5):304–313, DOI 10.1007/s00190-004-0396-z

REFERENCES

Migliaccio F, Reguzzoni M, Gatti A, Sansò F, Herceg M (2011) A GOCE-only global gravity field model by the space-wise approach. In: Ouwehand L (ed.) Proceedings of the 4th International GOCE User Workshop, ESA Publication SP-696, ESA/ESTEC

Montenbruck O, Gill E (2000) Satellite Orbits: Models, Methods and Applications, 1st edn. Springer, Berlin

Montenbruck O, Gill E, Kroes R (2005a) Rapid orbit determination of LEO satellites using IGS clock and ephemeris products. GPS Solutions 9(3):226–235, DOI 10.1007/s10291-005-0131-0

Montenbruck O, van Helleputte T, Kroes R, Gill E (2005b) Reduced dynamic orbit determination using GPS code and carrier measurements. Aerospace Science and Technology 9(3):261–271, DOI 10.1016/j.ast.2005.01.003

Oppenheim AV, Schafer RW (2009) Discrete-Time Signal Processing, 3rd edn. Addison Wesley

Pail R, Metzler B, Preimesberger T, Lackner B, Wermuth M (2007) GOCE quick-look gravity field analysis in the framework of hpf. In: Fletcher K (ed.) Proceedings of the 3rd International GOCE User Workshop, ESA SP-627, ESA, pp 325–332

Pail R, Goiginger H, Schuh WD, Hck E, Brockmann JM, Fecher T, Gruber T, Mayer-Gürr T, Kusche J, Jäggi A, Rieser D (2010) Combined satellite gravity field model GOCO01S derived from GOCE and GRACE. Geophysical Research Letters 37:L20314, DOI 10.1029/2010GL044906

Pail R, Bruinsma S, Migliaccio F, Förste C, Goiginger H, Schuh WD, Höck E, Reguzzoni M, Brockmann JM, Abrikosov O, Veicherts M, Fecher T, Mayrhofer R, Krasbutter I, Sansò F, Tscherning CC (2011a) First GOCE gravity field models derived by three different approaches. Journal of Geodesy DOI 10.1007/s00190-011-0467-x

Pail R, Goiginger H, Schuh WD, Hck E, Brockmann JM, Fecher T, Mayrhofer R, Krasbutter I, Mayer-Gürr T (2011b) Goce-only gravity field model derived from 8 months of goce data. In: Ouwehand L (ed.) Proceedings of the 4th International GOCE User Workshop, ESA Publication SP-696, ESA/ESTEC

Pavlis NK, Holmes SA, Kenyon SC, Factor JK (2008) An Earth Gravitational Model to Degree 2160:EGM2008, Presented to EGU-2008, Vienna, Austria

Peterseim N, Schlicht A, Stummer C, Yi W (2011) Impact of cross winds in polar regions on goce accelerometer and gradiometer data. In: Ouwehand L (ed.) Proceedings of the 4th International GOCE User Workshop, ESA Publication SP-696, ESA/ESTEC

Petit G, Luzum B (eds.) (2010) IERS Conventions

Putney B, Kolenkiewicz R, Smith D, Dunn P, Torrence MH (1990) Precision orbit determination at the NASA Goddard Space Flight Center. Advances in Space Research 10(3-4):197–203, DOI 10.1016/0273-1177(90)90350-9

Reubelt T (2009) Harmonische Gravitationsfeldanalyse aus GPS-vermessenen kinematischen Bahnen niedrig fliegender Satelliten vom Typ CHAMP, GRACE und GOCE mit einem hoch auflösenden Beschleunigungsansatz. PhD Thesis, Geodätisches Institut der Universität Stuttgart

Rowlands D, Marschall JA, McCarthy J, Moore D, Pavlis D, Rowton S, Luthcke S, Tsaoussi L (1995) GEODYN II system description. Contractor report, Hughes STX Corp., Greenbelt, MD

Rummel R (1986) Satellite gradiometry. In: Sünkel H (ed.) Mathematical and Numerical Techniques in Physical Geodesy, Lecture Notes in Earth Sciences, vol 7, Springer, pp 317–363, DOI 10.1007/BFb0010135

Rummel R (1992) Geodesy. In: Nierenberg W (ed.) Encyclopedia of Earth System Science, Cr-L, vol 2, Academic Press, pp 253–262

Rummel R (1996) Symposium G7 "New Concepts in Space Geodesy". ZfV - Zeitschrift für Vermessungswesen 121(4):166–168

Rummel R, van Gelderen M (1992) Spectral analysis of the full gravity tensor. Geophysical Journal International 111(1):159–169, DOI 10.1111/j.1365-246X.1992.tb00562.x

Rummel R, Yi W, Stummer C (2011) GOCE gravitational gradiometry. Journal of Geodesy 85(11):777–790, DOI 10.1007/s00190-011-0500-0

Savcenko R, Bosch W (2008) EOT08a - empirical ocean tide model from multi-mission satellite altimetry. DGFI Report 81, Deutsches Geodätisches Forschungsinstitut (DGFI), München

Schneider M (1968) Zur dynamischen Nutzung der Bahnen knstlicher Satelliten. Bundesministerium für wissenschaftliche Forschung (BMwF), Weltraumforschung, Forschungsbericht FB W 68-55, Deutsche Gesellschaft für Flugwissenschaften (DFG)

Schneider M (1969) Outline of a general orbit determination method. In: Champion KSW, Smith PA, Smith-Rose RL (eds.) Space Research IX, Proceedings of Open Meetings of Working Groups (OMWG) on Physical Sciences of the 11th Plenary Meeting of the Committee on Space Research (COSPAR), Tokyo, North-Holland Publishing Company, pp 37–40

Schuh WD (2002) Improved modeling of SGG-data sets by advanced filter strategies. In: ESA-Project: ESA-Project "From Eötvös to mGal+", WP 2, Final-Report, European Space Agency

Sechi G, Andrè G, Andreis D, Saponara M (2006) Magnetic attitude control of the GOCE satellite. In: Danesy D (ed.) Proceedings of the 6th International ESA Conference on Guidance, Navigation and Control Systems, ESA Publication SP-606, European Space Agency, vol 606, p 37

Shampine LF, Gordon MK (1975) Computer Solution of Ordinary Differential Equations: The Initial Value Problem. Freeman

Sillard P, Boucher C (1996) Improvement of the transformation between ITRF and Doppler-Realized WGS84. Journal of Geodesy 70(11):768–780, DOI 10.1007/BF00867155

Sneeuw N (2000) A semi-analytical approach to gravity field analysis from satellite observations. DGK, Reihe C 527, Verlag der Bayerischen Akademie der Wissenschaften

Stummer C, Fecher T, Pail R (2011) Alternative method for angular rate determination within the GOCE gradiometer processing. Journal of Geodesy DOI 10.1007/s00190-011-0461-3

Tapley BD (1989) Fundamentals of orbit determination. In: Sansó F, Rummel R (eds.) Lecture Notes in Earth Sciences, vol 25, Springer Verlag, DOI 10.1007/BFb0010546

Teunissen PJG (2009) Dynamic data processing: Recursive least-squares. Vereniging voor Studie-en Studentenbelangen te Delft

REFERENCES

Teunissen PJG, Amiri-Simkooei AR (2008) Variance component estimation by the method of Least-Squares. In: Xu P, Liu J, Dermanis A (eds.) VI Hotine-Marussi Symposium on Theoretical and Computational Geodesy, vol 132, Springer, Berlin, Heidelberg, pp 273–279

Tscherning CC (1993) Computation of covariances of derivatives of the anomalous gravity potential in a rotated reference frame. manuscripta geodaetica 18(3):115–123

Visser P (2007) GOCE gradiometer validation by GPS. Advances in Space Research 39(10):1630–1637, DOI 16/j.asr.2006.09.014

Visser P (2009) GOCE gradiometer: estimation of biases and scale factors of all six individual accelerometers by precise orbit determination. J Geod 83(1):69–85, DOI doi:10.1007/s0019000802358

Visser P, van den Ijseel J, van Helleputte T, Bock H, Jäggi A, Beutler G, Heinze M (2010) Rapid and precise orbit determination for the goce satellite. In: Lacoste-Francis H (ed.) Proceedings of the ESA Living Planet Symposium, ESA Publication SP-686, ESA/ESTEC

Wahr J, Swenson S, Zlotnicki V, Velicogna I (2004) Time-variable gravity from GRACE: first results. Geophysical Research Letters 31:4 PP., DOI 200410.1029/2004GL019779

Watson D (1992) Contouring: A Guide to the Analysis and Display of Spatial Data, 1st edn. Pergamon

Yi W (2007) GRACE and gravity field - observation models, simulations and analysis. Master Thesis, Institut für Astronomische und Physikalische Geodäsie, Technischen Universität München

Reports in the *CGE Reports* series (ISSN 2195-7126)
Veröffentlichungen in der Schriftenreihe „CGE Reports" (ISSN 2195-7126)

No. 1: Pail R., Hugentobler U., Rummel R., Seitz F., Bosch W., Angermann D., Steigenberger P., Gruber T., Bouman J., Schmidt M., Völksen C., Neidhardt A., Schreiber U., Horwath M. (2012): Research and Development Programme 2011–2015, Forschungs- und Entwicklungsprogramm 2011–2015, ISBN 978-3-934205-32-1.

No. 2: Yi, Weiyong (2012): The Earth's gravity field from GOCE, ISBN 978-3-934205-34-5.